

Final Report for the Period of Performance

6/1/1996 - 30/11/2000

Grant number: NAG8-1229 (Material Science, Ground)

## **INVESTIGATION OF VIBRATIONAL CONTROL OF THE BRIDGMAN CRYSTAL GROWTH TECHNIQUE**

Prepared by

Alexandre I. Fedoseyev

Principal Investigator

Contributing researchers:

J.I.D. Alexander

R.S. Feigelson

E.V. Zharikov

A.G. Ostrogorsky

C. Marin

M.P. Volz

E.J. Kansa

M.J. Friedman

**Center for Microgravity and Materials Research**

**THE UNIVERSITY OF ALABAMA IN HUNTSVILLE**

## TABLE OF CONTENTS

ACKNOWLEDGEMENTS	3
1. INTRODUCTION	4
2. MODEL OVERVIEW	8
2.1 Heat and mass transfer in Bridgman melt configurations	8
2.2 Theory and numerical modeling approach	9
2.2.1 The physical model	9
2.2.2. Translational, polarized (CVS) vibrations and “g-jitter” induced flows	10
2.2.3. Angular, rotational vibrations and ACRT flows	13
2.3. Solution methods and software	14
3. INVESTIGATION OF THERMAL VIBRATIONAL CONVECTION	15
4. CONCLUSIONS	20
5. REFERENCES	21
6. PUBLICATIONS AND PRESENTATIONS	26
<b>APPENDIX A:</b> SELECTED JOURNAL AND CONFERENCE PAPERS PUBLISHED	

## ACKNOWLEDGEMENTS

Funding for this project was provided by NASA under grant NAG8-1229.

The authors would like to acknowledge the following for their collaboration in this research effort: Prof. Robert Feigelson and colleagues at the Center for Materials Research of Stanford University; Prof. Eugene Zharikov at the General Physics Institute, Russian Academy of Sciences, Moscow; and Prof. Iwan Alexander at Mechanical and Aerospace Engineering and National Center for Microgravity Research at Case Western Reserve University, Cleveland.

In addition, we would like to thank the following university groups that provided valuable data and consultation: Prof. Alex Ostrogorsky and Dr. C. Marin of Rensselaer Polytechnic Institute, Troy, NY; Prof. Mark Friedman of University of Alabama in Huntsville. We would like to acknowledge the contribution of Dr. Edward Kansa from the Lawrence Livermore National Laboratory, Dr. Martin Volz from Marshall Space Flight Center, and Prof. George Dulikravich of the University of Texas at Arlington on the analysis of magnetic field suppression of flows in semiconductor melts.

Finally, we would like to thank Ms. Lynne Carver for invaluable help in preparing journal papers, conference presentations, and this report.

## 1. INTRODUCTION

The character of natural buoyant convection in rigidly contained inhomogeneous fluids can be drastically altered by vibrating the container. Vibrations are expected to play a crucial influence on heat and mass transfer onboard the ISS. It is becoming evident (especially as demonstrated during the workshop held in ESTEC, September 98 [1]) that substantial vibrations will exist on the ISS in the wide frequency spectrum.

In general, vibrational flows are very complex and governed by many parameters. It is almost impossible to correctly predict vibrational effects empirically; a sophisticated theoretical approach and numerical modeling are therefore essential. Available flight experiment data clearly show that, once initiated by "g-jitter", convective flows can exist for a long period of time in a follow-up period of low gravity environment [2-7].

In many terrestrial crystal growth situations, convective transport of heat and constituent components is dominated by buoyancy driven convection arising from compositional and thermal gradients. Thus, it may be concluded that vibro-convective flow can potentially be used to influence and even control transport in some crystal growth situations.

Control of convective transport continues to be an important aspect of crystal growth research. A control of convection through static and rotating magnetic fields has been used by several groups. In some cases, experimenters seeking to avoid buoyancy effects through use of microgravity environments have expressed interest in the use of magnetic fields even under low gravity conditions. However, there are many instances, whether due to materials properties or other practical considerations, where the use of magnetic fields to induce stirring or suppress flow may not be an option. In such cases, vibrational control becomes an attractive alternative.

Experimental results clearly show that vibrational convection can provide enhanced nutrient fluxes[8-14]. Numerical modeling work at the Institute de Mécaniques des Fluides de Marseille has confirmed that vibration can also be used to suppress buoyancy-driven flows. Furthermore, it was shown that such suppression would be very effective at reduced gravity levels of  $10^{-4}$  g or less. This raises the exciting possibility that, under microgravity conditions, specific controlled vibration can be used to mask undesirable "g-jitter" induced convective effects. Such g-jitter convection can be caused by quasi-steady residual acceleration [15,16] (due to gravity gradient and atmospheric drag effects [7]), as well as transient and oscillatory acceleration disturbances [18,19]. It is understood that high-quality low gravity environments can only be provided for specific limited time intervals. For a space station, interruptions and disturbances are inevitable consequences of docking, pointing maneuvers, astronaut activity, etc., and will limit the maximum attainable duration of high quality microgravity periods. While active vibration isolation can be a partial solution, it will not solve the problems that might arise due to the quasi-steady and very low-frequency acceleration components related to the gravity gradient and other orbital factors. Alternatively, rather than using vibration to suppress low-gravity flows, one might envisage using vibration to provide flow regimes tailored to particular crystal growth experiments. These flows would not be accessible under terrestrial conditions due to strong natural convection effects.

Bouyancy driven vibro-convective motion occurs when oscillatory displacement of a container wall induces the acceleration relative to the inner fluid. The vibration may be viewed as a time-dependent modulation of steady gravity in some cases.

In a closed container filled with a homogeneous fluid, the fluid moves as a rigid body with a container. If, however, the fluid density is nonuniform, fluid motion may ensue. Of course, the magnitude of this motion, depends on the orientation of the vibrational direction with respect to the local density gradients. Note that similar to Rayleigh-Bernard configurations there may be a "critical" threshold for the coupled vibrational frequency and amplitude, to cause convection. Interestingly, in the case of a constant density fluid, the fluid motion may also take place at angular vibration, axial rotational vibration or ACRT flows (caused by accelerated - decelerated rotation of a crucible) due to inertia forces. For density gradients caused by temperature, such motion is called thermo-vibrational.

It has been recognized for some time that oscillatory or pulsatile flow can significantly alter the transfer of mass, heat and momentum in fluid systems [2,8-14,20-33]. For example, analyses of heat transfer in laminar oscillating flows have shown that at high frequencies the effective diffusivity,  $k_{\text{eff}}$ , behaves like  $k_{\text{eff}} \sim \Delta x^2 (\omega \nu)^{1/2} / L$  and, at low frequencies,  $k_{\text{eff}} \sim \Delta x^2 \omega^{3/2} \nu^{1/2} / L$ , where  $\nu$  is the kinematic viscosity,  $\Delta x$  is the cross stream average of a fluid element over half the period of the oscillation and  $L$  is a characteristic geometric distance (e.g., between the plates). It was also shown that heat transfer was most enhanced when the characteristic heat transfer time was equal to half the oscillation period [24].

A great deal of work related to the theory of thermo-vibrational convection has been carried out by Russian research groups. The main focus has been on thermo-vibrational convection starting with the work of Zenkovskaya and Simonenko [34], who first obtained the equations of thermo-vibrational convection in a high frequency limit. Since then, there have been many theoretical [2,35-42] and some experimental (e.g., [12,13,43]) studies of the stability of thermo-vibrational flows. One of the main conclusions that can be drawn from these works is that for vibrations with specially chosen axes, the natural buoyancy driven convection which would prevail in the absence of vibration can be suppressed at certain frequencies and amplitudes [39]. This has recently been analyzed in more detail [44] using the full equations of motion and Gershuni's time-averaged equations. The possibility of using vibration as a means of controlling and suppressing convection was confirmed. A comprehensive introduction to vibrational convection and other time-dependent modulation can be found in reference [45].

The problem of vibrational convection arising due to other buoyancy sources, such as compositional density gradients, has also been approached. The onset of purely solutal and thermosolutal convection has been examined for horizontally stratified layers subject to vertical vibration [46,47].

There are several examples of experimental work concerning the influence of vibration on crystal growth from melts and solutions [28-37]. These works involved a wide range of intensities and frequencies (including ultrasound). Experimental attempts to understand how low frequency vibrational stirring might be used to effect rapid mixing in melts and solutions have been made by Liu et al. [54]. The influence of low frequency vibration on interface location and shape during Bridgman growth of cadmium telluride was examined by Lu et al. [55]. Other effects of low frequency vibrational convection on crystal growth include the increase in local perfection of binary compound semiconductors [57], changes in interface shape [30], and the faceting of germanium crystals [58]. The elimination of striations in indium antimonide may also be due to the formation of a stationary melt flow due the torsional vibration [59].

Experimental results also clearly show that in certain cases vibrational convection can provide enhanced nutrient fluxes during the solution growth of Rochelle salt and potassium dihydrogen phosphate (KDP) [60,61]. Zharikov [62, 14] identified a characteristic low

frequency ( $< 100$  Hz) vibrational flow regime in the liquid near a growing crystal. The form, dimensionality and intensity of the flow were studied and the effects of vibration on heat and mass transfer were analyzed for the case of Czochralski and Bridgman growth of sodium nitrate ( $\text{NaNO}_3$ ). He showed that the vibration could drastically alter the character of flow and concluded that vibration could exert a strong influence on transport and impurity incorporation and locally influence growth kinetics.

Uspenskii and Favier [63] considered the interaction between high frequency and natural convection in Bridgman-type crystal growth. They used the average thermo-vibrational flow equations to theoretically examine the problem of suppressing natural convection using high frequency ( $\sim 10^4$  Hz) low amplitude vibration and compared the efficiency of vibrational damping to that of magnetic field damping. Using the physical properties representative of GaSb, GaAs, etc., they found that under terrestrial conditions, (for high electroconductivities) the magnetic field is more effective than vibration in damping flow in the horizontal Bridgman configuration. In contrast, for vertical Bridgman, lateral vibration was most effective. The horizontal velocity decreased by a factor of 10 and the vertical velocity by about 20. In comparison a 1 Tesla vertical magnetic field only resulted in a factor of 6 decrease in maximum velocity. They speculated that it might be possible to combine magnetic fields with vibration to reach optimal damping conditions.

Vibrational flows are very complex and governed by many parameters. Here is an incomplete list:  $Pr$ ,  $Ra$ ,  $Ra_v$ ,  $Ra_c$ ,  $\alpha_c$ ,  $\omega$ ,  $L/R$  (Prandtl, Rayleigh, vibrational Rayleigh, compositional Rayleigh numbers,  $\alpha_c = Ra_v / Ra_{vc}$ , and aspect ratio),  $\phi$ ,  $\alpha$  (angles between gravity vector, vibrational direction and the axis (temperature gradient)),  $E$ ,  $R_0/L$  (Ekman number, relative distance to the center of rotation for angular, rotational vibrations, a type of vibrational action) and others. The range of parameter values is very wide:  $Pr$  is of the order of 0.01 for semiconductors, and of the order of 10 for oxide melts; gravity variation result in  $Ra$  values of  $10^6$  to  $10^{10}$  on a ground to  $1 - 10^3$  in space, and similar for  $Ra_v$ ; the frequency range is from 0.01Hz to 100Hz and higher, etc. (see Table 1).

Farooq and Homsy [41] examined in depth the 2D case of a rectangular cavity, but an understanding of 3D thermo-vibrational flows has not yet developed. Therefore, a sophisticated theoretical approach and numerical modeling together with experimental research are essential for the investigation of vibrational control of convective flows.

**Table 1. Typical material properties for semiconductor and oxides melts, and nondimensional problem parameters for numerical experiments**

Dynamic parameters

Frequency	0.001 ... 1 ... 100 Hz
Angular amplitude	$\varepsilon = 0 \dots 15 \dots 45^\circ$

Geometry

Height	$L = 2 \text{ to } 10 \text{ cm}$
Diameter	$D = 1 \text{ to } 2 \text{ cm} \Rightarrow L/D = 10 \text{ to } 5$

Material properties

Pr	0.01 (Ge, Si) ... to 15 (oxides)
Viscosity	$\nu = 1.3 \cdot 10^{-2} \text{ cm}^2/\text{s}$
Diffusivity	$D = 1.3 \cdot 10^{-4} \text{ cm}^2/\text{s}$
Thermal diffusivity	$k = 1.3 \cdot 10^{-1} \text{ cm}^2/\text{s}$
Thermal expansion coeff.	$\beta = 2.5 \cdot 10^{-4} \text{ K}^{-1}$

Body forces and related parameters

Gravity	$g = 1 \dots 0.01 \dots 10^{-5} \dots 10^{-6} g_0$
Temperature gradient	$G = 25 \text{ to } 100 \text{ K/cm}$
Magnetic field	$Ha = 0 \dots 2,000 \dots 20,000$

Nondimensional parameters

$$Pr = \frac{\nu}{\kappa}, Ra = \frac{\beta \Delta T g L^3}{\kappa \nu}, Ra_\Omega = \frac{\beta \Delta T \Omega_0^2 L^4}{\kappa \nu}, E = \frac{\nu}{\Omega_0 L^2},$$

$$Ra_\nu, L/D, h/R, Ha, Sc = \nu/D, Ra_C^*, \omega = \Omega_0 / L^2 \kappa$$

Vibration types:

translational, circular polarized, angular, g-jitter

## **2. MODEL OVERVIEW**

### **2.1 Heat and Mass Transport in Bridgman melt configurations**

The research involved a numerical and experimental investigation of vibro-convective transport regimes applied to the control of convection and transport during crystal growth by the Bridgman technique. A typical Bridgman crystal growth configuration is shown in Fig. 1. This work was motivated by recent developments in the understanding of low frequency thermo-vibrational convection, results from recent Space Flight experiments on “g-jitter” induced flows, and by current and planned experimental work at Stanford University and the General Physics Institute, Russian Academy of Sciences in Moscow [1-5,40,64,65]. Although in principle, the theoretical research described below can be carried out independently of a particular experimental program, close collaboration with experimental groups created a firm practical foundation.

We investigated five types of vibro-convective flows caused by translational, angular, rotational vibrations (these results may be extended also for ACRT flows [92,94], due to accelerated-decelerated rotation of a crucible-tank), and flows due to “g-jitter”. The flow regimes were investigated by applying each type of vibrations to different materials to find regimes beneficial to control or suppress of convection.

In section 2.2, the physical model and basic equations are described. The equations for translational, polarized vibrations and “g-jitter” are given in section 2.2.2. Section 2.2.3 describes the equations for angular, rotational and ACRT type vibrations. Solution methods are discussed in section 2.3.

The basic problem analyzed was the suppression or control of buoyancy-driven convection in melts during plane-front directional solidification. The work involved the analysis of vibrational interaction with natural convection and its effects on the temporal evolution of melt temperature and composition during growth (section 3). The philosophy behind our approach is to use numerical modeling in two ways: synergistically, with experimental developments, and as a predictive tool. The synergism with experiment allows careful interpretation of both experimental and modeling results for what can be a highly non-linear physical situation. To explore regimes and system properties currently inaccessible to the experiment, the model was also used as a predictive tool. Initially guided by previous results [34-67,70,73-76], the work involved an extensive investigation of vibrational flow regimes with and without the presence of natural buoyancy-driven convection. As we progressed toward our goal of defining the applicability of vibrational control of convection, we compared the ability of vibration to suppress flow with that of a magnetic field.



## 2.2. Theory and numerical modeling

### 2.2.1 The physical model

The plane-front directional solidification of a binary solid from a melt of initial composition  $c_\infty$  in a cylindrical ampoule of radius  $R$  was considered. Fig.1. shows a physical model. Calculations were made for two basic physical set-ups.

The first involves purely 3D thermo-vibrational convection in a differentially cylindrical cavity with no consideration of solidification. These calculations were performed in conjunction with the flow visualization experiments, ongoing experiments conducted by R.S. Feigelson at Stanford University.

The second setup is closer to a practical solidification situation and involves explicit consideration of plane-front solidification in a long cylindrical ampoule. Solidification takes place as the ampoule is translated along a temperature gradient. For this model system, translation of the ampoule is simulated by supplying a doped melt of bulk composition  $c_\infty$  at a constant velocity  $V_m$  at the top of the computational space (inlet), and withdrawing a solid of composition  $c_s = c_s(x, t)$  from the bottom. The crystal-melt interface is located at a distance  $L$  from the inlet; the radius of the ampoule is  $R$ . The temperature at the interface is taken to be  $T_m$ , the melting temperature of the crystal, while the upper boundary is held at a higher temperature  $T_h$  (Fig. 2). On the ampoule walls the heat transfer between the furnace and the ampoule will be

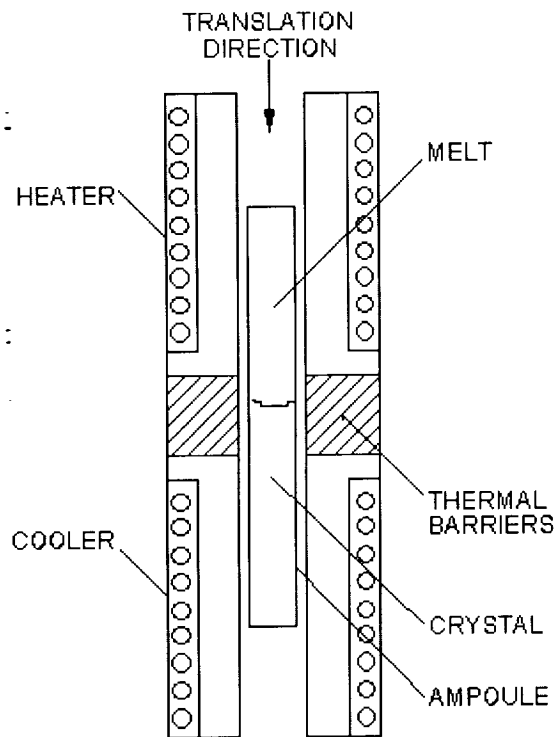


Fig. 1 The Bridgman-Stockbarger method in which the crystal is directionally solidified by translating an ampoule between hot and cold zones of a furnace.

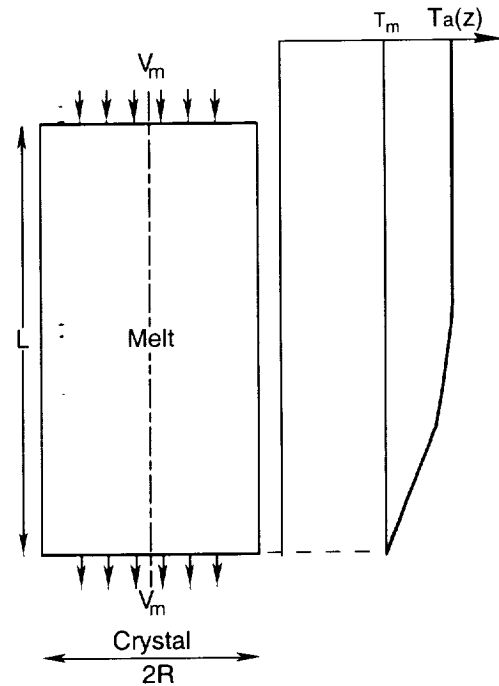


Fig. 2. The model Bridgman system.  $V_m$  is the ampoule translation rate,  $T_a(z)$  is the heater profile and  $T_m$  is the melting temperature

modeled using a suitable heat transfer condition. The heating profile includes a long isothermal hot zone. In this case, thermo-vibrational convection in the upper portion of the melt will be weak or nonexistent. Thus, the effect of our implicit neglect of the no-slip condition at the top of a real ampoule will be negligible.

Both thermal, solutal and thermo-solutal convection were considered. For thermo-vibrational convection we considered two types of vibration, translational and angular. The frame of reference for the calculations is an experimental frame attached to the walls of the ampoule. Thus, depending on the type of displacement induced by the vibrating walls, the equations governing momentum mass and heat transport will take on a different form. In section 2.2.2 we consider translational and polarized vibrations, followed by angular and rotational vibration in section 2.2.3.

### 2.2.2. Translational, polarized vibration and “g-jitter”

Translational vibration corresponds to a linear displacement such as, for example,  $u = d_1 \cos \alpha$ , where  $d_1$  is a real vector corresponding to the displacement amplitude. Thus, a point is displaced back and forth upon the same line. Polarized vibrations are characterized by a displacement  $u = \text{Re}\{d e^{-i\omega t}\}$  where  $d = d_1 - i d_2$  (see Fig. 3). Here the instantaneous vibration direction rotates in the polarization plane defined by the real vectors  $d_1$  and  $d_2$ . A case of orthogonal equal length vectors  $d_1$  and  $d_2$ , the circular polarized vibration, is called a CVS method [32]

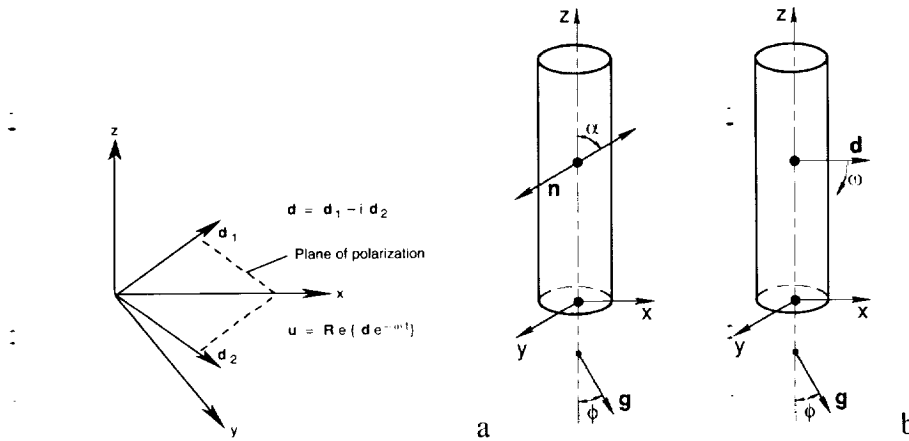


Figure 3: Translational vibration (a),  $d_1$  or  $d_2 = 0$ , and polarized vibration (b),  $d_1, d_2 \neq 0$ ;  $\phi$  is the angle between gravity vector and axis of ampoule,  $\alpha$  is the angle between direction of vibrations and axis of ampoule

For a reference frame fixed to the vibrating ampoule both these types of vibrations result in equations of the following form [17,46,47]. The momentum and continuity equations are

$$\frac{\partial \mathcal{N}}{\partial t} + (\mathbf{V} \cdot \nabla) \mathbf{V} + \nabla p - \text{Pr} \nabla^2 \mathbf{V} = \text{RaPr}(\Theta + \alpha_c c) \mathbf{k} + \text{Ra}_v \text{Pr}(\Theta + \alpha_c c) \mathbf{f}(\mathbf{x}, \omega, t) \quad (1)$$

$$\nabla \cdot \mathbf{V} = 0 \quad (2)$$

while the continuity and heat - mass transport equations are:

$$\frac{\partial \Theta}{\partial t} + \mathbf{V} \cdot \nabla \Theta = \nabla^2 \Theta \quad (3)$$

$$\frac{\partial c}{\partial t} + \mathbf{V} \cdot \nabla c = \text{Pr} \text{Sc}^{-1} \nabla^2 c \quad (4)$$

where length, time and velocity have been scaled by  $R_0$ ,  $R_0^2/\kappa$  and  $\kappa/R_0$ , where  $R_0$  is the radius of the ampoule and  $\kappa$  is the thermal diffusivity,  $\mathbf{k}$  is a unit vector in the direction of gravity.

The Prandtl, Schmidt, Rayleigh and solutal -thermal buoyancy ratio are given by

$$\text{Pr} = \frac{\nu}{\kappa}, \quad \text{Sc} = \frac{\nu}{D}, \quad \text{Ra} = \frac{\beta \Delta T g R^3}{\nu \kappa}, \quad \alpha_c = \frac{\beta_c c_\infty}{\beta \Delta T},$$

where  $\beta$  and  $\beta_s$  are the thermal and solutal expansion coefficients and  $\Delta T$ ,  $g$ ,  $\nu$  and  $D$  are the characteristic longitudinal temperature difference in the melt, gravitational acceleration, kinematic viscosity and solute diffusivity, respectively. The dimensionless number  $\text{Ra}_v$  and  $\text{Ra}_{vc}$  are vibrational Rayleigh numbers defined as

$$\text{Ra}_v = \frac{d \omega^2 \beta \Delta T R^3}{\nu \kappa}, \quad \text{Ra}_{vc} = \frac{d \omega^2 \beta_c \Delta c R^3}{\nu \kappa},$$

For the solidification calculations, the following boundary conditions apply at the crystal-melt interface.

$$\theta=0, \mathbf{V} \cdot \mathbf{N} = \text{Pe}, \mathbf{V} \times \mathbf{N} = \mathbf{0} \quad (5)$$

$$\frac{\partial c}{\partial n} = \text{Pe} \text{Sc} \text{Pr}^{-1} (1 - k) c$$

where  $\text{Pe} = V_m R / k$  is the Peclet number,  $k$  is the distribution coefficient and  $\mathbf{N}$  is the unit vector normal to the planar crystal melt interface. At the top of the ampoule,

$$\theta=1, \mathbf{V} \cdot \mathbf{N} = \text{Pe}, \mathbf{V} \times \mathbf{N} = \mathbf{0} \quad (6)$$

$$\frac{\partial c}{\partial n} = \text{Pe} \text{Sc} \text{Pr}^{-1} (c - 1)$$

where, due to the fact that we consider the top of the computational space as an inlet, the last condition represents conservation of mass. Finally, on the ampoule walls we have

$$\mathbf{V} \cdot \mathbf{N} = \text{Pe}_g \text{Sc} \text{Pr}^{-1}, \quad \mathbf{V} \cdot \mathbf{e}_w = 0, \quad \nabla \Theta \cdot \mathbf{e}_w = h(\Theta - \Theta_a(z)), \quad \nabla C \cdot \mathbf{e}_w = 0, \quad (7)$$

where  $\Theta_a(z)$  is the heating profile,  $h$  is a dimensionless heat transfer coefficient and  $\mathbf{e}_w$  is normal to the walls.

The body force  $\mathbf{f}(\mathbf{x}, t) = \mathbf{n} \sin(\Omega t)$  for translational vibration, where  $\mathbf{n}$  is direction of vibration (Fig. 3b);  $\mathbf{f}(\mathbf{x}, t) = [\cos(\Omega t), \sin(\Omega t), 0]^T$  for polarized vibrations and  $\mathbf{f}(\mathbf{x}, t) = \mathbf{J}_g(t)$ , the 3D vector of “g-jitter” microaccelerations (e.g. measured SAMS microacceleration data or the numerical “g-jitter” model).

*Vibrating immersed body.* The application of vibration through placement of vibrating bodies at specific locations in the melt can also be modeled as a variant of the translational and polarized vibration problems.

*Average equations for small amplitude vibrational displacements*

The dimensionless groups  $Ra_v$  and  $Ra_{vc}$  in equation (1) should not be confused with the vibrational Rayleigh number  $Ra_g$  of Gershuni [34-39,45-76], which arises for monochromatic vibration as follows. If the amplitude  $|\mathbf{d}|$  of a sinusoidal vibration is sufficiently small, i.e.,  $|\mathbf{d}| \ll \min(R/\beta\Delta T, R/\beta c_\infty)$ , the velocity, temperature and concentration fields may be represented as the superposition of mean (averaged) fields and small oscillating components [34,74]. In this case, application of the averaging method [45] yields

$$\frac{\partial \bar{\mathbf{v}}}{\partial t} + (\bar{\mathbf{v}} \cdot \nabla) \bar{\mathbf{v}} = -\nabla \bar{p} + \text{Pr} \nabla^2 \bar{\mathbf{v}} + \text{Pr} Ra_g (\bar{\Theta} + \alpha_c \bar{C}) \mathbf{k} + \text{Pr} Ra_g (\bar{\mathbf{w}} \cdot \nabla) [(\bar{\Theta} + \alpha_c \bar{C}) \mathbf{n} - \bar{\mathbf{w}}], \quad (8)$$

$$\nabla \cdot \bar{\mathbf{v}} = 0, \quad (9)$$

where  $Ra_g = (\beta \omega d R \Delta T)^2 / \kappa \nu$  is Gershuni's thermo-vibrational Rayleigh number and  $\alpha_c = \beta c_\infty / \beta \Delta T$  is the ratio of the solutal and thermal buoyancy. The vector  $\bar{\mathbf{w}}$  is the slowly time-varying part (may be stationary) of the oscillating part of the velocity field and satisfies

$$\nabla \cdot \bar{\mathbf{w}} = 0, \quad \nabla \wedge \bar{\mathbf{w}} = \nabla [(\bar{\Theta} + \alpha_c \bar{C})] \wedge \mathbf{n}, \quad (10)$$

and is the solenoidal part of the vector field  $(\bar{\Theta} + \alpha_c \bar{C}) \mathbf{n} = \bar{\mathbf{w}} + \nabla \varphi$ . The average temperature and solute fields satisfy

$$\frac{\partial \bar{\Theta}}{\partial t} + (\bar{\mathbf{v}} \cdot \nabla) \bar{\Theta} = \nabla^2 \bar{\Theta}, \quad (11)$$

and

$$\frac{\partial \bar{C}}{\partial t} + (\bar{\mathbf{v}} \cdot \nabla) \bar{C} = \frac{\text{Pr}}{\text{Sc}} \nabla^2 \bar{C}. \quad (12)$$

The boundary conditions for the averaged equations are of the same form as (4)-(8) and the component of  $\bar{\mathbf{w}}$  normal to the boundaries must be equal to 0 on the ampoule walls and equal to  $Pe$  at the top of the ampoule and at the melt-crystal interface. For thermally buoyant natural and vibrational convection we simply set  $\alpha_c = 0$  and for no solidification,  $Pe = 0$ .

For the problems under consideration, the averaged equations result in the steady-state equations. Our recently developed novel methods of numerical bifurcation theory [69] are suitable for the analysis of stability and onset of vibrational flow regimes.

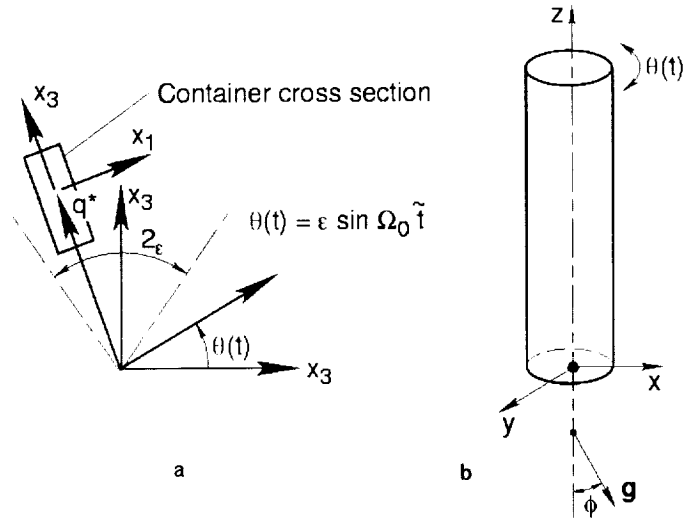


Figure 4: Diagram of the system for angular vibration to be modeled (a),  $\mathbf{x}^*$  and  $\mathbf{x}$  are the two coordinate systems related by (10). The container is rotated at an angle  $T(t) = \epsilon \sin(\Omega_0 t)$  about a center of rotation at  $\mathbf{x}^* = \mathbf{0}$ . Axial vibrations and ACRT (b), are rotation about the axis  $z$ , the angle  $T(t) = \epsilon \sin(\Omega_0 t)$  for vibrations or  $T = T(t)$  (selected ACRT law).

### 2.2.3. Angular, rotational vibration and ACRT flows

The equations of motion for angular and rotational vibrations take on a more complicated form.

*Angular vibration.* Let  $\mathbf{x}^* = (x_1^*, x_2^*, x_3^*)$  be a fixed Cartesian coordinate system (see Fig. 4a). A container of length  $L$  is subjected to an angular vibration  $q(t)$  in the  $x_1^*-x_3^*$  plane. The position vector to the mass center of the cylinder is parallel to the side of the cylinder and is given by

$$\mathbf{q}^* = R_0[-\sin \theta \mathbf{i}_1^* + \cos \theta \mathbf{i}_3^*], \quad (13)$$

where  $R_0$  is the distance from the origin  $\mathbf{0}^*$  to the mass center of the cylinder and

$$\theta(t) = \varepsilon \sin \Omega_0 \bar{t}, \quad (14)$$

where  $\bar{t}$  is time.

*Rotational vibration and ACRT (Fig. 4b).* The container is rotated about the axis  $z$ , the angle  $T(t) = \varepsilon \sin(\Omega_0 t)$  for vibrations or  $T = T(t)$  (selected ACRT law, see [77]);  $\varphi$  is the angle between the gravity vector and axis of ampoule. The ACRT type of vibration was not in the original research plan. We just note here, that the software developed in the frame of current research is capable for the investigation of ACRT flows without any modifications.

In the reference frame moving (rotating) with the ampoule the momentum equation has a form

$$\frac{\partial \mathbf{V}}{\partial t} + (\mathbf{V} \cdot \nabla) \mathbf{V} + \rho^{-1} \nabla p - \nu \nabla^2 \mathbf{V} = \gamma T \mathbf{g} + (\boldsymbol{\omega} \times \mathbf{q}) \times \boldsymbol{\omega} + 2\mathbf{V} \times \boldsymbol{\omega} + \mathbf{q} \times \boldsymbol{\omega} \quad (15)$$

where  $\boldsymbol{\omega} = [0, \varepsilon \Omega_0 \cos(\Omega_0 t), 0]^T$  for angular vibration and  $\boldsymbol{\omega} = [0, 0, \varepsilon \Omega_0 \cos(\Omega_0 t)]^T$  for rotational vibration and  $\boldsymbol{\omega} = [0, 0, dT(t)/dt]^T$  for ACRT. The problem has the following nondimensional determining parameters:  $\Omega = \Omega_0 L^2 / \kappa$ , the dimensionless frequency and  $\vartheta = R_0 / L$ ; the Prandtl,  $Pr$ , Rayleigh,  $Ra$ , vibrational Rayleigh  $Ra_\Omega$ , and Ekman,  $E$ , numbers are

$$Pr = \frac{\nu}{\kappa}, Ra = \frac{\beta \Delta T g L^3}{\kappa \nu}, Ra_\Omega = \frac{\beta \Delta T \Omega_0^2 L^4}{\kappa \nu}, E = \frac{\nu}{\Omega_0 L^2},$$

where  $\beta$ ,  $\nu$ ,  $g$  and  $\kappa$  are the coefficient of thermal expansion, kinematic viscosity, gravitational acceleration and thermal diffusivity, respectively. Note that, the system of equations (15) differ from the usual equations in the absence of rotation in that two additional terms are present in each equation; the Coriolis term which is proportional to  $\varepsilon Pr / E$ , and the centrifugal term which is proportional to  $\varepsilon^2 \vartheta Ra_\Omega Pr$  at  $\mathbf{x} = \mathbf{0}$  and varies with position in the ampoule. The importance of the latter term depends on the dimensions of the amplitude of the angular vibration,  $\varepsilon$ , and the ratio  $\vartheta$ . Note that the centrifugal terms give rise to periodic forcing that fluctuates about a mean value at twice the period of the angular vibration.

Since the above system of equations has not been well studied, we used a conservative approach for the study of angular vibrations and confined our investigation to a parametric study of flow regimes and transitions for thermo-vibrational situations only, without solidification.

### 2.3. Solution method and software

The equations are solved in primitive variable form (velocity-pressure, temperature, etc.) using a Finite Element Method package developed by the Principle Investigator [65-67,71-73]. The package, *FEMINA/3D*, is designed to solve 2D and 3D problems and includes four basic groups of modules each distinguished by its function: automatic 2D/3D mesh generation, optimal renumbering or matrix-bandwidth/front optimization, a computational part including efficient algebraic solvers and visualization/graphics software. The novel methods developed and implemented allow a use of efficient, same order finite element approximation, for velocity and pressure, and robust iterative solution techniques of a high accuracy (up to  $10^{-9}$ ).

The *FEMINA/3D* code has overcome most of the disadvantages associated with the memory requirements of FEM methods by using an efficient combination of solution methods. These include the iterative solution of large non-symmetric algebraic systems using iterative IDR-CGS type techniques [72,82-84,91] with preconditioning by incomplete decomposition of high order in a compact matrix storage scheme. That reduced the computation time by one to two orders of magnitude and memory requirements by an order for 3D flows over currently available commercial codes (e.g. CFD2000). Typical solution time for a transient 3D problem with a 200,000 unknowns is a couple of hours on a SGI O2 workstation (much faster on CRAY-C90); solution time for a 3D steady convective flow problem is a couple of minutes.

*FEMINA/3D* simultaneously considers the continuity equation directly with the momentum equations at each solution step. This eliminates many problems related to boundary conditions and places only slight limitations on the time step size for transient problems (these limitations are related to the physical nature of the problem rather than the numerical method itself).

The package has been carefully verified by comparison of numerical and analytical solutions as well as comparison with results obtained by other methods and experimental data for 2D and 3D viscous flows and thermal convection problems [65,67,73,86,91].

A wide range of problems has been investigated using this package, including time-dependent fluid flow (64, see also [72] and references therein) and mass and heat transfer in complex geometries [64,78,79]. Other practical applications include thermal convection and transport during crystal growth processes [33,40,79,80,81] and other engineering problems.

### 3. INVESTIGATION OF VIBRATIONAL CONTROL OF CONVECTIVE FLOWS IN BRIDGMAN MELT CONFIGURATIONS

Results of the investigation of vibrational control of the Bridgman crystal growth technique have been published in journal papers, conference proceedings and presented at conferences, workshops and colloquia, listed in Section 6.

A summary of results from our publications [33,40,64-70,86-92,99] is presented below.

(i) An efficient numerical code, a main research tool, for the modeling of three-dimensional thermal-vibrational convection for several types of vibrations has been developed by the PI based on the finite element code FEMINA/3D created by the PI [71,72]. The code was carefully tested on experimental benchmarks, and published numerical data for a variety of 2D and 3D viscous flows and thermal convection problems [65,67,73]. The novel methods developed and implemented allow a use of efficient, same order finite element approximation, for velocity and pressure, and robust iterative solution techniques of a high accuracy (up to  $10^{-9}$ ). This reduced the computation time by one to two order of magnitude and memory (by 8 times less) for 3D flows over currently available commercial codes (e.g. CFD2000). Typical solution time for a transient 3D problem with 200,000 unknowns is a couple of hours on a SGI O2 workstation; solution time for a 3D steady convective flow problem is a couple of minutes [86,90,91]. A new efficient numerical continuation approach, based on the multiquadric method, for the stability and bifurcation analysis was developed [69, 89].

(ii) A parametric study of the general 3D buoyant-vibrational flow in a Bridgman growth system has been performed. This includes the characterization of flows induced by translational, rotational and circular polarized (also known as CVS, after R. Feigelson [32]) vibrations under selected microgravity and Earth conditions for typical semiconductor and oxide melts [33,40]. A typical flow pattern for translational vibration is presented in Fig. 5. Even in **0g** we have found flows, i.e. characterized by a fluid flowing up one side and down the other (relative to the Figure). The temperature distribution remain almost unperturbed for semiconductor melts (due to the low  $Pr$  number), therefore a separate plot for  $\Delta T$  is provided.

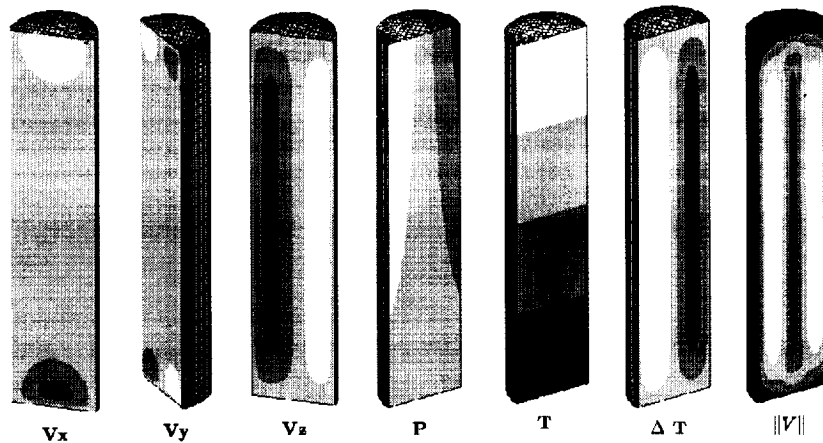


Figure 5. Typical instantaneous 3D melt flow patterns for translational vibration at  $0g$ ,  $Ra=0$ ,  $Ra_v=7.25 \cdot 10^4$ ,  $\omega = 100Hz$ , lateral vibration: velocity components  $V_x, V_y, V_z$ , pressure  $P$ , temperature  $T$ , temperature disturbance  $\Delta T$ , and velocity module  $|V|$ . Black color designate the minimal value plotted, white one - the maximal value

The angular orientation between the direction of vibration and ampoule axis (with imposed  $T$ -gradient) has been studied for translational vibrations. When that angle is zero, there is no influence



of the vibration on a flow even if vibrational Raleigh number is very high. The maximum observed effect corresponds to an angle of 90 degrees.

The flow patterns for rotational vibrations flow regimes are presented in Fig. 6. Maximal values of flow velocity are observed at the end of the ampoule which is more far from the rotation origin.

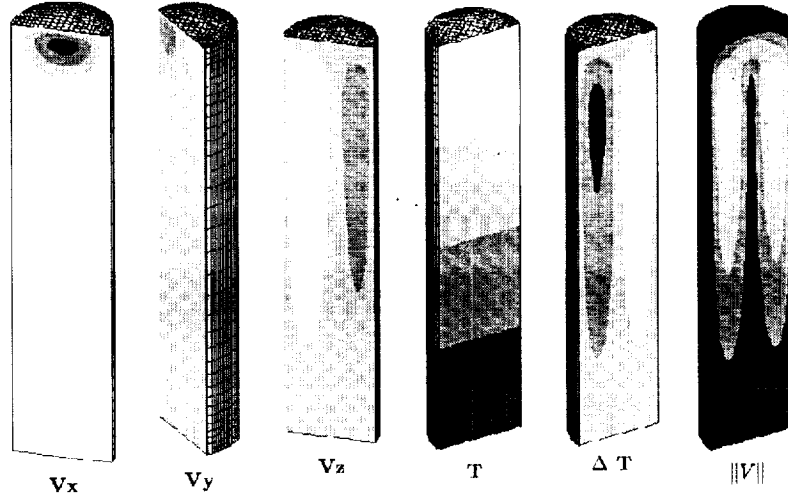


Figure 6. Typical instantaneous 3D flow patterns for angular vibration at  $0g$ ,  $Ra=0$ ,  $Ra_v=4.6 \cdot 10^5$ ,  $\omega = 100\text{Hz}$ , lateral vibration: velocity components  $V_x, V_y, V_z$ , temperature  $T$ , temperature disturbance  $\Delta T$ , and velocity module  $|V|$ .

We found that both translational and angular vibration can cause average melt flow for a range of parameters typical of practical semiconductor and oxide growth. For a given vibration amplitude and frequency, angular and circular polarized vibrations result in more intensive melt flow than translational ones.

(iii) The influence of vibrations on the heat - mass transfer becomes much more significant for oxide melts due to their low thermodiffusivity (Prandtl number  $\sim 10$ , that is four orders higher than for semiconductors). These flow patterns are shown in Fig. 7 for the case of circular polarized vibration.

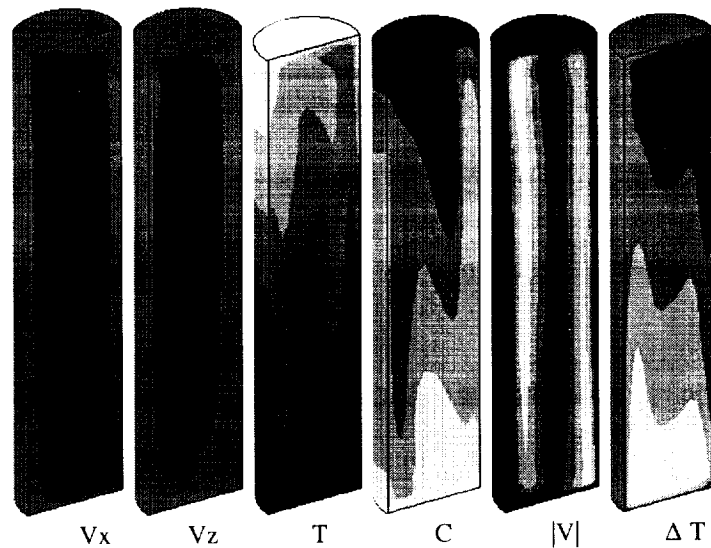


Figure 7. Instantaneous 3D flow patterns for circular polarized vibration,  $Ra = 7.25 \cdot 10^3$ ,  $Ra_v = 7.4 \cdot 10^6$ ,  $\omega = 10\text{Hz}$ : velocity components  $V_x, V_z$ , temperature  $T$ , concentration  $C$ , velocity module  $|V|$ , and temperature disturbance  $\Delta T$ .

Initially (at the  $time = 0$ ) the species concentration was  $c=1$  at the lower quarter of the cylinder and  $c = 0$  elsewhere. The evolution of the species concentration (process of mixing) is shown in Fig.8 together with minimum and maximum values of velocity components. Complete mixing

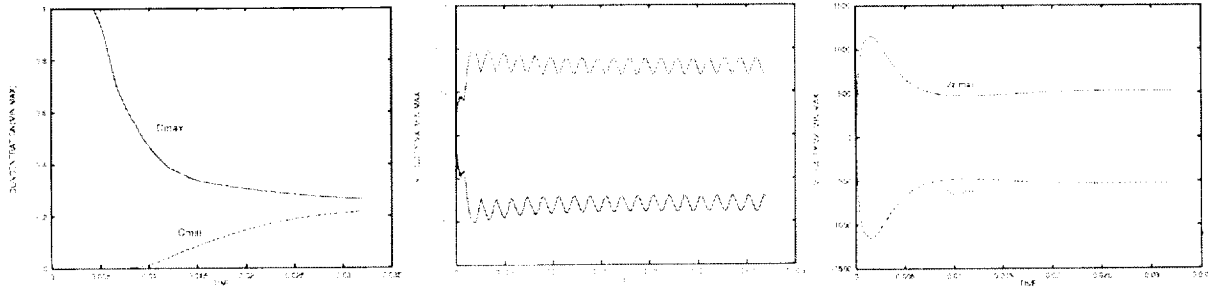


Figure 8. Temporal evolution of concentration  $C$  (left, min. and max. of  $C$ ) and velocity extremums ( $V_x$ , center, and  $V_z$ , right) for circular polarized vibration,  $Ra=7.25 \cdot 10^3$ ,  $Ra_t=7.4 \cdot 10^6$ ,  $\omega = 10\text{Hz}$ .

occurs in about ten seconds. The heat transfer (local Nusselt number at the top and the bottom) is also enhanced by about an order of magnitude. If the frequency of vibration is higher, of the order of 100Hz (for fixed  $Ra_t$ ), then the change of heat and mass transfer due to vibrations becomes less significant. That corresponds to the experimental observations by R.Feigelson [32,74]. The visualization of results of numerical modeling, the 3D movies of vibrational flows, heat and mass transfer are available on the Web, [http://uahtitan.uah.edu/alex/cvs\\_numeric.html](http://uahtitan.uah.edu/alex/cvs_numeric.html) for some cases.

(iv) The oscillation of flow values, in addition to a drive frequency, shows  $\omega/2$  subharmonic in the pressure field. Similar experimental spectra was observed by M.Schatz [75]. With the increasing of vibration intensity, additional oscillating flow frequencies (superharmonics) appear.

(v) The results on the influence of forced vibration on g-jitter induced flows are available [64]. G-jitter was implemented using SAMS microacceleration data from the USML-2 (Fig. 9). Initially the translational vibration were applied in the direction parallel to the ampoule axis (T-gradient), trying to damp flow variation with time caused by g-jitter (predicted by the averaged equation theory [45]).

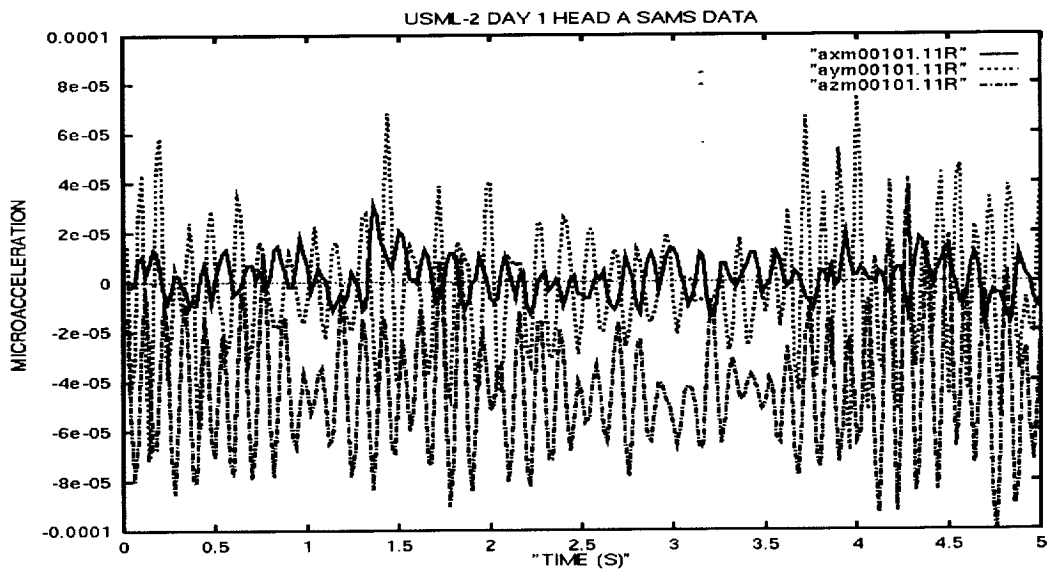


Figure 8: G-jitter microacceleration SAMS data from USML-2 mission, used in numerical simulations.

While the flow variation with time becomes more regular, a suppressing temporal variation of the melt velocity due the g-jitter was not succeeded. Alternatively, the use of the same amplitude vibration in the direction orthogonal to the ampoule axis induces intensive thermal vibration flows and flow disturbances due to g-jitter become practically not visible. Nevertheless recent results show that axial translational vibrations have a tendency to prevent the development of a strong stationary vortex cell, that otherwise may occur.

(v) Convective flows in a semiconductor melt with strong static axial magnetic field applied were investigated, and we compared three different numerical methods for the solution of thermal convection [87]. Although the generated flows are extremely low, the computational task is very complicated because of the thin boundary layer at high Hartmann numbers,  $Ha \gg 1$ . We considered melt region geometry with different aspect ratios, and gravity direction aligned and misaligned with the magnetic field vector. The comparison shows that the finite element approach with regularization can obtain stable and reliable solutions in a wide range of  $Ha$  number, up to  $10^4$ . These results compare favorably with asymptotic solutions [99,100]. Numerical solution of these problems by available commercial CFD codes may be not efficient or not possible at all.

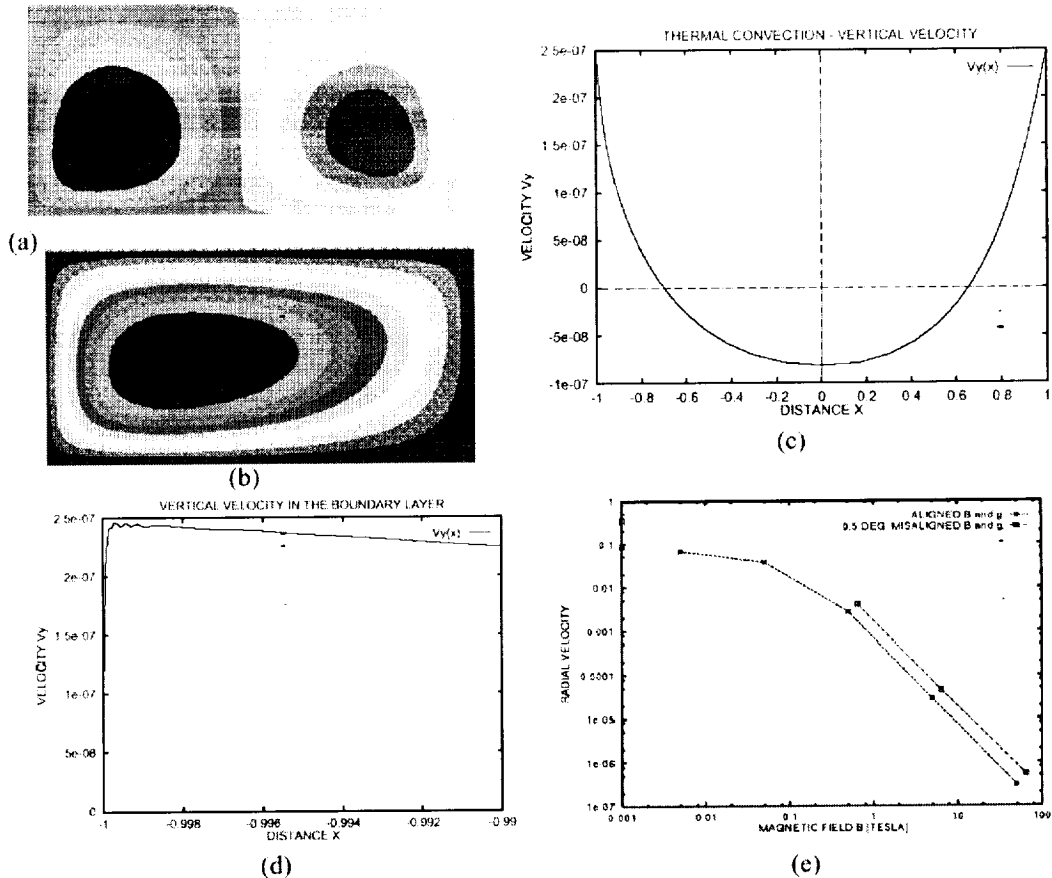


Figure 9: Stream function for aligned (a) and (b) misaligned by 0.5 degree gravity and magnetic field directions,  $Ha=2170$  ( $B = 5Tl$ ) (c) Vertical velocity profile  $V_y(x)$  at  $y=0.25H$ ,  $x$  in  $[-1,1]$ , (note boundary layer),  $Ha=2.2 \cdot 10^4$ ,  $B = 50 Tl$  (d) Detail of the velocity profile (c) in a boundary layer,  $x$  from -1 to -0.99. (e) Summary of the magnetic field suppression of melt flow: maximum value of horizontal velocity magnitude versus magnetic field  $B$  for aligned and misaligned by 0.5 degree magnetic field and gravity vectors. Predicted theoretical asymptotic dependence for the velocity  $V_{max} \sim Ha^{-2}$  is observed from about  $B=0.5 Tl$ . Results are obtained with our FEMINA/3D code for  $Ha$  number up to  $Ha=2 \cdot 10^4$ ; other tested in methods did not provide acceptable results or failed for  $Ha > 100$

The efficiency of the convective flow suppression by axial magnetic field at  $Ig$  is very sensitive to misalignment of the gravity vector with ampoule axis direction. For example, in case of misalignment by 0.5 deg., the axial temperature gradient (which was stabilizing) becomes a main driving force for the thermal convection, resulting in the increase of convection velocity magnitude by a factor of 3 to 10.

#### 4. CONCLUSIONS

- We verified and confirmed the validity of the Boussinesq model for semiconductor and oxide melts under microgravity conditions for all the flow regimes under consideration.
- Powerful tool, the 3D finite element code FEDIMA/3D has been developed. Efficient numerical methods for 3D thermal vibrational convection are implemented; carefully tested; good agreement with experimental data is obtained. This tool is capable for high accuracy modeling of 3D thermo-vibrational convection, and flows under strong magnetic field in a wide range of problem parameters.
- A parametric study of the general buoyant-vibrational flow in a Bridgman growth system was performed for both semiconductor and oxide melts.
  - The influence of angle between a direction of vibration and ampoule axis (temperature gradient) has been studied for translational vibrations. Zero angle - no influence of the vibration on a flow. The maximum effect corresponds to an angle of 90 degrees. Here transport is significantly enhanced.
  - Influence of g-jitter and forced vibrations has been analyzed.
  - All kinds of vibration can cause average melt flow for a parameter range for practical semiconductor/oxide growth. Rotational (angular) and polarized vibrations result in more intensive melt flows than translational ones. Typical flow patterns for different flow regimes have been identified.
  - The vibrational influence is stronger for oxides than for semiconductors.
  - The frequency range was identified where vibrational influence efficient.
  - Suppression of convective flows in a semiconductor melt with strong static axial magnetic field applied were investigated. High sensitivity of magnetic field direction and gravity vector misalignment has been found and analyzed.

## 5. REFERENCES

- [1] Ed. Don Hurle, ESTEC-98, Proceedings of, *Microgravity Science and Engineering*, **Vol. 11**, No. 2 and 3, 1999 (to appear)
- [2] J.I.D. Alexander, J.-P. Garandet, J.J. Favier, and A. Lizee, g-Jitter effects on segregation during directional solidification of tin-bismuth in the MEPHISTO furnace facility, *J. Crystal Growth*, **178** (1997) 657-661.
- [3] J.D. Trollinger, M. Rottenkolber and F. Elandalous, Development and application of holographic particle image velocimetry techniques for microgravity applications, *Meas. Sci. Technol.*, **8** (1997) 1573-1583.
- [4] J.D. Trollinger, R. Ranel and R.B. Lai, Holographic particle image velocimetry for the first International Microgravity Laboratory aboard the space shuttle Discovery, *Appl. Opt.* **35** (1996) 681-689.
- [5] R. Naumann, An analytical model for transport from transient and periodic acceleration on Spacecraft, AIAA 99-1028 paper, Proc. 37th AIAA Meeting, Reno, 11-17 Jan. 1999.
- [6] W. F. Kaukler and G. L. Workman, Convective flow analysis on the KC-135 Aircraft, AIAA 92-0844 paper, AIAA 30th Meeting, Reno, NV, Jan. 6-9, 1992.
- [7] G. L. Workman and W. F. Kaukler, Process modeling the KC-135 Aircraft, Final report for Contract NASA NAS8-36955, 1991, 25p.
- [8] Y.-C. Lu, J.-J. Shiau, R.S. Feigelson and R.K. Route, Effect of vibrational stirring on the quality of Bridgman grown CdTe, *J. Crystal Growth*, **102** (1990) 807;  
R.C. DeMattei and R.S. Feigelson, The effect of forced convection on the melt gradient and growth rate during the Bridgman and gradient freeze crystal growth of silver-doped lead bromide, *J. Crystal Growth*, **128** (1993) 1062-1068.
- W.-S. Liu, J. F. Wolf, D. F. Elwell, and R. S. Feigelson, "Low Frequency Vibrational Stirring: A New Method for Rapidly Mixing Solutions and Melts During Growth," *J. Crystal Growth* **82** (1987) 589-597
- [9] E.V. Zharikov, L.V. Prihodko, N.R. Storozhev, Fluid flow formation resulting from forced vibration of a growing crystal, *J. Cryst. Growth* **99** (1990) 910-914.
- [10] A.R. Bergles, Survey and evaluation of techniques to augment convective heat and mass transfer, *Progress in Heat and Mass Transfer*, Eds. U.Grigull, E. Hahne, Pergamon Press, Oxford, Vol.1, 1969, 331-424.
- [11] K.K. Gabdrahmanov, V.G. Kozlov, *Microgravity Q.*, **5** (1995) 146-151
- [12] V.G. Kozlov, V.V. Rivola, Mean heat convection in a cavity rotating around a horizontal axis, *Proc. Xth European symposium on Phys. Sci. in Microgravity*, Moscow, 1997, 266
- [13] V.S. Yuferev et al. Effect of space craft rotation on convection and transport. *Ibid.*, 37
- [14] N.A. Verezub, E.V. Zharikov, A.Z. Myaldun, and A.I. Prostomolotov, Effects of Low-Frequency on Temperature Fluctuations in the Melt for Growth by the Czochralski Method, *Crystallography Reports*, **41** (1996) 354-361.
- [15] J.I.D. Alexander, Low gravity experiment sensitivity to residual acceleration: A review, *Microgravity Science and Technology*, III (1990) 52.
- [16] J.I.D. Alexander and C.A. Lundquist, Motions in fluids caused by microgravitational acceleration and their modification by relative rotation, *AIAA Journal*, **26** (1988) 34.
- [17] H. Hamacher, R. Jilg and U. Mehrbold, Analysis of microgravity measurements performed during D-1, Proc. 6th European Symposium on Materials Sciences in Microgravity Conditions, Bordeaux, France (ESA SP-256 1987).

- [18] M.J.B. Rogers and J.I.D. Alexander, Analysis of spacelab-3 acceleration data, *AIAA J. Spacecraft and Rockets*, 28 (1992) 52.
- [19] J.I.D. Alexander, J. Ouazzani, S. Amiroudine and F. Rosenberger, Analysis of the low gravity tolerance of Bridgman-Stockbarger crystal growth II. Transient and periodic acceleration, *J. Crystal Growth*, 113 (1990) 21.
- [20] G.I. Taylor, *Proc. Roy. Soc. London A* 219 (1953) 186.
- [21] R. Aris, *Proc. Roy. Soc. London A* 259 (1960) 370.
- [22] W.N. Gill and R. Shankarsubramanian, *Proc. Roy. Soc. London A* 316 (1970) 370.
- [23] E. Brocher, *J. Fluid Mech.*, 133 (1983) 245.
- [24] U.H. Kurzweg, *J. Fluid Mech.*, 156 (1983) 291.
- [25] U.H. Kurzweg, *J. Heat Transfer*, 107 (1985) 459.
- [26] M. Kaivany, *Int. J. Heat Mass Trans.*, 29 (1985) 2002.
- [27] C. H. Joshi, R.D. Kamm, J.M. Drazen, and A.S. Slutsky, *J. Fluid Mech.*, 114 (1983) 245.
- [28] R. Smith, *J. Fluid Mech.*, 114 (1982) 379.
- [29] E.J. Watson, 113 (1983) 233.
- [30] D. Farrell and W. E. Larsen, *Water Resources Res.*, 9 (1973) 173.
- [31] Y. Kamotani, A. Prasad and S. Ostrach, *AIAA Journal* 19 (1981) 511.
- [32] W.S. Liu, M.F. Wolf, D. Elwell and R.S. Feigelson, Low frequency vibrational stirring: a new method for rapidly mixing solutions and melts, *J. Crystal Growth*, **82** (1987) 589.
- [33] A.I. Fedoseyev and J.I.D. Alexander, "Investigation of Vibrational Control of the Bridgman Crystal Growth Technique", *Proc. NASA Microgravity Material Science Conference*, Huntsville, Alabama, July 12-16, 1998.
- [34] S. M. Zen'kovskaya and I. B. Simonenko, On the effect of high-frequency vibrations on the convection onset. *Izv. Akad. Nauk SSSR, Mekh. Zhidk. Gaza* **5** (1966) 51 (in Russian)
- [35] G. Z. Gershuni and E. M. Zhukhovitsky, On free thermal convection in vibrational field in weightlessness. *Dokl. Akad. Nauk SSSR* **249** (1979) 580. (in Russian).
- [36] G. Z. Gershuni and E. M. Zhukhovitsky, On convective instability of fluid in vibrational field in weightlessness. *Izv. Akad. Nauk SSSR, Mekh. Zhidk. Gaza* **4** (1981) 12. (in Russian).
- [37] G. Z. Gershuni, E. M. Zhukhovitsky and Yu. S. Yurkov, On vibrational thermal convection in weightlessness conditions. *Hydromechanics and Heat - Mass Transfer in Weightlessness.*, Nauka, Moscow (1982) (in Russian).
- [38] G. Z. Gershuni, E. M. Zhukhovitski and A. Nepomniashi, *Stability of convective flows*, (Nauka, Moscow, 1966) p. 109.
- [39] G. Z. Gershuni and E. M. Zhukhovitski, *Convective stability of incompressible Fluids*,
- [40] A.I. Fedoseyev, J.I.D. Alexander, Vibrational control of heat and mass transfer in Bridgman melt growth configurations, *AIAA-2000-0859*, 38th AIAA Aerospace meeting, 14th Annual Microgravity Science and Space Processing Symposium, Reno, Nevada, Jan. 10 -14, 2000.
- [41] A. Farooq and G.M. Homsy, Linear and nonlinear dynamics of a differentially heated slot under gravity modulation, *J. Fluid Mech* **313** (1996) 1-38.
- [42] M. Yao, A. Chait, A.L. Fripp, and W.J. Debnam, Numerical simulation of Bridgman crystal growth of PbSnTe in Microgravity, *Microgravity Sci. Technol*, **VIII/4** (1995) 214-225.

- [43] V. G. Kozlov and S. B. Shatunov, Experimental study of the onset of vibrational convection in a horizontal flat fluid layer with internal heat release. Numerical and Experimental Modelling of Hydromechanic Phenomena in Weightlessness., Sverdlovsk (1988) 79 (in Russian).
- [44] A. Lizee, Contribution à la convection vibrationnelle; contrôle actif de la convection naturelle, Thesis, Université of Aix-Marseille II (1995) (In French).
- [45] G. Gershuni, D. Lyubimov, *Thermal Vibrational Convection*, Wiley, N.Y., 1997
- [46] B.T. Murray, S.R. Coriell and G.B. McFadden, The effect of gravity modulation on thermosolutal convection during directional solidification, *J. Crystal Growth*, 110 (1990) 713.
- [47] B. V. Saunders, B.T. Murray, G.B. McFadden, S.R. Coriell and A.A. Wheeler, The effect of gravity modulation on thermosolutal convection in an infinite layer of fluid, *Phys. Fluids A* 4 (1992) 1176-1189.
- [48] A.P. Kaputsin, Influence of ultrasound on crystallization kinetics, (Acad. Sci, USSR. Moscow, 1962) (in Russian).
- [49] V. Ship and V. Vanichek in: Rots Kristallov, Vol. III (Acad. Sci, USSR. Moscow, 1961).
- [50] B. Langenecker and W.H. Fransen, *Phil. Mag.* 7 (1962) 2079.
- [51] A.F. Witt and H.C. Gatos, *J. Electrochem. Soc.* 114 (1967) 413.
- [52] A.A. Wheeler, *J. Crystal Growth* 56 (1982) 67.
- [53] S.M. Manucharyan and H.G. Nalbandyan, *Crystal Res. Technol.* 17 (1982) 295.
- [54] W.S. Liu, M.F. Wolf, D. Elwell and R.S. Feigelson, Low frequency vibrational stirring: a new method for rapidly mixing solutions and melts, *J. Crystal Growth*, 82 (1987) 589.
- [55] Y.-C. Lu, J.-J. Shiau, R.S. Feigelson and R.K. route, Effect of vibrational stirring on the quality of Bridgman grown CdTe, *J. Crystal Growth*, 102 (1990) 807.
- [56] E.V. Zharikhov, L.V. Prihod'ko and N. Storozhev, *Crystal Res. Technol.* 24(1989) 761.
- [57] G.V. Nikitina, V.N. Romanenko and V.M. Tuchkevitch, in : *Crystallization and phase transitions*, (Acad. Sci, BSSR. Minsk, 1962) (in Russian).
- [58] A.P. Izergin, Yu.S. Pavlenko and S.A. Strotlev, *Izv. Vysshikh Uchebnykh Zavedenii, Ser. Fiz.* 1 (1959) 107 (in Russian).
- [59] Y. Hawakawa, M. Nagura and M. Kunagawa, *Semicond. Sci. Tech.* 3 (1988) 372.
- [60] V.V. Klubovitch, I.F. Kashevitch, V.V. Mikhevitch and N.K. Tolotchko, *Krystallografiya* 29 (1984) 822.
- [61] V.V. Klubovitch, S.E. Mozzharov, N.N. Sobolenko, N.K. Tolotchko and V.V. Azarov, in: *Digest of Tech. Papers, 7th All-Union Conf. on Crystal Growth*, 2 (VINITI, Moscow, 1988) 114 (in Russian).
- [62] E.V. Zharikov, L.V. Prihod'ko and N. Storozhev, *J. Crystal Growth* 99 (1990) 910-914.
- [63] V.V. Uspenskii and J.J. favier, High frequency vibration and natural convection in Bridgman-scheme crystal growth, *Int. J. Heat Mass Transfer*, 37 (1994) 691-698.
- [64] A.I. Fedoseyev, J.I.D. Alexander, Thermovibrational flow in Bridgman melt growth configurations, 37th AIAA Aerospace meeting, 13th Annual Microgravity Science and Space Processing Symposium, Reno, NV, Jan.11 -14, 1999.
- [65] A.I. Fedoseyev, B.V. Alexeev. High Order Continuum Model for Incompressible Viscous Fluid Flow and Application to Numerical Modeling of Thermo-Vibrational Convection. *Proc. 9th Int. Symp. on Continuum Models and Discrete Systems 9 - CMDS9* (Eds. E. Inan, A. Markov), Istanbul, Turkey, 1998, 130-137.
- [66] A. Fedoseyev and J.I.D. Alexander, *NASA Microgravity Mat. Sci. Conf.*, 1996, 205-210

- [67] A.I. Fedoseyev, B.V. Alexeev. Mathematical Model For Viscous Incompressible Fluid flow using Alexeev equations and comparison with experimental data. Proc. IMACS'98, Advances in Scientific Computing and Modeling (Eds. S.K. Dey, J. Ziebarth, and M. Ferrandiz), University of Alicante, Spain, 1998, 158-163.
- [68] A.I. Fedoseyev and J.I.D. Alexander, An inverse finite element method for pure and binary solidification problems. *Journal of Computational Physics*, **130** (1997) 243-255.
- [69] A.I. Fedoseyev, M.J. Friedman, and E.J. Kansa, Continuation for Nonlinear Elliptic Partial Differential Equations Discretized by the Multiquadric Method, *Int. J. Bifur. Chaos*, **10**, No. 2, 481-492 (2000).
- [70] A.I. Fedoseyev, Investigation of Vibrational Control in the Bridgman Crystal Growth Technique", Proc., NASA Microgravity Material Science Conf., July 14-17, 1998, Huntsville, Alabama.
- [71] V. I. Polezhaev, A. I. Fedoseyev et al. Mathematical Modeling of Convective Heat and Mass Transfer on the Basis of Navier-Stokes Equations, Nauka, Moscow, 1987, 272pp. (Also Hemisphere, 1991).
- [72] V.I. Polezhaev, A.I. Prostomolotov, A.I. Fedoseyev. Finite Element Method in Viscous Fluid Mechanics Problems (A Review). In: Advances in Science and Technology. Fluid mechanics series, v21, 3-92, VINITI, Moscow, 1987.
- [73] A.I. Fedoseyev and J.I.D. Alexander. An efficient method for modeling of incompressible viscous flow, thermal and vibrational convection, *16th Int. Conf. Numer. Meth. Fluid Dynamics*, Arcachon, France, 6-11 July, 1998.
- [74] R.S. Feigelson, Private communications
- [75] M.F. Schatz, J. Rogers. Ground based experiments on vibrational convection, Proc. Fourth Microgravity Fluid Physics & Transport Phenomena Conf., Ed. Bhim S. Sinhg, Aug. 12-14, Cleveland, Ohio, 1998. 58-61.
- [76] V.I. Chernatynsky, G.Z. Gershuni and R. Monti, Transient regimes of thermo-vibrational convection in a closed cavity, *Microgravity Q.*, 3 (9193) 55-67.
- [77] W. Tolksdorf, Flux growth, *Handbook of Crystal Growth*, Ed. by R. Hurle, **Vol. 2a** (1993), p. 563-612.
- [78] A. I. Fedoseyev, I.I. Petrenko, S.V. Purtov. Large problem solving by multigrid methods in complicated domains. *Computer Mechanics of Solids*, Issue 1, 75-108, 1990, Moscow, Engineering Research Center.
- [79] A. Fedoseyev, J.I.D. Alexander, Numerical Modelling of Solidification under Microgravity Conditions, International Aerospace Congress IAC'94, Moscow, August 15-19, 1994 (to appear in AIAA J.).
- [80] A. Roux, A. Fedoseyev, B. Roux, Thermal Radiation and Low- Temperature- vapour growth of HgI<sub>2</sub> Crystal in Production Furnace, *J. Crystal Growth*, **130** (1993) 523-532.
- [81] A.I. Fedoseyev, V. Polezhaev and A. Prostomolotov, Finite Element Method for Viscous Flows and Technology Applications, Proc. Fifth World Congress and Exhibition on Finite Element Methods, 1987, *Finite Element News*, 5 (1987) 44-48.
- [82] P. Wesseling, P. Sonneveld. Numerical experiments with a multiple grid and a preconditioned Lanczos type methods. *Lect. Notes Math.*, 1980, **771**, p.543-562.
- [83] D.S. Kershaw. On the problem of unstable pivots in the incomplete LU-conjugate gradient method, *J. Comput. Phys.*, 1980, V.38, p.114-123.
- [84] R. Barrett, M. Berry, T. Chan, J. Demmel, J. Donato, J. Dongarra H. van der Vorst et al. Templates for the Solution of Linear Systems: Building Blocks for Iterative Methods, SIAM publications, 1993, 112p.



- [85] B. H.-P. Shen, A. Ostrogorsky. Vibrational convection. RPI Report, 1996, 42p.
- [86] A.I. Fedoseyev and J.I.D. Alexander, Investigation of Vibrational Control of Convective Flows in Bridgman Melt Growth Configurations, *J. of Crystal Growth*, **211**, 34-42 (2000).
- [87] A.I. Fedoseyev, E.J. Kansa, C. Marin, and A.G. Ostrogorsky, Magnetic field suppression of semiconductor melt flow in crystal growth: comparison of three methods for numerical modeling, *Computational Fluid Dynamics Journal*, vol. **9** No.1 (2000), (accepted, in print);
- [88] A.I. Fedoseyev, A regularization approach to solving the Navier-Stokes Equations for Problems with Boundary Layer, *Computational Fluid Dynamics Journal*, vol. **9** No.1 (2000), (accepted, in print).
- [89] A.I. Fedoseyev, M.J. Friedman, and E.J. Kansa, Improved Multiquadric Method for Elliptic Partial Differential Equations via PDE Collocation on the Boundary, *Comput. Math. Appic.* (2001) (accepted)
- [90] A.I. Fedoseyev, O.A. Bessonov, Iterative solution for large linear systems for unstructured meshes with preconditioning by high order incomplete decomposition, *Computational Fluid Dynamics Journal*, (2001), (accepted).
- [91] A.I. Fedoseyev, A Higher Accuracy Finite Element Model for Viscous Flows with Boundary Layer, *Communications in Numerical Methods in Engineering* (submitted)
- [92] A. I. Fedoseyev, Theoretical and Experimental investigation of Vibrational Control of the Bridgman Crystal Growth Technique, *Proc. NASA Microgravity Materials Science Conference*, June 6 - 8, 2000, Huntsville, Alabama
- [93] J.C. Brice, P. Capper, C.I. Jones and J.J.G. Gosney, *Prog. Cryst. Growth Charact.* **13** (1986) 197.
- [94] W. A. Tiller, *The science of crystallization: Macroscopic phenomena and defect formation*, Cambridge University Press, 1991, p. 35.
- [95] A. Lizee, J.I.D. Alexander, Chaotic thermovibrational flow in a laterally heated cavity, *Phys. Rev. E* **56** (1997) 4152-4158.
- [96] G.P. Bogatirev, G.F. Putin, V.I. Polezhaev. A System for Measurement of Convection aboard Space Station, *Proc. 3rd Microgravity Fluid Physics Conf.*, Cleveland, Ohio, July 13-15, 1996, p.813.
- [98] U. Krzysiminski, A.G. Ostrogorsky, *J. Crystal Growth*, Visualization of convection in Czochralski melts using salts under realistic thermal boundary conditions, **174** (1997) 19-27.
- [99] A.I. Fedoseyev, E.J. Kansa, C. Marin, A. G. Ostrogorsky, Numerical Modeling of Semiconductor Melt Flow in Crystal Growth under Magnetic Field, *Proc. Int. Conf. on Scientific Computing and Mathematical Modeling*, D. Schultz, B. Wade, J. Vigo-Aguiar, S.K. Dey, eds., (2000) 194-197.
- [100] A.I. Fedoseyev, E.J. Kansa, C. Marin, A.G. Ostrogorsky, M. Volz, Magnetic field suppression of flow in semiconductor melt, AIAA-2000-0898, 38th AIAA Aerospace meeting, 14th Annual Microgravity Science and Space Processing Symposium, Reno, Nevada, Jan. 10 -14, 2000.

## 6. PUBLICATIONS AND PRESENTATIONS

### Journal papers

A.I. Fedoseyev and J.I.D. Alexander, Investigation of Vibrational Control of Convective Flows in Bridgman Melt Growth Configurations, *J. of Crystal Growth*, **211**, 34-42 (2000).

A.I. Fedoseyev, M.J. Friedman, and E.J. Kansa, Continuation for Nonlinear Elliptic Partial Differential Equations Discretized by the Multiquadric Method, *Int. J. Bifur. Chaos* **10**, No. 2, 481-492 (2000).

A.I. Fedoseyev, E.J. Kansa, C. Marin, and A.G. Ostrogorsky, Magnetic field suppression of semiconductor melt flow in crystal growth: comparison of three methods for numerical modeling, *Computational Fluid Dynamics Journal*, vol. **9** No.1 (2000), (accepted, in print).

A.I. Fedoseyev, A regularization approach to solving the Navier-Stokes Equations for Problems with Boundary Layer, *Computational Fluid Dynamics Journal*, vol. **9** No.1 (2000), (accepted, in print).

A.I. Fedoseyev, M.J. Friedman, and E.J. Kansa, Improved Multiquadric Method for Elliptic Partial Differential Equations via PDE Collocation on the Boundary, *Comput. Math. Appic.* (2001) (accepted).

A.I. Fedoseyev, O.A. Bessonov, Iterative solution for large linear systems for unstructured meshes with preconditioning by high order incomplete decomposition, *Computational Fluid Dynamics Journal*, (2001), (accepted).

A.I. Fedoseyev, A Higher Accuracy Finite Element Model for Viscous Flows with Boundary Layer, *Communications in Numerical Methods in Engineering* (submitted)

L.A. Slobozhanin, J.I.D. Alexander, A.I. Fedoseyev, Shape and Stability of Doubly Connected Axisymmetric Free Surfaces in a Cylindrical Container, *Physics of Fluids*, Vol. **11**, No.12 (1999).

A.I. Fedoseyev and J.I.D. Alexander, "An inverse finite element method for pure and binary solidification problems", *Journal of Computational Physics*, **130** (1997) 243-255.

### Conference Proceedings

A.I. Fedoseyev, J.I.D. Alexander, Vibrational control of heat and mass transfer in Bridgman melt growth configurations, AIAA-2000-0859, 38th AIAA Aerospace meeting, 14th Annual Microgravity Science and Space Processing Symposium, Reno, Nevada, Jan. 10 -14, 2000.

A.I. Fedoseyev, E.J. Kansa, C. Marin, A. G. Ostrogorsky, Numerical Modeling of Semiconductor Melt Flow in Crystal Growth under Magnetic Field , Proc. Int. Conf. on Scientific Computing and Mathematical Modeling, D. Schultz, B. Wade, J. Vigo-Aguiar, S.K. Dey, eds., 194-197 (2000).

A. I. Fedoseyev, Theoretical and Experimental investigation of Vibrational Control of the Bridgman Crystal Growth Technique, Proc. NASA Microgravity Materials Science Conference, June 6 - 8, 2000, Huntsville, Alabama

A. I. Fedoseyev, Higher Accuracy Numerical Solution Methods for High Re number Viscous Flows and Flows with Boundary Layer, Proc. Int. Conf. on Scientific Computing and Mathematical Modeling, D. Schultz, B. Wade, J. Vigo-Aguiar, S.K. Dey, eds., 116-119 (2000).

A. I. Fedoseyev, M. J. Friedman, and E. J. Kansa. Improved Multiquadric Method Algorithms for Elliptic Partial Differential Equations, Proc. Int. Conf. on Scientific Computing and Mathematical Modeling, Proc. Int. Conf. on Scientific Computing and Mathematical Modeling, D. Schultz, B. Wade, J. Vigo-Aguiar, S.K. Dey, eds., 174-177 (2000).

R.N. Grugel, A.I. Fedoseyev. Characterizing the use of Ultrasonic Energy in Promoting Uniform Composite Growth in Immiscible Alloys, Proc. Proc. Int. Conf. on Scientific Computing and Mathematical Modeling, Proc. Int. Conf. on Scientific Computing and Mathematical Modeling, D. Schultz, B. Wade, J. Vigo-Aguiar, S.K. Dey, eds., 120-123 (2000).

A.I. Fedoseyev, Solution of the Navier-Stokes equation with the regularization approach for two and three-dimensional flow problems, Proc. Int. Conf. on Modeling, Computing, Design under Indeterminacy Conditions, February 2-5, 2000, Ufa State Aviation University, Ufa, Russia, V. P. Zhitnikov, ed., Vol. 1/3, 20-30 (2000)

A.I. Fedoseyev, E.J. Kansa, C. Marin, A.G. Ostrogorsky, M. Volz, Magnetic field suppression of flow in semiconductor melt, AIAA-2000-0898, 38th AIAA Aerospace meeting, 14th Annual Microgravity Science and Space Processing Symposium, Reno, Nevada, Jan. 10 -14, 2000.

A.I. Fedoseyev, E.J. Kansa, C. Marin, and A.G. Ostrogorsky, Magnetic field suppression of semiconductor melt flow in crystal growth: comparison of three methods for numerical modeling, Proc. of ISCFD-99, Eds. H.J. Rath, K. Oshima, G. Schmidt, ZARM, Universität Bremen, September 6-10, 1999, Bremen, Germany.

A.I. Fedoseyev, J.I.D. Alexander, Thermovibrational flow in Bridgman melt growth configurations, AIAA Paper 99-0839, Proc. of 37th AIAA Aerospace meeting, 13th Annual Microgravity Science and Space Processing Symposium, Reno, NV, Jan.11 -14, 1999.

A.I. Fedoseyev, Numerical Model with Regularized Navier-Stokes Equation for Solutions with Boundary Layer, Proc. of ISCFD-99, Eds. H.J. Rath, K. Oshima, G. Schmidt, ZARM, Universität Bremen, September 6-10, 1999, Bremen, Germany.

L. A. Slobozhanin, J. I. D. Alexander, A.I. Fedoseyev, Doubly Connected Axisymmetric Free Surfaces in a Cylindrical Container: Shape, Stability and Application, AIAA Paper 99-1029,

Proc. of 37th AIAA Aerospace meeting, 13th Annual Microgravity Science and Space Processing Symposium, Reno, NV, Jan.11 -14, 1999.

A.I. Fedoseyev, B.V. Alexeev. Higher Order Continuum Model for Incompressible Viscous Fluid Flow and Application to Numerical Modeling of Thermo-Vibrational Convection. In: *Continuum Models and Discrete Systems* (Eds. E. Inan, A. Markov), World Scientific, London, 1998, 130-137.

A.I. Fedoseyev, B.V. Alexeev. Mathematical Model For Viscous Incompressible Fluid flow using Alexeev equations and comparison with experimental data. Proc. IMACS'98, Advances in Scientific Computing and Modeling (Eds. S.K. Dey, J. Ziebarth, and M. Ferrandiz), University of Alicante, Spain, 1998, 158-163.

A.I. Fedoseyev and J.I.D. Alexander. "An Efficient Method for Numerical Modeling of Thermo-Vibrational Convection", Int. Conf. on Numerical Methods in Fluid Dynamics, July 6-10, 1998, Arcachon, France, Extended abstracts, 173-174.

A.I. Fedoseyev and J.I.D. Alexander, "Investigation of Vibrational Control of the Bridgman Crystal Growth Technique", Proc. NASA Microgravity Material Science Conference, Huntsville, Alabama, July 12-16, 1998.

A.I. Fedoseyev, O.B. Bessonov, "Efficient Solution of viscous fluid flow problems in finite element method". Proc. of seminar on Numerical Methods in Heat and Mass Transfer Problems, Moscow, Institute for Problem in Mechanics of the Russian Academy of Sciences, 1997, 67-86.

J.I.D. Alexander, Y.Zhang, S. Delafontaine and A.I.Fedosyev, "Numerical simulation of liquid bridge dynamics and statics". Proc. of seminar on Numerical Methods in Heat and Mass Transfer Problems, Moscow, Institute for Problem in Mechanics of the Russian Academy of Sciences, 1997, 109-138.

A.I. Fedoseyev, J.I.D. Alexander and Y. Zhang, "Numerical simulation of transient and quasi-steady directional solidification using IFEM and Chebyshev spectral methods", Extended abstracts of the 2-nd International Workshop on Modelling in Crystal Growth, Durbuy, Belgium, October 14-17, 1996.

A.I. Fedoseyev and J.I.D. Alexander, "A Theoretical and Experimental Investigation of Vibrational Control of the Bridgman Crystal Growth Technique", Proc. NASA Microgravity Material Science Conference, Huntsville, Alabama, June, 1996.

### **Presentations**

E.V. Zharikov, R.S. Feigelson, A.I. Fedoseyev. Vibration technologies of crystal growth by Bridgman technique. IX National Conference on Crystal Growth, Moscow Institute of Crystallography, Russian Academy of Sciences, Moscow, Russia, October 16-20, 2000.

E.V. Zharikov, R.S. Feigelson, A.I. Fedoseyev, Vibrational technologies in Bridgman crystal growth, Third International Aerospace Congress IAC'2000, Moscow, Russia, 23-27 August 2000.

A. I. Fedoseyev, J.I.D. Alexander, R.S. Feigelson, E.V. Zharikov, Investigation of thermo-vibrational flows in Bridgman melt growth: numerical modeling and experiments, "Mechanics of microgravity and gravitationally-sensitive systems", Seminar, Institute for Problems in Mechanics, Russian Academy of Sciences, Moscow, Russia, 21 August, 2000, <http://www.ipmnet.ru/~polezh/seminars/seminar1/seminar1.htm>.

A. I. Fedoseyev, C. Marin, A.G. Ostrogorsky, Modeling of heat and mass transfer in semiconductor melt under axial and transverse magnetic field, 7th ISCFD'2000, The seventh Russian-Japanese International Symposium on Computational Fluid Dynamics, July 31- August 6, 2000, Russian Academy of Sciences and Moscow Lomonosov State University, Moscow, Russia.

R. N. Grugel, A.I. Fedoseyev, Modeling of ultrasonically generated liquid-liquid dispersions during controlled directional solidification, Third Int. Workshop on Modeling in Crystal Growth, Hauppauge, New York, USA, October 18-20, 2000.

A. I. Fedoseyev, Higher Accuracy Numerical Solution for High Re number Flows by Restoring Conservation Laws at the Boundary, 7th ISCFD'2000, The seventh Russian-Japanese International Symposium on Computational Fluid Dynamics, July 31- August 6, 2000, Russian Academy of Sciences and Moscow Lomonosov State University, Moscow, Russia.

A.I. Fedoseyev, O.A. Bessonov, Iterative solution for large linear systems for unstructured meshes with preconditioning by high order incomplete decomposition, 7th ISCFD'2000, The seventh Russian-Japanese International Symposium on Computational Fluid Dynamics, July 31- August 6, 2000, Russian Academy of Sciences and Moscow Lomonosov State University, Moscow, Russia.

K.T. Zawilski, R.S. Feigelson, M.C.C. Custodio, R. DeMattei, P. Patel, A. Fedoseyev. Coupled Vibrational Stirring: Modeling of Bridgman Growth Systems. ACCG-11, The 11th American Conference on Crystal Growth and Epitaxy in Tuscon, Arizona, August 1-6, 1999.

A. I. Fedoseyev, Theoretical and Experimental investigation of Vibrational Control of the Bridgman Crystal Growth Technique, NASA Microgravity Materials Science Conference, June 6 - 8, 2000, Huntsville, Alabama

A. I. Fedoseyev, Mathematical modeling of 3D electromagnetic fields and fluid flows (applications to MHD), FERMILAB, Batavia, IL, May 30, 2000.

A. I. Fedoseyev, Higher Accuracy Numerical Solution Methods for High Re number Viscous Flows and Flows with Boundary Layer, Int. Conf. on Scientific Computing and Mathematical Modeling, Milwaukee, Wisconsin, May 25-27, 2000

A. I. Fedoseyev, M. J. Friedman, and E. J. Kansa. Improved Multiquadric Method Algorithms for Elliptic Partial Differential Equations, Int. Conf. on Scientific Computing and Mathematical Modeling, Milwaukee, Wisconsin, May 25-27, 2000

A.I. Fedoseyev, E.J. Kansa, C. Marin, A. G. Ostrogorsky , Numerical Modeling of Semiconductor Melt Flow in Crystal Growth under Magnetic Field , Int. Conf. on Scientific Computing and Mathematical Modeling, Milwaukee, Wisconsin, May 25-27, 2000

R.N. Grugel, A.I. Fedoseyev. Characterizing the use of Ultrasonic Energy in Promoting Uniform Composite Growth in Immiscible Alloys, Int. Conf. on Scientific Computing and Mathematical Modeling, Milwaukee, Wisconsin, May 25-27, 2000

A.I. Fedoseyev, A Higher Accuracy Finite Element Model for Two- and Three-Dimensional Viscous Flows with Boundary Layer, Finite Elements in Flow Problems-2000 Conference, Austin, Texas, April 30-May 4, 2000.

A.I. Fedoseyev, O.A. Bessonov, Preconditioning by a High Order Incomplete Decomposition and Iterative Solution of the FEM Equations for 2D/3D Unstructured Meshes, Finite Elements in Flow Problems-2000 Conference, Austin, Texas, April 30-May 4, 2000.

A.I. Fedoseyev, E.J. Kansa, C. Marin, A.G. Ostrogorsky, M. Volz, Magnetic field suppression of flow in semiconductor melt, 38th AIAA Aerospace meeting, 14th Annual Microgravity Science and Space Processing Symposium, Reno, Nevada, January 10 -14, 2000.

A.I. Fedoseyev, J.I.D. Alexander, Vibrational control of heat and mass transfer in Bridgman melt growth configurations, 38th AIAA Aerospace meeting, 14th Annual Microgravity Science and Space Processing Symposium, Reno, Nevada, January 10 - 14, 2000.

A.I. Fedoseyev and J.I.D. Alexander, Thermovibrational Flow Control In Bridgman Melt Growth Configurations, Gordon Research Conference on Gravitational Effects in Physico-Chemical Systems, June 27-July 2, 1999, New England College, Henniker, New Hampshire, USA

R.N. Grugel, A. Fedoseyev, and M. Friedman, Novel Processing and Modeling of Solute Distribution at a Dendritic Interface, Microgravity SPIE Session, Denver, July 21-23, 1999.

M.J. Friedman, A.I. Fedoseyev, and E.J. Kansa, Continuation of solutions to 1D and 2D Nonlinear Elliptic PDEs by the Multiquadric Method, Workshop on Bifurcations : Analysis, Numerical Methods, Software, June 24 - 25, 1999, University of Gent, Belgium.

A.I. Fedoseyev, Numerical experiments with regularized Navier-Stokes equation for high Re-number flows with 2D/3D finite elements, Fourth Mississippi State Conference on Differential Equations and Computational Simulations, May 21-22, 1999, MSU, Starkville, Mississippi, USA.

A.I. Fedoseyev and J.I.D. Alexander, Investigation of Vibrational Control of Convective Flows in Bridgman melt Growth Configurations, ACCGE-11, August 1-6, 1999, Tuscon, AZ, USA

A.I. Fedoseyev, E.J. Kansa, C. Marin, and A.G. Ostrogorsky, Magnetic field suppression of semiconductor melt flow in crystal growth: comparison of three methods for numerical modeling, ISCFD-99, ZARM, Universität Bremen, September 6-10, 1999, Bremen, Germany.

A.I. Fedoseyev, Numerical Model with Regularized Navier-Stokes Equation for Solutions with Boundary Layer, ISCFD-99, ZARM, Universität Bremen, September 6-10, 1999, Bremen, Germany.

A.I. Fedoseyev, Numerical experiments with regularized Navier-Stokes equation for Problems with Boundary Layer, Seminar of Department of Mechanical and Aerospace Engineering, October 1, 1999, University of Alabama in Huntsville.

A.I. Fedoseyev, J.I.D. Alexander, Thermovibrational flow in Bridgman melt growth configurations, 37th AIAA Aerospace meeting, 13th Annual Microgravity Science and Space Processing Symposium, Reno, NV, Jan.11 -14, 1999.

L. A. Slobozhanin, J. I. D. Alexander, A.I. Fedoseyev, Doubly Connected Axisymmetric Free Surfaces in a Cylindrical Container: Shape, Stability and Application, 37th AIAA Aerospace meeting, 13th Annual Microgravity Science and Space Processing Symposium, Reno, NV, Jan.11 -14, 1999.

A.I. Fedoseyev, "Numerical experiments with regularized Navier-Stokes equation for high  $Re$  number flows with 2D/3D finite elements", 4th Mississippi State Conference on Differential Equations and Computational Simulations, May 21-22, Mississippi State University, 1999.

A.I. Fedoseyev, B.V. Alexeev. Higher Order Continuum Model for Incompressible Viscous Fluid Flow and Application to Numerical Modeling of Thermo-Vibrational Convection. *9th Int. Symp. on Continuum Models and Discrete Systems 9 - CMDS9*, Istanbul, Turkey, June 29-July 3, 1998.

A.I. Fedoseyev, B.V. Alexeev. Mathematical Model For Viscous Incompressible Fluid flow using Alexeev equations and comparison with experimental data. IMACS'98- Advances in Scientific Computing and Modeling, Univ. of Alicante, Spain, June 28-30, 1998.

A.I. Fedoseyev and J.I.D. Alexander. "An Efficient Method for Numerical Modeling of Thermo-Vibrational Convection", Int. Conf. on Numerical Methods in Fluid Dynamics, July 6-10, 1998, Arcachon, France.

A.I. Fedoseyev and J.I.D. Alexander, "Investigation of Vibrational Control of the Bridgman Crystal Growth Technique", NASA Microgravity Material Science Conference, Huntsville, Alabama, July 12-16, 1998.

A.I. Fedoseyev, J.I.D. Alexander, "Inverse Finite Element Method for Problem with Unknown Moving Boundaries", 3rd Mississippi State Conference on Differential Equations and Computational Simulations, May 16-17, Mississippi State University, 1997.

A.I. Fedoseyev, J.I.D. Alexander and Y. Zhang, "Numerical simulation of transient and quasi-steady directional solidification using IFEM and Chebyshev spectral methods", Second International Workshop on Modelling in Crystal Growth, Durbuy, Belgium, October 14-17, 1996.

A.I. Fedoseyev and J.I.D. Alexander, "A Theoretical and Experimental Investigation of Vibrational Control of the Bridgman Crystal Growth Technique", NASA Microgravity Material Science Conference, Huntsville, Alabama, June, 1996.



## APPENDIX A:

### SELECTED JOURNAL AND CONFERENCE PAPERS PUBLISHED (ATTACHED)

1. A.I. Fedoseyev and J.I.D. Alexander, Investigation of Vibrational Control of Convective Flows in Bridgman Melt Growth Configurations, *J. of Crystal Growth*, **211**, 34-42 (2000).
2. A.I. Fedoseyev, E.J. Kansa, C. Marin, and A.G. Ostrogorsky, Magnetic field suppression of semiconductor melt flow in crystal growth: comparison of three methods for numerical modeling, *Computational Fluid Dynamics Journal*, vol. **9** No.1 (2000), (accepted, in print).
3. A. I. Fedoseyev, Theoretical and Experimental investigation of Vibrational Control of the Bridgman Crystal Growth Technique, Proc. NASA Microgravity Materials Science Conference, June 6 - 8, 2000, Huntsville, Alabama
4. A.I. Fedoseyev, M.J. Friedman, and E.J. Kansa, Continuation for Nonlinear Elliptic Partial Differential Equations Discretized by the Multiquadric Method, *Int. J. Bifur. Chaos* **10**, No. 2, 481-492 (2000).
5. A.I. Fedoseyev, J.I.D. Alexander, Vibrational control of heat and mass transfer in Bridgman melt growth configurations, AIAA-2000-0859, 38th AIAA Aerospace meeting, 14th Annual Microgravity Science and Space Processing Symposium, Reno, Nevada, Jan. 10 -14, 2000.
6. A.I. Fedoseyev, E.J. Kansa, C. Marin, A.G. Ostrogorsky, M. Volz, Magnetic field suppression of flow in semiconductor melt, AIAA-2000-0898, 38th AIAA Aerospace meeting, 14th Annual Microgravity Science and Space Processing Symposium, Reno, Nevada, Jan. 10 -14, 2000.
7. A.I. Fedoseyev, M.J. Friedman, and E.J. Kansa, Improved Multiquadric Method for Elliptic Partial Differential Equations via PDE Collocation on the Boundary, *Comput. Math. Appic.* (2001) (accepted).
8. A.I. Fedoseyev, A regularization approach to solving the Navier-Stokes Equations for Problems with Boundary Layer, *Computational Fluid Dynamics Journal*, vol. **9** No.1 (2000), (accepted, in print).
9. A. I. Fedoseyev, Higher Accuracy Numerical Solution Methods for High Re number Viscous Flows and Flows with Boundary Layer, Proc. Int. Conf. on Scientific Computing and Mathematical Modeling, D. Schultz, B. Wade, J. Vigo-Aguiar, S.K. Dey, eds., 116-119 (2000).
10. A.I. Fedoseyev, O.A. Bessonov, Iterative solution for large linear systems for unstructured meshes with preconditioning by high order incomplete decomposition, *Computational Fluid Dynamics Journal*, (2001), (accepted).
11. A.I. Fedoseyev, A Higher Accuracy Finite Element Model for Viscous Flows with Boundary Layer, *Communications in Numerical Methods in Engineering* (submitted)



ELSEVIER

Journal of Crystal Growth 211 (2000) 34–42

JOURNAL OF **CRYSTAL  
GROWTH**

www.elsevier.nl/locate/jcrysgro

# Investigation of vibrational control of convective flows in Bridgman melt growth configurations

Alexandre I. Fedoseyev<sup>a,\*</sup>, J. Iwan D. Alexander<sup>b</sup>

<sup>a</sup>Center for Microgravity and Materials Research, University of Alabama in Huntsville, Huntsville, AL 35899, USA

<sup>b</sup>Department of Mechanical and Aerospace Engineering and National Center for Microgravity Research, Case Western Reserve University, Cleveland, OH 44106, USA

## Abstract

It is generally recognized that oscillatory, or pulsatile, flow significantly alters the transfer of mass, heat and momentum in fluid systems. A numerical investigation of thermovibrational buoyancy-driven flow in differentially heated cylindrical containers is presented as part of a study of thermovibrational transport regimes in Bridgman-type systems. The formulation of a physical and mathematical model for this problem is outlined and its application to the study of investigation of thermal vibrational flows is discussed. Three types of vibration are considered: translational, circularly polarized and rotational. It is demonstrated that forced vibration can significantly affect flows that have been induced by *g*-jitter and selected results for the cases of longitudinal and lateral vibrations are presented. © 2000 Elsevier Science B.V. All rights reserved.

PACS: 81.10.Aj; 81.10.Mx

Keywords: Thermal vibrational flow; *g*-jitter; Flow control

## 1. Introduction

The character of natural buoyant convection in rigidly contained inhomogeneous fluids can be drastically altered by vibration of the container. For certain experiments and operating conditions, vibrations are expected to have a significant influence on heat and mass transfer onboard the International Space Station (ISS). Furthermore, it appears that (see for example, the recent ESTEC

Workshop proceedings [1]) *g*-jitter vibrations will exist on ISS over a wide range of frequencies.

In general, vibrational flows are very complex and are governed by many parameters. This complexity makes it almost impossible to correctly predict vibrational effects empirically. Thus, a careful theoretical approach combined with numerical modeling is essential. Available flight experiment data clearly show that, once initiated by “*g*-jitter”, the effects of convective flows can persist for long times even when the *g*-jitter disturbance (and consequent flow) were short-lived [2–7].

In many terrestrial crystal growth situations convective transport of heat and constituent components is dominated by buoyancy-driven convection. Control of convective transport continues to

\*Corresponding author. Tel.: +1-256-890-6889; fax: +1-256-890-6944.

E-mail addresses: alex@cmmr.uah.edu (A.I. Fedoseyev), ida2@po.cwru.edu (J.I.D. Alexander)

be an important aspect of crystal growth research. Several groups are actively pursuing control of convection using static and rotating magnetic fields. In some cases, experimenters seeking to avoid buoyancy effects by conducting their experiments in microgravity environments have expressed interest in the use of magnetic fields even under low gravity conditions. However, there are many instances, whether due to materials properties or other practical considerations, use of magnetic fields to induce stirring or to suppress unwanted flows may not be an option. Magnetic fields cannot be used for flow control in melts and solutions that are poor conductors. Flow suppression through vibration or vibro-convective mixing may offer an attractive alternative in such cases.

It is understood that high-quality low-gravity environments can only be provided for specific limited time intervals. For space stations, interruptions and disturbances are inevitable consequences of docking, pointing maneuvers, astronaut activity, etc., and will limit the maximum attainable duration of high-quality microgravity periods. While active vibration isolation can be a partial solution, it will not solve the problems that might arise due to the quasi-steady and very low-frequency acceleration components related to the gravity gradient and other orbital factors. Alternatively, rather than using vibration to suppress low-gravity flows, one might envisage using vibration to provide flow regimes tailored to particular crystal growth experiments.

Recent work has shown that the character of natural buoyant convection in nonuniformly heated, rigidly contained inhomogeneous fluids can be drastically altered by vibration of the container. A review and relevant theoretical and experimental research can be found in publications [1–13]. Thus, vibrational, induced flow can potentially be used to influence and even control transport in some crystal growth situations. A practical quantitative understanding of vibrational convection as a control parameter in crystal growth situations is currently not available. The objective of the work is to assess the feasibility of the use of vibration to suppress, or control, convection in order to achieve transport control during crystal growth.

## 2. Theory and numerical modeling

Buoyancy driven vibro-convective motion occurs when oscillatory displacement of a container wall induces the acceleration of a container wall relative to the inner fluid. The vibration may be viewed as a time-dependent modulation of steady gravity. In a closed container the fluid will move as a rigid body with a container. If, however, the fluid density is nonuniform, fluid motion may ensue. The magnitude of this motion, of course, depends on the orientation of the vibrational direction with respect to the local density gradients. Note that, similar to Rayleigh–Benard configurations, there may be a “critical” threshold for the coupled vibrational frequency and amplitude, to cause convection. Interestingly, it should be noted that in case of a constant density fluid subjected to spatially non-uniform vibration, fluid motion can also occur (for example, angular vibration [11]).

To properly investigate influence of translational, circularly polarized and rotational (angular) vibration necessitates the use of the full 3D equations governing the transport of heat, mass and momentum. Selected examples of our ongoing work on this topic are outlined below.

### 2.1. The physical model

We consider a purely thermo-vibrational convection in a differentially heated cylindrical cavity with no consideration of solidification. The fluid is taken to be Newtonian, with a constant viscosity and the Boussinesq approximation is assumed to hold. The validity of this approximation is discussed in Section 3. The calculations were performed for identification and characterization of thermovibrational flow and are part of an ongoing project involving flow visualization model experiments being conducted by Feigelson [10].

### 2.2. Mathematical model for translational vibration

Translational vibration corresponds to a linear displacement such as, for example,  $u = d \cos \omega t$ , where  $d$  is a real vector giving the displacement magnitude and  $\omega$  is the frequency. In this case the ampoule is displaced back and forth upon the same

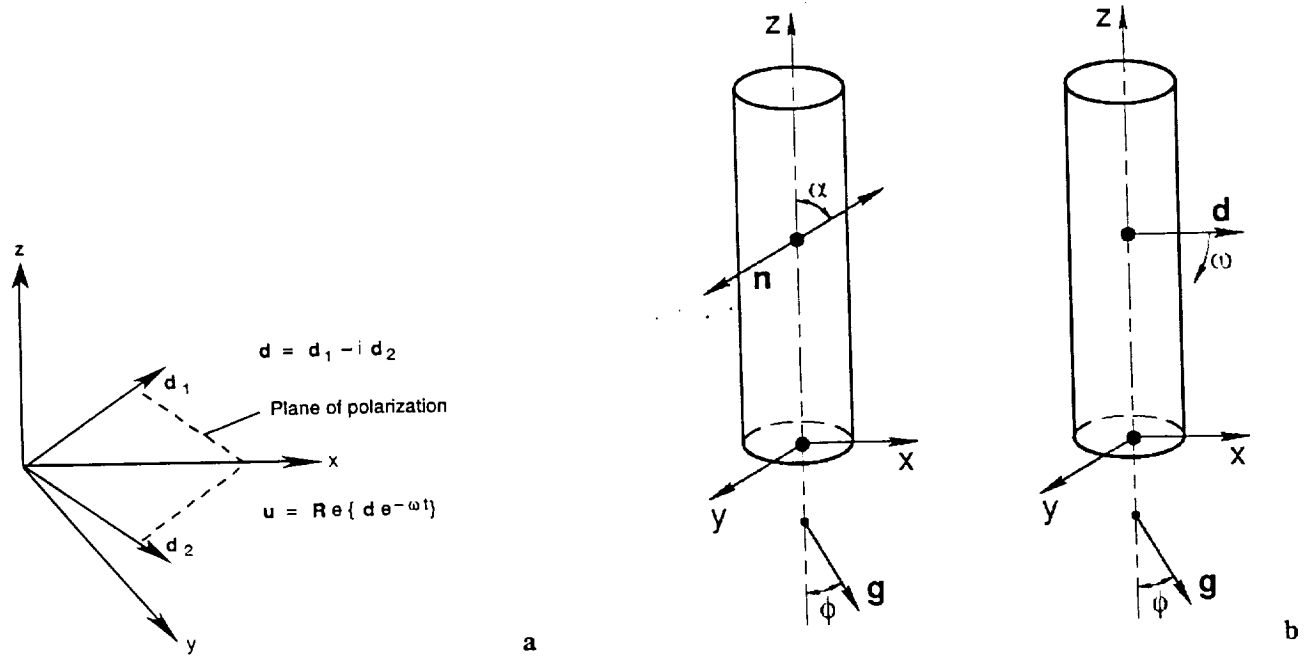


Fig. 1. Translational vibration (a),  $\mathbf{d}_1$  or  $\mathbf{d}_2 = 0$ , and polarized vibration (b),  $\mathbf{d}_1, \mathbf{d}_2 \neq 0$ ;  $\phi$  is the angle between gravity vector and the ampoule axis,  $\alpha$  is the angle between the vibration direction and the ampoule axis.

line. Polarized vibrations are characterized by a displacement  $\mathbf{u} = \text{Re}\{\mathbf{d}e^{i\omega t}\}$  where  $\mathbf{d} = \mathbf{d}_1 - i\mathbf{d}_2$  (see Fig. 1). Here the instantaneous vibration direction rotates in the polarization plane defined by the real vectors  $\mathbf{d}_1$  and  $\mathbf{d}_2$ . A sketch showing both translational and circular polarized vibrations is presented in Fig. 1. In a reference frame fixed to a vibrating ampoule, these types of vibrations result in the following form of the momentum equation:

$$\frac{\partial \mathbf{v}}{\partial t} + (\mathbf{v} \cdot \nabla) \mathbf{v} = -\nabla p + \text{Pr} \nabla^2 \mathbf{v} + \text{Ra}_T \text{Pr}(\Theta + \alpha C) \mathbf{k} + \text{Ra}_T^* \text{Pr}(\Theta + \alpha C) \mathbf{f}(\Omega, t), \quad (1)$$

where length, time and velocity are scaled by  $R_0$ ,  $R_0^2/\kappa$  and  $\kappa/R_0$ . Here  $R_0$  is the ampoule radius and  $\kappa$  is the thermal diffusivity. The nondimensional concentration and temperature, are given by  $\Theta$ , and  $C$ , respectively. The function  $\mathbf{f}(\Omega, t)$  is the acceleration of the vibrating ampoule and  $\Omega = \omega R_0^2/\kappa$  is a dimensionless frequency. The continuity and heat-mass transfer equations complete the problem formulation. The Prandtl, Schmidt, thermal and solutal Rayleigh and vibrational

Rayleigh numbers and the buoyancy ratio are, respectively, given by

$$\text{Pr} = \frac{\nu}{\kappa}, \quad \text{Sc} = \frac{\nu}{D}, \quad \text{Ra}_T = \frac{\beta \Delta T g R^3}{\nu \kappa}, \quad \alpha = \frac{\beta_c c_\infty}{\beta \Delta T}, \quad \text{Ra}_T^* = \frac{d \omega^2 \beta \Delta T R^3}{\nu \kappa}. \quad (2)$$

Here  $\beta$  and  $\beta_c$  are the thermal and solutal expansion coefficients and  $\Delta T$ ,  $c_\infty$ ,  $g$ ,  $d$ ,  $\omega$ ,  $\kappa$ ,  $\nu$ ,  $D$  are the characteristic longitudinal temperature difference, reference concentration in the melt, gravitational acceleration, vibrational displacement amplitude and frequency, direction of gravity, kinematic viscosity and solute diffusivity, respectively. The dimensionless number  $\text{Ra}_T^*$  is the vibrational Rayleigh number and  $\text{Ra}_T^* = \alpha \text{Ra}_T$ . Eq. (2) is solved together with the equations governing heat and species transfer and the condition that the velocity is divergence free.

### 2.3. Rotational vibration

The equations of motion for angular vibration take on a more complicated form (see Fig. 2)

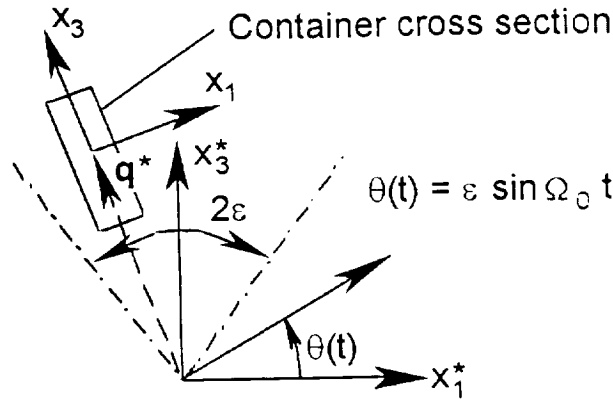


Fig. 2. Diagram of the rotational (angular) vibration. The container is rotated at an angle  $\theta(t)$  about a center of rotation at  $x^* = 0$ . The vector  $q^*$  connects the center of rotation to the mass center of the container.

A container of length  $L$  is subjected to an angular displacement  $\theta(t)$  in the  $x_1^*-x_3^*$  plane. Here the coordinates  $x^*$  are referred to a fixed laboratory frame of reference. The position vector to the mass center of the cylinder is parallel to the side of the cylinder and is given by  $q^* = R_0[-\sin \theta i_1^* + \cos \theta i_3^*]$  where  $R_0$  is the distance from the origin  $0^*$  to the mass center of the cylinder and  $\theta(t) = \varepsilon \sin \Omega_0 t$ . In a frame of reference moving with the container, the equations of motion have the form

$$\begin{aligned} \rho \frac{Dv}{Dt} = & \operatorname{div} \tau - \rho k(\sin \theta i_1 + \cos \theta i_3) \\ & + \rho[2\tilde{\Omega}v - \tilde{\Omega}^2 x + \dot{\tilde{\Omega}}x \\ & + \varepsilon^2 \Omega_0^2 R_0 \cos \Omega_0 t i_1], \end{aligned} \quad (3)$$

where  $D/Dt$  denotes the material derivative,  $v$  is the velocity of the fluid relative to the moving reference frame,  $\rho$  is the density of the fluid,  $\tilde{\Omega}$  is the rate of rotation tensor for the moving frame with respect to the fixed frame of reference,  $\dot{\tilde{\Omega}}$  is its time derivative and  $T$  is the Newtonian stress tensor for the fluid. As in the previous example, the fluid is taken to have a constant viscosity and the Boussinesq approximation is assumed to hold. The dimensionless equations governing the transport of momentum, mass and heat in the cylinder are obtained after using  $L$ ,  $L^2/\kappa$ ,  $\kappa/L$ , and  $\Delta T = T_H - T_C$  to scale, respectively, length, time, velocity and temperature. The governing dimensionless parameters

are the dimensionless frequency  $\Omega = \Omega_0 L^2/\kappa$ , the dimensionless container radius,  $\vartheta = R_0/L$ , the Prandtl,  $Pr$ , and the Rayleigh,  $Ra$ , vibrational Rayleigh  $Ra_\Omega$ , and Ekman,  $E$ , numbers. The latter are given by

$$\begin{aligned} Pr = \frac{\nu}{\kappa}, \quad Ra = \frac{\beta \Delta T g L^3}{\kappa \nu}, \\ Ra_\Omega = \frac{\beta \Delta T \Omega_0^2 L^4}{\kappa \nu}, \quad E = \frac{\nu}{\Omega_0 L^2} \end{aligned} \quad (4)$$

where  $\beta$ ,  $\nu$ ,  $g$  and  $\kappa$  are the coefficient of thermal expansion, kinematic viscosity, gravitational acceleration and thermal diffusivity, respectively. This system of equations differ from the usual equations in the absence of rotation in which additional terms are present; the Coriolis term which is proportional to  $\varepsilon Pr/E$ , and the centrifugal term which is proportional to  $\varepsilon^2 \vartheta Ra_\Omega Pr$  and varies linearly with position in the ampoule. The importance of the latter term depends on the dimensions of the amplitude of the angular vibration,  $\varepsilon$ , and the ratio  $\vartheta$ . The rocking motion of the angular vibration under consideration means that centrifugal terms give rise to a periodic forcing that fluctuates about the mean value at twice the period of the angular vibration.

Since the above system of equations has not been well studied, a conservative approach was adopted for the study of angular vibrations and we confine our investigation to a parametric study of flow regimes and transitions for thermo-vibrational situations in the absence of solidification.

#### 2.4. Solution method

The equations are solved in primitive variable form (velocity–pressure, temperature, concentration, etc.) using a finite element method package FEMINA/3D [14]. The continuity equation and momentum equations are considered simultaneously at each time step. This eliminates many problems related to boundary conditions and places only slight limitations on the time step size for transient problems (due to the physical nature of the problem). The regularization for the incompressibility condition makes the solution procedure more efficient, and allows the same order finite element approximation for both the velocity and

pressure [15]. This approach makes it possible to solve large time-dependent problems (up to 300 000 unknowns) on a SGI O2 workstation with reasonable computation times.

We implemented the above 3D models of convective buoyancy-driven melt flow in differentially heated cylindrical containers using the FEMINA/3D code. This code was carefully tested on benchmarked experimental and numerical data for a variety of 2D/3D viscous and thermo-convective flow problems [15,16].

For rotational vibrations the Ekman number can be of the order  $10^{-4}$ – $10^{-5}$  for frequencies on the order of 1 Hz. This results in large coefficients,  $\text{Pr}/E$ , for the Coriolis terms in the governing equations and causes difficulties in the numerical solution. To resolve this we implemented a high-accuracy solution method using preconditioning by high-order incomplete decomposition. This allowed us to obtain high-precision solutions with accuracy up to  $10^{-9}$ . Preconditioning also reduced the computation times by one to two orders of magnitude and the memory size by a factor of 8 for 3D flows compared to currently available commercial codes (e.g. CFD2000). A typical solution time

for a transient problem is about 2 h on a SGI O2 workstation.

### 3. Results and discussion

We verified the validity of the Boussinesq model for semiconductor and oxide melts under microgravity conditions. This topic has been discussed recently by Perera and Sekerka [17], Pukhnachev [18] and Gershuni and Lyubimov [11]. If the non-dimensional criteria, proposed by Pukhnachev,  $\text{Pu} = gL^3\nu^{-1}\kappa^{-1}$  is less than 1, then the Boussinesq model for thermal convection may not be valid. Our estimates show that the Boussinesq model is quite adequate for the differentially heated closed ampoule and the range of parameters and material properties under investigation. The values of  $\text{Pu}$  are of the order  $10^4$ – $10^5$  for semiconductor and oxide melts for  $g/g_0 = 10^{-5}$ – $10^{-4}$ , clearly well above 1.

A parametric study of translational and rotational vibrations under typical microgravity and terrestrial conditions for typical semiconductor melts was performed. A snapshot of a typical flow pattern for translational vibration is presented in Fig. 3. Even in the total absence of gravity the

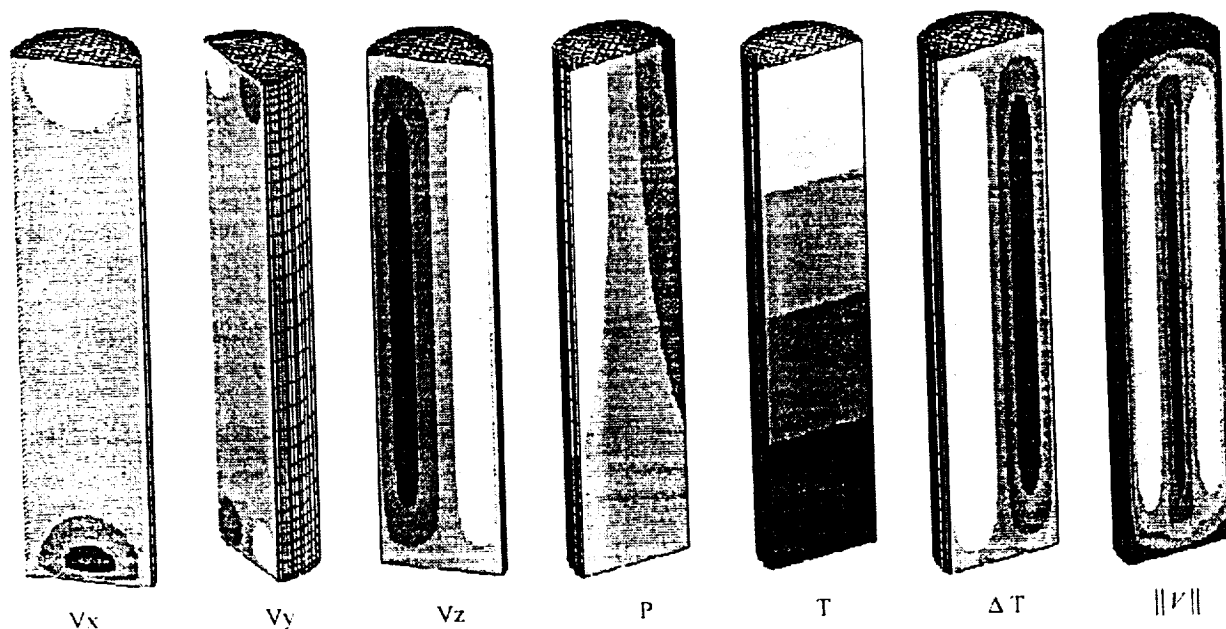


Fig. 3. Typical instantaneous 3D melt flow patterns for a lateral translational vibration at zero-g.  $\text{Ra} = 0$ ,  $\text{Ra}_T = 7.25 \times 10^4$ ,  $\text{Pr} = 0.01$ ,  $\omega = 100$  Hz. The velocity components are  $V_x$ ,  $V_y$ ,  $V_z$ ,  $P$  is the pressure,  $T$  is the temperature,  $\Delta T$  is the instantaneous temperature disturbance and  $\|V\|$  is the velocity magnitude. The grayscale range corresponds to maximum values (white) of the velocity, temperature and pressure variables to their minimum values (black). Vibrations are applied along the horizontal ( $x$ -direction).

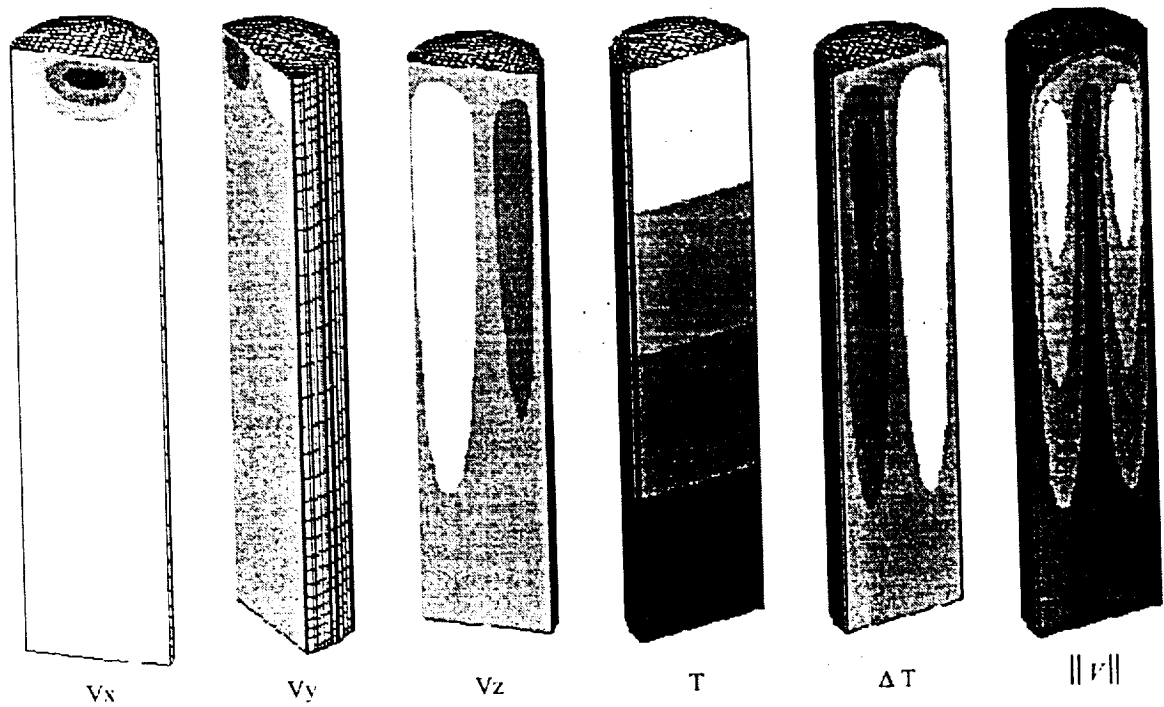


Fig. 4. Typical instantaneous 3D melt flow patterns for angular vibration at zero-g,  $Ra = 0$ ,  $Ra_0 = 4.6 \times 10^5$ ,  $Pr = 0.01$ ,  $\omega = 100$  Hz. The velocity components are  $V_x$ ,  $V_y$ ,  $V_z$ ,  $T$  is the temperature,  $\Delta T$  is the instantaneous temperature disturbance and  $|V|$  is the velocity magnitude. The grayscale range corresponds to maximum values of the velocity, temperature variables (white) to their minimum values (black).

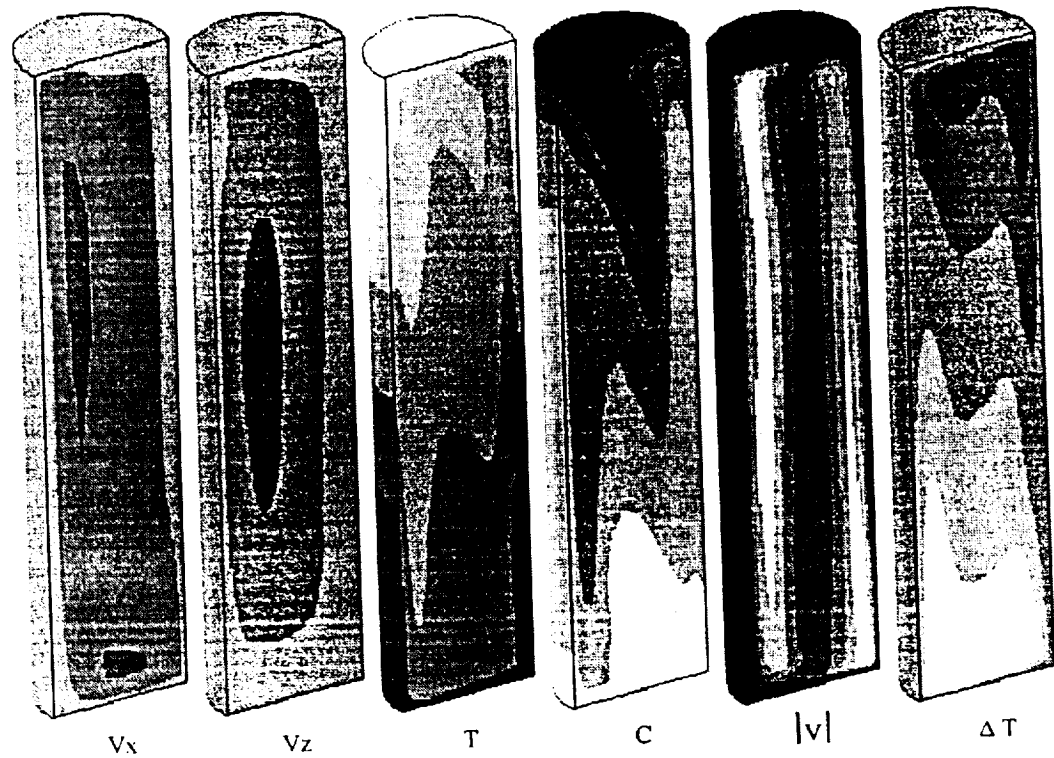


Fig. 5. Instantaneous 3D flow patterns for circularly polarized vibration,  $Ra = 7.25 \times 10^3$ ,  $Ra_0 = 7.4 \times 10^6$ ,  $Pr = 15$ ,  $\omega = 10$  Hz. The velocity components are  $V_x$ ,  $V_y$ ,  $V_z$ ,  $T$  is the temperature,  $\Delta T$  is the instantaneous temperature disturbance,  $C$  is the concentration and  $|V|$  is the velocity magnitude. The grayscale range corresponds to maximum values (white) of the velocity, temperature and concentration variables to their minimum values (black).

vibrations have resulted in detectable flows. For the cases examined, the temperature distribution remains almost unperturbed (due to the low  $Pr$  and weak flow strength).

The angle between the direction of vibration and the ampoule has been studied for translational vibrations in the presence of an axial temperature gradient. At high frequencies and when the angle is zero, no influence of the vibration on the flow was observed, even when vibrational the Rayleigh number is very high. The maximum observed effect corresponds to an angle of  $90^\circ$ . Here transport is significantly enhanced.

Typical flow patterns for rotational vibrations flow regimes are presented in Fig. 4. Maximal values of flow velocity are observed at the end of the ampoule that is farthest from the rotation origin.

The influence of vibrations on heat and mass transfer becomes significant for oxide melts due to their low thermal diffusivity ( $Pr \sim 10$ ). These flow patterns are shown in Fig. 5 for the case of circular polarized vibration. Initially (at time  $t = 0$ ), the species concentration was  $c = 1$  at the lower quarter of the cylinder and  $c = 0$  elsewhere. The evolution of the species concentration (process of mixing) is shown in Fig. 6 together with minimum and maximum values of velocity (for the whole domain) components. Complete mixing occurs in about 10 s. The heat transfer (local Nusselt number at the top and the bottom) is also enhanced by about an order of magnitude. If the frequency of vibration is high, of the order of 100 Hz (for fixed  $Ra_D$ ), then the changes in heat and mass transfer due to vibrations become less significant. This corresponds to earlier experimental observations [7,8].

Our results show that both translational, circular polarized and angular vibration can cause average melt flow for a range of parameters typical of practical semiconductor growth. For a given vibration amplitude and frequency, circular polarized and rotational (angular) vibrations result in more intensive melt flows than translational ones.

The influence of forced vibration on  $g$ -jitter-induced flows using SAMS microacceleration data from the USML-2 mission (Fig. 7a) was also investigated. Motivated by the predictions of the averaged equation theory presented in Ref. [11],

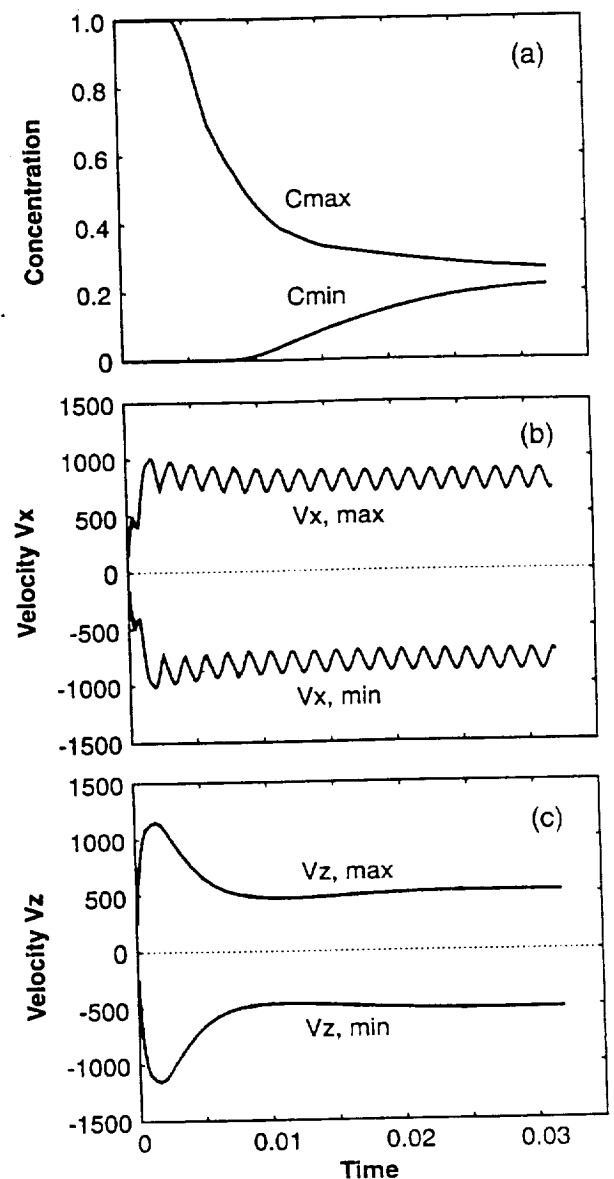


Fig. 6. Temporal evolution of (a) species concentration  $C$ , minimum and maximum values of  $C$ , (b) velocity extrema  $V_x$ , and (c)  $V_z$  for circularly polarized vibration applied to an oxide melt.  $Ra = 7.25 \times 10^3$ ,  $Ra_f = 7.4 \times 10^6$ ,  $Pr = 15$ ,  $\omega = 10$  Hz.

translational vibration was applied parallel to the ampoule axis (and thus, the temperature gradient) in an attempt to damp unwanted irregular time-dependent flow caused by  $g$ -jitter. While the flow variation with time becomes more regular, we did not succeed in completely suppressing the  $g$ -jitter flow (see Fig. 7b).

We found that the use of the same amplitude vibration in the direction orthogonal to the ampoule axis is more effective. This induces intensive



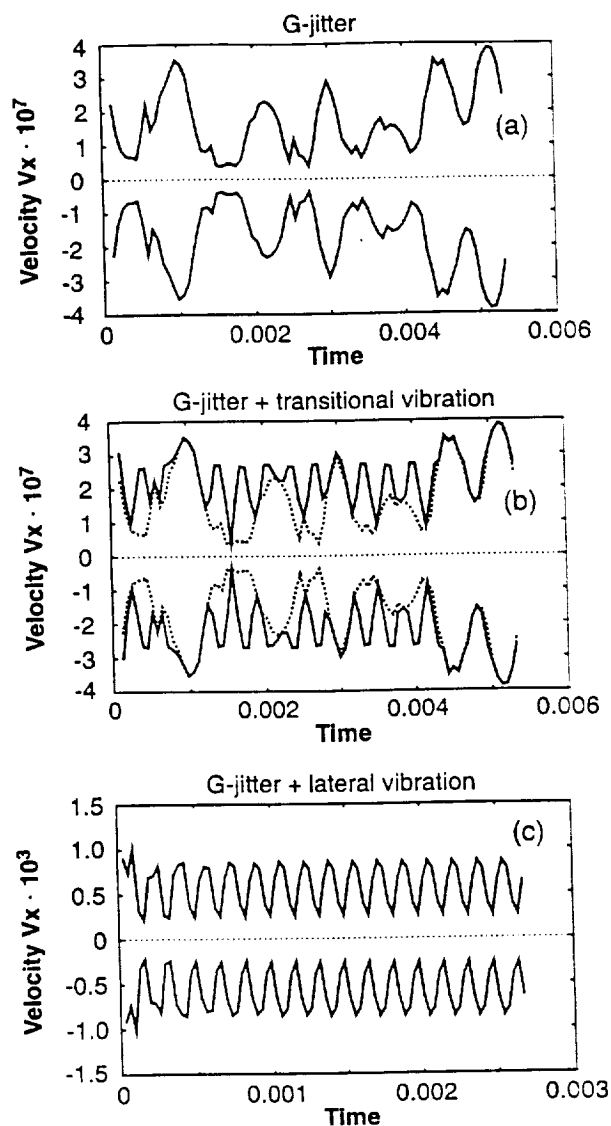


Fig. 7. Minimum and maximum values of the  $V_x$  velocity component versus time corresponding to a melt flow response to  $g$ -jitter (a),  $g$ -jitter and longitudinal vibration,  $Ra_T = 7.25 \times 10^4$ , and (b)  $g$ -jitter and lateral vibration,  $Ra_T = 7.40 \times 10^4$ .

thermal vibration flows and flow disturbances due to  $g$ -jitter become practically insignificant (Fig. 7c).

#### 4. Conclusions

The influence of translational, circularly polarized and rotational (angular) vibration in analysis in a model Bridgman melt growth configuration was investigated. The nature of the flows produced by

the types of vibration under consideration necessitated the use of the full 3D equations governing the transport of heat, mass and momentum. The governing equations were solved numerically. Flow patterns for translational, circular polarized and rotational (angular) vibrations and  $g$ -jitter micro-accelerations were analyzed. For translational vibration, thermovibrational flow is strongly dependent on the angle between the vibration direction and the temperature gradient. Circular polarized and rotational vibrations result in more intensive melt flows than translational ones. The simultaneous action of  $g$ -jitter and translational vibrations is currently being studied from the viewpoint of using applied vibration as a means of flow control.

#### Acknowledgements

Support from NASA grants NAG8-1229 and NAG3-1740 is gratefully acknowledged. The authors are grateful to R.S. Feigelson (Stanford University) for fruitful discussions.

#### References

- [1] D. Hurler (Ed.), Proceedings of the Physical Sciences Working Group Workshop on  $g$ -sensitivity of Planned Experimentation on the International Space Station, ESTEC, Noordwijk, The Netherlands, 10–11 September; Microgravity Sci. Technol. 11 (2/3) (1998) 1.
- [2] J.I.D. Alexander, J.-P. Garandet, J.J. Favier, A. Lizee, J. Crystal Growth 178 (1997) 657.
- [3] J.D. Trollinger, M. Rottenkolber, F. Elandalous, Meas. Sci. Technol. 8 (1997) 1573.
- [4] J.D. Trollinger, R. Ranel, R.B. Lai, Appl. Opt. 35 (1996) 681.
- [5] R. Naumann, An analytical model for transport from transient and periodic acceleration on Spacecraft, AIAA 99-1028, Proceedings of the 37th AIAA Meeting, Reno 11–17 January, 1999.
- [6] Y.-C. Lu, J.-J. Shiau, R.S. Feigelson, R.K. Route, J. Crystal Growth 102 (1990) 807.
- [7] R.C. DeMattei, R.S. Feigelson, J. Crystal Growth 12 (1993) 1062.
- [8] W.-S. Liu, J.F. Wolf, D.F. Elwell, R.S. Feigelson, J. Crystal Growth 82 (1987) 589.
- [9] E.V. Zharikov, L.V. Prihodko, N.R. Storozhev, J. Crystal Growth 99 (1990) 910.

- [10] R. Feigelson, E. Zharikov, Investigation of the crystal growth of dielectric materials by the Bridgman techniques using vibrational control, NASA Micr. Mat. Sci. Conference, 1998.
- [11] G. Gershuni, D. Lyubimov, Thermal Vibrational Convection, Wiley, New York, 1997.
- [12] A. Lizee, J.I.D. Alexander, Phys. Rev. E 56 (1997) 4152.
- [13] V.S. Yuferev et al., Effect of space craft rotation on convection and transport, Proceedings of the Xth European Symposium on Phys. Sci. in Microgravity, Moscow, 1997, p. 37.
- [14] V.I. Polezhaev, A.I. Fedoseyev et al., Mathematical Modeling of Convective Heat and Mass Transfer on the Basis of Navier–Stokes Equations, Nauka, Moscow, 1987.
- [15] A.I. Fedoseyev, J.I.D. Alexander. An efficient method for modeling of incompressible viscous flow, thermal and vibrational convection, 16th International Conference Numerical Methods and Fluid Dynamics, Extended abstracts, Arcachon, France, 6–11 July, 1998.
- [16] A.I. Fedoseyev, B.V. Alexeev, High order continuum model for incompressible viscous flow and application to numerical modeling of thermo-vibrational convection, in: E. Inan, K. Markov (Eds.), Continuum Models and Discrete Systems, World Scientific, London, 1998, pp. 131–137.
- [17] P.S. Perera, R.F. Sekerka, Phys. Fluids 9 (1997) 376.
- [18] V. Pukhnachev, Fluid Dynamics 5 (1994) 76.

# MAGNETIC FIELD SUPPRESSION OF SEMICONDUCTOR MELT FLOW IN CRYSTAL GROWTH: COMPARISON OF THREE METHODS FOR NUMERICAL MODELING

Alexandre I. Fedoseyev, Edward J. Kansa<sup>†</sup>, Carlos Marin,  
and Aleksandar G. Ostrogorsky

Center for Microgravity and Materials Research  
The University of Alabama in Huntsville  
Huntsville, Alabama 35899, U.S.A.  
E-mail: alex@cmmr.uah.edu

<sup>†</sup>Embry-Riddle Aeronautical University,  
East Bay Campus, Oakland, California 94621, U.S.A.

## Abstract

A numerical solution for thermal convection flows in a semiconductor melt with strong static magnetic field is presented. Rectangular cavity with different aspect ratios and gravity direction aligned and misaligned with the magnetic field vector are considered. Three numerical methods are compared. Although, the generated flows have extremely low velocity, the numerical solution of the governing equations involved is very complicated due to the thin boundary layers. It is shown that the finite element approach with regularization can provide numerical solutions in a wide range of  $Ha$  numbers (up to  $10^{-1}$ ). The results compare favorably with the asymptotic theoretical solutions.

## 1 Introduction

Application of magnetic fields is a promising approach for the reduction of convection during directional solidification of electrically conductive melts. Current technology allows the experiments with very strong static fields (up to 80 KGauss) for which nearly convection free segregation is expected in melts exposed to stabilizing temperature gradients (vertical Bridgman melts with bottom seeding) [1].

However, the reported experimental studies have yielded controversial results [2],[3]. Therefore, the computational methods are, a fundamental tool that may enhance our understanding of the phenomena occurring during the solidification of semiconductor melts. Moreover, the effects like the bending of the isomagnetic lines, dif-

ferent aspect ratios and misalignments between the gravity and magnetic field vectors which are difficult to model analytically, be studied through numerical simulations.

The reported numerical models and results are not able to explain the published experimental data [4],[5]. The computational task is complicated because of the thin boundary layers [6], although velocity of the generated flows is extremely low.

Here, for comparison, three different numerical approaches we have been used :

- (1) The spectral method implemented in [7],
- (2) The finite element method with regularization for boundary layers [8],
- (3) The multiquadric method, a novel method with global radial basis functions [9].

The results obtained by these three methods are presented for a wide range of Hartmann numbers corresponding to magnetic fields  $B$  from 0.05 to 5.0 Tesla (0.5 to 50.0 KGauss). Comparison and discussion of accuracy, efficiency, reliability and agreement with the asymptotic solution are presented.

## 2 Governing equations

The two dimensional steady state thermal convection of an incompressible viscous fluid (melt) in a rectangular cavity having width  $D$  and height  $H$  was considered. More general geometries are discussed in [17], [18], [19].

The governing momentum, continuity and energy equations (using the Boussinesq approximation) are respectively:

$$(\nabla \nabla) \mathbf{V} - Pr \nabla^2 \mathbf{V} + \nabla p = Ra Pr \cdot \Theta \cdot \mathbf{e}_g - \mathbf{F} \quad (1)$$

$$\nabla \cdot \mathbf{V} = 0 \quad (2)$$

$$(\nabla \nabla) \Theta = \nabla^2 \Theta \quad (3)$$

where length, time and velocity are scaled by  $L$ ,  $L^2/\kappa$  and  $\kappa/L$  respectively. Here  $L$  is equal to the the smaller of the two characteristic dimensions involved ( $D$  and  $H$ ), and  $\kappa = \frac{\lambda}{\rho}$  is the thermal diffusivity of the melt.  $\mathbf{F}$  is a body force due to magnetic field (Lorenz force). The Lorenz force is given by

$$\mathbf{F} = Pr Ha^2 [(\mathbf{V} \times \mathbf{e}_B) \times \mathbf{e}_B] = (Pr Ha^2 V_1, 0) \quad (4)$$

where  $V_1$  is the horizontal component of the velocity. The electrical potential was neglected, because, when a vertical magnetic field is applied, the electrical potential is uniform ( $\nabla \phi = 0$ ) [1]. The electrical potential can not be neglected if the symmetry is broken, e.g. if the magnetic field direction and the gravity vector are slightly misaligned. However, to simplify the study, we neglect this effect. According to [1], Joule heating due to electromagnetic field can be neglected as well. The nondimensional temperature  $\Theta$  is scaled by  $\Theta = (T - T_{cold})/\Delta T$ ,  $\Delta T = GL$ .  $G$  is a vertical temperature gradient  $\frac{\partial T}{\partial y}$ . The Prandtl, Rayleigh and Hartmann numbers are, respectively, given by

$$Pr = \frac{\nu}{\kappa}, Ra = \frac{\beta \Delta T g L^3}{\nu \kappa}, Ha = LB_0 \sqrt{\frac{\sigma}{\nu \rho}}$$

Here  $\beta, g, \nu, \rho, \sigma$  are thermal expansion coefficient, gravitational acceleration, kinematic viscosity, density, and electrical conductivity;  $B_0$  is the magnetic field intensity.  $\mathbf{e}_g, \mathbf{e}_B$  are the unit vectors in the direction of gravitational acceleration and magnetic field.

The boundary conditions for eq. (1)-(3) are: (i) the non-slip condition for the velocity,  $\mathbf{V} = 0$ , on the walls, and (ii) specified temperature distribution,  $\Theta = y$  on side walls, and  $\Theta_B = -\Theta_0(x-L)^2$  at the bottom. To exclude the undefined constant, the pressure was set to zero at an arbitrary location,  $p(x_0, y_0) = 0$ .

### 3 Problem parameters

The problem was solved using the properties of Germanium (*Ge*) melt exposed to magnetic fields having intensity  $B_0$  in a range from 0 to 5 Tesla (and in few cases up to

50 Tesla). The direction of magnetic field vector is axial,  $\mathbf{e}_B = (0, 1)$ . The corresponding Hartmann number varies from  $Ha = 0$  to 2170 (and in few cases to  $Ha = 2.17 \cdot 10^4$ ). The flow domain is rectangular cavity having height  $H$  and width  $L$ . Two cases were considered (a)  $L = 1$  cm,  $H = 2$  cm, and (b)  $L = 2$  cm,  $H = 1$  cm.

The temperature gradient on a side wall is  $G = 70$  K/cm. The average lateral temperature gradient at the bottom boundary was 0.5 K/cm. The corresponding Rayleigh number is  $Ra = 1.24 \cdot 10^5$ . Earth gravity  $g$  was considered to be (i) aligned to the magnetic field direction,  $g = g_0(0, -1)$  and (ii) misaligned by 0.5 degrees.

## 4 Numerical methods

Three numerical methods were used to solve the system of eq. (1) - (3) for the boundary conditions and parameters given above.

### 4.1 Spectral element method

To use the spectral element (SE) code NEKTON [7], the domain was divided into quadrilateral elements, refined near the walls (Fig. 1a).  $8 \times 8$  Chebyshev polynomials were used inside each of elements for field variables approximation. In our tests total number of elements was 362. The total number of unknowns was  $5 \cdot 10^4$ .

### 4.2 Finite element method with regularization for the Navier-Stokes equations

The finite element method with regularization for the Navier-Stokes equations (FEMR) was proposed in [8] for high  $Re$  number flows. It was shown that such a regularization works well in case of flows with thin boundary layers, even with few mesh nodes placed inside the boundary layer. For the present problem, the continuity equation (2) is modified as follows

$$\nabla \cdot \mathbf{V} = \tau \nabla \cdot (\nabla p - \mathbf{F} - Ra Pr \cdot \Theta \cdot \mathbf{e}_g) \quad (5)$$

where  $\tau$  is a small regularization parameter. For  $\tau \rightarrow 0$  eq. (5) approaches the original equation (2). The boundary condition for the pressure on the wall is

$$(\nabla p - \mathbf{F} - Ra Pr \cdot \Theta \cdot \mathbf{e}_g) \cdot \mathbf{n} = 0, \quad (6)$$

where  $\mathbf{n}$  is a unit wall normal vector. Eqs. (5) and (6) present the main feature of this method, and ensure the balance of the component of the force normal to the region boundary. This approach allows the use of the same order finite element approximation for the velocity and pressure

with all unknowns located at the same nodal points. The justification of this regularization is given in [10]. Similar terms have been obtained as a result of the consistent treatment of time-advancement for the divergence-equation by Löhner (see [11]). Löhner has also shown that similar terms appear in the discrete equations as a result of different order finite element approximations used for interpolation of velocity and pressure.

The numerical solution is insensitive to the value of  $\tau$ . In our calculations we have chosen the value of  $\tau$  within the range  $10^{-8}$  to  $10^{-4}$  and obtained nearly identical solutions. For a smaller value of  $\tau$  the discrete equations become nearly incompatible, and numerical solution exhibits strong spatial oscillations.

Simple linear finite elements were used for numerical approximation of velocity, pressure and temperature. Triangular meshes with  $40 \times 100$  and  $80 \times 100$  nodes were refined near the walls (Fig. 1b). Since on both meshes yielded nearly identical results, we used the  $40 \times 100$  mesh in most runs. Total number of nodes and unknowns was respectively  $4 \cdot 10^3$  and  $16 \cdot 10^3$ . The FEMINA/3D CFD code (Finite Element Method IN Applications) [12] was modified to implement the proposed regularization method. Discrete finite element equations corresponding to the eqs. (1), (5), (3) were solved together simultaneously by the CNSPACK solver [12] using the CGS-type iterative technique and high order preconditioning by incomplete decomposition.

#### 4.3 Multiquadric radial basis function method

The Multiquadric Radial Basis Function (MQ) Method is a novel meshless collocation method with global basis functions. The concept of solving partial differential equations (PDE) using radial basis functions (RBFs) was introduced by Kansa in 1990 [9]. He implemented this approach for the solution of hyperbolic, parabolic, and elliptic PDEs using the MQ RBFs proposed by Hardy [13],[14] for interpolation of scattered data.

An RBF is a function that depends only upon the distance between a point  $(x, y)$  and a reference node  $(x_j, y_j)$ . Among studied RBFs, only the MQ RBFs have been proven to have an exponential convergence for the function interpolation [16]. A MQ RBF is given by  $g_j(x, y) = \sqrt{(x - x_j)^2 + (y - y_j)^2 + c_j^2}$ , where  $c_j$  is called the *shape parameter*. The numerical experiments for parabolic and elliptic PDEs by Kansa [9] show high accuracy and efficiency of the MQ scheme. A brief review on MQ RBF for the solution of PDE can be found in [15] and on the RBF-PDE Web site [22]. This approach results in modest size

systems of nonlinear algebraic equations which can be efficiently solved by using widely available library routines and linear solvers for dense matrices.

For a given set of  $N$  nodes the solution for unknown  $V$ ,  $p$  or  $\Theta$  is approximated as a sum of MQ functions with the coefficients as unknown. These coefficients are found by collocating governing equations at the internal nodes and boundary conditions at the boundary nodes. The nonlinear algebraic system is solved by Newton method.

$25 \times 25$  uniformly distributed nodes and constant shape parameters  $c_j = c_0 = \text{const}$  were used for all functions. Total number of unknowns was 2500.

## 5 Results and discussion

### 5.1 Convection in rectangular cavity with $H/D=2$

The nondimensional parameters  $Pr = 0.006$ ,  $Ra = 1.25 \cdot 10^5$  were used in all calculations.

#### Flow without magnetic field: $B=0$ , $Ha=0$

The flow domain has  $D = 1$ ,  $H = 2$  and the length scale was  $L = D$ . The temperature distribution at the bottom boundary is given by  $\Theta_B = -3.575 \cdot 10^{-3}(1 - 4x^2)$ . The results for the case  $\alpha = 0$  are shown in Fig. 2 ( $\alpha$  is the angle between the gravity vector and the vertical axis). The solution obtained by all three methods are nearly identical. The flow is driven by radial temperature gradient caused by parabolic temperature profile imposed on the bottom boundary. The flow pattern consists of two counter-rotating symmetric cells, located at the lower corners. Note that the stabilized axial temperature gradient is suppressing the flow.

If the direction of gravity vector is misaligned with the ampoule axis by  $0.5^\circ$ , the flow pattern becomes quite different. The component of gravity normal to the temperature gradient becomes a driving force for the convection. A single roll is formed, while the magnitude of melt velocity is higher by a factor of two to three.

### Flows under magnetic fields

#### 5.1.1 $B = 0.05$ Tesla, $Ha=21.7$ .

The MQ method did not yield a solution, because the Newton method did not converge (since the Jacobian becomes ill-conditioned).

The solution by the SEM and FEMR methods show notable differences. The SE solution for the velocity field exhibits numerical oscillations between the mesh nodes.

The flow pattern from FEMR is the same as in the absence of a magnetic field (Fig. 3). The vertical velocity profile at  $y = 0.25$  shows a boundary layer. The flow velocity is decreased by about a factor of two.

### 5.1.2 $B = 0.5$ Tesla, $Ha=217$ .

The boundary layer becomes very thin, and the flow velocity is about two order of magnitude lower compared to  $B = 0$  (not shown). The velocity profiles from the SE computation exhibit spatial oscillation with velocity sign change between mesh nodes. The FEMR can provide the results still without difficulty, the velocity profiles remain smooth.

### 5.1.3 $B = 5.0$ Tesla, $Ha=2170$ .

The results from the SE computation showed strong numerical instability. The FEMR solution indicates that the flow pattern is about the same, while the velocity is lower about two order of magnitude compared to  $B = 0.5$  Tesla. The boundary layers are extremely thin ( $0.01cm$ ), and therefore almost invisible on a plot (Fig.4).

In case of a misalignment of gravitational acceleration with ampoule axis, the flow pattern changes to one big cell for this and all other values of magnetic field considered.

### 5.1.4 $B = 50$ Tesla, $Ha=21700$ .

This case was done just to test the ability of proposed FEMR method, the solution still remains smooth with even three times more thin boundary layer compared to  $B = 5.0$  Tesla. Stream lines for this case are shown in Fig. 5, and the velocity amplitude is presented by the most right point on a plot in Fig.6.

Stretching of the stream lines caused by the magnetic field is shown in Fig. 5. This stretching presented schematically in [1], [5] but, to our knowledge, computational results were not shown.

## Discussion

Figure 6 shows the maximum radial velocity calculated, using the FEMR method, for different values of the imposed magnetic field  $B$ . The maximum of horizontal (radial) velocity versus  $B$  is presented by few curves, marked as " $Vr(b)$ " for FEMR on  $40 \times 100$  mesh uniform in the vertical direction, by " $Vr(f)$ " for  $40 \times 100$  mesh refined at the walls and by " $Vr(d)$ " for  $80 \times 100$  mesh refined at the walls. Results for misaligned case are presented by the curve with squares, labeled as " $Vr(a = 0.5)$ ". One can observe the predicted asymptotic dependence  $V_{max} \sim Ha^{-2}$

[1] for all the cases, starting at about  $B = 0.05$  Tesla ( $Ha \approx 20$ ).

The main computational difficulty of this problem is due to the viscous flow with thin boundary layer. Despite the fact that actual flow velocities are very low and the Reynolds number obtained using the computed velocities, is  $Re \sim 10^{-1}$  to  $10^{-6}$ , a big value of the Hartmann number results in a relatively small coefficient at the highest derivative of the velocity in the momentum equation. Solution of such a problem exhibits thin boundary layer with the thickness  $\delta \sim Ha^{-1}$ , and the "equivalent" Reynolds number  $Re_{eqv} \sim Ha^2$ , for  $B=0.5$  Tesla  $Re_{eqv} = 4.7 \cdot 10^4$  and  $B=50.0$  Tesla  $Re_{eqv} = 4.7 \cdot 10^8$ .

## 5.2 Thermal convection in rectangular cavity with aspect ratio $H/D=0.5$

The nondimensional temperature distribution at the bottom boundary is given by  $\Theta_B = -7.150 \cdot 10^{-3}(1 - x^2)$ . The axial temperature gradient applied on the vertical wall is also  $G = 70$  K/cm.

### Flow without magnetic field: $B=0$ , $Ha=0$

The solution obtained by all three methods are close to each other. The flow pattern consists of two counter-rotating symmetric cells, that occupy most of the volume. Fig. 7.

In the case of the gravity misalignment with the ampoule axis direction by  $0.5 \text{ deg.}$ , the axial temperature gradient becomes a main driving force for the thermal convection. This results in the change of flow pattern that becomes consisting of one big convective cell.

### Flow under magnetic fields

The results are shown in Fig. 8. Again when  $Ha$  number is high, all the methods except FEMR, exhibit the same difficulties as in a case of aspect ratio  $H/D = 2$ . A summary of the results is shown in Fig. 9. The suppression of the flow is essentially same efficient as before with similar asymptotic dependences  $V_{max} \sim Ha^{-2}$ . The velocity profile in the boundary layer obtained by FEMR is shown in Fig. 10. One of the advantages of FEMR is that its solution remains smooth even at the big change of the slope. One can see that the thickness of the vertical boundary layer is in agreement with asymptotic solution,  $\delta \sim Ha^{-1}$ . The tangent velocity derivative at the boundary decreases with  $Ha$  number as  $\frac{\partial V_r}{\partial n} \sim \frac{V_{max}}{\delta} \sim Ha^{-1}$ .

Comparing between Fig. 6 and 9 it is found that misalignment's impact on the reducing of the convection is more important for the aspect ratio  $H/D = 1$ .

## Conclusions

We compared three different numerical methods for the solution of thermal convection flows in a semiconductor melt with strong static magnetic field applied. These are spectral element method, finite element method with regularization for the Navier-Stokes equations and multiquadric method, a method with global basis functions. Although the generated flows are extremely low, the computational task is very complicated because of the thin boundary layer at high Hartmann numbers,  $Ha \gg 1$ . We considered melt region geometry with different aspect ratios, and gravity direction aligned and misaligned with the magnetic field vector. The comparison shows that the finite element approach with regularization can obtain stable and reliable solutions in a wide range of  $Ha$  number, up to  $10^4$ . These results compare favorably with asymptotic solutions.

The main difficulty of this problem is that a flow has a very thin boundary layer. Despite the fact that actual Reynolds number is very low,  $Re \sim 10^{-1}$  to  $10^{-6}$ , a high value of the Hartmann number results in a relatively small coefficient at the velocity Laplacian in the momentum equation. Solution of such problem exhibit thin boundary layers with related, like for high Reynolds number flows, difficulties. That is one of the reasons for the discrepancy in the results that numerical studies reported. Both the spectral method and the multiquadric method with global basis functions needs improvement to deal with thin boundary layers. Multilevel approximation by Fasshauer [20],[21] can be one of the ways.

Numerical solution of these problems by available commercial CFD codes may be not efficient or not possible. Adaptive algorithms can be a promising solution. Development of more accurate and efficient solution methods for this problem is necessary.

## Acknowledgements

This work was supported in part by National Aeronautics and Space Administration through grant NAG8-1229. The authors are grateful to G. S. Dulikravich for fruitful discussions.

## References

- [1] J. P. Garandet and T. Alboussiere, Bridgman growth: Modeling and experiments. In: "The role of magnetic field in Crystal Growth", Pergamon Press (to be published).
- [2] D.H. Matthiesen, M. J. Wargo, S. Motakef, D. J. Carlson, J. S. Nakos and A. F. Witt, J. Crystal Growth, **85** (1987) 557.
- [3] Y. Kang, K. Okano, Hoshikawa and T. Fukuda, J. Crystal Growth, **140** (1994).
- [4] D. H. Kim, P.M. Adornato and R. A. Brown, J. Crystal Growth, **80** (1987) 155.
- [5] S. Motakef, Magnetic field elimination of convective interference with segregation during growth of doped semiconductors, J. Crystal Growth, **104** (1990) 833.
- [6] M. Yao, A. Chait, A. L. Fripp and W. J. Debnam, Magnetically damped convection and segregation in Bridgman growth of PbSnTe, J. Crystal Growth, **173** (1997) 467.
- [7] NEKTON 2.85 Tutorial Guide, FLUENT Inc., Second Edition, May 1996.
- [8] A. I. Fedoseyev, and B. V. Alexeev, Higher Order Continuum Model for Incompressible Viscous Fluid Flow. In: Continuum Models and Discrete Systems, Eds. E. Inan, A. Markov, World Scientific, London, 1998, 130-137.
- [9] E. J. Kansa, Multiquadrics-a scattered data approximation scheme with applications to computational fluid dynamics-II. Solutions to hyperbolic, parabolic, and elliptic partial differential equations, Comput. Math. Applic., **19**, No. 8/9 (1990), 147-161.
- [10] B. V. Alexeev, The generalized Boltzmann equation, generalized hydrodynamic equations and their applications, Phil. Trans. Roy. Soc. London, **A. 349** (1994) 417-443.
- [11] R. Löhner, Design of Incompressible Flow Solver: Practical Aspects, In: Incompressible computational fluid dynamics, Eds. M. D. Gunzburger and R. A. Nicolaides, Cambridge Press, 1993, 267-294.
- [12] V. I. Polezhaev, A. I. Prostomolotov, and A. I. Fedoseyev, Finite Element Method in Viscous Fluid Mechanics Problems, In: Advances in Science and Technology, Fluid Mechanics series, **21**, No. 3, VINITI, Moscow, 1987, 3-92.
- [13] R. L. Hardy, Multiquadric equations of topography and other irregular surfaces, J. Geophys. Res., **76** (1971), 1905-1915.

- [14] R. L. Hardy. Theory and applications of the multiquadric- biharmonic method: 20 years of discovery. *Comput. Math. Applic.*, **19**, No. 8/9 (1990), 163-208
- [15] A. I. Fedoseyev, M. J. Friedman, and E. J. Kansa. Continuation for nonlinear elliptic partial differential equations discretized by the multiquadric method. to appear in *Int. J. Bifur. and Chaos*.
- [16] W. R. Madych and S. A. Nelson. Multivariate interpolation and conditionally positive definite functions II. *Math. Comp.*, **54** (1990), 211-230.
- [17] G. S. Dulikravich, and V. Ahuja. Modeling Dielectric Fluids Solidification With Charged Particles in Electric Fields and Reduced Gravity. *Numerical Heat Transfer, Fundamentals, Part B*, **25** (1994), 357-373.
- [18] G. S. Dulikravich and S. R. Lynn. Unified Electro-Magneto-Fluid Dynamics (EMFD): A Survey of Mathematical Models. *International Journal of Non-Linear Mechanics*, **32**, No. 5 (1997), 913-922.
- [19] G. S. Dulikravich and S. R. Lynn. Unified Electro-Magneto-Fluid Dynamics (EMFD): A Survey of Mathematical Models. *International Journal of Non-Linear Mechanics*, **32**, No. 5 (1997), 923-932.
- [20] G. E. Fasshauer. On Smoothing for Multilevel Approximation with Radial Basis Functions. In: *Approximation Theory IX*, Eds. C. K Chui and L. L. Schumaker, Vanderbilt University Press, Nashville, TN, 1998
- [21] G. E. Fasshauer and J. W. Jerome. Multistep Approximation Algorithms: Improved convergence rates through postconditioning with Smoothing Kernels. *Advances in Computational Mathematics* (to appear).
- [22] RBF-PDE. Radial basis function methods for solution of partial differential equation. Web site <http://rbf-pde.uah.edu>



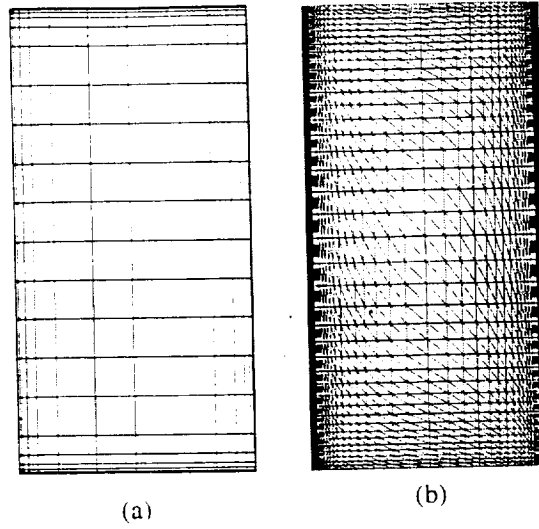


Figure 1: Meshes used in: (a) Spectral elements calculations (each element has  $8 \times 8$  internal nodes) and (b) finite elements calculations (8,000 triangular with 4000 nodes).

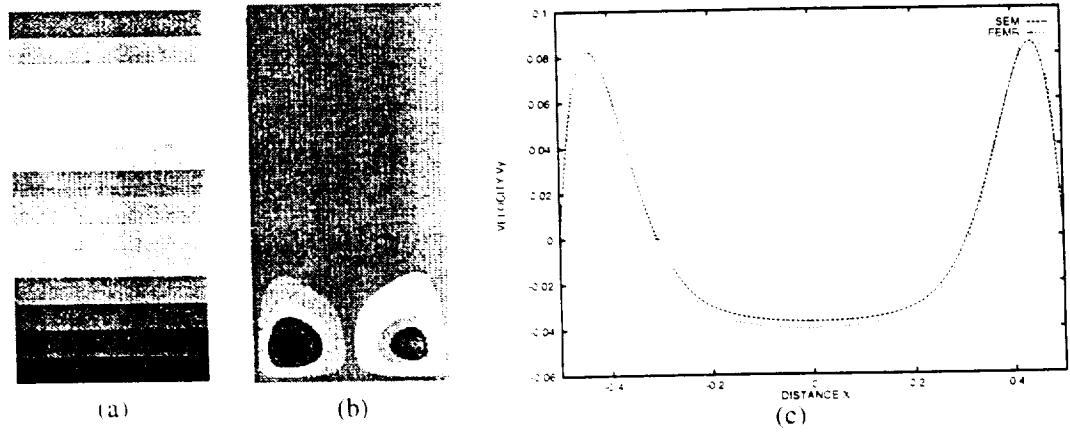


Figure 2:  $H/D = 1$ ,  $Ra = 1.25 \cdot 10^5$  ( $B=0.5$  Tesla). Stream functions for gravity vector (a) aligned and (b) 0.5 degrees misaligned relative to the vertical direction. (c) Nondimensional vertical velocity profile  $V_y(x)/(0.225 \text{ cm/s})$  calculated using the FEMR method  $0.25H$  from the bottom of the cavity ( $y/H = 0.25$ )

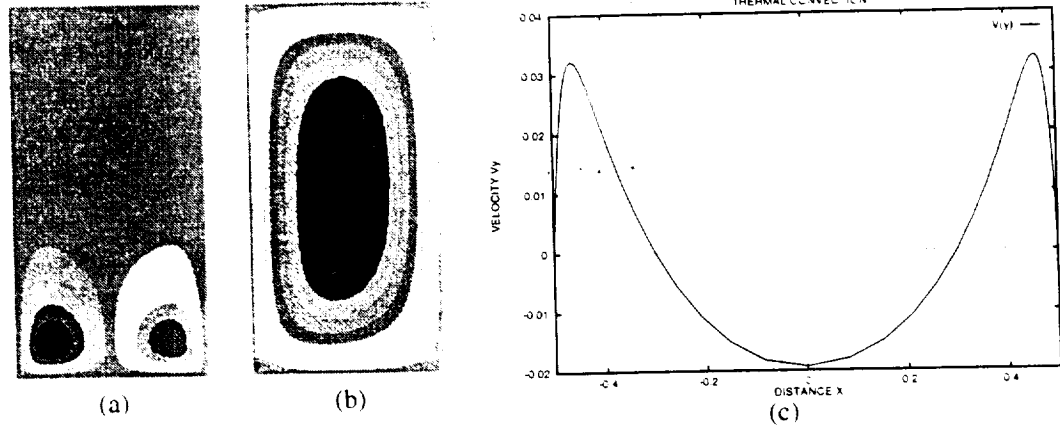


Figure 3: Thermal convection with magnetic field for geometry 1.  $D = 1$ ,  $H = 2$ ,  $Ra = 1.25 \cdot 10^5$ ,  $Ha = 21.7$  ( $B = 0.05 \text{ Tesla}$ ): (a) stream function for aligned and (b) misaligned by 0.5 degree gravity direction, (c) vertical velocity profile  $V_y(x)/(0.225 \text{ cm/s})$  for (a) at  $y/H = 0.25$  by FEMR.

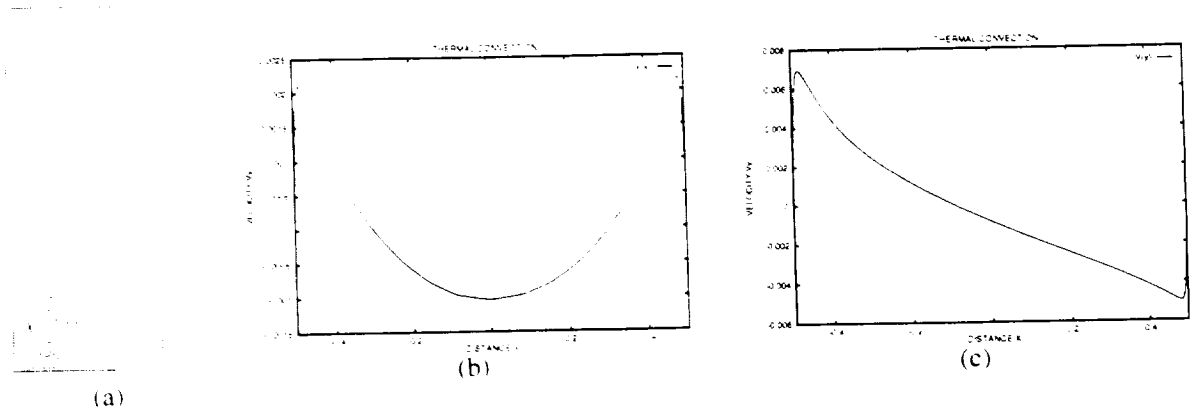


Figure 4: Thermal convection with magnetic field for  $D = 1$ ,  $H = 2$ ,  $Ra = 1.25 \cdot 10^5$ ,  $Ha = 2170.0$  ( $B = 5.0 \text{ Tesla}$ ): (a) stream function; (b) vertical velocity profile  $V_y(x)/(0.225 \text{ cm/s})$  at  $y = 0.25$ ; (c) velocity profile  $V_y(x)/(0.225 \text{ cm/s})$  for misaligned by 0.5 degree gravity direction at  $y = 0.25$ .

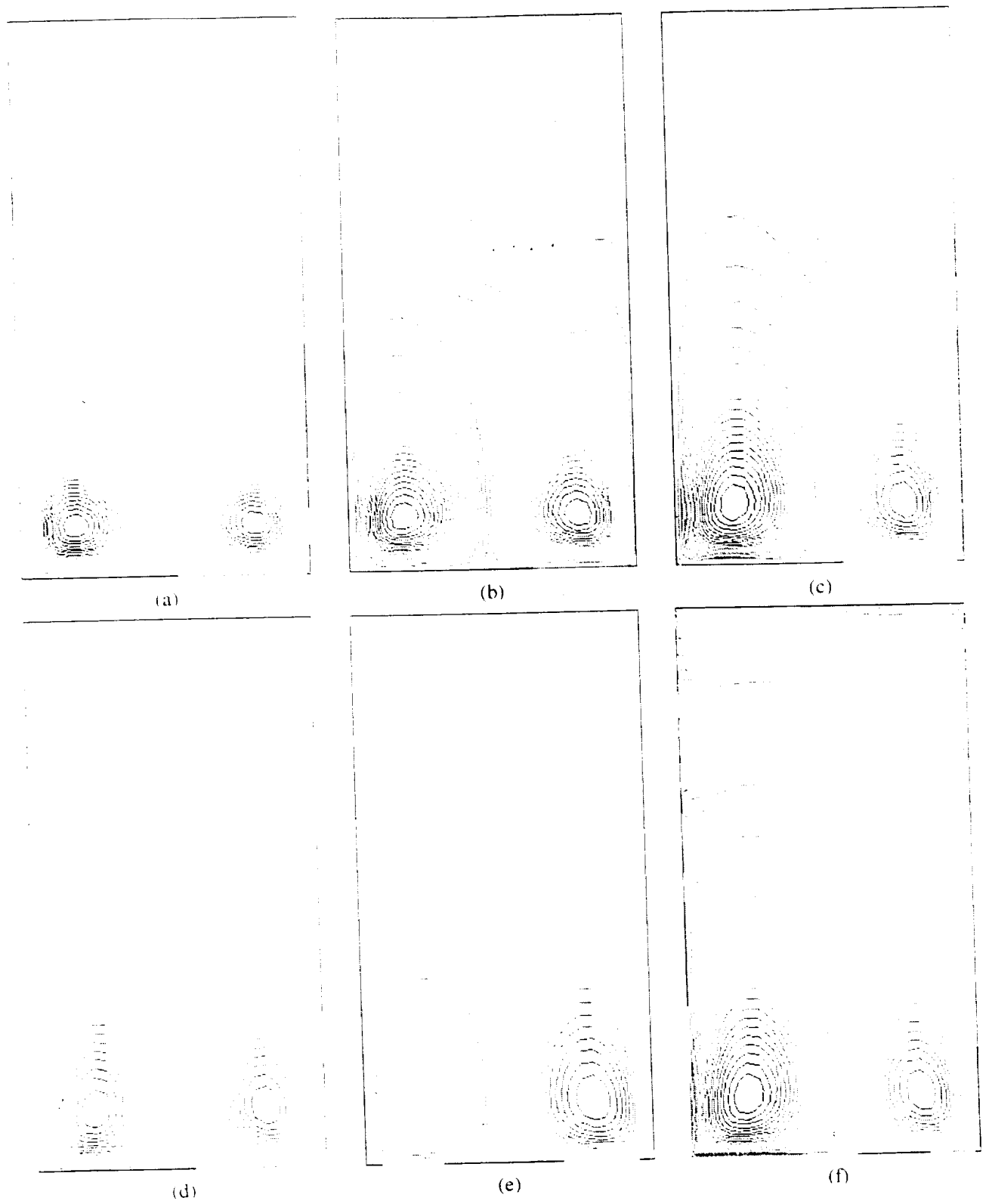


Figure 5: Stretching of the flow streamlines with increasing magnetic field. (a)  $B = 0$ . (b)  $B = 0.005$  Tesla, and (c) to (f) correspond, respectively, to  $B = 0.05, 0.5, 5.0$  and  $50.0$  Tesla

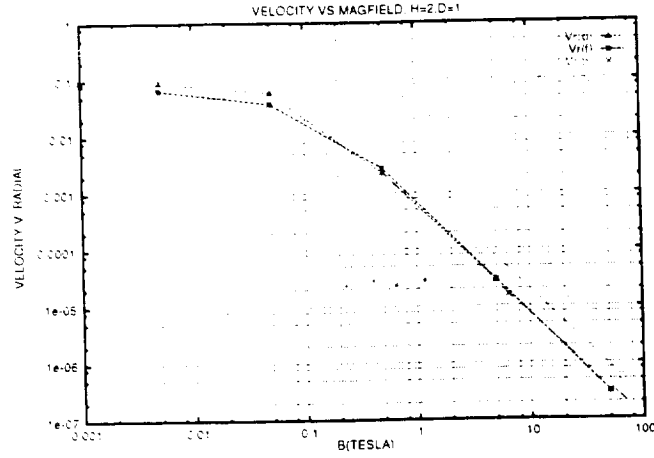


Figure 6: A summary of magnetic field suppression of the flow for  $H = 2$ ,  $D = 1$ . Maximum value of horizontal (radial) velocity versus  $B$ :  $Vr(b)$  on  $40 \times 100$  uniform in vertical direction mesh,  $Vr(f)$  for  $40 \times 100$  refined near walls mesh, and  $Vr(d)$ ,  $80 \times 100$  mesh refined at the walls. Predicted asymptotic dependence  $V_{max} \sim Ha^{-2}$  is observed for all the cases including the misaligned one, starting from about  $B = 0.25$  Tesla.

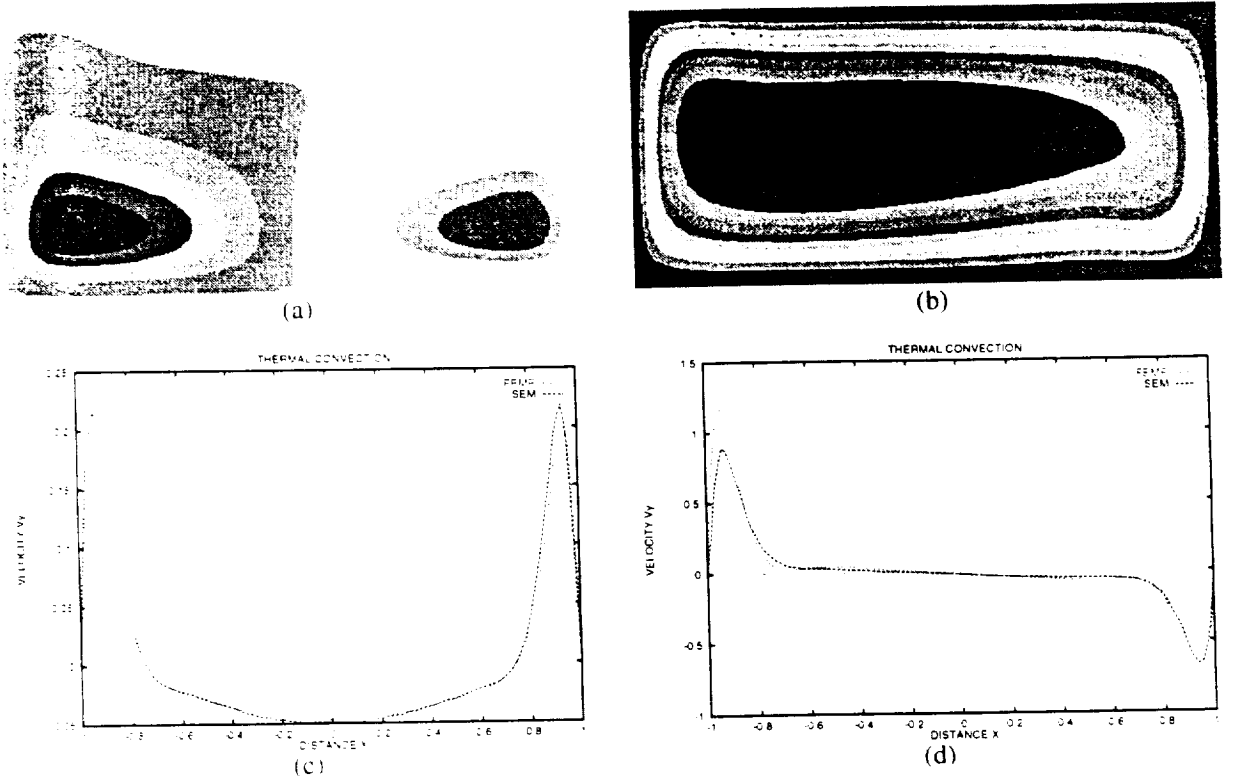


Figure 7: Thermal convection without magnetic field for  $D = 2$ ,  $H = 1$ ,  $Ra = 1.25 \cdot 10^5$ : (a) stream function, (b) stream function for misaligned configuration, (c) vertical velocity profiles by SEM and FEMR,  $V_y(x)$  for (a) at  $y = 0.25$ , and (d) vertical velocity profiles by SEM and FEMR,  $V_y(x)$  for (b) at  $y = 0.25$ . Velocity scale is  $0.225$  cm/s.

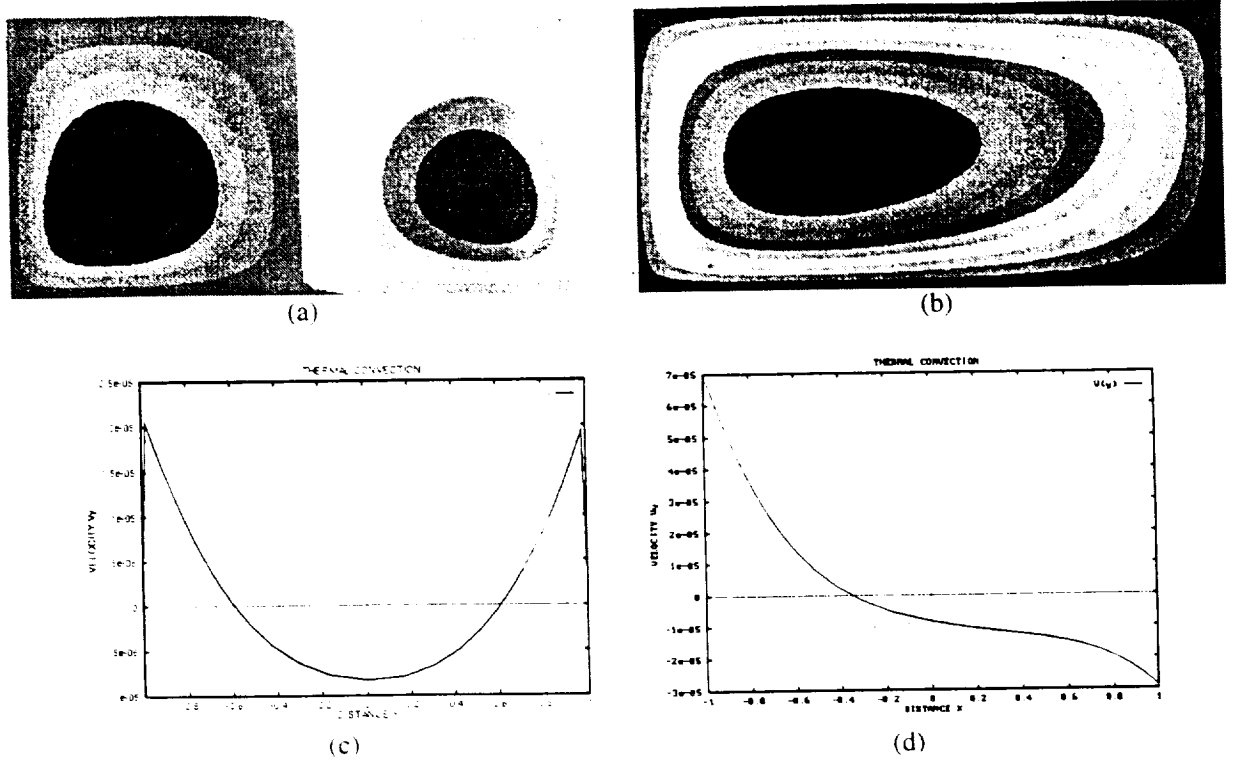


Figure 8: Thermal convection with magnetic field.  $D = 2$ ,  $H = 1$ ,  $Ra = 1.25 \cdot 10^5$ ,  $Ha = 2170$  ( $B = 5.0$  Tesla): (a) stream function. (b) stream function for misaligned case. (c) vertical velocity profile  $V_y(x)$  for (a) at  $y/H = 0.25$  and (d) vertical velocity profile  $V_y(x)$  for (b) at  $y/H = 0.25$ ; velocity scale is 0.225 cm/s.

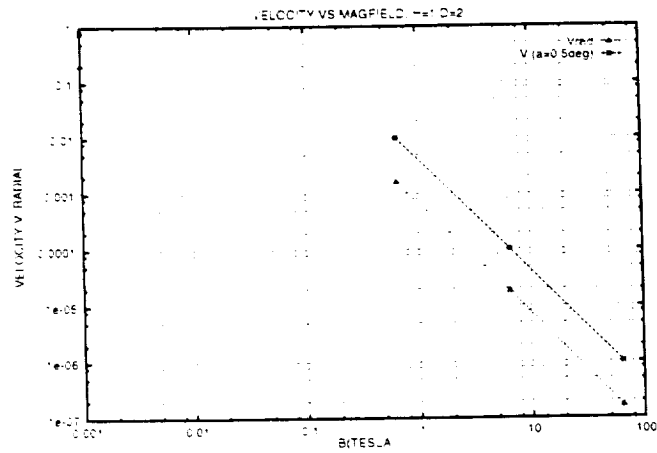


Figure 9: Summary of magnetic field suppression of the flow for  $H = 1$ ,  $D = 2$ : maximum value of horizontal (radial) velocity versus  $B$  for aligned and misaligned configurations. Predicted asymptotic dependence  $V_{max} \sim Ha^{-2}$  is observed for both cases.

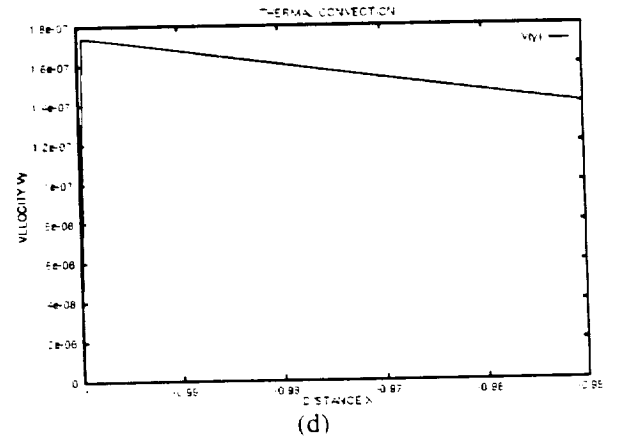
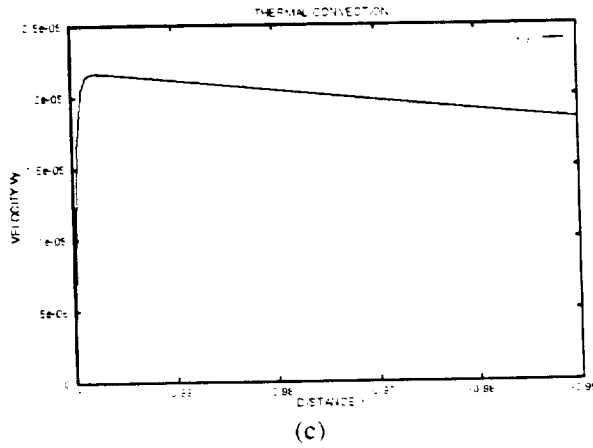
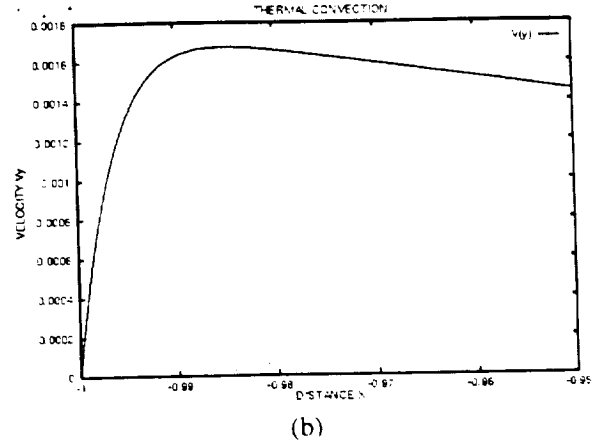
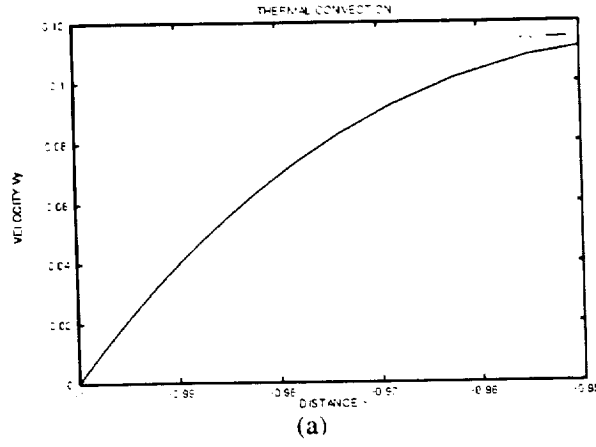


Figure 10: The velocity profile in the boundary layer ( $X$  coordinate from -1.0 to -0.95) at  $y/H = 0.25$  with increasing the magnetic field for  $D = 2$ ,  $H = 1$ ,  $Ra = 1.25 \cdot 10^5$ : (a) to (d) correspond, respectively to  $B = 0, 0.5, 5.0$  and  $50.0$  Tesla. The velocity amplitude decreases as  $Ha^{-2}$  and its gradient on the wall decreases as  $Ha^{-1}$  with increasing the Hartmann number  $Ha$ .

## INVESTIGATION OF VIBRATIONAL CONTROL OF CONVECTIVE FLOWS OF THE BRIDGMAN CRYSTAL GROWTH TECHNIQUE

Alexandre I. Fedoseyev

Center for Microgravity and Materials Research, University of Alabama in Huntsville, Huntsville, Alabama

### Introduction

The character of natural buoyant convection in rigidly contained inhomogeneous fluids can be drastically altered by vibration of the container. For certain experiments and operating conditions, vibrations are expected to have a significant influence on heat and mass transfer onboard the International Space Station (ISS). Furthermore, it appears that g-jitter vibrations will exist on ISS over a wide range of frequencies [1]. In general, vibrational flows are very complex and are governed by many parameters. This complexity makes it almost impossible to correctly predict vibrational effects empirically. Thus, a careful theoretical approach combined with numerical modeling is essential. Available flight experiment data clearly show that, once initiated by "g-jitter", the effects of convective flows can persist for long times even when the g-jitter disturbance (and consequent flow) were short-lived [2-7].

In many terrestrial crystal growth situations, convective transport of heat and constituent components is dominated by buoyancy driven convection. Control of convective transport continues to be an important aspect of crystal growth research. Several groups are actively pursuing control of convection using static and rotating magnetic fields. Magnetic fields cannot be used for flow control in melts and solutions that are poor conductors. Flow suppression through vibration or vibro-convective mixing may offer an attractive alternative in such cases.

Recent work has shown that the character of natural buoyant convection in non-uniformly heated, rigidly contained inhomogeneous fluids can be drastically altered by vibration of the container. A review and relevant theoretical and experimental research can be found in publications [1-13]. Thus, vibrational induced flow can potentially be used to influence and even control transport in some crystal growth situations. A practical quantitative understanding of vibrational convection as a control parameter in crystal growth situations is currently not available. The objective of the work is to assess the feasibility of the use of vibration to suppress, or control, convection in order to achieve transport control during crystal growth.

Buoyancy driven vibro-convective motion occurs when oscillatory displacement of a container wall induces the acceleration of a container wall relative to the inner fluid. The vibration may be viewed as a time-dependent modulation of steady gravity. In a closed container the fluid will move as a rigid body with a container. If, however, the fluid density is nonuniform, fluid motion may ensue. The magnitude of this motion, of course, depends on the orientation of the vibrational direction with respect to the local density gradients. Note that, similar to Rayleigh-Benard configurations, there may be a "critical" threshold for the coupled vibrational frequency and amplitude, to cause convection. Interestingly, it should be noted that in case of a constant density fluid subject to spatially nonuniform vibration, fluid motion can also occur (for example, angular vibration [11]).

To properly investigate influence of translational, circularly polarized and rotational (angular) vibration necessitates the use of the full 3D equations governing the transport of heat, mass and momentum. Selected examples of our ongoing work on this topic are outlined below.

We consider a purely thermo-vibrational convection in a differentially heated cylindrical cavity with no consideration of solidification. The fluid is taken to be Newtonian and the Boussinesq approximation is assumed to hold. The calculations were performed for identification and characterization of thermovibrational flow and are part of an ongoing project involving flow visualization model experiments being conducted by Feigelson [10].

### Mathematical model for translational and polarized vibration

Translational vibration corresponds to a linear displacement such as, for example,  $u = d \cos \omega t$ , where  $d$  is a real vector giving the displacement magnitude and  $\omega$  is the frequency. In this case the ampoule is displaced back and forth upon the same line. Polarized vibrations are characterized by a displacement  $u = \text{Re}\{d e^{i\omega t}\}$  where  $d = d_1 - i d_2$  (see Fig. 1(a,b)). Here the instantaneous vibration direction rotates in the polarization plane defined by the real vectors  $d_1$  and  $d_2$ . A sketch showing both translational and circular polarized vibrations is presented in Fig.1. In a reference frame fixed to a vibrating ampoule, the momentum equation is

$$\frac{\partial v}{\partial t} + (v \cdot \nabla)v = -\nabla p + Pr \nabla^2 v + Ra_T Pr(\Theta + \alpha C)k + Ra_T^* Pr(\Theta + \alpha C)f(\Omega, t), \quad (1)$$

where length, time and velocity are scaled by  $R_0$ ,  $R_0^2/\kappa$  and  $\kappa/R_0$ . Here  $R_0$  is the ampoule radius and  $\kappa$  is the thermal diffusivity. The nondimensional concentration and temperature, are given by  $\Theta$ , and  $C$ , respectively. The function  $f(\Omega, t)$  is the acceleration of the vibrating ampoule and  $\Omega = \omega R_0^2 / \kappa$  is a dimensionless frequency. The continuity and heat-mass transfer equations complete the problem formulation. The Prandtl, Schmidt, thermal and vibrational Rayleigh numbers and the buoyancy ratio are given by

$$Pr = \frac{\nu}{\kappa}, \quad Sc = \frac{\nu}{D}, \quad Ra_T = \frac{\beta \Delta T g R^3}{\nu \kappa}, \quad \alpha = \frac{\beta_c c_\infty}{\beta \Delta T}, \quad Ra_T^* = \frac{d \omega^2 \beta \Delta T R^3}{\nu \kappa}. \quad (2)$$

Here  $\beta$  and  $\beta_c$  are the thermal and solutal expansion coefficients and  $\Delta T$ ,  $c_\infty$ ,  $g$ ,  $d$ ,  $\omega$ ,  $k$ ,  $\nu$ ,  $D$  are the characteristic longitudinal temperature difference, reference concentration in the melt, gravitational acceleration, vibrational displacement amplitude and frequency, direction of gravity, kinematic viscosity and solute diffusivity, respectively. The dimensionless number  $Ra_T^*$  is the vibrational Rayleigh number and  $Ra_s^* = \alpha Ra_T^*$ . Equation (2) is solved together with the equations governing heat and species transfer and the continuity equation.

### Rotational vibration

The equations of motion for angular vibrations take on a more complicated form (see Fig. 1c). A container of length  $L$  is subjected to an angular displacement  $\theta(t)$  in the  $x_1^*-x_3^*$  plane. Here the coordinates  $x^*$  are referred to a fixed laboratory frame of reference. The position vector to the mass center of the cylinder is parallel to the side of the cylinder and is given by  $q^* = R_0[-\sin \theta \mathbf{i}_1^* + \cos \theta \mathbf{i}_3^*]$  where  $R_0$  is the distance from the origin  $\mathbf{0}^*$  to the mass center of the cylinder and  $\theta(t) = \varepsilon \sin \Omega t$ . In a frame of reference moving with the container, the equations of motion have the form



$$\rho \frac{Dv}{Dt} = \text{div} T - \rho k (\sin \theta i_1 + \cos \theta i_2) + \rho \left[ 2\tilde{\Omega}v - \tilde{\Omega}^2 x + \dot{\tilde{\Omega}}x + \varepsilon^2 \Omega_0^2 R_0 \cos \Omega_0 t i_1 \right] \quad (3)$$

where  $D/Dt$  denotes the material derivative,  $v$  is the velocity of the fluid relative to the moving reference frame,  $\rho$  is the density of the fluid,  $\tilde{\Omega}$  is the rate of rotation tensor for the moving frame with respect to the fixed frame of reference,  $\dot{\tilde{\Omega}}$  is its time derivative and  $T$  is the Newtonian stress tensor for the fluid. The dimensionless equations governing the transport of momentum, mass and heat in the cylinder are obtained after using  $L$ ,  $L^2/\kappa$ ,  $\kappa/L$ , and  $\Delta T = T_H - T_C$  to scale, respectively, length, time, velocity and temperature. The governing dimensionless parameters are the dimensionless frequency  $\Omega = \Omega_0 L^2/\kappa$ , the dimensionless container radius,  $\vartheta = R_0/L$ , the Prandtl,  $Pr$ , and the Rayleigh,  $Ra$ , vibrational Rayleigh  $Ra_\Omega$ , and Ekman,  $E$ , numbers. The latter are given by

$$Pr = \frac{\nu}{\kappa}, \quad Ra = \frac{\beta \Delta T g L^3}{\kappa \nu}, \quad Ra_\Omega = \frac{\beta \Delta T \Omega_0^2 L^4}{\kappa \nu}, \quad E = \frac{\nu}{\Omega_0 L^2}, \quad (4)$$

where  $\beta$ ,  $\nu$ ,  $g$  and  $\kappa$  are the coefficient of thermal expansion, kinematic viscosity, gravitational acceleration and thermal diffusivity, respectively. This system of equations differ from the usual equations in the absence of rotation in that additional terms are present: the Coriolis term which is proportional to  $\varepsilon Pr/E$ , and the centrifugal term which is proportional to  $\varepsilon^2 \vartheta Ra_\Omega Pr$  and varies with linearly with position in the ampoule. The importance of the latter term depends on the dimensions of the amplitude of the angular vibration,  $\varepsilon$ , and the ratio  $\vartheta$ . The rocking motion of the angular vibration under consideration means that centrifugal terms give rise to a periodic forcing that fluctuates about the mean value at twice the period of the angular vibration.

Since the above system of equations has not been well studied, a conservative approach was adopted for the study of angular vibrations and we confine our investigation to a parametric study of flow regimes and transitions for thermo-vibrational situations in the absence of solidification.

### Solution method

The equations are solved in primitive variable form using a Finite Element Method code FEMINA/3D developed by the PI [14]. The continuity equation and momentum equations are considered simultaneously at each time step. This eliminates many problems related to boundary conditions and places only slight limitations on the time step size for transient problems. The regularization for the incompressibility condition makes the solution procedure more efficient, and allows the same order finite element approximation for both the velocity and pressure [15]. This approach makes it possible to solve large 3D time-dependent problems (up to 300.000 unknowns) on a SGI O2 workstation with reasonable computation times.

We implemented the above 3D models of convective buoyancy-driven melt flow in differentially heated cylindrical containers using the FEMINA/3D code. This code was carefully tested on benchmarked experimental and numerical data for a variety of 2D/3D viscous and thermo-convective flow problems and flows under magnetic field [15,16,19].

For rotational vibrations the Ekman number can be of the order  $10^{-4}$  to  $10^{-5}$  for frequencies on the order of 1Hz. This results in large coefficients,  $Pr/E$ , for the Coriolis terms in the governing

equations and causes difficulties in the numerical solution. To resolve this we implemented a high accuracy solution method using preconditioning by high order incomplete decomposition (accuracy up to  $10^{-9}$ ). The computation times reduced by one to two orders of magnitude and the memory size by a factor of 8 for 3D flows compared to currently available commercial codes (e.g. CFD2000). A typical solution time for a transient problem is about two hours on a SGI O2.

## Results and discussion

We verified the validity of the Boussinesq model for semiconductor and oxide melts under microgravity conditions. This topic has been discussed recently by Perera, Sekerka [17], Pukhnachev [18] and Gershuni, Lyubimov [11]. If the nondimensional criteria, proposed by Pukhnachev,  $Pr = gL^3 \nu^{-1} \kappa^{-1}$  is less than 1, then the Boussinesq model for thermal convection may not be valid. Our estimates show that the Boussinesq model is quite adequate for a differentially heated closed ampoule and the range of parameters and material properties under investigation. The values of  $Pr$  are of the order  $10^4$  to  $10^5$  for semiconductor and oxide melts for  $g/g_0 = 10^{-5}$  to  $10^{-4}$ , clearly well above 1.

A parametric study of translational and rotational vibrations under typical microgravity and terrestrial conditions for typical semiconductor melts was performed. A snapshot of a typical flow pattern for translational vibration is presented in Fig. 2(a). Even in the total absence of gravity the vibrations have resulted in detectable flows. For the cases examined, the temperature distribution remains almost unperturbed (due to the low  $Pr$  and weak flow strength).

The angle between the direction of vibration and the ampoule has been studied for translational vibrations in the presence of an axial temperature gradient. At high frequencies and when the angle is zero, no influence of the vibration on the flow was observed, even when vibrational the Raleigh number is very high. The maximum observed effect corresponds to an angle of 90 degrees. Here transport is significantly enhanced.

Typical flow patterns for rotational vibrations flow regimes are presented in Fig. 2(b). Maximal velocity values are observed at the end of the ampoule that is farthest from the rotation origin.

The influence of vibrations on heat and mass transfer becomes significant for oxide melts due to their low thermal diffusivity ( $Pr \sim 10$ ). These flow patterns are shown in Fig. 3(a) for the case of circular polarized vibration. Initially (at time  $t = 0$ ), the species concentration was  $c=1$  at the lower quarter of the cylinder and  $c = 0$  elsewhere. The evolution of the species concentration (process of mixing) and velocity (minimal and maximal values of  $V_z$ ) is shown in Fig. 3(b,c). Complete mixing occurs in about ten seconds. The heat transfer (local Nusselt number at the top and the bottom) is also enhanced by about an order of magnitude. If the frequency of vibration is high, of the order of 100Hz (for fixed  $Ra_0$ ), then the changes in heat and mass transfer due to vibrations become less significant. This corresponds to earlier experimental observations [7, 8].

Our results show that both translational, circular polarized and angular vibration can cause average melt flow for a range of parameters typical of practical semiconductor growth. For a given vibration amplitude and frequency, circular polarized and rotational (angular) vibrations result in more intensive melt flows than translational ones.

The influence of forced vibration on g-jitter induced flows using SAMS microacceleration data from the USML-2 mission was also investigated [13]. Motivated by the predictions of the averaged equation theory presented in Ref. [11], translational vibration was applied parallel to the ampoule axis (and thus, the temperature gradient) in an attempt to damp unwanted irregular

time-dependent flow caused by g-jitter. While the flow variation with time becomes more regular, we did not succeed in completely suppressing the g-jitter flow. We found that the use of the same amplitude vibration in the direction orthogonal to the ampoule axis is more effective. This induces intensive thermal vibration flows and flow disturbances due to g-jitter become practically insignificant.

### Summary

The influence of translational, circularly polarized and rotational (angular) vibration in analysis in a model Bridgman melt growth configuration was investigated. The nature of the flows produced by the types of vibration under consideration necessitated the use of the full 3D equations governing the transport of heat, mass and momentum. The governing equations were solved numerically. Flow patterns for translational, circular polarized and rotational (angular) vibrations and g-jitter microaccelerations were analyzed. For translational vibration, thermovibrational flow is strongly dependent on the angle between the vibration direction and temperature gradient. Circular polarized and rotational vibrations result in more intensive melt flows than translational ones. The simultaneous action of vibrations and magnetic field [19] is currently being studied.

### References

- [1] Don Hurlé (Ed.), Proc. of the Physical Sciences Working Group Workshop on g-sensitivity of planned experimentation on ISS, *Microgravity Sci. Technol.*, **11**, 2/3 (1998).
- [2] J.I.D. Alexander, J-P. Garandet, J.J. Favier, A. Lizee, *J. Cryst. Growth*, **178** (1997) 657-661.
- [3] J.D. Trollinger, M. Rottenkolber and F. Elandalous, *Meas. Sci. Technol.*, **8** (1997) 1573.
- [4] J.D. Trollinger, R. Ranel and R.B. Lai, *Appl. Opt.*, **35**, (1996) 681-689.
- [5] R. Naumann, AIAA 99-1028, Proc. 37th AIAA Meeting, Reno, 11-17 Jan. 1999.
- [6] Y-C. Lu, J.-J. Shiau, R.S. Feigelson and R.K. Route, *J. Cryst. Growth*, **102** (1990) 807.
- [7] R.C. DeMattei and R.S. Feigelson, *J. Cryst. Growth*, **128** (1993) 1062-1068.
- [8] W-S. Liu, J. F. Wolf, D. F. Elwell, R. S. Feigelson, *J. Cryst. Growth*, **82** (1987) 589-597.
- [9] E.V. Zharikov, L.V. Prihodko, N.R. Storozhev, *J. Cryst. Growth*, **99** (1990) 910-914.
- [10] R. Feigelson and E. Zharikov, *NASA/CP 1999-209092*, 1999.
- [11] G. Gershuni, D. Lyubimov, *Thermal Vibrational Convection*, Wiley, N.Y., 1997
- [12] A. Lizee, J.I.D. Alexander, *Phys. Rev., E* **56** (1997) 4152.
- [13] A.I. Fedoseyev, J.I.D. Alexander, *J. Cryst. Growth*, **211** (2000), 34-42.
- [14] V.I. Polezhaev, A. I. Fedoseyev et al. *Mathematical Modeling of Convective Heat and Mass Transfer on the Basis of Navier-Stokes Equations*, Nauka, Moscow, 1987.
- [15] A.I. Fedoseyev, *CFD Journal*, No. 1, **9** (2000), to appear.
- [16] A.I. Fedoseyev, E.J. Kansa, C. Marin, M.P. Volz, A.G. Ostrogorsky, AIAA-2000-0859.
- [17] P.S. Perera and R.F. Sekerka, *Physics of Fluids*, **9** (1997) 376-391
- [18] V. Pukhnachev, Microconvection in a vertical layer, *Fluid Dynamics*, **5** (1994) 76-84.
- [19] A.I. Fedoseyev, J.I.D. Alexander, AIAA-2000-0698, Proc. 38th AIAA Meeting, Reno, 2000.

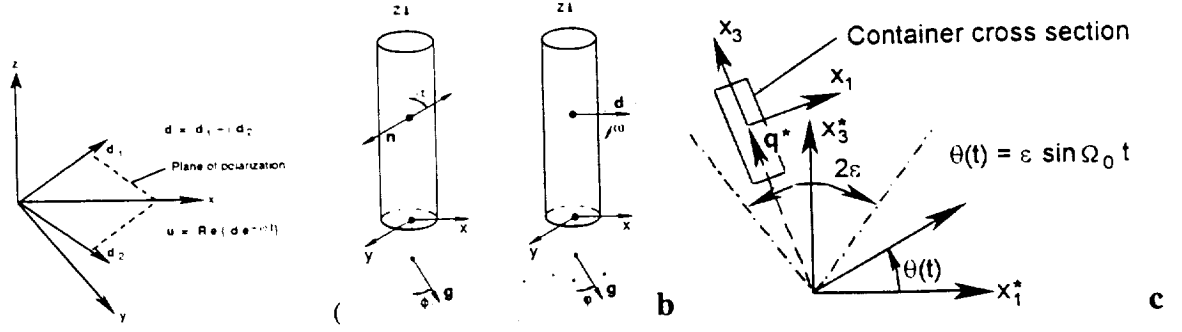


Fig. 1: Translational vibration (a),  $d_1$  or  $d_2 = 0$ : polarized vibration (b),  $d_1, d_2 \neq 0$ ;  $\varphi$  is the angle between gravity vector and the ampoule axis.  $\alpha$  is the angle between the vibration direction and the ampoule axis: (c) rotational (angular) vibration. The container is rotated at an angle  $\theta(t)$  about a center of rotation at  $x^* = 0$ . The vector  $q^*$  connects the center of rotation to the mass center of the container.

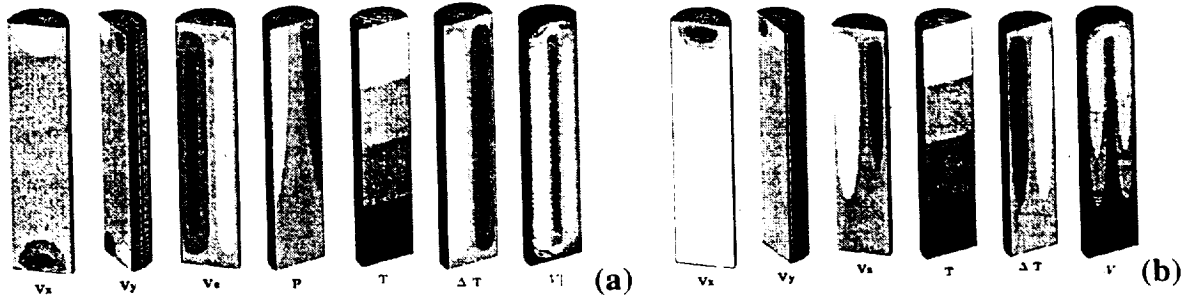


Fig. 2: (a) Instantaneous 3D flow patterns for a lateral translational vibration at  $0g$ ,  $Ra = 0$ ,  $Ra_T = 7.25 \cdot 10^4$ ,  $Pr=0.01$ ,  $\omega = 100Hz$ . The velocity components are  $V_x, V_y, V_z$ ,  $P$  is the pressure,  $T$  is the temperature,  $\Delta T$  is the temperature disturbance and  $|V|$  - velocity magnitude. The grayscale range corresponds to maximum values (white) of the velocity, temperature and pressure variables to their minimum values (black). Vibrations are applied along the horizontal ( $x$ -direction); (b). 3D melt flow patterns for angular vibration at zero- $g$ ,  $Ra=0$ ,  $Ra_a = 4.6 \cdot 10^5$ ,  $Pr=0.01$ ,  $\omega = 100Hz$ .

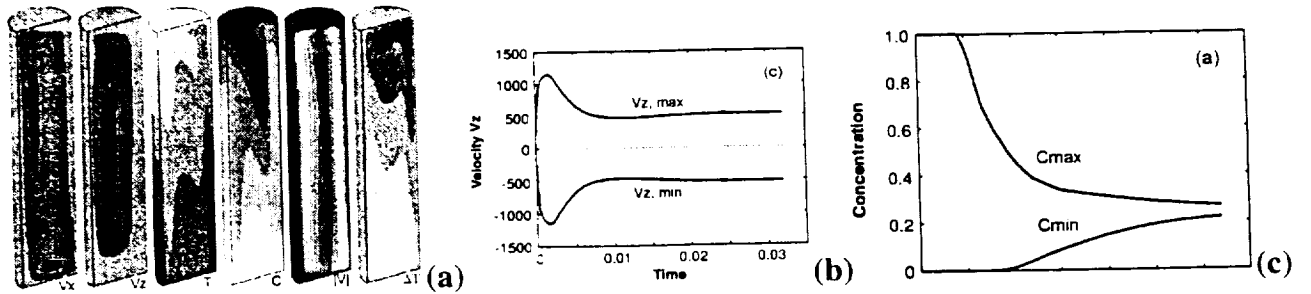


Fig.3: (a) 3D flow patterns for circularly polarized vibration,  $Ra = 7.25 \cdot 10^3$ ,  $Ra = 7.4 \cdot 10^6$ ,  $Pr = 15$ ,  $\omega = 10Hz$ ,  $C$  is the concentration; (b) Temporal evolution of velocity extrema  $V_z$ , and, (c) species concentration  $C$ .



# CONTINUATION FOR NONLINEAR ELLIPTIC PARTIAL DIFFERENTIAL EQUATIONS DISCRETIZED BY THE MULTIQUADRIC METHOD

A. I. FEDOSEYEV\*

*Center for Microgravity and Materials Research,  
University of Alabama in Huntsville,  
Huntsville, AL 35899, USA*

M. J. FRIEDMAN†

*Department of Mathematical Sciences,  
University of Alabama in Huntsville,  
Huntsville, AL 35899, USA*

E. J. KANS‡

*Lawrence Livermore National Laboratory,  
Livermore, CA 94551, USA*

Received January 19, 1999; Revised May 14, 1999

The Multiquadric Radial Basis Function (MQ) Method is a meshless collocation method with global basis functions. It is known to have exponential convergence for interpolation problems. We discretize nonlinear elliptic PDEs by the MQ method. This results in modest-size systems of nonlinear algebraic equations which can be efficiently continued by standard continuation software such as AUTO and CONTENT. Examples are given of detection of bifurcations in 1D and 2D PDEs. These examples show high accuracy with small number of unknowns, as compared with known results from the literature.

## 1. Introduction

Nonlinear multidimensional elliptic partial differential equations (PDEs) are the basis for many scientific and engineering problems, such as viscous fluid flow phenomena, chemical reactions, crystal growth processes, pattern formation in biology, etc. In these problems it is crucial to understand the qualitative dependence of the solution on the problem parameters.

During the past two decades the numerical continuation approach has become popular for qualitative study of solutions to nonlinear equations,

see e.g. [Rheinboldt, 1986; Allgower & Georg, 1990; Doedel *et al.*, 1991; Seydel, 1998] and references therein. Several software packages, such as AUTO97 [Doedel *et al.*, 1997] and CONTENT [Kuznetsov & Levitin, 1995–1997], are currently available for bifurcation analysis of systems of nonlinear algebraic equations and ODEs, with only limited bifurcation analysis for 1D elliptic PDEs. For 2D PDEs, we mention the software package PLTMG [Bank, 1998] that allows to solve a class of boundary value problems on regions in the plane, to continue the solution with respect to a parameter and even to compute limit and branching

---

\*E-mail: alex@uahtitan.uah.edu

†E-mail: friedman@math.uah.edu

‡E-mail: kansa1@llnl.gov

points. This software combines a sophisticated finite element discretization with advanced linear algebra techniques. Numerical continuation for 1D and 2D elliptic PDEs is currently an active research area, see e.g. [Neubert, 1993; Shroff & Keller, 1993; Schwetlick *et al.*, 1996; Chien *et al.*, 1997; Davidson, 1997; Kuznetsov *et al.*, 1996; Chien & Chen, 1998; Doedel & Sharifi, to appear] and [Govaerts, 2000, Chap. 10] for reaction-diffusion equations; and [Mamun & Tuckermann, 1995; Poliashenko & Aidun, 1995] for CFD. The typical approaches used are based on the finite element or finite difference discretization of the PDEs. They result in very large (thousands or tens of thousands for 2D problems) systems of nonlinear algebraic equations with sparse matrices. The continuation process is typically based on the predictor-corrector algorithms that require solving nonlinear systems by the Newton type method at each continuation step. For the bifurcation analysis during the continuation process, one usually needs to compute at least a few eigenvalues of the Jacobian matrix at each continuation step. The methods currently used both for the continuation and the corresponding eigenvalue problems are variants of Krylov subspace methods and recursive projection (RPM). Solving the resulting linear system and the eigenvalue problem require sophisticated algorithms and considerable computer resources (CPU time, memory, disk space, etc.).

In this paper we report results of numerical experiments with continuation and detection of bifurcations for 1D and 2D elliptic PDEs discretized by the Multiquadric Radial Basis Function (MQ RBF or, simply, MQ) method. The MQ method, introduced for solving PDEs in [Kansa, 1990a, 1990b], is a meshless collocation method with global basis functions which leads to finite-dimensional problems with full matrices. It was shown to give very high accuracy with a relatively small number of unknowns (tens or hundreds for 2D problems). The corresponding linear systems can be efficiently solved by direct methods. This opens a possibility for using standard continuation software, such as AUTO and CONTENT, designed for bifurcation analysis of modest-size problems. We also note that the MQ method does not require predetermined location of the nodes as the spectral method does.

In Sec. 2 we summarize previous results on solving PDEs by the MQ method. In Sec. 3 we formulate an adaptation of the MQ method suitable for the discretization of parametrized elliptic PDEs. In Sec. 4 we present results of our numerical

experiments with a 1D eigenvalue problem and in Sec. 5 we present results of our numerical experiments with continuation of solutions and detection of bifurcations for 1D and 2D elliptic PDEs. In Sec. 6 we discuss our results.

## 2. Review of the MQ Method for Elliptic PDEs

The concept of solving PDEs using radial basis functions (RBFs) was introduced by Kansa in 1990 [1990a, 1990b]. He implemented this approach for the solution of hyperbolic, parabolic, and elliptic PDEs using the MQ RBFs proposed by Hardy [1971, 1990] for interpolation of scattered data.

There exists an infinite class of RBFs. An RBF is a function  $f_j(x) \in \mathbb{R}$ ,  $x \in \mathbb{R}$  (say, in 1D case) that depends only upon the distance between  $x$  and a reference node  $x_j$ . A MQ RBF is  $g_j(c_j, x) = ((x - x_j)^2 + c_j^2)^{1/2}$ , where  $c_j$  is called the *shape parameter*. In a comprehensive study, Franke [1982] compared (global) RBFs against many popular compactly supported schemes for 2D interpolation, and he found that the global RBF schemes were superior on six criteria. Among the studied RBFs still only the MQ RBFs are proven to have an exponential convergence for the function interpolation [Madych & Nelson, 1990; Wu & Shaback, 1993]. Madych [1992] showed theoretically that the MQ interpolation scheme converges faster as the constant MQ shape parameter becomes progressively larger.

The numerical experiments for parabolic and elliptic PDEs by Kansa [1990a, 1990b] and Golberg and Chen [1996] show high accuracy and efficiency of the MQ scheme. For example, for a 1D convection-diffusion problem, Kansa [1990b] showed that the MQ solution with 20 nodes had the maximum norm error within  $10^{-4}$ , while a second-order finite difference scheme with  $K = 200$  nodes and an optimal combination of the central and upwind differences for the problem resulted in a much larger error of  $3 \cdot 10^{-2}$ .

In the numerical experiments with a nonlinear time-dependent problem modeling the 1D von Neumann blast wave Kansa [1990b] compared the exact solution and its derivatives with the MQ solution (35 nodes) and with a second-order finite difference one. The error in the maximum norm for pressure, density, energy and their gradients was  $10^{-6}$  or less for the MQ method, and in the range from  $10^{-4}$  to  $10^{-2}$  for the finite difference method with 5000 nodes.

Golberg and Chen [1997] showed that the solution of the 3D Poisson equation in an ellipsoid could be obtained with only 60 randomly distributed nodes to the same degree of accuracy as a FEM solution with 71 000 linear elements.

Sharan *et al.* [1997] showed that the MQ method yields accurate solutions for 2D Poisson and biharmonic equation, and that the MQ approach is simple to implement on domains with irregular boundaries. Cook *et al.* [1993] noted many benefits of using MQ RBFs to solve an initial value problem for a 3D nonlinear equation for the collision of two black holes. The resulting discrete system had 2000 unknowns and was solved directly.

Buhmann [1995] showed that RBFs and, in particular, MQ RBFs are useful for constructing prewavelets and wavelets. Wavelets are most frequently used in time-series analysis, but there are results for using wavelets to solve PDEs [Fasshauer & Jerome, 1999; Narcowich *et al.*, 1999]. As Buhmann points out, one can generate true wavelets by an orthonormalization process. The wavelets are an elegant way to achieve the same results as multigrid schemes. The MQ RBFs are attractive for prewavelet construction due to exceptional rates of convergence and their infinite differentiability.

The paper by Franke and Schaback [1998] provides the first theoretical analysis for solving PDEs by collocation using the RBF methods.

Kansa and Hon [1998] studied several methods for solving linear systems that arise from the MQ collocation problems. They studied the 2D Poisson equation, and showed that ill-conditioning of the system could be circumvented by using block-partitioning methods.

Kansa [1990b] introduced the concept of variable shape parameters  $c_j$  in the MQ scheme that appeared to work well in some cases. In [Kansa & Hon, 1998], a recipe for selecting  $c_j$  based upon the local radius of curvature of the solution surface was found to give better results than a constant  $c_j$  MQ scheme. Kansa and Hon [1998] tested the MQ method for the 2D Poisson equation with a set of exact solutions  $F = \exp(ax + by)$ ,  $\cos(ax + by)$ ,  $\sin(ax + by)$ ,  $\log(ax + by + c)$ ,  $\exp(-a(x - 1/2)^2 - b(y - 1/2)^2)$  and  $\arctan(ax + by)$ . They obtained an accuracy up to  $10^{-5}$  using a modest size, 121, set of nodes, while locally adapting the shape parameter  $c_j$ .

The multizone method of Wong *et al.* [1999] is yet another alternative method for improving computational efficiency. This method is readily

parallelizable, and the conditioning of the resulting matrices are much better.

Hon and Mao [1998] showed that an adaptive algorithm that adjusted the nodes to follow the peak of the shock wave can produce accurate results in 1D Burgers equation with only 10 nodes, even for steep shocks with  $Re = 10^4$ .

### 3. Discretization of Nonlinear Elliptic PDEs by the MQ Method

We consider the second-order system of  $n$  parametrized nonlinear elliptic partial differential equations

$$D(\alpha)\Delta u - f(\nabla u, u, x, y, \alpha) = 0, \quad (1)$$

$$\alpha \in \mathbb{R}, u(\cdot), f(\cdot) \in \mathbb{R}^n, (x, y) \in \Omega \subset \mathbb{R}^2,$$

where  $D(\alpha)$  is a positive diagonal  $n \times n$  matrix that is dependent smoothly on  $\alpha$ , subject to boundary conditions

$$f^b\left(\frac{\partial u}{\partial n}, u, x, y, \alpha\right)\Big|_{\partial\Omega} = 0, \quad f^b(\cdot) \in \mathbb{R}^n. \quad (2)$$

Here  $\alpha$  is a control parameter, and we are interested in studying the dependence of the solutions to the boundary-value problem (1), (2) on  $\alpha$ .

We discretize the continuous problem by the multiquadric radial basis function (MQ) method [Kansa, 1990a, 1990b; Madych & Nelson, 1990] as follows. Introduce a set  $\Theta_h$  of nodes ( $N$  internal and  $N_b$  on the boundary)

$$\Theta_h = \{(x_i, y_i) | i=1, N \subset \Omega, \\ (x_i, y_i) | i=N+1, N+N_b \subset \partial\Omega\}$$

and look for the approximate solution to (1), (2) in the form [Madych & Nelson, 1990]

$$u_h(x, y) = a_0 + \sum_{j=1}^{j=N+N_b} a_j g_j(c_j, x, y), \quad (3)$$

where  $\sum_{j=1}^{j=N+N_b} a_j = 0$ . We use this relationship to eliminate  $a_N$  from (3) which results in

$$u_h(x, y) \\ = a_0 + \sum_{j=1}^{j=N-1} a_j (g_j(c_j, x, y) - g_N(c_N, x, y)) \\ + \sum_{j=N+1}^{j=N+N_b} a_j (g_j(c_j, x, y) - g_N(c_N, x, y)), \quad (4)$$

where  $a_j \in \mathbb{R}^n$  are the unknown expansion coefficients and

$$g_j(c_j, x, y) = \sqrt{(x - x_j)^2 + (y - y_j)^2 + c_j^2},$$

$$j = 1, \dots, N + N_b.$$

are the MQ basis functions, and  $c_j > 0$  are called *shape parameters* [Kansa, 1990b]. We then substitute  $u_h(x, y)$  into (1), (2) and use collocation at the nodes  $\Theta_h$  to obtain a finite-dimensional system

$$\begin{aligned} \varphi_i(a^1, a^2, \alpha) \\ \equiv D(\alpha)\Delta u_h(x_i, y_i) \\ - f(\nabla u_h(x_i, y_i), u_h(x_i, y_i), x_i, y_i, \alpha) = 0, \\ i = 1, \dots, N, \end{aligned} \quad (5)$$

$$\begin{aligned} \varphi_{i-N}^b(a^1, a^2, \alpha) \\ \equiv f^b\left(\frac{\partial u_h(x_i, y_i)}{\partial n}, u_h(x_i, y_i), x_i, y_i, \alpha\right) = 0, \\ i = N + 1, \dots, N + N_b, \end{aligned} \quad (6)$$

where  $a^1 = (a_0, \dots, a_{N-1}) \in \mathbb{R}^{n \times N}$ ,  $a^2 = (a_{N+1}, \dots, a_{N+N_b}) \in \mathbb{R}^{n \times N_b}$ . We next modify the discretized system to make it more suitable for continuation and bifurcation analysis. (1) We eliminate  $a^2$ , associated with the boundary nodes, so as to minimize the number of unknowns. (2) We reformulate the resulting problem in terms of (internal) nodal values  $u_i \equiv u_h(x_i, y_i)$ ,  $i = 1, \dots, N$ , so as to have the correct eigenvalue problem (to avoid dealing with matrix pencils) for the Jacobian matrix of (5) for detecting bifurcations during the continuation process. This is accomplished as follows.

1. We solve (6) for  $a^2$  (assuming that the Implicit Function Theorem is applicable here) to obtain

$$\begin{aligned} a^2 = \psi(a^1, \alpha), \text{ or, in components,} \\ a_j = \psi_j(a^1, \alpha), \\ j = N + 1, \dots, N + N_b. \end{aligned} \quad (7)$$

Substituting this into (5) and using the notation  $\varphi = (\varphi_1, \dots, \varphi_N)$ , yields

$$\varphi(a^1, \psi(a^1, \alpha), \alpha) = 0. \quad \varphi(\cdot) \in \mathbb{R}^{n \times N}. \quad (8)$$

2. We now want to reformulate (8) in terms of the nodal values  $U = (u_1, u_2, \dots, u_N) \in \mathbb{R}^{n \times N}$ . To

this end, we first eliminate  $a^2$  from (4) by substituting (7) into (4) to obtain

$$\begin{aligned} u_h(x, y) \\ = a_0 + \sum_{j=1}^{j=N-1} a_j(g_j(c_j, x, y) - g_N(c_N, x, y)) \\ + \sum_{j=N+1}^{j=N+N_b} \psi_j(a^1, \alpha)(g_j(c_j, x, y) \\ - g_N(c_N, x, y)). \end{aligned} \quad (9)$$

We now define the map  $\Gamma : a^1 \mapsto U = \Gamma(a^1)$ . For  $i = 1, \dots, N$ :

$$\begin{aligned} u_i = a_0 + \sum_{j=1}^{j=N-1} (g_j(c_j, x_i, y_i) \\ - g_N(c_N, x_i, y_i))a_j \\ + \sum_{j=N+1}^{j=N+N_b} (g_j(c_j, x_i, y_i) \\ - g_N(c_N, x_i, y_i))\psi_j(a^1, \alpha) \end{aligned} \quad (10)$$

Finally, substituting  $a^1 = \Gamma^{-1}(U)$  into (8), we arrive at the finite-dimensional continuation problem

$$G(U, \alpha) = 0, \quad U, G(\cdot) \in \mathbb{R}^{n \times N}, \alpha \in \mathbb{R}, \quad (11)$$

where

$$\begin{aligned} G(U, \alpha) = \varphi(\Gamma^{-1}(U), \psi(\Gamma^{-1}(U), \alpha), \alpha), \\ \Gamma : \mathbb{R}^N \rightarrow \mathbb{R}^N, \psi(\cdot) \in \mathbb{R}^{n \times N_b}. \end{aligned}$$

**Remark 1.** Note that in the case that the boundary condition (2) is linear,  $\psi_j$  are linear, and consequently  $\Gamma$  is an  $N \times N$  matrix.

In Sec. 5 we consider examples of continuation of 1D PDEs with  $\Omega = (0, 1)$  and 2D PDEs with  $\Omega = (0, 1) \times (0, 1)$ . In all 2D examples we have the same number of nodes  $N_s$  in  $x$  and  $y$  directions. We choose a constant shape parameter  $c_j = s/(N_s - 1)$ . Our typical choice for  $s$  is  $4 \leq s \leq 12$ .

We use two types of node distributions. In the case of uniform node distribution  $(x_k, y_l) = (kh, lh)$ ,  $k, l = 0, \dots, N_s$ ,  $h = 1/N_s$ . In the case



of nonuniform node distribution, the nodes adjacent to the boundary  $\partial\Omega$  are placed at the distance  $\bar{h} = h_1 h$  from  $\partial\Omega$ ,  $0.1 \leq h_1 \leq 0.5$ , while the remaining nodes are distributed uniformly. A criteria for the choice of  $h_1$  was a minimum of  $L_2$ -norm of the residual in  $\Omega$ .

#### 4. Numerical Experiments for a 1D Eigenvalue Problem

Accurate approximation of eigenvalue problems is essential for bifurcation analysis of PDEs. We have not found references in literature on the MQ-solution of eigenvalue problems. We therefore present here results for an eigenvalue problem for 1D Laplace operator. For details on the MQ discretization see Sec. 3. This is a scalar problem

$$-u'' = \lambda u, \quad u(0) = u(1) = 0, \quad (12)$$

that has the exact solution:

$$(\lambda_m, U^m(x)) = ((\pi m)^2, \sin(\pi m x)), \\ m = 1, 2, \dots$$

where  $(\lambda_m, U^m(x))$  is the  $m$ th eigenpair of (12). Introduce the mesh  $x_n = nh$ ,  $n = 0, 1, \dots, N$ ,  $h = 1/N$ , and consider the standard second-order finite difference (FDM) discretization of (12):

$$-\frac{u_{n+1} - 2u_n + u_{n-1}}{h^2} = \lambda u_n, \quad (13) \\ n = 1, \dots, N-1, \quad u_0 = u_N = 0.$$

The corresponding approximate eigenpairs are given by

$$(\lambda_m^h, U_m^h) = \left( 4N^2 \sin^2 \frac{\pi m}{2N}, \begin{bmatrix} \sin \frac{\pi m}{N} \\ \sin \frac{\pi 2m}{N} \\ \dots \\ \sin \frac{\pi(N-1)m}{N} \end{bmatrix} \right), \\ m = 1, \dots, N-1.$$

We also solved (12) using the MQ discretization for several values of the number  $K$  of internal nodes. Denote by  $(\lambda_m^{MQ}, U_m^{MQ})$ ,  $m = 1, \dots, K$  the corresponding approximate eigenpairs.

The results of our computations are summarized in Table 1. We use the notation  $\varepsilon_\lambda^{MQ}$ ,  $\varepsilon_\lambda^h$  for

the relative errors in  $\lambda_m^{MQ}$ ,  $\lambda_m^h$ , respectively, and the notation  $\varepsilon_U^{MQ}$  for the  $L_\infty$ -norm error in  $U_m^{MQ}$ . For each MQ solution we provide a comparison with the FDM solution that has a sufficient number of nodes to give the same accuracy for  $\lambda_1$  as the MQ method. In Part (a) of the table we use the uniform node distribution for the MQ method. Part (b) of the table shows that the accuracy of the MQ method can be significantly improved by adapting the node distribution: we moved only two nodes adjacent to boundary to reduce their distance from the boundary to  $h_1 = h/4$  (while the remaining nodes are distributed uniformly).

One can see that the MQ method can give a highly accurate solution with a small number of unknowns, 10–100 times smaller than the number of unknowns in the FDM for the same accuracy.

#### 5. Numerical Experiments for 1D and 2D Elliptic PDEs

We present several examples of continuation of solutions to systems of nonlinear 1D and 2D elliptic PDEs. Each problem is discretized by the MQ method described in Sec. 3. We then perform continuation of the resulting system of algebraic equations (11) with AUTO97. The principal goal of our examples is to assess the accuracy of the detection of bifurcation points. We compare our results with some published results and, in one case, the results of our computations with an example in AUTO97 and CONTENT. We will use throughout the notation  $K$  for the number of unknowns in a particular method. For our MQ method  $K = n \times N$ , where  $n$  is the dimension of the system and  $N$  is the number of internal nodes. We denote by MQ(u) and MQ(nu) our MQ method with the uniform and nonuniform node distributions, respectively.

**Example 1.** 1D Gelfand–Bratu equation. This is a scalar problem

$$u'' + \lambda e^u = 0, \quad \text{in } \Omega = (0, 1), \\ u(0) = u(1) = 0, \quad (14)$$

that appears in combustion theory and is used as the demo example **exp** in AUTO97 [Doedel *et al.*, 1997] (fifth-order adaptive orthogonal spline collocation method) and demo example **brg** in CONTENT [Kuznetsov & Levitin, 1995–1997] (third-order adaptive finite difference method). There is

Table 1. A 1D eigenvalue problem: comparison of results for eigenvalues, results for eigenfunctions.

(a) The MQ method with a uniform node distribution for  $K = 5, 7$  and  $9$ .

$m$	$\lambda_m$ (Exact)	$\lambda_m^{MQ}, K = 5$	Rel. Err. $\epsilon_\lambda^{MQ}$	Rel. Err. $\epsilon_U^{MQ}$	Rel. Err. $\epsilon_\lambda^h, K = 47$
1	9.86961	9.86596	$3.7 \times 10^{-4}$	$3.7 \times 10^{-4}$	$3.7 \times 10^{-4}$
2	39.4784	39.6492	$4.3 \times 10^{-3}$	$5.2 \times 10^{-3}$	$1.5 \times 10^{-3}$
$m$	$\lambda_m$ (Exact)	$\lambda_m^{MQ}, K = 7$	Rel. Err. $\epsilon_\lambda^{MQ}$	Rel. Err. $\epsilon_U^{MQ}$	Rel. Err. $\epsilon_\lambda^h, K = 76$
1	9.86961	9.86821	$1.4 \times 10^{-4}$	$9.9 \times 10^{-5}$	$1.4 \times 10^{-4}$
2	39.4784	39.4738	$1.2 \times 10^{-4}$	$1.8 \times 10^{-4}$	$5.7 \times 10^{-4}$
3	88.8264	89.3648	$6.0 \times 10^{-3}$	$1.1 \times 10^{-2}$	$1.3 \times 10^{-3}$
$m$	$\lambda_m$ (Exact)	$\lambda_m^{MQ}, K = 9$	Rel. Err. $\epsilon_\lambda^{MQ}$	Rel. Err. $\epsilon_U^{MQ}$	Rel. Err. $\epsilon_\lambda^h, K = 117$
1	9.86961	9.86901	$6.0 \times 10^{-5}$	$5.0 \times 10^{-5}$	$6.0 \times 10^{-5}$
2	39.4784	39.4846	$1.6 \times 10^{-4}$	$2.1 \times 10^{-4}$	$2.4 \times 10^{-4}$
3	88.8264	89.1667	$3.8 \times 10^{-3}$	$7.3 \times 10^{-3}$	$5.4 \times 10^{-4}$
4	157.913	159.689	$1.1 \times 10^{-2}$	$2.5 \times 10^{-2}$	$9.6 \times 10^{-4}$

(b) The MQ method with nonuniform node distribution for  $K = 7$  and  $9$ .

$m$	$\lambda_m$ (Exact)	$\lambda_m^{MQ}, K = 7$	Rel. Err. $\epsilon_\lambda^{MQ}$	Rel. Err. $\epsilon_U^{MQ}$	Rel. Err. $\epsilon_\lambda^h, K = 3477$
1	9.86961	9.86961	$6.8 \times 10^{-8}$	$3.0 \times 10^{-6}$	$6.8 \times 10^{-8}$
2	39.4784	39.4782	$3.2 \times 10^{-6}$	$3.0 \times 10^{-4}$	$2.7 \times 10^{-7}$
3	88.8264	88.8139	$1.4 \times 10^{-4}$	$6.5 \times 10^{-4}$	$6.1 \times 10^{-7}$
$m$	$\lambda_m$ (Exact)	$\lambda_m^{MQ}, K = 9$	Rel. Err. $\epsilon_\lambda^{MQ}$	Rel. Err. $\epsilon_U^{MQ}$	Rel. Err. $\epsilon_\lambda^h, K = 950$
1	9.86961	9.86960	$9.1 \times 10^{-7}$	$2.3 \times 10^{-6}$	$9.1 \times 10^{-7}$
2	39.4784	39.4783	$1.4 \times 10^{-6}$	$2.0 \times 10^{-5}$	$3.6 \times 10^{-6}$
3	88.8264	88.8241	$2.6 \times 10^{-5}$	$1.8 \times 10^{-4}$	$8.2 \times 10^{-6}$
4	157.913	157.882	$1.9 \times 10^{-4}$	$1.8 \times 10^{-3}$	$1.5 \times 10^{-5}$

a limit (fold) point on the solution curve. We take the value of  $\lambda$  at the limit point found from `demoexp` ( $K \geq 50$ ) as exact. Table 2 shows the comparison between numerical results in [Davidson, 1997], our numerical results and our experiments with CONTENT.

**Example 2.** 1D Brusselator problem, a well-known model system for autocatalytic chemical reactions with diffusion:

$$\begin{aligned} \frac{d_1}{l^2} u'' - (b+1)u + u^2 v + a &= 0, \\ \frac{d_2}{l^2} v'' + bu - u^2 v &= 0, \quad \text{in } \Omega = (0, 1), \\ u(0) = u(1) &= a, \quad v(0) = v(1) = \frac{b}{a}, \end{aligned} \quad (15)$$

proposed in [Lefever & Prigogine, 1968]. This problem exhibits a rich bifurcation scenario and has been

used in the literature as a standard model for bifurcation analysis, see e.g. [Schaeffer & Golubitsky, 1981; Golubitsky & Schaeffer, 1985; Dangelmayr, 1987; Chien *et al.*, 1997, Eq. (24)] and [Mei, 1997]. A stationary bifurcation occurs [Chien *et al.*, 1997, Eq. (24)] at

$$b_n = 1 + \frac{d_1}{d_2} a^2 + \frac{\pi^2 n^2}{l^2} d_1 + \frac{l^2}{\pi^2 n^2} \frac{a^2}{d_2} > 0.$$

For  $l = d_1 = 1$ ,  $d_2 = 2$ ,  $a = 4$ ,  $n = 1, 2$  this gives simple bifurcations:  $b_1 = 9 + \pi^2 + 8/\pi^2 = 19.680174$ ,  $b_2 = 9 + 4\pi^2 + 2/\pi^2 = 48.681060$ , correspondingly. For the second-order central difference method with uniform mesh of 41 mesh points ( $K = 80$  unknowns), the corresponding approximate bifurcation points were found in [Chien *et al.*, 1997, Sec. 6.1]. Table 3 shows the comparison between analytical, numerical results [Chien *et al.*,

Table 2. 1D Gelfand-Bratu equation: The limit point comparison.

(a) Results for the MQ method correspond to a uniform node distribution.

	[Doedel <i>et al.</i> , 1997], Exact	[Davidson, 1997], $K = 800$	MQ(u), $K = 5$	MQ(u), $K = 7$	MQ(u), $K = 9$
$\lambda$	3.513831	3.5137	3.512609	3.514224	3.514047
rel. error		$3.7 \times 10^{-5}$	$3.5 \times 10^{-4}$	$-1.1 \times 10^{-4}$	$-6.1 \times 10^{-5}$

(b) Results for the MQ method correspond to a nonuniform node distribution.

	[Kuznetsov & Levitin, 1995-1997], $K = 50$	[Kuznetsov & Levitin, 1995-1997], $K = 500$	MQ(nu), $K = 5$	MQ(nu), $K = 7$	MQ(nu), $K = 9$
$\lambda$	3.51145	3.51380	3.514010	3.513809	3.513828
rel. error	$6.8 \times 10^{-4}$	$8.8 \times 10^{-6}$	$-5.1 \times 10^{-5}$	$6.3 \times 10^{-6}$	$8.5 \times 10^{-7}$

Table 3. 1D Brusselator equation: Comparison for the bifurcation points.

(a) Results for the bifurcation point  $b_1$ .

	Exact	[Chien <i>et al.</i> , 1997], $K = 80$	MQ(u), $K = 10$	MQ(u), $K = 14$	MQ(u), $K = 18$
$b_1$	19.680174	19.67547	19.67366	19.67786	19.67919
rel. error		$2.4 \times 10^{-4}$	$3.3 \times 10^{-4}$	$1.2 \times 10^{-4}$	$5.0 \times 10^{-5}$

(b) Results for the bifurcation point  $b_2$ .

	Exact	[Chien <i>et al.</i> , 1997], $K = 80$	MQ(u), $K = 10$	MQ(u), $K = 14$	MQ(u), $K = 18$
$b_2$	48.681060	48.6004	48.57476	48.63168	48.65605
rel. error		$1.7 \times 10^{-3}$	$2.2 \times 10^{-3}$	$1.0 \times 10^{-3}$	$5.1 \times 10^{-4}$

1997, Sec. 6.1] and our numerical results for values of  $b_1$  and  $b_2$  at simple bifurcation points.

**Example 3.** Pattern formation in a 1D system with mixed boundary conditions [Dillon *et al.*, 1994].

$$\begin{aligned} \frac{d_1}{\omega l^2} u'' + 3 - \kappa u - uv^2 &= 0, \\ \delta \frac{d_1}{\omega l^2} v'' + \kappa u + uv^2 - v &= 0, \quad \text{in } \Omega = (0, 1) \\ \theta_1 \frac{\partial u}{\partial n} &= \rho(1 - \theta_1)(\theta_3 u^s - u), \\ \delta \theta_2 \frac{\partial u}{\partial n} &= \delta \rho(1 - \theta_2)(\theta_3 v^s - v), \quad \text{on } \partial\Omega = \{0, 1\}. \end{aligned} \quad (16)$$

Here  $\theta_i \in [0, 1]$ ,  $i = 1, 2, 3$ , are homotopy parameters. For  $d_1 = 10^{-5}$ ,  $\omega = 10^{-2}$ ,  $\delta = 0.14$ ,  $3 = 1.0$ ,

$\kappa = 0.001$ ,  $(\theta_1, \theta_2, \theta_3) = (1, 1, 0)$  (Neumann problem). Equation (16) was discretized by the second-order central difference method with equidistant mesh of 41 mesh points ( $K = 80$  unknowns). Table 4 [Dillon *et al.*, 1994, Table 1] shows a comparison between analytic and numerical results for values of  $l$  at simple bifurcation points.

Our numerical results (MQ(nu) method) with  $K = 18$  coincide with the analytic results above.

**Example 4.** 2D Gelfand-Bratu problem

$$\begin{aligned} \Delta u + \lambda e^u &= 0, \quad \Omega = (0, 1) \times (0, 1), \\ u|_{\partial\Omega} &= 0. \end{aligned} \quad (17)$$

This problem was studied in [Schwetlick *et al.*, 1996] and [Doedel & Sharifi, to appear]. In [Schwetlick

Table 4. A 1D pattern formation problem, comparison for simple bifurcation points.

[[Dillon et al., 1994], numerical]	0.047	0.080	0.093	0.159	0.140	0.238	0.186	0.317	0.232
[[Dillon et al., 1994], analytic]	0.0465	0.0793	0.093	0.159	0.140	0.238	0.186	0.317	0.233
MQ(nu)	0.0465	0.0793	0.093	0.159	0.140	0.238	0.186	0.317	0.233

Table 5. 2D Bratu equation, results for the limit point.

## (a) Uniform node distribution.

[Schwetlick et al., 1996], 225 ≤ K ≤ 3025		MQ(u), K = 25	MQ(u), K = 49	MQ(u), K = 81
λ	not reported	6.8359	6.8183	6.8119
rel. error		4.1 × 10 <sup>-3</sup>	1.5 × 10 <sup>-3</sup>	5.6 × 10 <sup>-4</sup>

## (b) nonuniform node distribution.

[Doedel & Sharifi, to appear], Exact		MQ(nu), K = 25	MQ(nu), K = 49	MQ(nu), K = 81
λ	6.808124423	6.793248	6.807978	6.808232
rel. error		-2.1 × 10 <sup>-3</sup>	-2.2 × 10 <sup>-5</sup>	-1.6 × 10 <sup>-5</sup>

et al., 1996] it was discretized with the second-order central difference method with uniform mesh and then continued using Implicit Block Elimination based on Recursive Projections. A limit point was detected for some value of  $\lambda$  (not reported in the paper), and spurious limit points were detected for  $K = 961, 1521, 2209, 3025$  and  $\lambda$  sufficiently small. In [Doedel & Sharifi, to appear] the problem was discretized with a high-order orthogonal spline collocation method with sparse Jacobian. We reproduced the bifurcation diagram in [Schwetlick et al., 1996]. Table 5 gives the values of  $\lambda$  at the limit point computed by the MQ method. The exact location of the limit point is assumed to be at the value of  $\lambda$  obtained in [Doedel & Sharifi, to appear] on a  $16 \times 16$  mesh with  $4 \times 4$  collocation points. See Sec. 6 for a discussion of the operation count.

**Example 5.** 2D Brusselator problem.

$$\frac{d_1}{l^2} \Delta u - (b+1)u + u^2v + a = 0,$$

$$\frac{d_2}{l^2} \Delta v + bu - u^2v = 0, \quad \text{in } \Omega = (0, 1) \times (0, 1),$$

$$u|_{\partial\Omega} = a, \quad v|_{\partial\Omega} = \frac{b}{a}.$$

A stationary bifurcation occurs [Chien & Chen, 1998, Eq. (2.26)] for

$$b_{m,n} = 1 + \frac{d_1}{d_2} a^2 + d_1 \pi^2 \left( \frac{m^2}{l^2} + n^2 \right) + \frac{a^2}{\pi^2 d_2} \left( \frac{l^2}{m^2 + l^2 n^2} \right) > 0.$$

For  $l = d_1 = 1, d_2 = 2, a = 4, (m, n) = (1, 1), (m, n) = (2, 2)$  this gives simple bifurcations:  $b_{1,1} = 9 + 2\pi^2 + 4/\pi^2, b_{2,2} = 9 + 8\pi^2 + 1/\pi^2$ , correspondingly. For the second-order central difference method with equidistant mesh of 21 mesh points, the corresponding approximate bifurcation points are found in [Chien & Chen, 1998, Sec. 5]. Tables 6 and 7 show comparisons between analytical, numerical results [Chien & Chen, 1998, Eq. (2.26)] and our numerical results for values of  $b_{1,1}$  and  $b_{2,2}$  at simple bifurcation points.

A Hopf bifurcation occurs [Chien & Chen, 1998, Eq. (2.26)] for

$$b_{m,n} = 1 + a^2 + (d_1 + d_2) \left( \frac{m^2}{l^2} + n^2 \right) \pi^2$$

for some  $m, n$ , and  $l$  large enough. For  $l = 10, d_1 = d_2 = 1, a = 10, (m, n) = (1, 2)$ , this gives a

Table 6. 2D Brusselator equation: comparison for the bifurcation points, a uniform node distribution for MQ method.

(a) Results for the bifurcation point $b_{1,1}$ .					
	Exact	[Chien & Chen, 1998], $K = 800$	MQ(u), $K = 50$	MQ(u), $K = 72$	MQ(u), $K = 98$
$b_{1,1}$	29.144494	29.104774	29.16280	29.17050	29.16062
rel. error		$1.4 \times 10^{-3}$	$-6.3 \times 10^{-4}$	$-8.9 \times 10^{-4}$	$-5.5 \times 10^{-4}$
(b) Results for the bifurcation point $b_{2,2}$ .					
	Exact	[Chien & Chen, 1998], $K = 800$	MQ(u), $K = 50$	MQ(u), $K = 72$	MQ(u), $K = 98$
$b_{2,2}$	88.058156	87.47325	87.61578	87.86924	88.00143
rel. error		$6.6 \times 10^{-3}$	$5.0 \times 10^{-3}$	$2.1 \times 10^{-3}$	$6.4 \times 10^{-4}$

Table 7. 2D Brusselator equation: Comparison for the bifurcation points, a nonuniform node distribution for the MQ method.

(a) Results for the bifurcation point $b_{1,1}$ .				
	Exact	MQ(nu), $K = 50$	MQ(nu), $K = 72$	MQ(nu), $K = 98$
$b_{1,1}$	29.144494	29.14621	29.14726	29.14431
rel. error		$-5.9 \times 10^{-5}$	$-9.5 \times 10^{-5}$	$6.3 \times 10^{-6}$
(b) Results for the bifurcation point $b_{2,2}$ .				
	Exact	MQ(nu), $K = 50$	MQ(nu), $K = 72$	MQ(nu), $K = 98$
$b_{2,2}$	88.058156	88.15470	87.93391	88.07288
rel. error		$-1.1 \times 10^{-3}$	$1.4 \times 10^{-3}$	$-1.7 \times 10^{-4}$

Table 8. 2D Brusselator equation, results for the Hopf bifurcation point.

	Exact	MQ(u), $K = 50$	MQ(nu), $K = 50$	MQ(u), $K = 72$	MQ(u), $K = 98$
$b_{1,2}$	180.15	181.8625	180.7880	181.0696	180.492
rel. error		$-9.5 \times 10^{-3}$	$-3.5 \times 10^{-3}$	$-5.1 \times 10^{-3}$	$-1.9 \times 10^{-3}$

Hopf bifurcation at  $b_{1,2} = 101 + 2((1/100) + 2^2)\pi^2 = 180.15$ . see Table 8.

## 6. Discussion

1. We have presented the results of our experiments with the continuation of solutions to 1D and 2D nonlinear elliptic PDEs discretized by the MQ method. We use a small number of unknowns and achieve a high accuracy for detected bifurcation points in our examples. Here are some sample results.

- (i) For the limit point in the 1D Gelfand-Bratu equation, the MQ method with nine unknowns gives the relative errors  $6.1 \times 10^{-5}$  and  $8.5 \times 10^{-7}$  for the uniform and nonuniform node distributions, respectively. The relative error in the third-order finite difference method with 500 nodes is  $8.8 \times 10^{-6}$ .
- (ii) For the two bifurcation points in the 2D Brusselator problem, the MQ method with 98 unknowns gives the relative errors  $5.5 \times 10^{-4}$ ,  $6.4 \times 10^{-4}$  for the uniform node distribution and  $6.3 \times 10^{-6}$ ,  $1.7 \times 10^{-5}$  for the nonuniform

node distribution. The corresponding relative errors in the second-order finite difference method with 800 nodes are  $1.4 \times 10^{-3}$ ,  $6.6 \times 10^{-3}$ .

- (iii) For the first eigenvalue in the eigenvalue problem for the 1D Laplace operator with nine unknowns gives the relative error  $6 \times 10^{-5}$  and  $9 \times 10^{-7}$  for the uniform and nonuniform node distributions, respectively. This is equivalent in accuracy to 117 and 950 node solutions, respectively by the second-order finite difference method.

2. As we noted in Introduction, the MQ method leads to systems with full matrices. Solving a related linear system for the number of nodes  $M \times M$  in 2D with a full  $M^2 \times M^2$  matrix by Gaussian elimination takes  $2/3M^6 + O(M^4)$  operations. By comparison, a band solver would take  $O(M^4)$  operations, and a collocation method on a square [Doedel, 1998; Doedel & Sharifi, to appear] would take  $\approx 62p^3M^3$ , where  $p$  is the number of matching points at an edge of a finite element [Doedel, 1998]. Further work is required to carefully compare the costs of solving linear systems and the corresponding eigenvalue problems arising in discretizing elliptic PDEs by the MQ method and by the finite difference, finite element, and collocation methods.

3. An increase of the number of unknowns and especially the shape parameter result in a better accuracy but also in a larger condition number of the operator  $\Gamma$  mapping the nodal values of the solution onto the expansion coefficients. This condition number is a limiting factor in our experiments. In fact, to reach high accuracy for the limit point in the 2D Gelfand–Bratu problem (e.g. the relative error  $1.6 \times 10^{-5}$  with 81 unknowns), we had to use quadruple precision. This is a temporary fix, as it considerably slows down computations. In future, we plan to implement the ideas of Kansa et al. [1990b] to circumvent this ill-conditioning problem.

We also found that even a simple adaptation of the nodes adjacent to the boundary can lead to a dramatic improvement of the accuracy in detecting bifurcation points. Adaptive choice of the shape parameter is another way to improve the accuracy that we plan to investigate.

## Acknowledgments

Support from the NASA grant NAG8-1229 is acknowledged by the first author. The authors wish

to thank the referees for helpful comments and for bringing to their attention references [Doedel, 1998; Doedel & Sharifi, to appear].

## References

- Allgower, E. L. & Georg, K. [1990] *Numerical Continuation Methods: An Introduction* (Springer-Verlag, Berlin, Heidelberg, NY).
- Bank, R. E. [1998] "PLTMG: A software package for solving elliptic partial differential equations," Users' Guide 8.0 (SIAM Publications, Philadelphia).
- Buhmann, M. D. & Micchelli, C. A. [1992] "Multiquadric interpolation improved," *Comput. Math. Appl.* **24**, 21–25.
- Buhmann, M. D. [1995] "Multiquadric prewavelets on nonequally spaced knots in one dimension," *Math. Comput.* **64**, 1611–1625.
- Carlson, R. E. & Foley, T. A. [1991] "The parameter R2 in multiquadric interpolation," *Comput. Math. Appl.* **21**(9), 29–42.
- Chien, C. S. & Chen, M.-H. [1998] "Multiple bifurcations in a reaction–diffusion problem," *Comput. Math. Appl.* **35**(8), 15–39.
- Chien, C. S., Mei, Z. & Shen, C.-L. [1997] "Numerical continuation at double bifurcation points of a reaction–diffusion problem," *Int. J. Bifurcation and Chaos* **8**(1), 117–139.
- Cook, G. B., Choptnik, M. W., Dubal, M. R., Klasky, S., Matzner, R. A. & Oliveira, S. R. [1993] "Three dimensional initial value data for collisions of two black holes," *Approximations to Numerical Relativity*, ed. d'Inverno, R. (Cambridge University Press), pp. 265–285.
- Dangelmayr, G. [1987] "Degenerate bifurcations near a double eigenvalue in the Brusselator," *J. Austr. Math. Soc.* **B28**, 486–535.
- Davidson, B. D. [1997] "Large scale continuation and numerical bifurcation for partial differential equations," *SIAM. J. Numer. Anal.* **24**(5), 2008–2027.
- Dillon, R., Maini, P. K. & Othmer, H. G. [1994] "Pattern formation in generalized Turing systems. I. Steady-state patterns in systems with mixed boundary conditions," *J. Math. Biol.* **32**, 345–393.
- Doedel, E. J. [1998] "On the construction of discretizations of elliptic partial differential equations," *J. Diff. Eq. Appl.* **3**, 389–416.
- Doedel, E. J., Champneys, A. R., Fairgrieve, T. F., Kuznetsov, Yu. A., Sandstede, B. & Wang, X. J. [1997] *AUTO97: Continuation and Bifurcation Software for Ordinary Differential Equations (with HomCont)*, User's Guide (Concordia University, Montreal, Canada).
- Doedel, E. J., Keller, H. B. & Kernévez, J. P. [1991] "Numerical analysis and control of bifurcation problems. Part I: Bifurcation in finite dimensions," *Int. J.*

- Bifurcation and Chaos* 1(3), 493–520; “Part II: Bifurcation in infinite dimensions,” *Int. J. Bifurcation and Chaos* 1(4), 745–772.
- Doedel, E. J. & Sharifi, H. “Collocation methods for continuation problems in nonlinear elliptic PDEs,” *Proc. ERCOFTAC and EUROMECH Colloquium, Continuation Methods in Fluid Mechanics*, Aussois, France September 1998, *Notes on Numer. Fluid. Mech.*, to appear.
- Fasshauer, G. E. & Jerome, J. W. [1999] “Multi-step approximation algorithms: Improved convergence rates though postconditioning and smoothing kernels,” *Adv. Comp. Math.* 10, 1–27.
- Franke, R. [1982] “Scattered data interpolation: Tests of some methods,” *Math. Comp.* 38, 181–199.
- Franke, C. & Schaback, R. [1998] “Solving partial differential equations by collocation using radial basis functions,” *Appl. Math. Comp.* 93(1), 73–91.
- Golberg, M. A. & Chen, C. S. [1996] “Improved multiquadric approximation for partial differential equations,” *Engin. Anal. Bound. Elem.* 18, 9–17.
- Golberg, M. A. & Chen, C. S. [1997] *Discrete Projection Methods for Integral Equations* (Comput. Mech. Publ., Boston, MA).
- Golberg, M. A. & Chen, C. S. [1994] “The theory of radial basis functions used in the dual reciprocity boundary element method,” *Appl. Math. Comput.* 60, 125–136.
- Golubitsky, M. & Schaeffer, D. G. [1985] *Singularities and Groups in Bifurcation Theory*, Vol. I (Springer-Verlag).
- Govaerts, W. [2000] *Numerical Methods for Bifurcations of Dynamical Equilibria* (SIAM Publications, Philadelphia).
- Hardy, R. L. [1971] “Multiquadric equations of topography and other irregular surfaces,” *J. Geophys. Res.* 76, 1905–1915.
- Hardy, R. L. [1990] “Theory and applications of the multiquadric-biharmonic method: 20 years of discovery,” *Comput. Math. Appl.* 19(8&9), 163–208.
- Hon, Y. C. & Mao, X. Z. [1998] “An efficient numerical scheme for Burgers equation,” *Appl. Math. Comput.* 95, 37–50.
- Kansa, E. J. [1990a] “Multiquadrics—a scattered data approximation scheme with applications to computational fluid dynamics—I. Surface approximations and partial derivative estimates,” *Comput. Math. Appl.* 19(8 & 9), 127–145.
- Kansa, E. J. [1990b] “Multiquadrics—a scattered data approximation scheme with applications to computational fluid dynamics—II. Solutions to hyperbolic, parabolic, and elliptic partial differential equations,” *Comput. Math. Appl.* 19(8 & 9), 147–161.
- Kansa, E. J. & Hon, Y. C. [1998] “Circumventing the ill-conditioning problem with multiquadrics radial basis functions: Applications to elliptic partial differential equations,” *Adv. Comp. Math.*, to appear.
- Kuznetsov, Yu. A. & Levitin, V. V. [1995–1997] “CONTENT, a multi-platform interactive environment for analyzing dynamical systems,” Dynamical Systems Laboratory, CWI, Amsterdam (ftp.cwi.nl/pub/CONTENT).
- Kuznetsov, Yu. A., Levitin, V. V. & Skovoroda, A. R. [1996] “Continuation of stationary solutions to evolution problems in CONTENT,” Report AM-R9611 Centrum voor Wiskunde en Informatica, Amsterdam, The Netherlands.
- Lefever, R. & Prigogine, I. [1968] “Symmetry-breaking instabilities in dissipative systems II,” *J. Chem. Phys.* 48, 1695–1700.
- Madych, W. R. [1992] “Miscellaneous error bounds for multiquadric and related interpolants,” *Comput. Math. Appl.* 24(12), 121–138.
- Madych, W. R. & Nelson, S. A. [1990] “Multivariate interpolation and conditionally positive definite functions II,” *Math. Comp.* 54, 211–230.
- Mamun, C. K. & Tuckermann, L. S. [1995] “Asymmetry and Hopf bifurcation in spherical Couette flow,” *Phys. Fluids* 7(1), 80–102.
- Mei, Z. [1997] “Numerical bifurcation analysis for reaction–diffusion equations,” Habilitation thesis, University of Marburg.
- Narcowich, F. J., Schaback, R. & Ward, J. D. [1999] “Multi-level interpolation and approximation,” *Appl. Comput. Harmonic Anal.* 7, 243–261.
- Neubert, R. [1993] “Predictor–Corrector techniques for detecting Hopf points,” *Int. J. Bifurcation and Chaos* 3, 1311–1318.
- Poliashenko, M. & Aidun, C. K. [1995] “Computational dynamics of ordinary differential equations,” *Int. J. Bifurcation and Chaos* 5(1), 159–174.
- Rheinboldt, W. C. [1986] *Numerical Analysis of Parameterized Nonlinear Equations* (John Wiley, NY).
- Schaeffer, D. & Golubitsky, M. [1981] “Bifurcation analysis near a double eigenvalue of a model chemical reaction,” *Arch. Rat. Mech. Anal.* 75, 315–347.
- Seydel, R. [1988] *From Equilibrium to Chaos—Practical Bifurcation and Stability Analysis*, 2nd Edition (Elsevier Publishing, NY, Amsterdam, London), (Springer-Verlag 1994).
- Schwetlick, H., Timmermann, G. & Lösche, R. [1996] “Path following for large nonlinear equations by implicit block elimination based on recursive projections,” *Lectures in Applied Mathematics* 32, 715–732.
- Sharan, M., Kansa, E. J. & Gupta, S. [1997] “Applications of the multiquadric method for the solution of elliptic partial differential equations,” *Appl. Math. & Comput.* 84, 275–302.
- Shroff, G. M. & Keller, H. B. [1993] “Stabilization of unstable procedures: The recursive projection method,” *SIAM J. Numer. Anal.* 30, 1099–1120.

- Wong, S. M., Hon, Y. C., Li, T. S., Chung, S. L. & Kansa, E. J. [1999] "Multi-zone decomposition for simulation of time-dependent problems using the multiquadric scheme," *Math. Comput. Appl.* **37**, 23-43.
- Wu, Z. & Shaback, R. [1993] "Local error estimates for radial basis function interpolation of scattered data," *IMA J. Num. Anal.* **13**, 13-27.





**AIAA-2000-0859**

**VIBRATIONAL CONTROL OF HEAT AND MASS  
TRANSFER IN BRIDGMAN MELT GROWTH  
CONFIGURATIONS**

**A. I. Fedoseyev  
University of Alabama  
Huntsville, AL**

**J. I. D. Alexander  
National Center for Microgravity Research,  
Case Western Reserve University,  
Cleveland, OH**

**38th Aerospace Sciences  
Meeting & Exhibit  
10-13 January 2000 / Reno, NV**

# VIBRATIONAL CONTROL OF HEAT AND MASS TRANSFER IN BRIDGMAN MELT GROWTH CONFIGURATIONS

Alexandre I. Fedoseyev<sup>†</sup> and J. Iwan D. Alexander<sup>‡</sup>

<sup>†</sup> Center for Microgravity and Materials Research  
University of Alabama in Huntsville, Huntsville, Alabama  
E-mail: alex@cmmr.uah.edu

<sup>‡</sup> Department of Mechanical and Aerospace Engineering and  
National Center for Microgravity Research,  
Case Western Reserve University, Cleveland, Ohio  
E-mail: ida2@po.cwru.edu

## Abstract

Convective transport of heat and constituent components is dominated by buoyancy driven convection in many terrestrial crystal growth situations. The character of natural buoyant convection in non-uniformly heated, rigidly contained inhomogeneous fluids can be drastically altered by vibration of the container. Therefore, vibrational induced flow can potentially be used to influence and even control transport in some crystal growth situations.

A parametric numerical investigation of 3D thermovibrational buoyancy-driven flow in differentially heated cylindrical containers has been conducted to investigate thermovibrational transport regimes in Bridgman-type systems. The objective of the work is to assess the feasibility of the use of vibration to suppress, or control, convection in order to achieve transport control during crystal growth.

The formulation of a model for this problem is outlined, numerical method is described and its application to the study of investigation of thermal vibrational flows is discussed. Two types of vibration are considered: translational, and circularly polarized. The results for flows induced by g-jitter and selected results for the cases of longitudinal and lateral vibrations are presented.

## 1 Introduction

It is generally recognized that oscillatory, or pulsative, flow significantly alters the transfer of mass, heat and momentum in fluid systems. For certain experiments and operating conditions, vibrations are expected to have a significant influence on heat and mass transfer onboard the International Space Station (see for example, the recent ESTEC Workshop proceedings [1]). Available flight experiment data clearly show that, once initiated by "g-jitter", the effects of convective flows can persist for long times even when the g-jitter disturbance (and consequent flow) were short-lived [2]-[7].

Control of convective transport continues to be an important aspect of crystal growth research. Several groups are actively pursuing control of convection using static and rotating magnetic fields. However, magnetic fields cannot be used for flow control in melts and solutions that are poor conductors. Flow control through vibration or vibro-convective mixing may offer an attractive alternative in such cases.

Recent works have shown that the character of natural buoyant convection in non-uniformly heated, rigidly contained inhomogeneous fluids can be drastically altered by vibration of the container. A review and relevant theoretical and experimental research can be found in publications [1]-[13]. Thus, vibrational induced flow can potentially be used to influence and even control transport in some crystal growth situations. A practical quantitative understanding of vibrational convection as a control pa-

\*Copyright ©2000 by A. I. Fedoseyev. Published by the American Institute of Aeronautics and Astronautics, Inc., with permission.

parameter in crystal growth situations is currently not available. The objective of the work is to assess the feasibility of the use of vibration to suppress, or control, convection in order to achieve transport control during crystal growth.

## 2 Problem formulation and numerical method

Buoyancy driven vibro-convective motion occurs when oscillatory displacement of a container wall induces the acceleration of a container wall relative to the inner fluid. If the fluid density is nonuniform, fluid motion may ensue. The magnitude of this motion depends on the orientation of the vibrational direction with respect to the local density gradients. It should be noted that even in case of a constant density fluid subject to spatially nonuniform vibration, fluid motion can also occur (for example, angular vibration [11]).

To properly investigate influence of translational and circularly polarized vibration necessitates the use of the full 3D equations governing the transport of heat, mass and momentum. Selected examples of our ongoing work on this topic are outlined below.

We consider a purely thermo-vibrational convection in a differentially heated cylindrical cavity. The fluid is taken to be Newtonian, and the Boussinesq approximation is assumed to hold. The calculations were performed for identification and characterization of thermovibrational flow and are part of an ongoing project involving flow visualization model experiments being conducted by Feigelson [10].

### 2.1 Governing equations

Translational vibration corresponds to a linear displacement such as, for example,  $\mathbf{u} = \mathbf{d} \cos \omega t$ , where  $\mathbf{d}$  is a real vector giving the displacement magnitude and  $\omega$  is the frequency. In this case the ampoule is displaced back and forth upon the same line. Polarized vibrations are characterized by a displacement  $\mathbf{u} = \text{Re}\{\mathbf{d} e^{i\omega t}\}$ , where  $\mathbf{d} = \mathbf{d}_1 - i\mathbf{d}_2$ . Here the instantaneous vibration direction rotates in the polarization plane defined by the real vectors  $\mathbf{d}_1$  and  $\mathbf{d}_2$ . A sketch showing both translational and circular polarized vibrations is presented in Fig. 1. In a reference frame fixed to a vibrating ampoule, these types of vibrations result in the following form of the momentum equation:

$$\frac{\partial \mathbf{V}}{\partial t} + (\mathbf{V} \cdot \nabla) \mathbf{V} = -\nabla p + Pr \nabla^2 \mathbf{V} + Ra_T Pr \cdot (\Theta + \alpha C) \mathbf{n}_g + Ra_T^* Pr \cdot (\Theta + \alpha C) \mathbf{f}(\Omega, t) \quad (1)$$

while the continuity equation:

$$\nabla \cdot \mathbf{V} = 0 \quad (2)$$

energy equation:

$$\frac{\partial \Theta}{\partial t} + (\mathbf{V} \cdot \nabla) \Theta = \nabla^2 \Theta \quad (3)$$

and species transport equation:

$$\frac{\partial C}{\partial t} + (\mathbf{V} \cdot \nabla) C = Pr Sc^{-1} \nabla^2 C \quad (4)$$

where length, time and velocity are scaled, respectively, by  $R_0$ ,  $R_0^2/\kappa$  and  $\kappa/R_0$ . Here  $R_0$  is the ampoule radius and  $\kappa$  is the thermal diffusivity. The nondimensional concentration and temperature, are given by  $\Theta$  and  $C$ , respectively. The function  $\mathbf{f}(\Omega, t)$  is the acceleration of the vibrating ampoule and  $\Omega = \omega R_0^2/\kappa$  is a dimensionless frequency;  $\mathbf{n}_g = (\sin \phi, 0, \cos \phi)$ . The Prandtl, Schmidt, thermal and solutal Rayleigh and vibrational Rayleigh numbers and the buoyancy ratio are, respectively, given by

$$Pr = \frac{\nu}{\kappa}, Sc = \frac{\nu}{D}, Ra_T = \frac{\beta \Delta T g R_0^3}{\nu \kappa}, Ra_S = \alpha Ra_T, \alpha = \beta_c c_\infty / (\beta \Delta T), Ra_T^* = \frac{d \omega^2 \Delta T R_0^3}{\nu \kappa}$$

Here  $\beta$  and  $\beta_c$  are the thermal and solutal expansion coefficients and  $\Delta T$ ,  $c_\infty$ ,  $g$ ,  $\omega$ ,  $d$ ,  $k$ ,  $\nu$ ,  $D$  are the characteristic longitudinal temperature difference, reference concentration in the melt, gravitational acceleration, vibrational displacement amplitude and frequency, direction of gravity, kinematic viscosity and solute diffusivity, respectively. The dimensionless number  $Ra_T^*$  is the vibrational Rayleigh number and  $Ra_S^* = \alpha Ra_T^*$ .

The boundary conditions for eq. (1)-(3) are: (i) the non-slip condition for the velocity,  $\mathbf{V} = 0$ , on the walls, and (ii) the given wall temperature distribution,  $\Theta = \Theta_w$ . An undefined constant in the pressure field is excluded by setting  $p(x_0, y_0, z_0) = 0$  at some location  $(x_0, y_0, z_0)$ .

Equations (1) are solved together with the equations governing heat and species transfer (3),(4) and the condition that the velocity is divergence free (2).

## 2.2 Finite element solution method

The equations are solved in primitive variable form (velocity-pressure, temperature, concentration, etc.) using a Finite Element Method.

### Finite element method with regularization for the Navier-Stokes equations

This method (RNS) was proposed in [15], [16] for high  $Re$  number flows. It was shown that such a regularization works also well in case of flows with thin boundary layers, even with few mesh nodes placed inside the boundary layer [17], [18]. For the considered problems, the continuity equation (2) is modified as follows

$$\nabla \cdot \mathbf{V} = \tau \nabla \cdot (\nabla p - \mathbf{F}) \quad (5)$$

where  $\tau$  is a small regularization parameter, and  $\mathbf{F}$  is a body force in eq. (1) for the thermo-vibrational convection. For  $\tau \rightarrow 0$  we approach the original equation (2). A boundary condition for the pressure on the wall is

$$(\nabla p - \mathbf{F}) \cdot \mathbf{n} = 0, \quad (6)$$

where  $\mathbf{n}$  is a unit wall normal vector. Eq. (5) and (6) present the main feature of this method, and ensure the balance of the component of the force normal to the region boundary.

Another advantage is that this approach allows to use the same order finite element approximation for the velocity, pressure, temperature and concentration with all unknowns located at the same nodal points. For a justification of this regularization one can be referenced to the new hydrodynamic equations proposed in [19] that have similar fluctuation terms. Löhner has also shown that similar terms actually appear in the discrete equations as a result of different order finite element approximations used for interpolation of velocity and pressure [20].

The continuity equation (5) and momentum equations (1) are solved simultaneously at each time step. This eliminates many problems related to boundary conditions and places only slight limitations on the time step size for transient problems (due to the physical nature of the problem).

### 3D CFD software

We implemented the above 3D model of vibro-convective buoyancy-driven flow in differentially in the FEMINA/3D

code [14]. The regularization proposed makes a solution procedure very efficient.

A high accuracy solution iterative CGS-like method using preconditioning by high order incomplete decomposition has been implemented. This allowed us to obtain high-precision solutions with accuracy up to  $10^{-9}$ . The preconditioning also reduced the computation time by one to two orders of magnitude and the memory size by a factor of 8 for 3D flows compared to currently available commercial codes (e.g. CFD2000) [24]. This approach makes it possible to solve large time-dependent problems (up to 300,000 unknowns) with reasonable computation times. A typical solution time for a transient problem is few hours on a SGI O2 workstation.

## 2.3 Benchmarks

This code was carefully tested on benchmarked experimental, theoretical and numerical data for a variety of 2D/3D viscous and thermo-convective flow problems [18], [16], [17]. Here we present some selected examples:

### Three dimensional thermal convection in a cylinder

The method bees applied to the problem of convective 3D flow in differentially heated horizontal cylinder. The experimental data by Bogatirev et al [21] have been used for comparison. These data have been obtained during ground tests for the device, the thermal convection sensor, before it was flown on *Mir* station. Numerical results from the 3D finite volume simulations by Bessonov [22] have been also used for comparison. The temperature distribution on a cylinder wall was (i) linear temperature profile, and (ii) computed using a real, finite wall conductivity (adjoint problem). The body force in eq. (1) is  $\mathbf{F} = (0, 0, Ra_T Pr \Theta)$ , no vibration was applied. The Rayleigh numbers is in the range from  $10^3$  to  $1.2 \cdot 10^5$ . The value of  $\tau^*$  used was  $10^{-7}$  to  $10^{-3}$ , and it did not change noticeably the results. Results are shown in Fig. 2. An agreement with the experimental data for  $Ra_T > 4 \cdot 10^4$  is quite good in the case (ii), when a real finite wall conductivity has been taken into account.

### Two dimensional and three dimensional lid-driven cavity problem

We compare our results with experimental data obtained by Koseff and Street [23] for isothermal flow at  $Re =$

3200 and  $10^4$ . We solved equations (1) and (5) numerically for the unknowns  $(\mathbf{V}, p)$  in the 2D region  $(x, z) = [0, 1][0, 1]$ . The 3D version of the problem corresponds to the Koseff & Street experiment [23] with the domain  $(x, y, z) = [0, 1][0, 3][0, 1]$ . The boundary conditions are:  $\mathbf{V} = (u, v, w) = (1, 0, 0)$  at the driven lid ( $z = 1$ );  $\mathbf{V} = 0$  on the other walls, and,  $(\nabla p \cdot \mathbf{n}) = 0$  on all the walls. The undefined constant in the pressure field is eliminated by setting pressure  $p = 0$  at  $(x, y, z) = (0, 0, 0)$ .

Fig. 3 and 4 present the experimental measurements and numerical results for  $u$  and  $w$  velocity components obtained by our method, RNS, by solving the original NS equations (1), (2), and by using a 2D  $k - \epsilon$  model with commercial code [24]. The experimental data are shown for the symmetry plane  $(x, z)$  at  $y = 1.5$  along the lines  $x = 0.5$  and  $z = 0.5$  of the 3D cavity, that has relative dimensions  $(x:y:z) = 1:3:1$ . The experimental points correspond to time averaged values of the measured velocities [23].

The results obtained with our model, eq. (1), (5) and (6) are in good agreement with the experimental data for  $Re = 3200$  and  $10,000$  and are an improvement upon previous results obtained by solving the NS equations (1), (2).

#### Magnetic field suppression of convective flow

Numerical solution for thermal convection flows in a semiconductor melt with strong static magnetic field applied is presented in Fig 5. Although the generated flows have extremely low velocity because of the large Hartmann numbers ( $Ha = 20$  to  $2000$ ), the numerical solution of the governing equations involved is very complicated due to the thin boundary layers. Different numerical methods have been tested for the solution of this problem [17]. The best results have been obtained with the presented RNS approach. It can provide the numerical solutions in a wide range of  $Ha$  numbers (up to  $10^4$ ), while other methods failed for  $Ha > 20$ . The RNS results compare favorably with the asymptotic theoretical solutions, Fig. 5c.

### 3 Thermal vibrational convection. Results and discussion

A parametric study of translational and circular polarized vibrations under typical microgravity and terrestrial conditions for typical semiconductor melts was performed. A snapshot of a typical flow pattern for translational vibration is presented in Fig. 6. Even in the total absence of

gravity the vibrations have resulted in detectable flows. For the cases examined, the temperature distribution remains almost unperturbed (due to the low  $Pr$  and weak flow strength).

The angle between the direction of vibration and the ampoule has been studied for translational vibrations in the presence of an axial temperature gradient. At high frequencies and when the angle is zero, no influence of the vibration on the flow was observed, even when vibrational the Raleigh number is very high. The maximum observed effect corresponds to an angle of  $90$  degrees. Here transport is significantly enhanced.

The influence of vibrations on heat and mass transfer becomes significant for oxide melts due to their low thermal diffusivity ( $Pr \sim 10$ ). These flow patterns are shown in Fig. 7 for the case of circular polarized vibration. Initially (at time  $t = 0$ ), the species concentration was  $c = 1$  at the lower quarter of the cylinder and  $c = 0$  elsewhere. The evolution of the species concentration (process of mixing) is shown in Fig. 8 together with minimum and maximum values of velocity (for the whole domain) components. Complete mixing occurs in about ten seconds. The heat transfer (local Nusselt number at the top and the bottom) is also enhanced by about an order of magnitude. If the frequency of vibration is high, of the order of  $100Hz$  (for fixed  $Ra$ ), then the changes in heat and mass transfer due to vibrations become less significant. This corresponds to earlier experimental observations [7],[8].

Our results show that both translational and circular polarized vibrations can cause average melt flow for a range of parameters typical of practical semiconductor growth. For a given vibration amplitude and frequency, circular polarized vibrations result in more intensive melt flows than translational ones.

The influence of forced vibration on g-jitter induced flows using typical SAMS micro acceleration data from the USML-2 mission was also investigated. Motivated by the predictions of the averaged equation theory presented in Ref. [11], translational vibration was applied parallel to the ampoule axis (and thus, the temperature gradient) in an attempt to damp unwanted irregular time-dependent flow caused by g-jitter Fig. 9a). While the flow variation with time becomes more regular, we did not succeed in completely suppressing the g-jitter flow (Fig.9b,c).

We found that the use of the same amplitude vibration in the direction orthogonal to the ampoule axis is more effective. This induces intensive thermal vibrational flows and flow disturbances due to g-jitter become practically insignificant (Fig. 9d).

## Conclusions

The influence of translational and circularly polarized vibration in analysis in a model Bridgman melt growth configuration was investigated. The nature of the flows produced by the types of vibration under consideration necessitated the use of the full 3D equations governing the transport of heat, mass and momentum. The governing equations were solved numerically. Flow patterns for translational and circular polarized vibrations and g-jitter microaccelerations were analyzed. For translational vibration, thermovibrational flow is strongly dependent on the angle between the vibration direction and the temperature gradient. Circular polarized and rotational vibrations result in more intensive melt flows than translational ones. The simultaneous action of g-jitter and translational vibrations is currently being study from the viewpoint of using applied vibration as a means of flow control.

## Acknowledgments

Support from NASA grants NAG8-1229 and NAG3-1740 is gratefully acknowledged. The authors are grateful to R. S. Feigelson (Stanford University) for fruitful discussions.

## References

- [1] Don Hurle (Ed.), Proceedings of the Physical Sciences Working Group Workshop on g-sensitivity of planned experimentation on the International Space Station, ESTEC, Noordwijk, The Netherlands, 10-11 September, 1998., Microgravity Sci. Technol., 11 2/3 (1998).
- [2] J.I.D. Alexander, J.-P. Garandet, J.J. Favier, and A. Lizee. g-Jitter effects on segregation during directional solidification of tin-bismuth in the MEPHISTO furnace facility, J. Cryst. Growth, 178 (1997) 657-661.
- [3] J. D. Trollinger, M. Rottenkolber and F. Elandalous, Development and application of holographic particle image velocimetry techniques for microgravity applications, Meas. Sci. Technol., 8 (1997) 1573-1583.
- [4] J. D. Trollinger, R. Ranel and R. B. Lai, Holographic particle image velocimetry for the first International Microgravity Laboratory aboard the space shuttle Discovery, Appl. Opt. 35 (1996) 681-689.
- [5] R. Naumann, An analytical model for transport from transient and periodic acceleration on Spacecraft, AIAA 99-1028, Proc. 37th AIAA Meeting, Reno, 11-17 Jan. 1999.
- [6] Y.-C. Lu, J.-J. Shiau, R.S. Feigelson and R.K. Route. Effect of vibrational stirring on the quality of Bridgman grown CdTe, J. Cryst. Growth, 102 (1990) 807.
- [7] R.C. DeMattei and R.S. Feigelson, The effect of forced convection on the melt gradient and growth rate during the Bridgman and gradient freeze crystal growth of silver-doped lead bromide, J. Cryst. Growth, 128 (1993) 1062-1068.
- [8] W.-S. Liu, J. F. Wolf, D. F. Elwell, and R. S. Feigelson. Low Frequency Vibrational Stirring: A New Method for Rapidly Mixing Solutions and Melts During Growth, J. Cryst. Growth 82 (1987) 589-597.
- [9] E. V. Zharikov, L.V. Prihodko, N.R. Storozhev, Fluid flow formation resulting from forced vibration of a growing crystal, J. Cryst. Growth 99 (1990) 910-914.
- [10] R. Feigelson and E. Zharikov, Investigation of the crystal growth of dielectric materials by the Bridgman techniques using vibrational control, NASA Micr. Mat. Sci. Conf., 1998.
- [11] G. Gershuni, D. Lyubimov, Thermal Vibrational Convection, Wiley, N.Y., 1997
- [12] A. Lizee, J.I.D. Alexander, Phys. Rev. E 56 (1997) 4152.
- [13] V.S. Yuferev et al. Effect of space craft rotation on convection and transport. Proc. Xth European symposium on Phys. Sci. in Microgravity, Moscow, 1997, 37.
- [14] V.I. Polezhaev, A. I. Fedoseyev et al. Mathematical Modeling of Convective Heat and Mass Transfer on the Basis of Navier-Stokes Equations, Nauka, Moscow, 1987.
- [15] A. I. Fedoseyev and J.I.D. Alexander. An efficient method for modeling of incompressible viscous flow, thermal and vibrational convection, 16th Int. Conf. Numer. Meth. Fluid Dynamics, Extended abstracts, Arcachon, France, 6-11 July, 1998.
- [16] A. I. Fedoseyev, B. V. Alexeev. High order continuum model for incompressible viscous flow

and application to numerical modeling of thermovibrational convection. *Continuum Models and Discrete Systems*, Eds. E. Inan, K. Markov, World Scientific, London, 1998, 131-137.

- [17] A. I. Fedoseyev, E.J. Kansa, C. Marin, A.G. Ostrogorsky, Magnetic field suppression of flow in semiconductor melt. AIAA-2000-0698 paper, 38th Aerospace Sciences Meeting & Exhibit, January 10-13, 2000, Reno, NV.
- [18] A. I. Fedoseyev, Numerical Model with Regularized Navier-Stokes Equation for Solutions with Boundary Layer, Proc. of ISCFD-99, ZARM, Universitt Bremen, September 6-10, 1999, Bremen, Germany, Eds. H. J. Rath, K. Oshima, G. Schmidt (accepted, in print).
- [19] B. V. Alexeev, The generalized Boltzmann equation, generalized hydrodynamic equations and their applications, *Phil. Trans. Roy. Soc. London, A*, 349 (1994) 417-443.
- [20] R. Löhner, Design of Incompressible Flow Solver: Practical Aspects, In: *Incompressible computational fluid dynamics*, Eds. M. D. Gunzburger and R. A. Nicolaides, Cambridge Press, 1993, 267-294.
- [21] G.P. Bogatirev, G.F. Putin, V.I. Polezhaev, A System for Measurement of Convection aboard Space Station. Proc. 3rd Microgravity Fluid Physics Conf., Cleveland, Ohio, July 13-15, 1996, NASA Conf. Publ., S13-818.
- [22] O.A. Bessonov, Private communications, 1998.
- [23] K.R. Koseff and R.L. Street, The Lid-Driven Cavity Flow: A Synthesis of Qualitative and Quantitative Observations, *Trans. ASME/Journal of Fluids Engineering* **106** (1984) 390-398.
- [24] CFD2000, Adaptive Research, Pacific-Sierra, California, 1996.

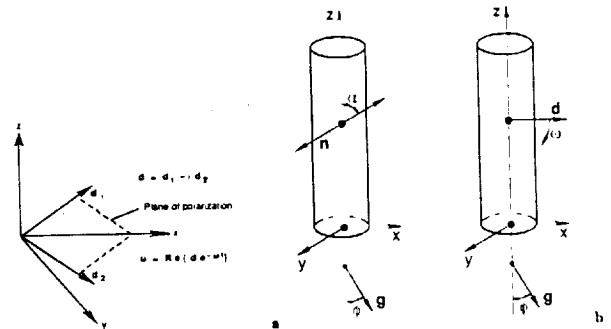


Figure 1: Translational vibration (a),  $d_1$  or  $d_2 = 0$ , and polarized vibration (b),  $d_1, d_2 = 0$ ;  $\phi$  is the angle between gravity vector and axis of ampoule,  $\alpha$  is the angle between direction of vibrations and axis of ampoule

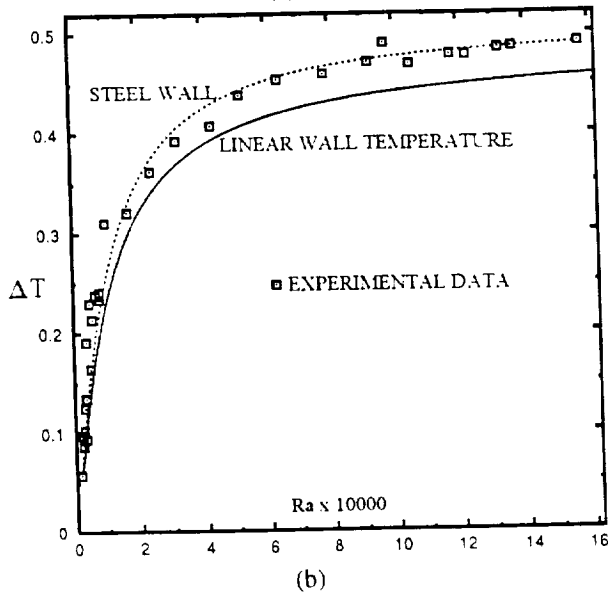
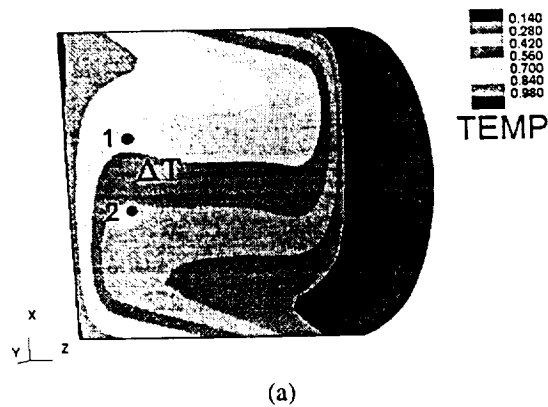


Figure 2: Thermal convection in 3D differentially heated horizontal cylinder: (a) temperature field in the central X-Z plane,  $Ra = 10^5$ ; (b) Comparison of temperature difference  $\Delta T$  versus  $Ra$  number with experiment [21]: squares - experimental data, solid line - numerical results for perfect wall conductivity, dashed line - results for finite wall conductivity;  $\Delta T$  is a measured temperature between locations 1 and 2 in (a).

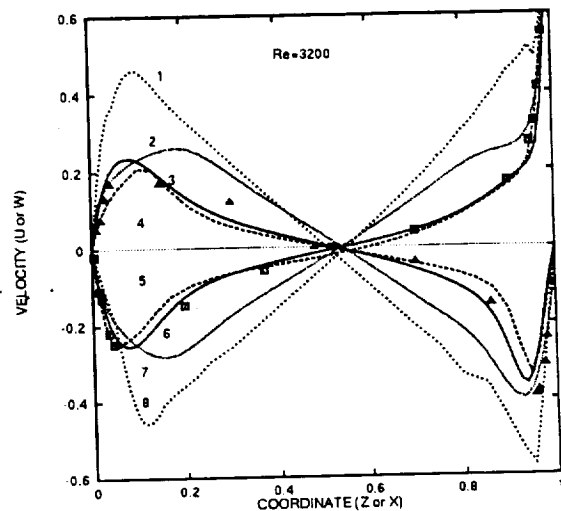


Figure 3: Driven cavity problem,  $Re = 3200$ . Comparison of horizontal velocity profiles (1-4) for numerical (solid and dashed lines) and experimental (squares) results and vertical velocity profiles (5-8) for numerical (solid and dashed lines) and experimental (triangles) results: 1-NS, 2 -  $k - \epsilon$  model, 3-RNS (2D), 4-RNS (3D); 5-RNS (3D), 6-RNS (2D), 7 -  $k - \epsilon$  model, 8-NS.

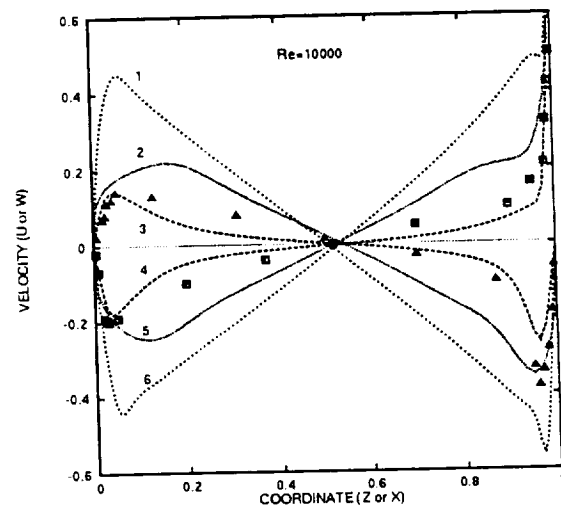
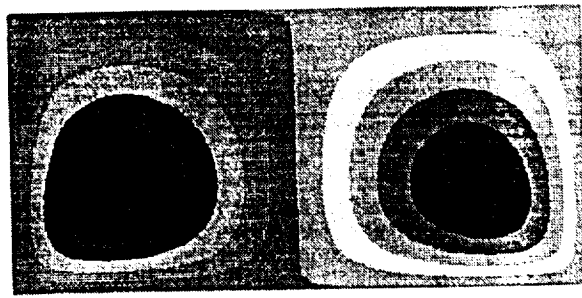
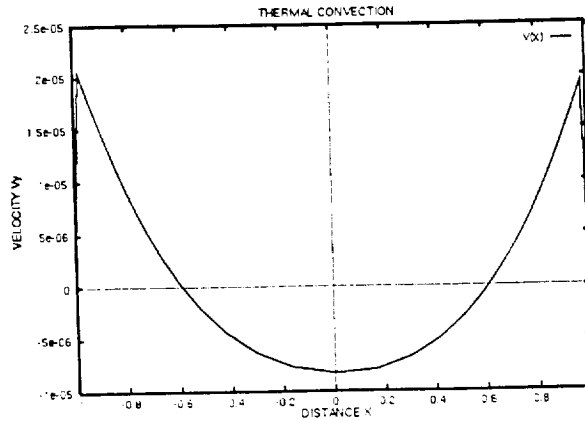


Figure 4: Driven cavity problem,  $Re = 10,000$ . Comparison of horizontal velocity profiles (1-3) for numerical (dashed lines) and experimental (squares) results and vertical velocity profiles (4-6) for numerical (dashed lines) and experimental (triangles) results: 1-NS, 2 -  $k - \epsilon$  model, 3-RNS (2D), 4-RNS (2D), 5 -  $k - \epsilon$  model, 6-NS

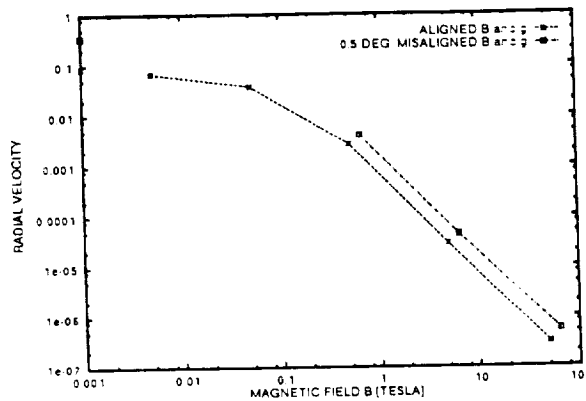




(a)



(b)



(c)

Figure 5: Thermal convection suppression by magnetic field.  $D = 2$ ,  $H = 1$ ,  $Ra = 1.25 \cdot 10^5$ ,  $Ha = 2170$  ( $B = 5.0 Tesla$ ): stream function (a), vertical velocity profile  $V_y(x)$  at  $y = 0.25$  (b), Summary of magnetic field suppression of the flow for  $H = 1$ ,  $D = 2$ : maximum value of horizontal (radial) velocity versus  $B$  (c). Predicted theoretical asymptotic dependence  $V_{max} \sim Ha^{-2}$  is observed

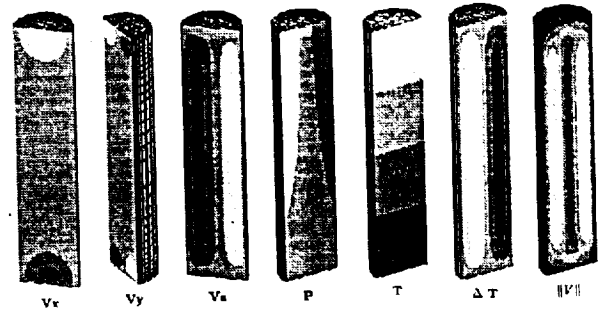


Figure 6: Typical instantaneous 3D melt flow patterns for translational vibration at  $0g$ ,  $Ra = 0$ ,  $Ra_v = 7.25 \cdot 10^4$ ,  $Pr = 0.01$ ,  $\omega = 100Hz$ , lateral vibration: velocity components  $V_x, V_y, V_z$ , pressure  $P$ , temperature  $T$ , temperature disturbance  $\Delta T$ , and velocity module. White color designate the maximal value plotted, black one - the minimal value. Vibrations are applied along x-directions (horizontal)

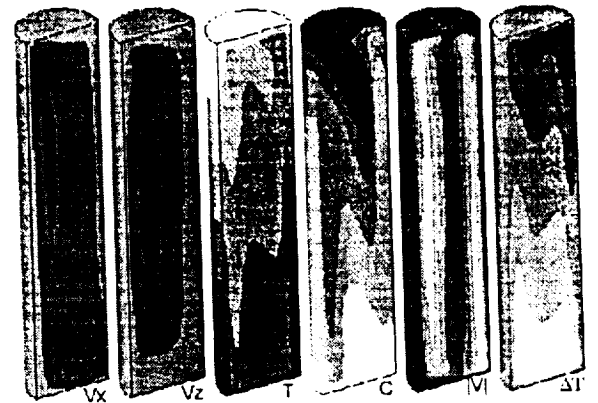


Figure 7: Instantaneous 3D flow patterns for circular polarized vibration,  $Ra = 7.25 \cdot 10^3$ ,  $Ra_v = 7.4 \cdot 10^6$ ,  $Pr = 15$ ,  $\omega = 10Hz$ : velocity components  $V_x, V_z$ , temperature  $T$ , concentration  $C$ , velocity module, and temperature disturbance  $\Delta T$ . White color designate the maximal value plotted, black one - the minimal value.

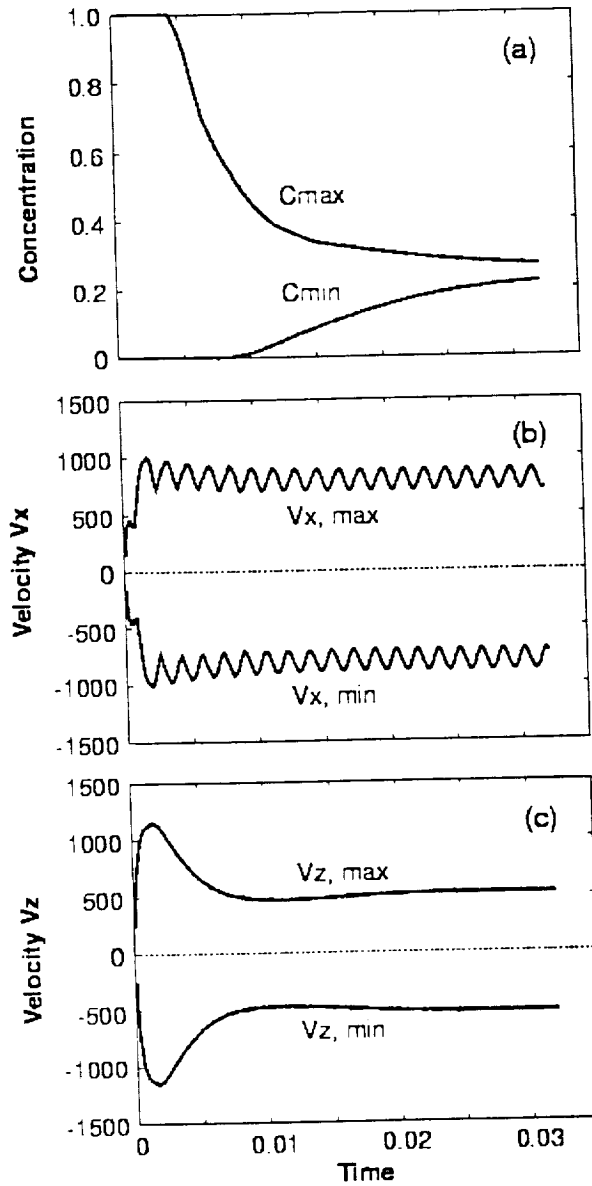


Figure 8: Temporal evolution of (a) species concentration  $C$ , min. and max. values of  $C$ . (b) velocity extremums  $V_x$ , and (c)  $V_z$  for circular polarized vibration applied to oxide melt.  $Ra = 7.25 \cdot 10^3$ ,  $Ra_v = 7.4 \cdot 10^6$ ,  $Pr = 15$ ,  $\omega = 10\text{Hz}$

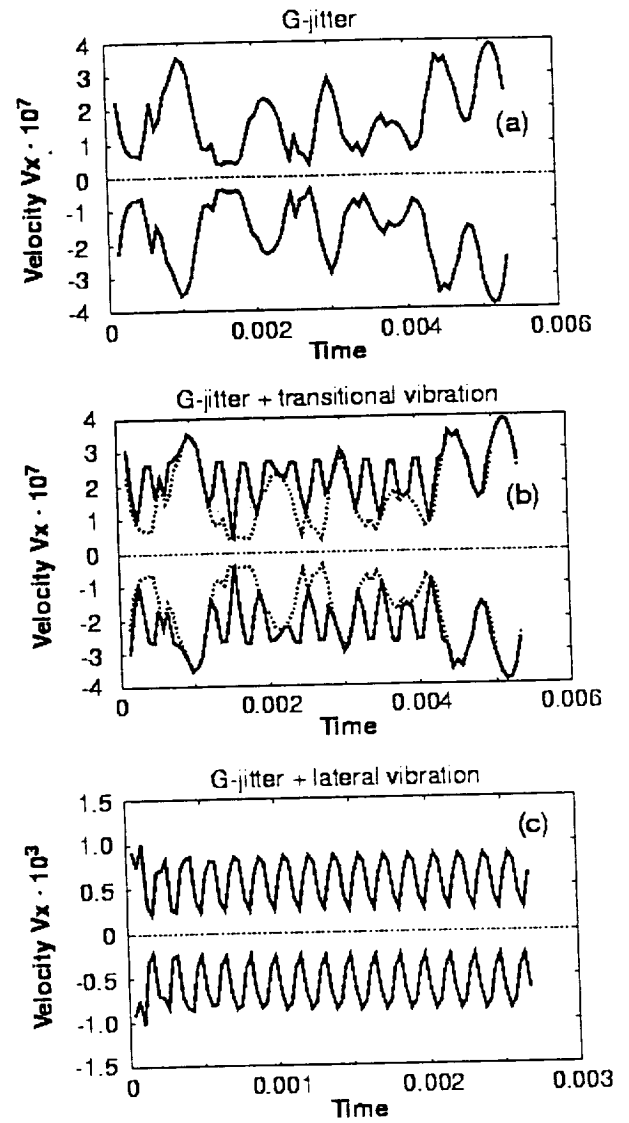


Figure 9: Melt flow response to g-jitter (a), g-jitter and longitudinal vibration,  $Ra_v = 7.4 \cdot 10^4$ , (b) and g-jitter and lateral vibration,  $Ra_v = 7.25 \cdot 10$ . Min-max values of  $V_x$  velocity component versus time are presented.



**AIAA-2000-0698**

**MAGNETIC FIELD SUPPRESSION OF  
FLOW IN SEMICONDUCTOR MELT**

A.I. Fedoseyev  
University of Alabama  
Huntsville, AL

E.J. Kansa  
Embry-Riddle Aeronautical University  
Oakland, CA

C. Marín  
University of Alabama  
Huntsville, AL

M.P. Volz  
NASA Marshall Space Flight Center  
Huntsville, AL

A.G. Ostrogorsky  
University of Alabama  
Huntsville, AL

**38th Aerospace Sciences  
Meeting & Exhibit  
10-13 January 2000 / Reno, NV**

# MAGNETIC FIELD SUPPRESSION OF FLOW IN SEMICONDUCTOR MELT

Alexandre I. Fedoseyev, Edward J. Kansa<sup>†</sup>, Carlos Marin,  
Martin P. Volz<sup>‡</sup>, and Aleksandar G. Ostrogorsky

Center for Microgravity and Materials Research  
University of Alabama in Huntsville  
Huntsville, Alabama 35899, U.S.A.  
E-mail: alex@cmmr.uah.edu

<sup>†</sup>Embry-Riddle Aeronautical University,  
East Bay Campus, Oakland, California 94621, U.S.A.

<sup>‡</sup>NASA Marshall Space Flight Center,  
Huntsville, Alabama 35812, U.S.A.

## Abstract

A numerical solution for thermal convection flows in a semiconductor melt with strong static magnetic field applied is presented. Although, the generated flows have extremely low velocity, the numerical solution of the governing equations involved is very complicated due to the thin boundary layers. Rectangular cavity with different aspect ratios and gravity direction aligned and misaligned with the magnetic field vector are considered. Three numerical methods are compared. It is shown that the finite element approach with regularization can provide the numerical solutions in a wide range of  $Ha$  numbers (up to  $10^4$ ). The results compare favorably with the asymptotic theoretical solutions.

## 1 Introduction

The application of magnetic fields is one of the most promising approaches for the reduction of convection during directional solidification of electrical conductive

melts (semiconductor crystals). Current technology allows the experiments with very strong static fields (up to 80 KGauss) for which, based on the simple scaling analysis in stabilized systems (vertical Bridgman method with axial magnetic field), nearly convection free segregation is expected, [1].

However, the reported experimental studies have yielded controversial results [2,3]. The computational methods are, therefore, a fundamental tool in the understanding of the phenomena accounting during the solidification of semiconductor materials. Moreover, effects like the bending of the isomagnetic lines, different aspect ratios and misalignments between the direction of the gravity and magnetic field vectors can not be easily analyzed with analytical methods.

The reported numerical results are not able to explain the experimental data [4,5]. Although the generated flows are extremely low, the computational task is complicated because of the thin boundary layers [6].

Here, three different numerical approaches we have used for comparison, :

- (1) The spectral method implemented in [7],
- (2) The finite element method with regularization for boundary layers [8],

\*Copyright ©2000 by A. I. Fedoseyev. Published by the American Institute of Aeronautics and Astronautics, Inc., with permission.

(3) The multiquadric method, a novel method with global radial basis functions [9].

The results obtained by these three methods are presented for a wide range of Hartmann numbers corresponding to magnetic fields  $B$  from 0.05 to 5.0 Tesla (0.5 to 50.0 KGauss). Comparison and discussion of accuracy, efficiency, reliability and agreement with the asymptotic solution are presented.

## 2 Governing equations

The two dimensional steady state thermal convection of incompressible viscous fluid (melt) in a rectangular ampoule of diameter  $D$  and height  $H$  was considered. More general cases are discussed in [17], [18], [19]

The governing equations (Boussinesq approximation) are :

The momentum equation:

$$(\nabla \nabla) \mathbf{V} - Pr \nabla^2 \mathbf{V} + \nabla p = Ra Pr \cdot \Theta \cdot \mathbf{e}_g + \mathbf{F} \quad (1)$$

while the continuity equation:

$$\nabla \cdot \mathbf{V} = 0 \quad (2)$$

and energy equation:

$$(\nabla \nabla) \Theta = \nabla^2 \Theta. \quad (3)$$

where length, time and velocity are scaled, respectively, by  $L$ ,  $L^2/\kappa$  and  $\kappa/L$ . Here  $L$  is the smallest of the ampoule diameter  $D$  and height  $H$ , and  $\kappa = \frac{k}{\rho}$  is the thermal diffusivity of the melt.  $\mathbf{F}$  is a body force due to magnetic field (Lorentz force). For an axially symmetric configuration the Lorentz force is given by

$$\mathbf{F} = Pr Ha^2 [(\mathbf{V} \times \mathbf{e}_B) \times \mathbf{e}_B] = (Pr Ha^2 V_1, 0) \quad (4)$$

in the two-dimensional case, where  $V_1$  is the horizontal component of the velocity. It does not depend on electrical potential, because the electrical potential is uniform ( $\nabla \phi = 0$ ), when a vertical magnetic field is applied (see, for example, [1]). This is not valid if the symmetry is broken, when the magnetic field direction and the gravity vector are slightly misaligned. However, to simplify the study, we neglect this effect. According to [1], Joule heating due to electromagnetic field can be neglected as well. The nondimensional temperature  $\Theta$  is scaled by

$\Theta = (T - T_{COLD})/\Delta T = GL$ ,  $G$  is a vertical temperature gradient  $\frac{\partial T}{\partial y}$ . The Prandtl, Rayleigh and Hartmann numbers are, respectively, given by

$$Pr = \frac{\nu}{\kappa}, Ra = \frac{\beta \Delta T g L^3}{\nu \kappa}, Ha = LB_0 \sqrt{\frac{\sigma}{\nu \rho}}$$

Here  $\beta, g, \nu, \rho, \sigma$  are thermal expansion coefficient, gravitational acceleration, kinematic viscosity, density and electrical conductivity, and  $B_0$  is the magnetic field intensity,  $\mathbf{e}_g, \mathbf{e}_B$  are unit vectors in the direction of gravitational acceleration and magnetic field.

The boundary conditions for eq. (1)-(3) are: (i) the non-slip condition for the velocity,  $\mathbf{V} = 0$ , on the walls, and (ii) the given wall temperature distribution,  $\Theta = y$  on side walls, and  $\Theta_B = -\Theta_0(x - L)^2$  at the bottom. The latter condition represents a parabolic temperature distribution at the bottom boundary. To exclude an undefined constant in the pressure field we set  $p(x_0, y_0) = 0$  at arbitrary location  $(x_0, y_0)$ .

## 3 Problem parameters

The problem was solved using properties for Germanium ( $Ge$ ) melt exposed to magnetic field having intensity  $B_0$  in a range from 0 to 5 Tesla (and in few cases up to 50 Tesla); the direction of magnetic field vector is axial,  $\mathbf{e}_B = (0, 1)$ . The corresponding Hartmann number varies from  $Ha = 0$  to 2170 (and in few cases to  $Ha = 2.17 \cdot 10^4$ ). Ampoule geometries considered are (a)  $L = 1 \text{ cm}$ ,  $H = 2 \text{ cm}$ , and (b)  $L = 2 \text{ cm}$ ,  $H = 1 \text{ cm}$ .

Solutions were obtained for the temperature gradient on a side wall  $G = 70 \text{ K/cm}$ . The average temperature gradient on the bottom (solid/liquid interface) was  $0.5 \text{ K/cm}$ . The corresponding Rayleigh number is  $Ra = 1.24 \cdot 10^5$ . Earth gravity  $g$  was considered to be (i) aligned to the magnetic field direction,  $g = g_0(0, -1)$  and (i) misaligned by 0.5 degrees.

## 4 Numerical methods

Three numerical methods were used to solve the system of eq. (1) - (3) for the boundary conditions and parameters given above.

## 4.1 Spectral element method

By using the spectral element method (SEM) code NEKTON [7], the domain was divided into quadrilateral elements, refined near the walls (Fig. 1a), and  $8 \times 8$  Chebyshev polynomials are used inside each element for field variables approximation. Total number of elements in our tests was 362, and total number of unknowns was about  $5 \cdot 10^4$ .

## 4.2 Finite element method with regularization for the Navier-Stokes equations

The finite element method with regularization for the Navier-Stokes equations (FEMR) was proposed in [8] for high  $Re$  number flows. It was shown that such a regularization works well in case of flows with thin boundary layers, even with few mesh nodes placed inside the boundary layer. For the present problem, the continuity equation (2) is modified as follows

$$\nabla \cdot \mathbf{V} = \tau \nabla \cdot (\nabla p - \mathbf{F} - RaPr \cdot \Theta \cdot \mathbf{e}_g) \quad (5)$$

where  $\tau$  is a small regularization parameter. For  $\tau \rightarrow 0$  we approach the original equation (2). A boundary condition for the pressure on the wall is

$$(\nabla p - \mathbf{F} - RaPr \cdot \Theta \cdot \mathbf{e}_g) \cdot \mathbf{n} = 0, \quad (6)$$

where  $\mathbf{n}$  is a unit wall normal vector. Eq. (5) and (6) present the main feature of this method, and ensure the balance of the component of the force normal to the region boundary.

Another advantage is that this approach allows to use the same order finite element approximation for the velocity and pressure with all unknowns located at the same nodal points. For a justification of this regularization one can be referenced to the new hydrodynamic equations proposed in [10] that have similar fluctuation term. Similar terms have been obtained as a result of the consistent treatment of time-advancement for the divergence-equation by Löhner (see [11]). Löhner has also shown that similar terms actually appear in the discrete equations as a result of different order finite element approximations used for interpolation of velocity and pressure.

The numerical solution is insensitive to the value of  $\tau$ . The value of  $\tau$  should be chosen within the range  $10^{-8}$  to  $10^{-4}$ . For a smaller value of  $\tau$  the discrete equations become nearly incompatible, and numerical solution exhibits strong spatial oscillations.

The simplest linear finite elements were used for numerical approximation of velocity, pressure and temperature. We used triangular meshes with  $40 \times 100$  and  $80 \times 100$  nodes refined near the walls (Fig. 1b). The results obtained on these meshes are very close, so we used  $40 \times 100$  mesh for most of the runs. Total number of nodes and unknowns is respectively 4000 and  $16 \cdot 10^3$ . FEMINA/3D CFD code (Finite Element Method IN Applications) [12] was modified to implement proposed regularization method. Discrete finite element equations corresponding to (1), (5), (3) were solved together simultaneously by CNSPACK solver [12] using the CGS-type iterative technique and high order preconditioning by incomplete decomposition.

## 4.3 Multiquadric radial basis function method

The Multiquadric Radial Basis Function (MQ) Method is a novel meshless collocation method with global basis functions. The concept of solving partial differential equations (PDE) using radial basis functions (RBFs) was introduced by Kansa in 1990 [9]. He implemented this approach for the solution of hyperbolic, parabolic, and elliptic PDEs using the MQ RBFs proposed by Hardy [13],[14] for interpolation of scattered data.

An RBF is a function that depends only upon the distance between a point  $(x, y)$  and a reference node  $(x_j, y_j)$ . Among studied RBFs still only the MQ RBFs are proven to have an exponential convergence for the function interpolation [16]. A MQ RBF is given by  $g_j(x, y) = \sqrt{(x - x_j)^2 + (y - y_j)^2 + c_j^2}$ , where  $c_j$  is called the *shape parameter*. The numerical experiments for parabolic and elliptic PDEs by Kansa [9] show high accuracy and efficiency of the MQ scheme. A brief review on MQ RBF for the solution of PDE can be found in [15] and on the RBF-PDE Web site [22]. This approach results in modest size systems of nonlinear algebraic equations which can be efficiently solved by using widely available library routines and linear solvers for dense matrices.

For a given set of  $N$  nodes in the domain and at the boundary, the solution for unknown  $\mathbf{V}$ ,  $p$  or  $\Theta$  is approximated as a sum of MQ functions with the coefficients as unknown. These coefficients are found by collocating governing equations at the internal nodes and boundary conditions at the boundary nodes. Nonlinear algebraic system is solved by Newton method.

We used up to  $25 \times 25$  uniformly distributed nodes and constant shape parameter  $c_j = c_0 = \text{const}$  for all functions. Total number of unknowns is 2500.

## 5 Results and discussion

### 5.1 Convection in rectangular cavity with $H/D=2$

The tests below represent the case of melt zone with aspect ratio  $H/D = 2$ .

#### 5.1.1 Flow without magnetic field

The nondimensional parameters are:  $Pr = 0.006$ ,  $Ra = 1.25 \cdot 10^5$ ,  $Ha = 0$ ,  $D = 1$ ,  $H = 2$  and  $L = D$ . The temperature distribution at the bottom is given by  $\Theta_B = -3.575 \cdot 10^{-3}(1 - 4x^2)$ . The results for the case  $\alpha = 0$  ( $\alpha$  is the angle between the gravity vector and the vertical axis) are shown in Fig. 2. The solution obtained by all three methods are close to each other.

The flow pattern consists of two counter-rotating symmetric cells, located at lower corners. The perturbation of the temperature distribution resulting from  $\Theta = y$ , set on the wall, can not be observed on the plot. Note that the temperature field is suppressing the flow, which is caused by the horizontal temperature gradient at the bottom.

If the gravity direction is misaligned with the ampoule axis by 0.5 deg, flow pattern becomes quite different. A normal to the gravity component of the temperature gradient becomes a main reason for the thermal convection. A single roll is formed, while the magnitude of melt velocity is higher by a factor of two to three.

#### 5.1.2 Flows under magnetic field

**$B = 0.05$  Tesla,  $Ha=21.7$ .** The MQ method did not yield a solution, because the Newton method did not converge (since the Jacobian becomes ill-conditioned).

The solution by the SEM and FEMR methods show notable difference. The SEM solution for the velocity field exhibit numerical oscillations between the mesh nodes. The flow pattern from FEMR is the same as in the absence of magnetic field (Fig. 3). Vertical velocity profile at  $y = 0.25$  shows a boundary layer. The flow velocity is decreased by about a factor of two.

**$B = 0.5$  Tesla,  $Ha=217$ .** The boundary layer becomes very thin, and the flow velocity is about two order of magnitude lower compared to  $B = 0$ . The velocity profiles from the SEM computation exhibit spatial oscillation with velocity sign change between mesh nodes. The FEMR can provide

the results still without difficulty, the velocity profiles remain smooth.

**$B = 5.0$  Tesla,  $Ha=2170$ .** The results from the SEM computation showed strong numerical instability. The FEMR solution is still quite reasonable: the flow pattern is about the same, but flow velocity is about two order of magnitude lower than in previous case  $B = 0.5$  Tesla. The boundary layers become extremely thin (0.01cm), and therefore almost invisible on a plot (Fig.4).

In case of a misalignment of gravitational acceleration with ampoule axis, the flow pattern changes to one big cell for this and all other values of magnetic field considered.

**$B = 50$  Tesla,  $Ha=21700$ .** This was done just to test the ability of proposed FEMR method, the solution still remains smooth with even three times more thin boundary layer compared to  $B = 5.0$  Tesla.

Stretching of the stream lines by the magnetic field demonstrated in Fig. 5 for all the cases above (aligned gravity vector) plus additional case  **$B = 0.005$  Tesla,  $Ha=2.17$** . This effect is mentioned in many papers schematically, but computational results were never shown.

#### 5.1.3 Discussion

Figure 6 shows the maximum radial velocity calculated, using the FEMR method, for different values of the imposed magnetic field  $B$ . The maximum of horizontal (radial) velocity versus  $B$  is presented by few curves, marked as " $Vr(b)$ " for FEMR on 40x100 uniform in vertical direction mesh, by " $Vr(f)$ " for 40x100 refined near all walls mesh and by " $Vr(d)$ " for 80x100 mesh refined at the walls. Results for misaligned case are presented by the curve, labeled as " $Vr(a = 0.5)$ ". We can observe a predicted asymptotic dependence  $V_{max} \sim Ha^{-2}$  for all the cases, starting from about  $B = 0.05$  Tesla ( $Ha \approx 20$ ), in accordance to asymptotic given in [1].

The main difficulty of this problem is a viscous flow with thin boundary layer. Despite the fact that actual flow velocities are very low and the Reynolds number obtained using the computed velocities, is  $Re \sim 10^{-1}$  to  $10^{-6}$ , a big value of the Hartmann number results in a relatively small coefficient at the highest derivative of the velocity in the momentum equation. Solution of such a problem exhibits thin boundary layer with the thickness  $\delta \sim Ha^{-1}$ , and the the "equivalent" Reynolds number  $Re_{eqv} \sim Ha^2$ , for  $B=0.5$  Tesla  $Re_{eqv} = 4.7 \cdot 10^4$  and  $B=50.0$  Tesla  $Re_{eqv} = 4.7 \cdot 10^8$ .

## 5.2 Thermal convection in cavity with aspect ratio $H/D=0.5$

The following tests present the case with aspect ratio  $H/D = 0.5$ ,  $D = 2$ ,  $H = 1$ . The temperature distribution at the bottom is given by  $\Theta_B = -7.150 \cdot 10^{-3}(1-x^2)$ . Applied axial temperature gradient is also  $G = 70$  K/cm.

### Flow without magnetic field

The solution obtained by all three methods are also close to each other. The flow pattern consists of two counter-rotating symmetric cells, that occupy most of the volume, Fig. 7.

In the case of the gravity misalignment with the ampoule axis direction by  $0.5^\circ$ , the axial temperature gradient becomes a main driving force for the thermal convection. This results in the change of flow pattern that becomes consisting of one big convective cell.

### Flow with magnetic field

The results are shown in Fig. 8. Again when  $Ha$  number is high, all the methods except FEMR, exhibit the same difficulties as in a case of aspect ratio  $H/D = 2$ . A summary of the results is shown in Fig. 9. The suppression of the flow is essentially same efficient as before with similar asymptotic dependences  $V_{max} \sim Ha^{-2}$ . The velocity profile in the boundary layer obtained by FEMR is shown in Fig. 10. One of the advantages of FEMR is that its solution remains smooth even at the big change of the slope. We can see that the thickness of the vertical boundary layer is in agreement with asymptotic solution,  $\delta \sim Ha^{-1}$ . The tangent velocity derivative at the boundary decreases with  $Ha$  number as  $\frac{\partial V_T}{\partial n} \sim \frac{V_{max}}{\delta} \sim Ha^{-1}$ .

Comparing between Fig. 6 and 9 it is found that misalignment's impact on the reducing of the convection is more important for aspect ratio 1.

## Conclusions

We compared three different numerical methods for the solution of thermal convection flows in a semiconductor melt with strong static magnetic field applied. These are spectral element method, finite element method with regularization for the Navier-Stokes equations and multiquadric method, a method with global basis functions. Although

the generated flows are extremely low, the computational task is very complicated because of the thin boundary layer at high Hartmann numbers,  $Ha \gg 1$ . We considered melt region geometry with different aspect ratios, and gravity direction aligned and misaligned with the magnetic field vector. The comparison shows that the finite element approach with regularization can obtain stable and reliable solutions in a wide range of  $Ha$  number, up to  $10^4$ . These results compare favorably with asymptotic solutions.

The main difficulty of this problem is that a flow has a very thin boundary layer. Despite the fact that actual Reynolds number is very low,  $Re \sim 10^{-1}$  to  $10^{-6}$ , a high value of the Hartmann number results in a relatively small coefficient at the velocity Laplacian in the momentum equation. Solution of such problem exhibit thin boundary layers with related, like for high Reynolds number flows, difficulties. That is one of the reasons for the discrepancy in the results that numerical studies reported. Both the spectral method and the multiquadric method with global basis functions needs improvement to deal with thin boundary layers. Multilevel approximation by Fasshauer [20],[21] can be one of the ways.

Numerical solution of these problems by available commercial CFD codes may be not efficient or not possible. Adaptive algorithms can be a promising solution. Development of more accurate and efficient solution methods for this problem is necessary.

## Acknowledgements

This work was supported in part by National Aeronautics and Space Administration through grant NAG8-1229. The authors are grateful to G. S. Dulikravich for fruitful discussions.

## References

- [1] J. P. Garandet and T. Alboussiere, Bridgman growth: Modeling and experiments, In: "The role of magnetic field in Crystal Growth", Pergamon Press (to be published).
- [2] D.H. Matthiesen, M. J. Wargo, S. Motakef, D. J. Carlson, J. S. Nakos and A. F. Witt, J. Crystal Growth, **85** (1987) 557.
- [3] Y. Kang, K. Okano, Hoshikawa and T. Fukuda, J. Crystal Growth, **140** (1994).



- [4] D. H. Kim, P.M. Adornato and R. A. Brown, *J. Crystal Growth*, **80** (1987) 155.
- [5] S. Motakef, Magnetic field elimination of convective interference with segregation during growth of doped semiconductors, *J. Crystal Growth*, **104** (1990) 833.
- [6] M. Yao, A. Chait, A. L. Fripp and W. J. Debnam, Magnetically damped convection and segregation in Bridgman growth of PbSnTe, *J. Crystal Growth*, **173** (1997) 467.
- [7] NEKTON 3.1 Tutorial Guide, FLUENT Inc., Second Edition, May 1997.
- [8] A. I. Fedoseyev, and B. V. Alexeev. Higher Order Continuum Model for Incompressible Viscous Fluid Flow. In: *Continuum Models and Discrete Systems*, Eds. E. Inan, A. Markov, World Scientific, London, 1998, 130-137.
- [9] E. J. Kansa, Multiquadrics-a scattered data approximation scheme with applications to computational fluid dynamics-II. Solutions to hyperbolic, parabolic, and elliptic partial differential equations, *Comput. Math. Applic.*, **19**, No. 8/9 (1990), 147-161.
- [10] B. V. Alexeev, The generalized Boltzmann equation, generalized hydrodynamic equations and their applications. *Phil. Trans. Roy. Soc. London, A*, **349** (1994) 417-443.
- [11] R. Löhner, Design of Incompressible Flow Solver: Practical Aspects, In: *Incompressible computational fluid dynamics*, Eds. M. D. Gunzburger and R. A. Nicolaides, Cambridge Press, 1993, 267-294.
- [12] V. I. Polezhaev, A. I. Prostomolotov, and A. I. Fedoseyev. Finite Element Method in Viscous Fluid Mechanics Problems, In: *Advances in Science and Technology. Fluid Mechanics series*, **21**, No. 3, VINITI, Moscow, 1987, 3-92
- [13] R. L. Hardy, Multiquadric equations of topography and other irregular surfaces, *J. Geophys. Res.*, **76** (1971), 1905-1915.
- [14] R. L. Hardy, Theory and applications of the multiquadric- biharmonic method: 20 years of discovery, *Comput. Math. Applic.*, **19**, No. 8/9 (1990), 163-208
- [15] A. I. Fedoseyev, M. J. Friedman, and E. J. Kansa. Continuation for nonlinear elliptic partial differential equations discretized by the multiquadric method, to appear in *Int. J. Bifur. and Chaos*.
- [16] W. R. Madych and S. A. Nelson, Multivariate interpolation and conditionally positive definite functions II, *Math. Comp.*, **54** (1990), 211-230.
- [17] G. S. Dulikravich, and V. Ahuja, Modeling Dielectric Fluids Solidification With Charged Particles in Electric Fields and Reduced Gravity, *Numerical Heat Transfer, Fundamentals, Part B*, **25** (1994), 357-373.
- [18] G. S. Dulikravich, and S. R. Lynn, Unified Electro-Magneto-Fluid Dynamics (EMFD): A Survey of Mathematical Models, *International Journal of Non-Linear Mechanics*, **32**, No. 5 (1997), 913-922.
- [19] G. S. Dulikravich, and S. R. Lynn, Unified Electro-Magneto-Fluid Dynamics (EMFD): A Survey of Mathematical Models, *International Journal of Non-Linear Mechanics*, **32**, No. 5 (1997), 923-932.
- [20] G. E. Fasshauer, On Smoothing for Multilevel Approximation with Radial Basis Functions. In: *Approximation Theory IX*, Eds. C. K Chui and L. L. Schumaker, Vanderbilt University Press, Nashville, TN, 1998
- [21] G. E. Fasshauer and J. W. Jerome, Multistep Approximation Algorithms: Improved convergence rates through postconditioning with Smoothing Kernels, *Advances in Computational Mathematics* (to appear).
- [22] RBF-PDE, Radial basis function methods for solution of partial differential equation, Web site <http://rbf-pde.uah.edu>

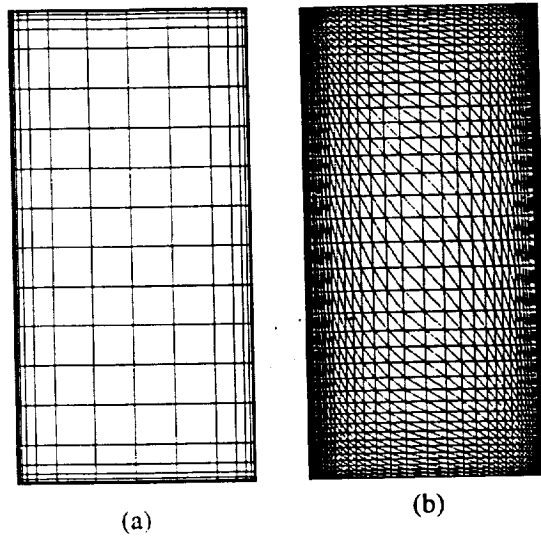


Figure 1: Mesh used in the spectral element method (a), 362 elements,  $8 \times 8$  Chebyshev polynomials approximation inside each element, and mesh used in the finite element method (b), 4000 nodes, 8,000 triangle elements.

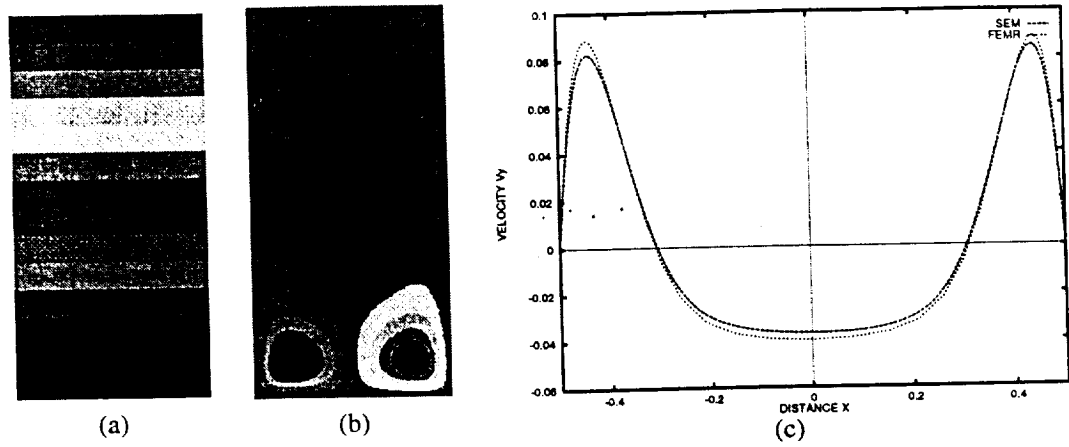


Figure 2: Thermal convection without magnetic field for geometry 1,  $D = 1$ ,  $H = 2$ ,  $Ra = 1.25 \cdot 10^5$ : temperature distribution (a), stream function (b), and vertical velocity profile  $V_y(x)$  at  $y = 0.25$  by SEM and FEMR methods (c). velocity scale is 0.225 cm/s.

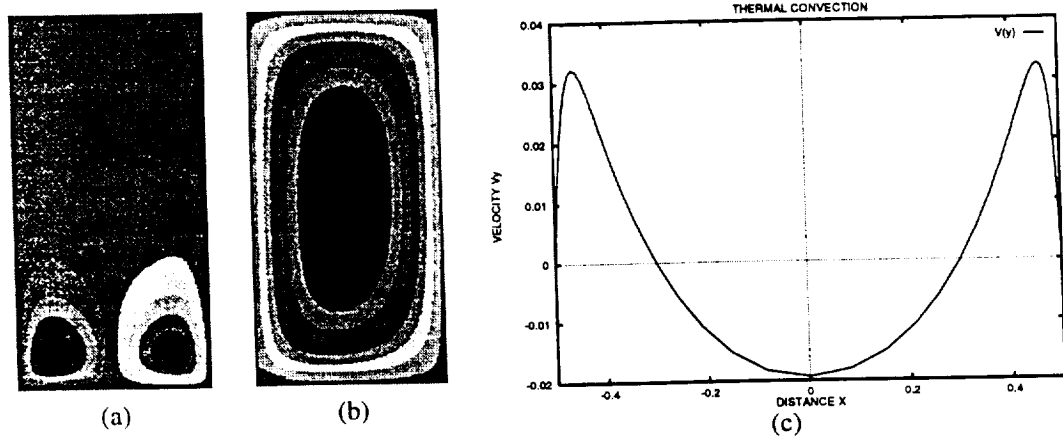


Figure 3:  $H/D = 2$ ,  $Ra = 1.25 \times 10^5$ ,  $Ha = 21.7$  ( $B = 0.05$  Tesla). Stream functions for gravity vector (a) aligned and (b) 0.5 degrees misaligned relative to the vertical direction. (c) Nondimensional vertical velocity profile  $V_y(x)/(0.225 \text{ cm/s})$  calculated using the FEMR method 0.25 H from the bottom of the cavity ( $y/H = 0.25$ )

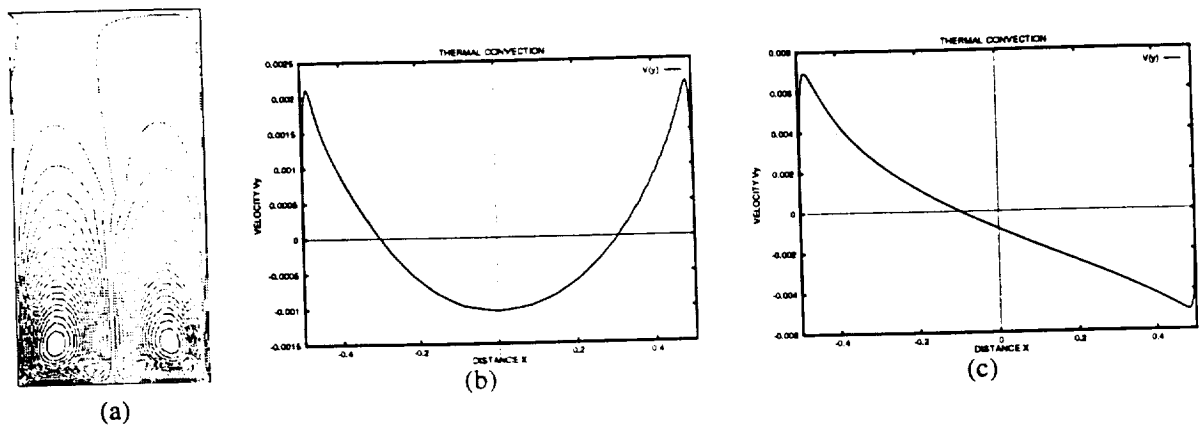


Figure 4: Thermal convection with magnetic field for geometry 1,  $D = 1$ ,  $H = 2$ ,  $Ra = 1.25 \cdot 10^5$ ,  $Ha = 2170.0$  ( $B = 5.0 \text{ Tesla}$ ): stream function (a), and vertical velocity profile  $V_y(x)$  at  $y = 0.25$ , velocity profile  $V_y(x)$  for misaligned by 0.5 degree gravity direction at  $y = 0.5$  (c).

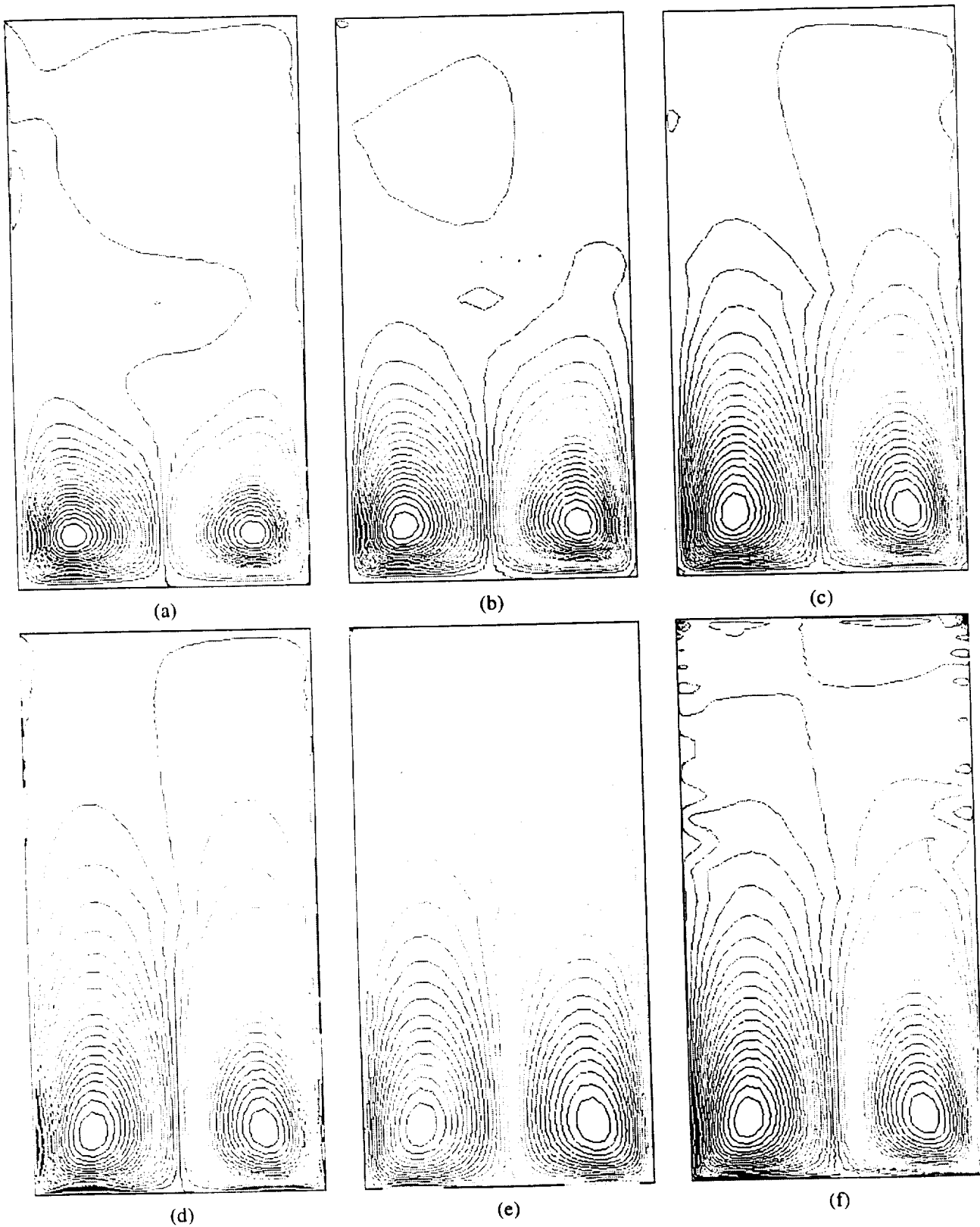


Figure 5: Stretching of the flow streamlines with increasing magnetic field, (a)  $B = 0$ , (b)  $B = 0.005$  Tesla, and (c) to (f) correspond, respectively, to  $B = 0.05, 0.5, 5.0$  and  $50.0$  Tesla

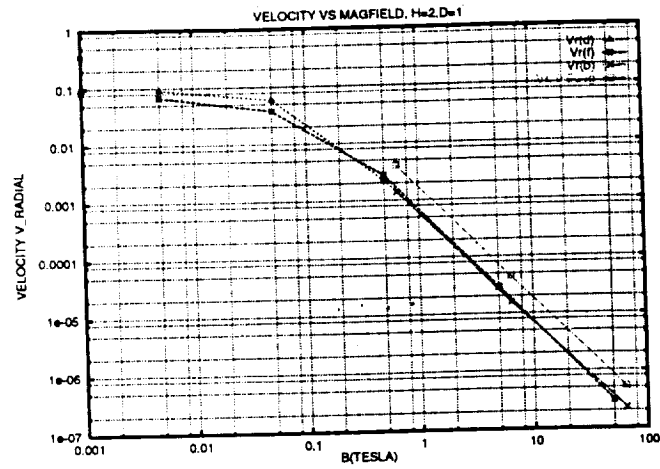


Figure 6: A summary of magnetic field suppression of the flow for  $H = 2$ ,  $D = 1$ . Maximum value of horizontal (radial) velocity versus  $B$ :  $Vr(b)$  on  $40 \times 100$  uniform in vertical direction mesh,  $Vr(f)$  for  $40 \times 100$  refined near walls mesh, and  $Vr(d)$ ,  $80 \times 100$  mesh refined at the walls. Predicted asymptotic dependence  $V_{max} \sim Ha^{-2}$  is observed for all the cases including the misaligned one, starting from about  $B = 0.25$  Tesla.

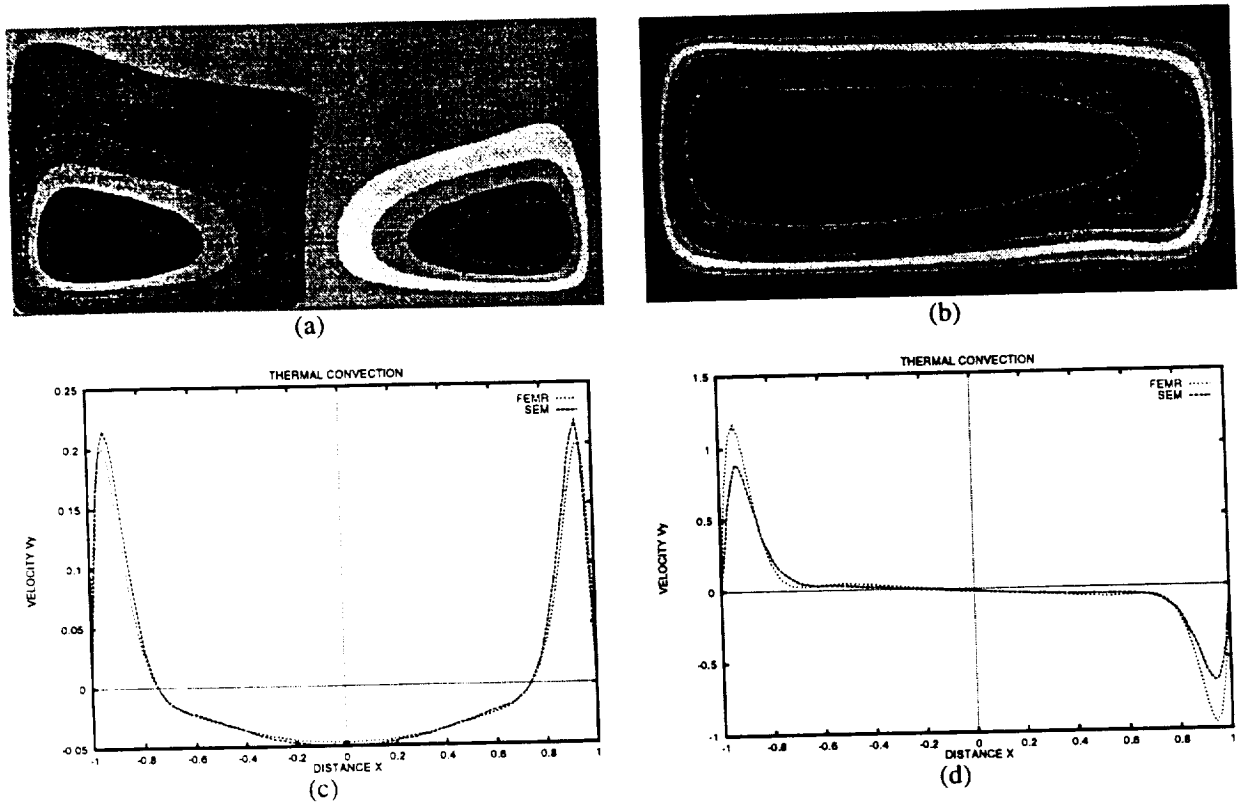


Figure 7: Thermal convection without magnetic field for  $D = 2$ ,  $H = 1$ ,  $Ra = 1.25 \cdot 10^5$ : stream function (a), stream function for misaligned configuration (b), vertical velocity profiles by SEM and FEMR,  $Vy(x)$  for (a) at  $y = 0.25$  (c), and for (b) at  $y = 0.5$  (d), velocity scale is  $0.225$  cm/s.

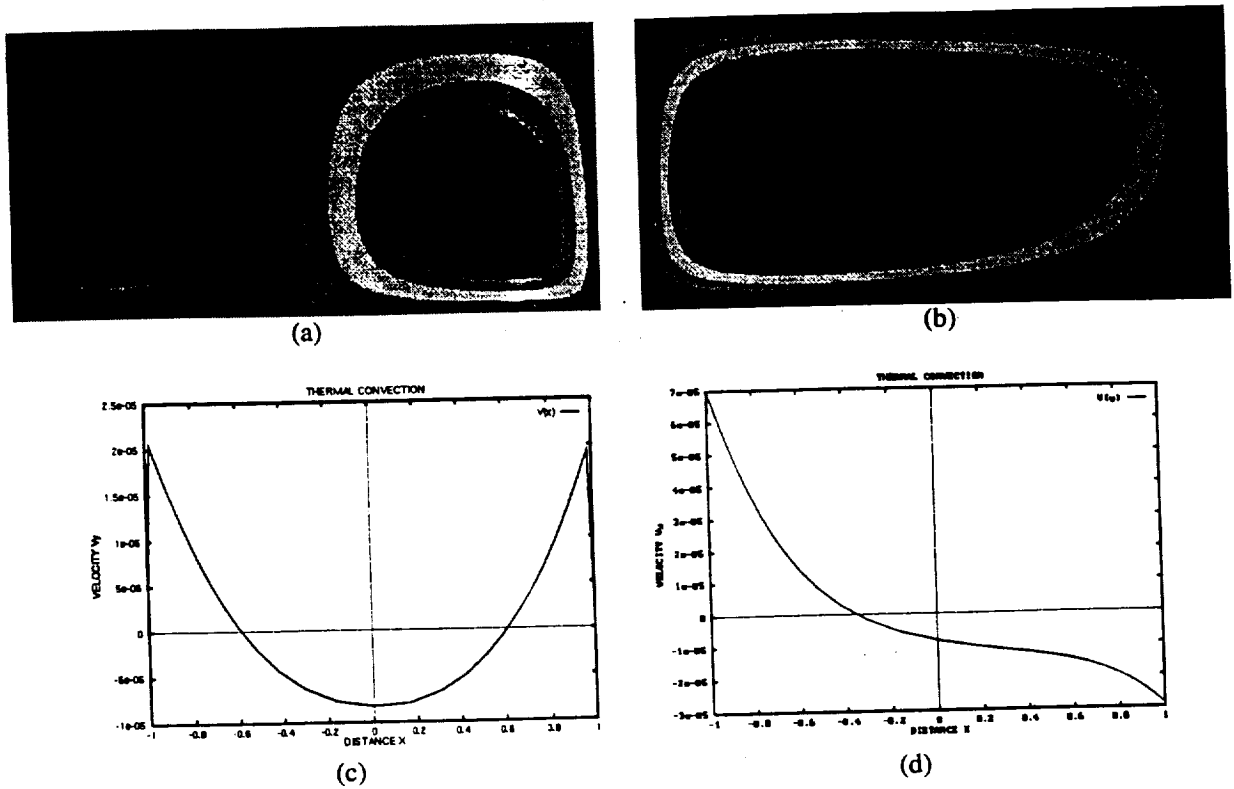


Figure 8: Thermal convection with magnetic field.  $D = 2$ ,  $H = 1$ ,  $Ra = 1.25 \cdot 10^5$ ,  $Ha = 2170$  ( $B = 5.0$  Tesla): stream function (a), same for misaligned case (b), vertical velocity profile  $V_y(x)$  for (a) at  $y = 0.25$  (c) and vertical velocity profile  $V_y(x)$  for (b) at  $y = 0.5$  (d), velocity scale is  $0.225$  cm/s.

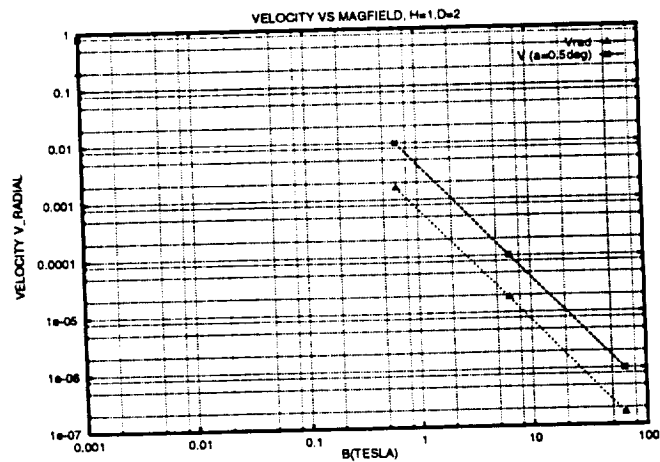


Figure 9: Summary of magnetic field suppression of the flow for  $H = 1$ ,  $D = 2$ : maximum value of horizontal (radial) velocity versus  $B$  for aligned and misaligned configurations. Predicted asymptotic dependence  $V_{max} \sim Ha^{-2}$  is observed for both cases.

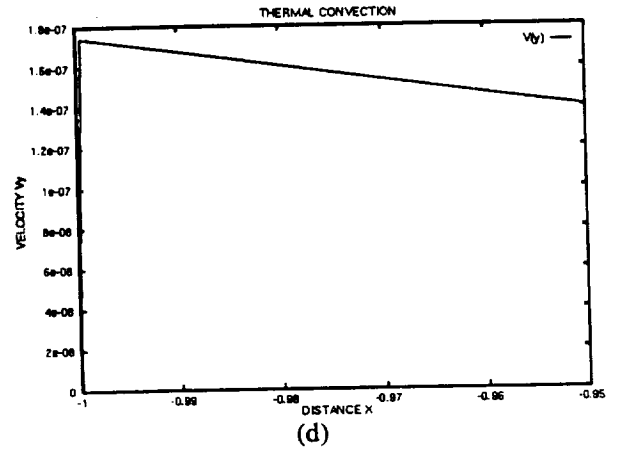
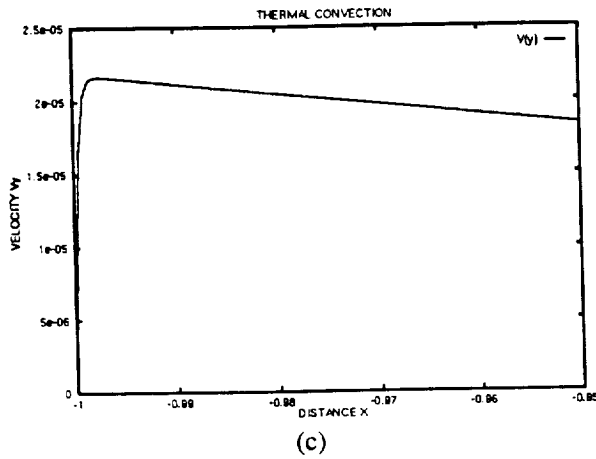
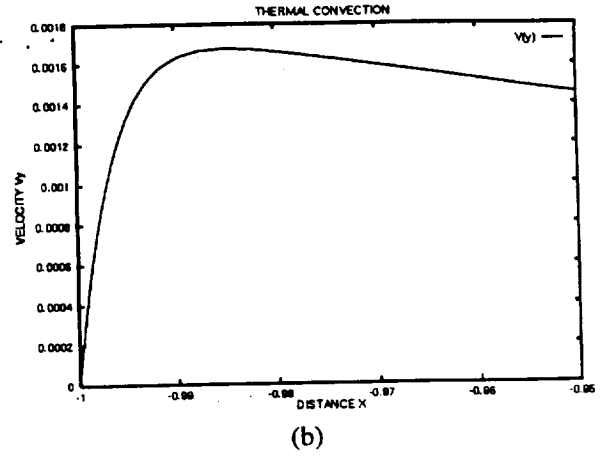
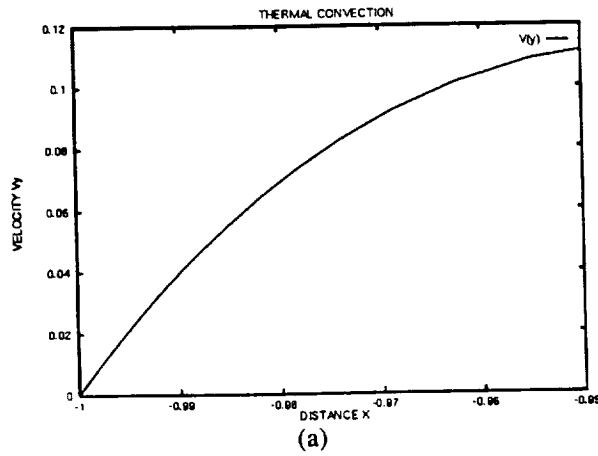


Figure 10: The velocity profile in the boundary layer ( $X$  coordinate from -1.0 to -0.95 ) with increasing the magnetic field for geometry 2,  $D = 2$ ,  $H = 1$ ,  $Ra = 1.25 \cdot 10^5$  : (a) to (d) correspond, respectively to  $B = 0, 0.5, 5.0$  and  $50.0$  Tesla. The velocity amplitude decreases as  $Ha^{-2}$  and its gradient on the wall decreases as  $Ha^{-1}$  with increasing the Hartmann number  $Ha$ .



# Improved Multiquadric Method for Elliptic Partial Differential Equations via PDE Collocation on the Boundary

A. I. Fedoseyev\*, M. J. Friedman† and E. J. Kansa‡

\*Center for Microgravity and Materials Research,  
University of Alabama in Huntsville, Huntsville, AL 35899

†Department of Mathematical Sciences,  
University of Alabama in Huntsville, Huntsville, AL 35899

‡Embry-Riddle Aeronautical University, East Bay Campus, Oakland, CA 94621

April 25, 2000

## Abstract

The Multiquadric Radial Basis Function (MQ) Method is a recent meshless collocation method with global basis functions. It was introduced for discretizing partial differential equations (PDEs) by Kansa in early nineties. The MQ method was originally used for interpolation of scattered data, and it was shown to have exponential convergence for interpolation problems.

In [11] we have extended the Kansa-MQ method to numerical solution and detection of bifurcations in 1D and 2D parametrized nonlinear elliptic PDEs. We have found there that the modest size nonlinear systems resulting from the MQ discretization can be efficiently continued by a standard continuation software, such as AUTO. We have observed high accuracy with small number of unknowns, as compared with most known results from the literature.

In this paper we formulate an improved Kansa-MQ method with *PDE collocation on the boundary* (MQ PDECB): we add an additional set of nodes (which can lie inside or outside of the domain) adjacent to the boundary and, correspondingly, add an additional set of collocation equations obtained via collocation of the PDE on the boundary. Numerical results are given that show a considerable improvement in accuracy of the MQ PDECB method over the Kansa-MQ method, with both methods having exponential convergence with essentially the same rates.

**Keywords:** Radial basis functions, multiquadric method, numerical solution, continuation, bifurcations, nonlinear elliptic PDEs.

## 1 Introduction.

The Multiquadric Radial Basis Function (MQ RBF or, simply, MQ) method is a recent meshless collocation method, with global basis functions, for discretizing PDEs. It was originally proposed in 1970 [19], [20] for interpolation of scattered data and was shown [27], [28], [31] to have an exponential convergence for function approximation. The MQ method was introduced for solving PDEs in Kansa [24], [25] in early nineties. Since then it was successfully applied for solving a number of 2D and 3D PDEs, see e.g. [4], [18], [29], [17], [21], [7] and references there, while some convergence results for solving PDEs, based directly on the interpolation error estimates, appeared only recently [14, 15]. Application of the MQ method to PDEs leads to finite dimensional problems with full matrices. The Kansa-MQ method was shown to give high accuracy with a relatively small number of unknowns (tens or hundreds for 2D problems). The corresponding linear systems can be efficiently solved by direct methods. In [11] we have extended the Kansa-MQ method to numerical solution of parametrized nonlinear elliptic PDEs. We presented there results of our numerical experiments

---

\*E-mail: alex@uahtitan.uah.edu

†E-mail: friedman@math.uah.edu

‡E-mail: kansa1@lml.gov

with continuation of solutions to and detection of bifurcations in 1D and 2D nonlinear elliptic PDEs. We found that the modest size nonlinear systems resulting from the MQ discretization can be efficiently continued by a standard continuation software, such as AUTO [5].

Our observations have shown that the residual error is typically largest near the boundary (by one to two orders) compared to the residual error in the domain far from the boundary.

In this paper we formulate an improved Kansa-MQ method with *PDE collocation on the boundary* (PDECB): we add an additional set of nodes (which can lie inside or outside of the domain) adjacent to the boundary and, correspondingly, add an additional set of *collocation equations obtained via collocation of the PDE on the boundary*. The motivation for this modification of the Kansa-MQ method comes from our observations that 1) the residual is typically the largest near the boundary (by one to two orders larger than in the domain far away from the boundary), and 2) the residual is dramatically reduced when we use the PDE collocation on the boundary. The MQ PDECB method leads not only to a *higher accuracy*, but, for nonlinear problems, also to a *higher efficiency* due to the reduction of the number of unknowns in the continuation process by using a preprocessing.

We apply our MQ PDECB method to several model 1D and 2D linear and nonlinear elliptic PDEs and present results of our numerical experiments. These results demonstrate considerable improvement in convergence of the MQ PDECB method over the Kansa-MQ method, with both methods having exponential convergence with essentially the same rates. To our knowledge, this is the first demonstration of the exponential convergence for the MQ method applied to PDEs.

A related idea was successfully used for high *Re* number fluid flows in the cases of the RNS model [8], [12] and Alexeev hydrodynamics equations [10] (in the framework of the finite element method), that was applied for the solution of 3D thermo-vibrational flows [9].

A class of global numerical methods for 1D and 2D problems, *the numerical algorithms without saturation*, was proposed by Babenko in early eighties [1]. These include a highly accurate discretization method for PDEs based on Chebyshev polynomials. This method was further developed by Belykh (see e.g. [2],[3]), who found it to be more accurate and better conditioned than the spectral method.

In Section 2 we formulate the Kansa-MQ and the MQ PDECB methods for a linear elliptic PDE. In Section 3 we describe in detail the Kansa-MQ and the MQ PDECB methods for continuation of solutions to parametrized nonlinear elliptic PDEs. For clarity of presentation, Section 3 is written independently of Section 2. In Section 4 numerical examples are given that illustrate the accuracy of our method. In Section 5 we summarize our results.

## 2 A linear elliptic PDE.

We consider a well-posed elliptic boundary value problem: for given  $g(x)$ ,  $f(x)$  find  $u(x)$  from

$$\begin{aligned} Lu(x) &= f(x), \quad \text{in } \Omega \subset \mathbb{R}^d, \\ Bu(x)|_{\partial\Omega} &= g(x), \end{aligned} \quad (1)$$

where  $\Omega$  is a bounded domain,  $L$  is a linear elliptic partial differential operator, and  $B$  is a boundary operator.

### 2.1 The Kansa-MQ method.

Introduce a set  $\Theta_h$  of nodes (Fig. 1)

$$\Theta_h = \left\{ \{x_i\}_{i=1}^N \subset \Omega, \quad \{x_i\}_{i=N+1}^{N+N_b} \subset \partial\Omega \right\} \quad (2)$$

and the MQ basis functions,

$$g_j(x) \equiv g_j(c_j, x) = \sqrt{\|x - x_j\|_{\mathbb{R}^d}^2 + c_j^2}, \quad j = 1, \dots, N + N_b, \quad g_{N+N_b+1}(x) = 1, \quad (3)$$

where  $\|x - x_j\|_{\mathbb{R}^d}$  is the Euclidean norm in  $\mathbb{R}^d$ ,  $c_j \geq 0$  are called *shape parameters* [25]. We look for the approximate solution  $u_h$  to (1) in the form

$$u_h(x) = \sum_{j=1}^{N+N_b+1} a_j g_j(x), \quad (4)$$

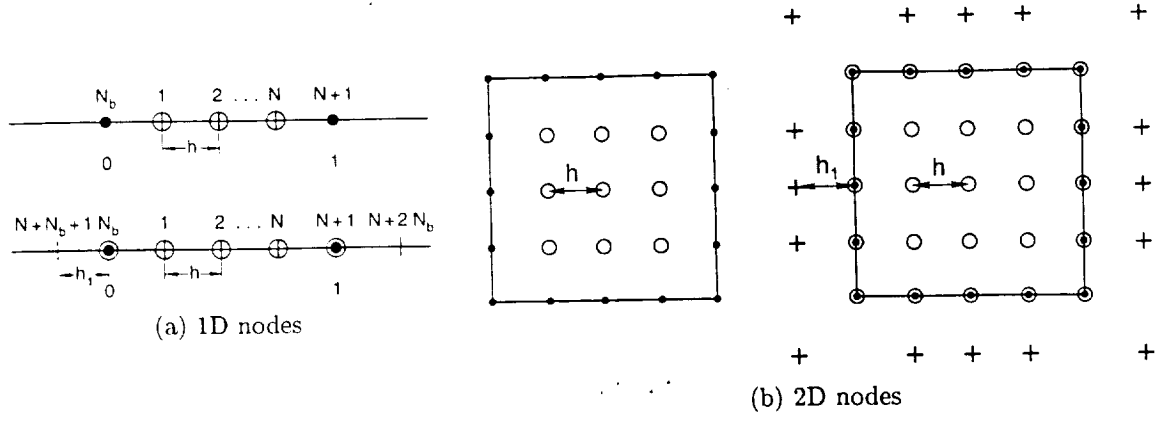


Figure 1: Nodes for the Kansa-MQ and MQ-PDECBC methods: (a) 1D Kansa-MQ nodes (top) and PDECBC (bottom), node numbering is shown; (b) 2D Kansa-MQ nodes (left) and PDECBC (right):  $\circ$  - nodes for PDE collocation,  $\bullet$  - BC collocation,  $\odot$  - PDE and BC collocation,  $+$  - nodes added for PDECBC,  $h_1$  is a distance to the boundary (may be negative, if nodes are inside);  $h$  is a mean distance between nodes.

Substituting  $u_h(x)$  into (1) and using collocation at the nodes  $\Theta_h$ , we obtain the finite dimensional problem

$$\begin{aligned} L \left( \sum_{j=1}^{N+N_b+1} a_j g_j(x_i) \right) &= \sum_{j=1}^{N+N_b+1} a_j L g_j(x_i) = f(x_i), \quad i = 1, \dots, N, \\ B \left( \sum_{j=1}^{N+N_b+1} a_j g_j(x_i) \right) &= \sum_{j=1}^{N+N_b+1} a_j B g_j(x_i) = g(x_i), \quad i = N+1, \dots, N+N_b, \\ \sum_{j=1}^{N+N_b} a_j &= 0. \end{aligned} \quad (5)$$

Introducing the notation:  $a = (a_1, \dots, a_{N+N_b+1})^T$ ,  $b = (f(x_1), \dots, f(x_N), g(x_{N+1}), \dots, g(x_{N+N_b}), 0)^T \in \mathbb{R}^{N+N_b+1}$

$$\begin{aligned} L_g &= \begin{bmatrix} L g_1(x_1) & \dots & L g_{N+N_b+1}(x_1) \\ \vdots & & \vdots \\ L g_1(x_N) & \dots & L g_{N+N_b+1}(x_N) \end{bmatrix}, \\ B_g &= \begin{bmatrix} B g_1(x_{N+1}) & \dots & B g_{N+N_b}(x_{N+1}) & B g_{N+N_b+1}(x_{N+1}) \\ \vdots & & \vdots & \vdots \\ B g_1(x_{N+N_b}) & \dots & B g_{N+N_b}(x_{N+N_b}) & B g_{N+N_b+1}(x_{N+N_b}) \\ 1 & \dots & 1 & 0 \end{bmatrix}, \quad W = \begin{bmatrix} L_g \\ B_g \end{bmatrix}, \end{aligned} \quad (6)$$

we can rewrite the system (5) in the matrix form as

$$W a = b, \quad (7)$$

whose solution is

$$\alpha = W^{-1} b. \quad (8)$$

## 2.2 The MQ PDECBC method.

Introduce a set  $\Theta_h$  of nodes (see Fig. 1)

$$\Theta_h^1 = \left\{ \{x_i\}_{i=1}^N \subset \Omega, \quad \{x_i\}_{i=N+1}^{N+N_b} \subset \partial\Omega, \quad \{x_i\}_{i=N+N_b+1}^{N+2N_b} \subset \mathbb{R}^d \setminus \partial\Omega \right\}, \quad (9)$$

where the nodes  $\{x_i\}_{i=N+2N_b+1}^{N+2N_b}$ , which can be inside  $\Omega$  or outside  $\bar{\Omega}$ , are adjacent to the boundary  $\partial\Omega$ , and the MQ basis functions,

$$g_j(x) \equiv g_j(c_j, x) = \sqrt{\|x - x_j\|_{\mathbb{R}^d}^2 + c_j^2}, \quad j = 1, \dots, N + N_b, \quad g_{N+2N_b+1}(x) = 1. \quad (10)$$

We look for the approximate solution  $u_h$  to (1) in the form

$$u_h(x) = \sum_{j=1}^{N+2N_b+1} a_j g_j(x), \quad (11)$$

Substituting  $u_h(x)$  into (1) and using collocation at the nodes  $\Theta_h^1$ , we obtain the finite dimensional problem

$$\begin{aligned} L \left( \sum_{j=1}^{N+2N_b+1} a_j g_j(x_i) \right) &= \sum_{j=1}^{N+2N_b+1} a_j L g_j(x_i) = f(x_i), \quad i = 1, \dots, N + N_b, \\ B \left( \sum_{j=1}^{N+2N_b+1} a_j g_j(x_i) \right) &= \sum_{j=1}^{N+2N_b+1} a_j B g_j(x_i) = g(x_i), \quad i = N + 1, \dots, N + N_b, \\ \sum_{j=1}^{N+2N_b} a_j &= 0. \end{aligned} \quad (12)$$

Introducing the notation:  $a = (a_1, \dots, a_{N+2N_b+1})^\top$ ,  $b = (f(x_1), \dots, f(x_{N+N_b}), g(x_{N+N_b+1}), \dots, g(x_{N+2N_b}), 0)^\top \in \mathbb{R}^{N+2N_b+1}$ ,

$$\begin{aligned} L_g &= \begin{bmatrix} Lg_1(x_1) & \dots & Lg_{N+2N_b+1}(x_1) \\ \vdots & \ddots & \vdots \\ Lg_1(x_{N+N_b}) & \dots & Lg_{N+2N_b+1}(x_{N+N_b}) \end{bmatrix}, \\ B_g &= \begin{bmatrix} Bg_1(x_{N+1}) & \dots & Bg_{N+2N_b}(x_{N+1}) & Bg_{N+2N_b+1}(x_{N+1}) \\ \vdots & \ddots & \vdots & \vdots \\ Bg_1(x_{N+N_b}) & \dots & Bg_{N+2N_b}(x_{N+N_b}) & Bg_{N+2N_b+1}(x_{N+N_b}) \\ 1 & \dots & 1 & 0 \end{bmatrix}, \quad W = \begin{bmatrix} L_g \\ B_g \end{bmatrix}, \end{aligned} \quad (13)$$

we can rewrite the system (12) in the matrix form as

$$Wa = b. \quad (14)$$

### 3 Continuation for nonlinear elliptic PDEs.

Consider a boundary value problem for a second order system of  $n$  parametrized nonlinear elliptic PDEs:

$$\begin{aligned} F(u(x), \lambda) &\equiv D(\alpha)\Delta u - f(\nabla u, u, x, \lambda) = 0, \quad \text{in } \Omega \subset \mathbb{R}^d, \lambda \in \mathbb{R}, u(\cdot) \in \mathbb{R}^n, \\ Bu(x)|_{\partial\Omega} &= 0, \end{aligned} \quad (15)$$

where  $\Omega$  is a bounded domain,  $D(\lambda)$  is a positive diagonal  $n \times n$  matrix,  $f$  is smooth, and  $B$  is a boundary operator which we assume, for simplicity, to be linear. For the bifurcation analysis in the process of continuation we also need to consider the eigenvalue problem for the linearization  $D_1 F(u, \lambda)$  of  $F$  about the solution  $u$  of (15)

$$\begin{aligned} D_1 F(u, \lambda)v(x) &= \mu v(x), \quad \text{in } \Omega, \\ Bv(x)|_{\partial\Omega} &= 0. \end{aligned} \quad (16)$$

### 3.1 The Kansa-MQ method.

To formulate the approximate problem, we first introduce the set  $\Theta_h$  of nodes

$$\Theta_h = \left\{ \{x_i\}_{i=1}^N \subset \Omega, \quad \{x_i\}_{i=N+1}^{N+N_b} \subset \partial\Omega \right\} \quad (17)$$

and the MQ basis functions,

$$g_j(x) \equiv g_j(c_j, x) = \sqrt{\|x - x_j\|_{\mathbb{R}^d}^2 + c_j^2}, \quad j = 1, \dots, N + N_b, \quad g_{N+N_b+1}(x) = 1, \quad (18)$$

We next define an MQ finite dimensional subspace

$$S_h := \left\{ \chi = \sum_{j=1}^{N+N_b+1} a_j g_j(\cdot) : \sum_{j=1}^{N+N_b} a_j = 0, \quad B\chi(x_i) = 0, \quad i = N+1, \dots, N+N_b \right\}. \quad (19)$$

The problems (15) and (16), respectively, are approximated by the collocation equations

$$F(u_h(x_i), \lambda) = 0, \quad u_h \in S_h, \quad i = 1, \dots, N, \quad (20)$$

$$Lv_h(x_i) \equiv D_1 F(u_h, \lambda) v_h(x_i) = \mu v_h(x_i), \quad v_h \in S_h, \quad i = 1, \dots, N. \quad (21)$$

Substituting

$$u_h(x) = \sum_{j=1}^{N+N_b+1} a_j g_j(x), \quad (22)$$

$$v_h(x) = \sum_{j=1}^{N+N_b+1} b_j g_j(x), \quad (23)$$

into (20) and (21), respectively, and using the definition (19) of  $S_h$ , we obtain the following finite dimensional problems:

$$\begin{aligned} (G(a, \lambda))_i &\equiv F\left(\sum_{j=1}^{N+N_b+1} a_j g_j(x_i), \lambda\right) = 0, \quad i = 1, \dots, N, \\ B\left(\sum_{j=1}^{N+N_b+1} a_j g_j(x_i)\right) &= 0, \quad i = N+1, \dots, N+N_b, \\ \sum_{j=1}^{N+N_b} a_j &= 0, \end{aligned} \quad (24)$$

$$\begin{aligned} L\left(\sum_{j=1}^{N+N_b+1} b_j g_j(x_i)\right) &= \mu \sum_{j=1}^{N+N_b+1} b_j g_j(x_i), \quad i = 1, \dots, N, \\ B\left(\sum_{j=1}^{N+N_b+1} b_j g_j(x_i)\right) &= 0, \quad i = N+1, \dots, N+N_b, \\ \sum_{j=1}^{N+N_b} b_j &= 0. \end{aligned} \quad (25)$$

Introducing the notation:  $a = (a_1, \dots, a_{N+N_b+1})^\top$ ,  $b = (b_1, \dots, b_{N+N_b+1})^\top \in \mathbb{R}^{n \times (N+N_b+1)}$ ,

$$B_g = \begin{bmatrix} Bg_1(x_{N+1}) & \dots & Bg_{N+N_b}(x_{N+1}) & Bg_{N+N_b+1}(x_{N+1}) \\ \vdots & \vdots & \vdots & \vdots \\ Bg_1(x_{N+N_b}) & \dots & Bg_{N+N_b}(x_{N+N_b}) & Bg_{N+N_b+1}(x_{N+N_b}) \\ 1 & \dots & 1 & 0 \end{bmatrix}, \quad (26)$$

$$L_g = \begin{bmatrix} Lg_1(x_1) & \dots & Lg_{N+N_b+1}(x_1) \\ \vdots & \vdots & \vdots \\ Lg_1(x_N) & \dots & Lg_{N+N_b+1}(x_N) \end{bmatrix}, \quad \Gamma = \begin{bmatrix} g_1(x_1) & \dots & g_{N+N_b+1}(x_1) \\ \vdots & \vdots & \vdots \\ g_1(x_N) & \dots & g_{N+N_b+1}(x_N) \end{bmatrix},$$

we can rewrite the problems (24) and (25) in the matrix form as

$$\begin{aligned} G(a, \lambda) &= 0, \\ B_g a &= 0, \end{aligned} \quad (27)$$

$$\begin{aligned} L_g b &= \mu \Gamma b, \\ B_g b &= 0. \end{aligned} \quad (28)$$

**Implementation 1.** Let

$$a^1 = (a_1, \dots, a_N)^T \in \mathbb{R}^{n \times N}, \quad a^2 = (a_{N+1}, \dots, a_{N+N_b+1})^T \in \mathbb{R}^{n \times (N_b+1)};$$

$$L_g^1 = \begin{bmatrix} Lg_1(x_1) & \dots & Lg_N(x_1) \\ \vdots & \vdots & \vdots \\ Lg_1(x_N) & \dots & Lg_N(x_N) \end{bmatrix}, \quad L_g^2 = \begin{bmatrix} Lg_{N+1}(x_1) & \dots & Lg_{N+N_b+1}(x_1) \\ \vdots & \vdots & \vdots \\ Lg_{N+1}(x_N) & \dots & Lg_{N+N_b+1}(x_N) \end{bmatrix},$$

$$\Gamma^1 = \begin{bmatrix} g_1(x_1) & \dots & g_N(x_1) \\ \vdots & \vdots & \vdots \\ g_1(x_N) & \dots & g_N(x_N) \end{bmatrix}, \quad \Gamma^2 = \begin{bmatrix} g_{N+1}(x_1) & \dots & g_{N+N_b+1}(x_1) \\ \vdots & \vdots & \vdots \\ g_{N+1}(x_N) & \dots & g_{N+N_b+1}(x_N) \end{bmatrix}$$

$$B_g^1 = \begin{bmatrix} Bg_1(x_{N+1}) & \dots & Bg_N(x_{N+1}) \\ \vdots & \vdots & \vdots \\ Bg_1(x_{N+N_b}) & \dots & Bg_N(x_{N+N_b}) \\ 1 & \dots & 1 \end{bmatrix},$$

$$B_g^2 = \begin{bmatrix} Bg_{N+1}(x_{N+1}) & \dots & Bg_{N+N_b}(x_{N+1}) & Bg_{N+N_b+1}(x_{N+1}) \\ \vdots & \vdots & \vdots & \vdots \\ Bg_{N+1}(x_{N+N_b}) & \dots & Bg_{N+N_b}(x_{N+N_b}) & Bg_{N+N_b+1}(x_{N+N_b}) \\ 1 & \dots & 1 & 0 \end{bmatrix}.$$

Substituting this into (27), we rewrite it as:

$$\mathcal{G}(a^1, \lambda) \equiv G(a^1, a^2, \lambda) = 0, \quad (29)$$

where  $a^2$  solves

$$B_g^2 a^2 = -B_g^1 a^1. \quad (30)$$

Similarly, we rewrite (28) as

$$\begin{aligned} L_g^1 b^1 + L_g^2 b^2 &= \mu (\Gamma^1 b^1 + \Gamma^2 b^2), \\ B_g^1 b^1 + B_g^2 b^2 &= 0. \end{aligned}$$

or, eliminating  $b^2$ , as

$$L_g^1 b^1 - L_g^2 (B_g^2)^{-1} B_g^1 b^1 = \mu (\Gamma^1 b^1 + \Gamma^2 (B_g^2)^{-1} B_g^1 b^1). \quad (31)$$

We are interested in continuation of solutions to (29). Therefore, in addition to  $a^1$ , we also treat  $\lambda$  as unknown, and add an algebraic constraint

$$G_c(a^1, \lambda) = 0, \quad (32)$$

which defines a parametrization of the solution curve.

**Algorithm 1** (Continuation algorithm for the system (29), (32)). Given current approximations to  $a^1 \in \mathbb{R}^{n \times N}$  and  $\lambda \in \mathbb{R}$ , a complete Newton iteration consists of the following steps:

- (0) Compute the matrices  $B_g^1$ ,  $B_g^2$ ,  $\Gamma^1$ ,  $\Gamma^2$ .
- (1) Solve the system (30) to find  $a^2$ .
- (2) Use the expressions (29), (32) to compute the residuals  $-\mathcal{G}(a^1, \lambda)$ ,  $-G_c(a^1, \lambda)$  and then compute the matrices  $D_1 \mathcal{G}$ ,  $D_2 \mathcal{G}$ ,  $D_1 G_c$ , and  $D_2 G_c$  by differencing.
- (3) Solve the system

$$\begin{aligned} D_1 \mathcal{G} \delta a^1 + \delta \lambda D_2 \mathcal{G} &= -\mathcal{G}(a^1, \lambda), \\ D_1 G_c \delta a^1 + \delta \lambda D_2 G_c &= -G_c(a^1, \lambda), \end{aligned} \quad (33)$$

where we omitted iteration indices for  $\delta a^1$  and  $\delta \lambda$  in (33).

- (4) Update  $a^1 \rightarrow a^1 + \delta a^1$  and  $\lambda \rightarrow \lambda + \delta \lambda$ .
- (5) Solve the generalized eigenvalue problem

$$D_1 \mathcal{G} b^1 = \mu (\Gamma^1 + \Gamma^2 (B_g^2)^{-1} B_g^1) b^1 \quad (34)$$

(to detect bifurcations). Note that  $D_1 \mathcal{G} b^1 = L_g^1 b^1 - L_g^2 (B_g^2)^{-1} B_g^1 b^1$ , see (31).

**Implementation 2.** Let  $U = (U_1, \dots, U_N)^T$  be the vector of nodal values of the solution  $u_h$  (22) of the collocation problem (20), and let  $\{\phi_i\}_{i=1}^N$  be the Lagrange basis in  $S_h$ :

$$\{\phi_j \in S_h : \phi_j(x_i) = \delta_{ij}, i, j = 1, \dots, N\}. \quad (35)$$

Then  $u_h$  can be written as

$$u_h(x) = \sum_{j=1}^N U_j \phi_j(x), \quad (36)$$

Combining this with the definitions (22) of  $u_h$  and (26) of  $B_g$  and  $\Gamma$ , we have

$$\begin{aligned} \Gamma a &= U, \\ B_g a &= 0, \end{aligned} \quad (37)$$

which defines the 1 – 1 correspondence between  $U \in \mathbb{R}^{n \times N}$  and  $a \in \mathbb{R}^{n \times (N+N_b+1)}$ .

The problems (20) and (21), respectively, are written as

$$\mathcal{G}(U, \lambda) \equiv G(a, \lambda) = 0, \quad (38)$$

where  $a$  solves (37), and

$$D_1 \mathcal{G}(U, \lambda) V = \mu V, \quad V \in \mathbb{R}^{n \times N}. \quad (39)$$

As before, to define a parametrization of the solution curve, we add an algebraic constraint

$$G_c(U, \lambda) = 0. \quad (40)$$

**Algorithm 2** (Continuation algorithm for the system (38), (40)). Given current approximations to  $U \in \mathbb{R}^{n \times N}$  and  $\lambda \in \mathbb{R}$ , a complete Newton iteration consists of the following steps:

- (0) Compute the matrices  $B_g, \Gamma$ .
- (1) Solve the system (37) to find  $a$ .
- (2) Use the expressions (38), (40) to compute the residuals  $-\mathcal{G}(U, \lambda)$ ,  $-\mathcal{G}_c(U, \lambda)$  and then compute the matrices  $D_1 \mathcal{G} \equiv D_1 \mathcal{G}(U, \lambda)$ ,  $D_2 \mathcal{G} \equiv D_2 \mathcal{G}(U, \lambda)$ ,  $D_1 \mathcal{G}_c \equiv D_1 \mathcal{G}_c(U, \lambda)$ , and  $D_2 \mathcal{G}_c \equiv D_2 \mathcal{G}_c(U, \lambda)$  by differencing.
- (3) Solve the system

$$\begin{aligned} D_1 \mathcal{G} \delta U + \delta \lambda D_2 \mathcal{G} &= -\mathcal{G}(U, \lambda), \\ D_1 \mathcal{G}_c \delta U + \delta \lambda D_2 \mathcal{G}_c &= -\mathcal{G}_c(U, \lambda), \end{aligned} \quad (41)$$

where we omitted iteration indices in (41) for  $\delta U$  and  $\delta \lambda$ .

- (4) Update  $U \rightarrow U + \delta U$  and  $\lambda \rightarrow \lambda + \delta \lambda$ .
- (5) Solve the eigenvalue problem (39) (to detect bifurcations).

**Remark 1** For our numerical experiments, we implemented in AUTO [5] Algorithm 2 for the Kansa-MQ method and Algorithm 2a, below, for the MQ PDECB method. The principle reason for choosing Algorithm 2 rather than Algorithm 1 is that the eigenvalue problem (39) (and (56)) is a standard eigenvalue problem whose solution is supported by AUTO. On the other hand, the eigenvalue problem (34) is a complicated generalized eigenvalue problem whose solution is not supported by AUTO.

### 3.2 The MQ PDECB method.

To formulate the approximate problem, we first introduce the set  $\Theta_h$  of nodes

$$\Theta_h^1 = \left\{ \{x_i\}_{i=1}^N \subset \Omega, \quad \{x_i\}_{i=N+1}^{N+N_b} \subset \partial\Omega, \quad \{x_i\}_{i=N+N_b+1}^{N+2N_b} \subset \mathbb{R}^d \setminus \partial\Omega \right\}, \quad (42)$$

where the nodes  $\{x_i\}_{i=N+N_b+1}^{N+2N_b}$ , which can be inside  $\Omega$  or outside  $\bar{\Omega}$ , are adjacent to the boundary  $\partial\Omega$ , and the MQ basis functions,

$$g_j(x) \equiv g_j(c_j, x) = \sqrt{\|x - x_j\|_{\mathbb{R}^d}^2 + c_j^2}, \quad j = 1, \dots, N + N_b, \quad g_{N+2N_b+1}(x) = 1. \quad (43)$$

We next define an MQ finite dimensional set (which is not a subspace, in general)

$$S_h^1 := \left\{ \chi = \sum_{j=1}^{N+2N_b+1} a_j g_j(\cdot) : \sum_{j=1}^{N+2N_b} a_j = 0, \quad B\chi(x_i) = 0, \quad F(\chi(x_i), \lambda) = 0, \quad i = N+1, \dots, N+N_b \right\}. \quad (44)$$



The problems (15) and (16), respectively, are approximated by the collocation equations

$$F(u_h(x_i), \lambda) = 0, \quad u_h \in S_h^1, \quad i = 1, \dots, N, \quad (45)$$

$$Lv_h(x_i) \equiv D_1 F(u_h, \lambda)v_h(x_i) = \mu v_h(x_i), \quad v_h \in S_h^1, \quad i = 1, \dots, N. \quad (46)$$

Substituting

$$u_h(x) = \sum_{j=1}^{N+2N_b+1} a_j g_j(x), \quad (47)$$

$$v_h(x) = \sum_{j=1}^{N+2N_b+1} b_j g_j(x), \quad (48)$$

into (45) and (46), respectively, and using the definition (44) of  $S_h^1$ , we obtain the following finite dimensional problems:

$$\begin{aligned} (G(a, \lambda))_i &\equiv F\left(\sum_{j=1}^{N+2N_b+1} a_j g_j(x_i), \lambda\right) = 0, \quad i = 1, \dots, N, \\ (G(a, \lambda))_i &\equiv F\left(\sum_{j=1}^{N+2N_b+1} a_j g_j(x_i), \lambda\right) = 0, \quad i = N+1, \dots, N+N_b, \\ B\left(\sum_{j=1}^{N+2N_b+1} a_j g_j(x_i)\right) &= 0, \quad i = N+1, \dots, N+N_b, \\ \sum_{j=1}^{N+2N_b} a_j &= 0, \end{aligned} \quad (49)$$

$$\begin{aligned} L\left(\sum_{j=1}^{N+2N_b+1} b_j g_j(x_i)\right) &= \mu \sum_{j=1}^{N+2N_b+1} b_j g_j(x_i), \quad i = 1, \dots, N+N_b, \\ B\left(\sum_{j=1}^{N+2N_b+1} b_j g_j(x_i)\right) &= 0, \quad i = N+1, \dots, N+N_b, \\ \sum_{j=1}^{N+2N_b} b_j &= 0. \end{aligned} \quad (50)$$

Introducing the notation:  $a = (a_1, \dots, a_{N+2N_b+1})^T$ ,  $b = (b_1, \dots, b_{N+2N_b+1})^T \in \mathbb{R}^{n \times (N+2N_b+1)}$ ,

$$\begin{aligned} B_g &= \begin{bmatrix} Bg_1(x_{N+1}) & \dots & Bg_{N+2N_b}(x_{N+1}) & Bg_{N+2N_b+1}(x_{N+1}) \\ \vdots & \vdots & \vdots & \vdots \\ Bg_1(x_{N+N_b}) & \dots & Bg_{N+2N_b}(x_{N+N_b}) & Bg_{N+2N_b+1}(x_{N+N_b}) \\ 1 & \dots & 1 & 0 \end{bmatrix}, \\ L_g &= \begin{bmatrix} Lg_1(x_1) & \dots & Lg_{N+2N_b+1}(x_1) \\ \vdots & \vdots & \vdots \\ Lg_1(x_{N+N_b}) & \dots & Lg_{N+2N_b+1}(x_{N+N_b}) \end{bmatrix}, \quad \Gamma = \begin{bmatrix} g_1(x_1) & \dots & g_{N+2N_b+1}(x_1) \\ \vdots & \vdots & \vdots \\ g_1(x_{N+N_b}) & \dots & g_{N+2N_b+1}(x_{N+N_b}) \end{bmatrix}, \end{aligned} \quad (51)$$

we can rewrite the problems (49) and (50) in the matrix form as

$$\begin{aligned} (G(a, \lambda))_i &= 0, \quad i = 1, \dots, N, \\ (G(a, \lambda))_i &= 0, \quad i = N+1, \dots, N+N_b, \\ B_g a &= 0, \end{aligned} \quad (52)$$

$$\begin{aligned} L_g b &= \mu \Gamma b, \\ B_g b &= 0. \end{aligned} \quad (53)$$

**Implementation 2a.** Let  $U = (u_h(x_1), \dots, u_h(x_N))^T$  be the vector of nodal values of the approximate solution  $u_h$ . Then by the definitions (47) of  $u_h$  and (51) of  $B_g$  and  $\Gamma$ , we have

$$\begin{aligned} (G(a, \lambda))_i &= 0, \quad i = N+1, \dots, N+N_b, \\ \Gamma a &= U, \\ B_g a &= 0, \end{aligned} \tag{54}$$

which defines the 1 – 1 correspondence between  $U \in \mathbb{R}^{n \times N}$  and  $a \in \mathbb{R}^{n \times (N+2N_b+1)}$ .

The problems (45) and (46), respectively, are written as

$$(\mathcal{G}(U, \lambda))_i \equiv (G(a, \lambda))_i = 0, \quad i = 1, \dots, N, \tag{55}$$

where  $a$  solves (54), and

$$D_1 \mathcal{G}(U, \lambda) V = \mu V, \quad V \in \mathbb{R}^{n \times N}. \tag{56}$$

As before, to define a parametrization of the solution curve, we add an algebraic constraint

$$G_c(U, \lambda) = 0. \tag{57}$$

**Algorithm 2a** (Continuation algorithm for the system (55), (57)). Given current approximations to  $U \in \mathbb{R}^{n \times N}$  and  $\lambda \in \mathbb{R}$ , a complete Newton iteration consists of the following steps:

- (0) Compute the matrices  $B_g, \Gamma$ .
- (1) Solve the system (54) to find  $a$ .
- (2) Use the expressions (55), (57) to compute the residuals  $-\mathcal{G}(U, \lambda)$ ,  $-\mathcal{G}_c(U, \lambda)$  and then compute the matrices  $D_1 \mathcal{G} \equiv D_1 \mathcal{G}(U, \lambda)$ ,  $D_2 \mathcal{G} \equiv D_2 \mathcal{G}(U, \lambda)$ ,  $D_1 \mathcal{G}_c \equiv D_1 \mathcal{G}_c(U, \lambda)$ , and  $D_2 \mathcal{G}_c \equiv D_2 \mathcal{G}_c(U, \lambda)$  by differencing.
- (3) Solve the system

$$\begin{aligned} D_1 \mathcal{G} \delta U + \delta \lambda D_2 \mathcal{G} &= -\mathcal{G}(U, \lambda), \\ D_1 \mathcal{G}_c \delta U + \delta \lambda D_2 \mathcal{G}_c &= -\mathcal{G}_c(U, \lambda), \end{aligned} \tag{58}$$

where we omitted iteration indices in (58) for  $\delta U$  and  $\delta \lambda$ .

- (4) Update  $U \rightarrow U + \delta U$  and  $\lambda \rightarrow \lambda + \delta \lambda$ .
- (5) Solve the eigenvalue problem (56) (to detect bifurcations).

## 4 Numerical experiments for 1D and 2D elliptic PDEs.

We present examples of solution of linear 1D and 2D elliptic PDEs and continuation of solutions to nonlinear 1D and 2D Gelfand-Bratu equation. Each problem is discretized by the Kansa-MQ method, see Eq. (38), and the MQ PDECB method, see Eq. (55).

In the case of nonlinear problems, we perform continuation of solutions by Algorithm 2 for the Kansa-MQ method and by Algorithm 2a for the MQ PDECB method. We compare the accuracy of the detection of the limit point (or fold) by the two methods. We recall that a solution  $(u_0, \lambda_0)$  of equation  $f(u, \lambda) = 0$  is a (simple) limit point if the solution curve in  $(u(s), \lambda(s))$ , for some parametrization  $s$ , makes a turn at  $(u_0, \lambda_0)$ . This is expressed formally as  $\dim \mathcal{N}(f_u(u_0, \lambda_0)) = 1$  and  $f_\lambda(u_0, \lambda_0) \notin \mathcal{R}(f_u(u_0, \lambda_0))$ .

We will use throughout the notation  $h$  for the average distance between the nodes. Then  $h = 1/(K-1)$  for a 1D problem on  $(0, 1)$  and for a 2D problem on  $(0, 1) \times (0, 1)$ , where  $K$  is the number of nodes along each axis.

To improve the accuracy, we employ 2 simple *adaptation strategies* for the shape parameters  $C = \{c_1, \dots, c_{N+N_b}\}$  for the Kansa-MQ method, see Eq. (18), and  $C^1 = \{c_1, \dots, c_{N+2N_b}\}$  for the MQ PDECB method, see Eq. (43); for the nodes  $\Theta_h$  for the Kansa-MQ method, see Eq. (17), and  $\Theta_h^1$  for the MQ PDECB

method, see Eq. (42). To be specific, assume that  $\Omega = (0, 1) \times (0, 1)$  and consider the case of the Kansa-MQ method. Let  $r(x, y, C, \Theta_h)$  be the residual. Our strategies are all based on the Nonlinear Least Squares Method which minimizes the  $L_2$  norm  $\varphi(C, \Theta_h) \equiv \|r\|_2$  of the residual. By the *quasi-uniform distribution of nodes* we will mean the distribution of nodes, where the nodes adjacent to the boundary  $\partial\Omega$  are placed at the distance  $\tilde{h} = \delta h_0$ ,  $0 < \delta \leq 1$ , from  $\partial\Omega$ . while the remaining nodes are distributed uniformly with the distance  $h_0$  between them.

**Strategy 1.** Uniform distribution of nodes  $\Theta_h$ ;  $c_1 = \dots = c_{N+N_b} = c$ ;  $\min_c \varphi(C, \Theta_h)$ ,

**Strategy 2.** Quasiuniform distribution of nodes  $\Theta_h$ ;  $c_1 = \dots = c_{N+N_b} = c$ ;  $\min_{c, \delta} \varphi(C, \Theta_h)$ .

In all examples below we use the adaptation strategy 2.

**Example 2** A 1D model linear problem

$$\begin{aligned} u_{xx} + (2\pi)^2 \sin(2\pi x) &= 0, \quad \text{in } \Omega = (0, 1), \\ u(0) = u(1) &= 0. \end{aligned} \quad (59)$$

The analytical solution is

$$u_{\text{exact}} = \sin(2\pi x).$$

Numerical results are presented in Fig. 2a.

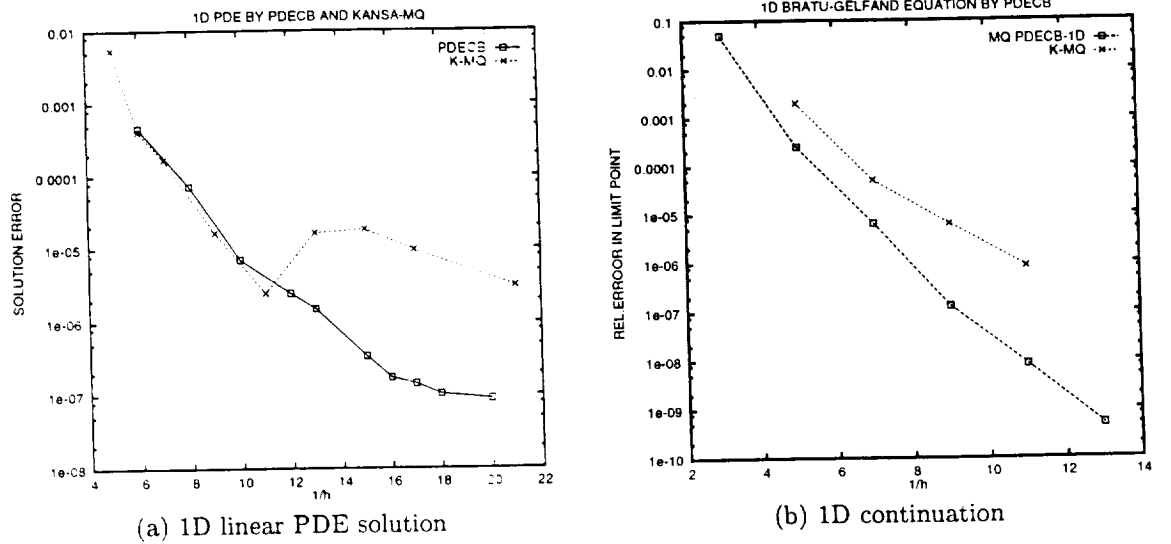
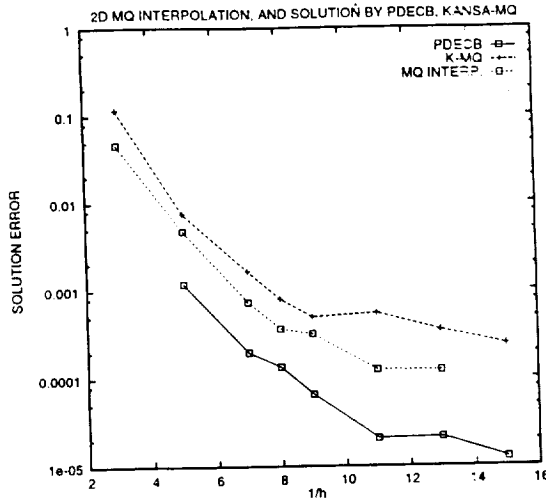


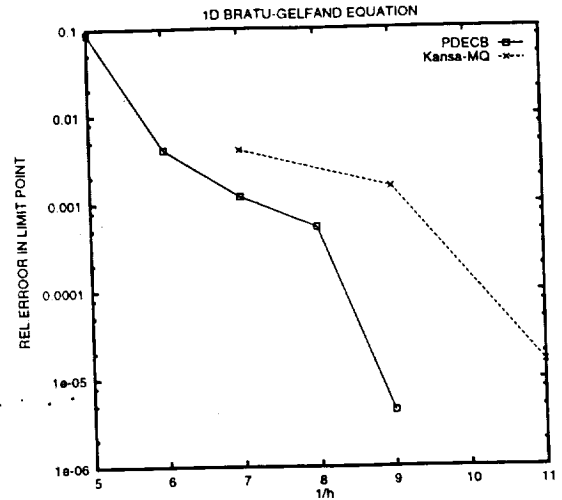
Figure 2: Convergence properties of the Kansa-MQ method and the MQ PDECB method:  
(a) 1D linear problem, Eq. (59); the  $L_\infty$  norm of the solution error is plotted, in the logarithmic scale, versus  $1/h$ , where  $h$  is the average distance between the nodes. The roundoff error starts to dominate at  $1/h \approx 11$  for Kansa-MQ method and at  $1/h \approx 18$  for the MQ PDECB method.  
(b) The location  $\lambda$  of the limit point for 1D Bratu-Gelfand problem, Eq. (61). Relative error in  $\lambda$  is plotted in the logarithmic scale versus  $1/h$ .

**Example 3** A 2D model linear problem

$$\begin{aligned} \Delta u - (2x^2y^2 + 2x^2y + 2xy^2 - 6xy)e^{(x+y)} &= 0 \quad \text{in } \Omega = (0, 1) \times (0, 1), \\ u|_{\partial\Omega} &= 0. \end{aligned} \quad (60)$$



(a) 2D linear PDE solution and interpolation



(b) 2D continuation

Figure 3: Convergence properties of the Kansa-MQ and the MQ PDECB methods:  
(a) 2D linear PDE, Eq. (60); the  $L_\infty$  norm of the solution error is plotted, in the logarithmic scale, versus  $1/h$ , where  $h$  is the average distance between the nodes. The roundoff error starts to dominate at  $1/h \sim 9$  for the Kansa-MQ method and at  $1/h \sim 11$  for the MQ PDECB method. We also provide, for comparison, the error in the MQ interpolation of the exact solution  $u_{exact}$ .  
(b) The location  $\lambda$  of the limit point for 2D Bratu-Gelfand problem, Eq. 62). Relative error in  $\lambda$  is plotted, in the logarithmic scale, versus  $1/h$ .

The analytical solution is

$$u_{exact} = x(x-1)y(y-1)e^{(x+y)}.$$

Numerical results are presented in Fig. 3a. We do not have an explanation of why the MQ PDECB solution is more accurate than the interpolation.

**Example 4** 1D Gelfand-Bratu problem. This is a scalar problem

$$\begin{aligned} u'' - \lambda e^u &= 0, \quad \text{in } \Omega = (0, 1), \\ u(0) &= u(1) = 0. \end{aligned} \quad (61)$$

that appears in combustion theory and is used as the demo example `exp` in AUTO97 [5] (fifth order adaptive orthogonal spline collocation method). There is a limit (fold) point on the solution curve. We take the value of  $\lambda$  at the limit point found from demo `exp` ( $K \geq 50$ ) as exact. The relative error in location of the limit point is shown in Fig. 2b. See also [11] for additional numerical results and references.

**Example 5** 2D Gelfand-Bratu problem

$$\begin{aligned} \Delta u + \lambda e^u &= 0, \quad \text{in } \Omega = (0, 1) \times (0, 1), \\ u|_{\partial\Omega} &= 0. \end{aligned} \quad (62)$$

This problem was studied by a number of authors. In [6] the problem was discretized with a high order orthogonal spline collocation method with sparse Jacobian. There is a limit (fold) point on the solution curve. The exact location of the limit point is assumed to be at the value of  $\lambda$  obtained in [6] on a  $16 \times 16$  mesh with  $4 \times 4$  collocation points. The relative error in location of the limit point is shown in Fig. 3b. Note that the curve for the Kansa-MQ method was obtained [11] using quadruple precision which considerably slowed down computations, while we use only double precision with the MQ PDECB method here. See also [11] for additional numerical results, references and a discussion of the operation count.

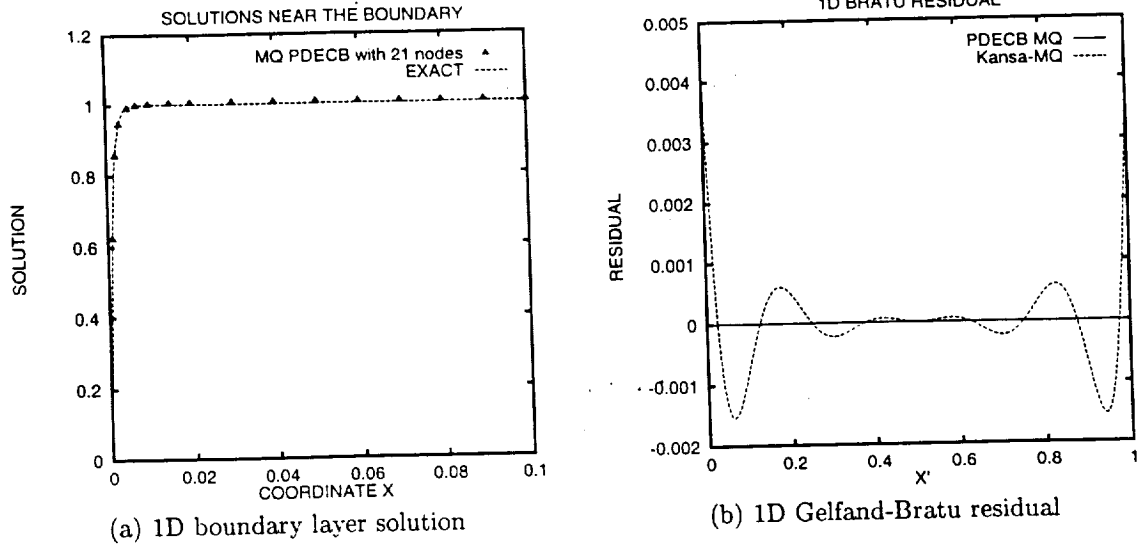


Figure 4: (a) 1D linear problem with a boundary layer, Eq. (63) with  $\epsilon = 10^{-3}$ . The MQ PDECB solution with 21 nodes and the analytical solution  $u_{exact}$  are plotted versus  $x$  in  $(0, 0.1)$ . (b) The residuals for the solutions of 1D Gelfand-Bratu problem (61) by the Kansa-MQ and the MQ PDECB methods are plotted versus  $x$  with  $1/h = 9$ ,  $\lambda = 2.5$ . The  $L_\infty$  residual norms are  $4.2 \times 10^{-3}$  and  $3.3 \times 10^{-6}$ , respectively.

**Example 6** A 1D model linear singular perturbation problem studied in [23]:

$$\begin{aligned} \epsilon u_{xx} + u_x &= 0, & \text{in } \Omega = (0, 1), \\ u(0) &= 0, \quad u(1) = 1. \end{aligned} \quad (63)$$

The analytical solution is

$$u_{exact} = (1 - e^{-x/\epsilon}) / (1 - e^{-1/\epsilon}).$$

It was demonstrated by Hon that this problem can not be solved by a standard Kansa-MQ approach for  $\epsilon \ll 1$ , and the adaptive technique proposed can be an efficient way to treat such problems [23].

Here we use the MQ PDECB to solve this problem for  $\epsilon \ll 1$  with relatively small number of nodes. For  $\epsilon = 10^{-3}$ , the MQ PDECB solution with 21 nodes and the exact solution are plotted versus  $x$  in Fig. 4a. The  $L_\infty$  norm of the solution error is 0.001 for the MQ PDECB method, while it is 0.22 for the Kansa-MQ method with 101 nodes (not shown). Note that for  $\epsilon = 10^{-4}$  one can attain the same error 0.001 in the MQ PDECB solution with 41 nodes (not shown).

**Example 7** Fig. 4b shows the residual distribution for the solutions of 1D Gelfand-Bratu problem (61) by the Kansa-MQ and the MQ PDECB methods with  $1/h = 9$ ,  $\lambda = 2.5$ . The  $L_\infty$  residual norms are  $4.2 \times 10^{-3}$  and  $3.3 \times 10^{-6}$ , and the  $L_2$  residual norms are  $7.8 \times 10^{-4}$  and  $1.1 \times 10^{-6}$  for the Kansa-MQ and the MQ PDECB methods, respectively.

## 5 Conclusions.

We have formulated an improved Kansa-MQ method with the PDE collocation on the boundary (MQ PDECB). The idea of the method is to add an additional set of nodes adjacent to the boundary and, correspondingly, an additional set of collocation equations obtained via collocation of the PDE on the boundary. We have applied the MQ PDECB method to several model 1D and 2D linear and nonlinear elliptic PDEs and have presented results of our numerical experiments. Numerical results demonstrate considerable improvement in convergence of the MQ PDECB method over the Kansa-MQ method, with both methods having exponential convergence with essentially the same rates.

## Acknowledgments

This work was supported in part by National Aeronautics and Space Administration through grant NAG8-1229. The first author is grateful to V.N. Belykh for fruitful discussions, that led us to the idea of the PDECB.

## References

- [1] K.I. Babenko, *Foundations of numerical analysis*, Moscow, Nauka, 1986, 743 pp. (in Russian).
- [2] V.N. Belykh, Algorithms without saturation in an axially symmetric boundary value problems, *Soviet Math. Dokl.*, **36**, no.1 (1988), 146-150.
- [3] V.N. Belykh, Overconverging unsaturated algorithms of numerical solving the Laplace equation // *Mathematics in Applications. Proc. of International Conference honoring academician Sergei K. Godunov*. Novosibirsk, 1999, (to be published).
- [4] G.B. Cook, M.W. Choptnik, M.R. Dubal, S.Klasky, R.A. Matzner, and S.R. Oliveira, Three dimensional initial value data for collisions of two black holes, in *Approaches to Numerical Relativity*, editor R. d'Inverno, Cambridge University Press (1993), 265-285.
- [5] E.J. Doedel, A.R. Champneys, T.F. Fairgrieve, Yu.A. Kuznetsov, B. Sandstede, and X.J. Wang, *AUTO97: Continuation and bifurcation software for ordinary differential equations (with HomCont)* (1997).
- [6] E.J. Doedel, H. Sharifi, Collocation Methods for Continuation Problems in Nonlinear Elliptic PDEs, Proc. ERCOFTAC and EUROMECH Colloquium, Continuation Methods in Fluid Mechanics, Aussois, France, September 1998, to appear in *Notes on Numer. Fluid. Mech.*
- [7] G.E. Fasshauer, Solving differential equations with radial basis functions: multilevel methods and smoothing, *Adv. Comp. Math.* **11**, No. 2/3 (1999), 139-159.
- [8] A. I. Fedoseyev, A regularization approach to solving boundary layer problems for Navier-Stokes equations, *CFD Journal*, **11**, No. 1 (2000), (*in print*).
- [9] A. I. Fedoseyev and J.I.D. Alexander, Investigation of Vibrational Control of Convective Flows in Bridgman Melt Growth Configurations, *J. of Crystal Growth*, 2000 (to appear).
- [10] A. I. Fedoseyev, B. V. Alexeev. Higher Order Continuum Model for Incompressible Viscous Fluid Flow. In: *Continuum Models and Discrete Systems*, Eds. E. Inan, A. Markov, World Scientific, London, 1998, 130-137.
- [11] A.I. Fedoseyev, M.J. Friedman, and E.J. Kansa, *Continuation for Nonlinear Elliptic Partial Differential Equations Discretized by the Multiquadric Method*, Preprint Math.NA/9812013 at E-PRINT, LANL (<http://xxx.lanl.gov/ps/math.NA/9812013>); to appear in *Int. J. Bifur. & Chaos* **10**, No. 2 (2000).
- [12] A.I. Fedoseyev, E.J. Kansa, C. Marin, and A.G. Ostrogorsky, Magnetic field suppression of semiconductor melt flow in crystal growth: comparison of three methods for numerical modeling, *CFD Journal*, **11**, No. 1 (2000), (*in print*).
- [13] R. Franke, Scattered data interpolation: tests of some methods, *Math.Comp.*, **38** (1982), 181-199.
- [14] C. Franke and R. Schaback, Solving partial differential equations by collocation using radial basis functions, *Appl. Math. Comp.*, **93**, No. 1 (1998), 73-91.
- [15] C. Franke and R. Schaback, Convergence order estimates of meshless collocation methods using radial basis functions (1998), preprint.
- [16] M.A. Golberg, and C.S. Chen, The theory of radial basis functions used in the dual reciprocity boundary element method, *Appl. Math. Comp.*, **60** (1994) 125-136.

- [17] M.A. Golberg and C.S. Chen, Improved multiquadric approximation for partial differential equations, *Engin. Anal with Bound. Elem.* **18** (1996), 9-17.
- [18] M.A. Golberg and C.S. Chen, *Discrete projection methods for integral equations*, Comput. Mech. Publ., Boston, MA (1997).
- [19] R.L. Hardy, Multiquadric equations of topography and other irregular surfaces, *J. Geophys. Res.*, **76** (1971), 1905-1915.
- [20] R.L. Hardy, Theory and applications of the multiquadric- biharmonic method: 20 years of discovery, *Comput. Math. Applic.*, **19**, No. 8/9 (1990), 163-208.
- [21] Y.C. Hon and X.Z. Mao, An efficient numerical scheme for Burgers equation, *Appl. Math. Comp.*, **95** (1998), 37-50.
- [22] Y.C. Hon, and R. Schaback, On ansymmetric collocation equations by Radial Basis Functions, preprint (1999).
- [23] Y.C. Hon, Multiquadric collocation method with adaptive technique for problems with boundary layer, *Int. J. Appl. Sci. Comput.*, **6**, No. 3 (1999).
- [24] E.J. Kansa, Multiquadrics-a scattered data approximation scheme with applications to computational fluid dynamics-I. Surface approximations and partial derivative estimates, *Comput. Math. Applic.*, **19**, No. 8/9 (1990), 127-145.
- [25] E.J. Kansa, Multiquadrics-a scattered data approximation scheme with applications to computational fluid dynamics-II. Solutions to hyperbolic, parabolic, and elliptic partial differential equations, *Comput. Math. Applic.*, **19**, No.8/9 (1990), 147-161.
- [26] E.J. Kansa, Y.C. Hon, Circumventing the ill-conditioning problem with Multiquadrics radial basis functions: Applications to elliptic partial differential equations, *Adv. Comp. Math.* (1998).
- [27] W.R. Madych, Miscellaneous error bounds for multiquadric and related interpolants, *Comput. Math. Applic.* **24**, No.12 (1992), 121-138.
- [28] W.R. Madych and S.A. Nelson, Multivariate interpolation and conditionally positive definite functions II. *Math. Comp.*, **54** (1990), 211-230.
- [29] M. Sharan, E.J. Kansa, and S. Gupta, Applications of the multiquadric method for the solution of elliptic partial differential equations, *Appl. Math. & Comput.*, **84** (1997), 275-302.
- [30] Wong, S.M., Y.C. Hon, T.S. Li, S.L. Chung, and E.J. Kansa, Multi-zone decomposition of time-dependent problems using the multiquadric scheme, to appear in *Math. Comp. Applic.* (1998).
- [31] Z. Wu and R. Shaback, Local error estimates for radial basis function interpolation of scattered data, *IMA J. Num. Anal.* **13** (1993), 13-27.

## A REGULARIZATION APPROACH TO SOLVING THE NAVIER-STOKES EQUATIONS FOR PROBLEMS WITH BOUNDARY LAYER

Alexandre I. Fedoseyev

Center for Microgravity and Materials Research,  
University of Alabama in Huntsville,  
Huntsville, Alabama 35899, USA  
E-mail: alex@cmmr.uah.edu  
<http://uahtitan.uah.edu/alex/>

### Abstract

We present an alternative method for treating numerically a problem of viscous flow with a boundary layer that is based upon regularization of the Navier-Stokes equations. Shishkin (1997) showed that grid methods perform poorly in dealing with the boundary layer. Traditional grid methods give poor agreement with the experimental data for high  $Re$  number flows. Shishkin showed that the remedy for these difficulties is the construction of special meshes in boundary layer. We present an alternative approach that is more efficient and less mesh dependent. Our approach is based upon the regularization of the Navier-Stokes equations, and we discuss the mathematical and physical aspects of this approach. Numerical results that we obtained by our regularization process in 2D and 3D are compared with the experimental measurements. We compared our model against: (1) The 3D driven cavity flow by Kosseff and Street (1982) at  $Re = 3200$  and  $10,000$ ; (2) a 2D backward facing step flow by Kim et al. (1980) at  $Re = 44,000$ ; and (3) a 3D thermal convection in a cylinder by Bogatirev et al. (1996) at  $Ra = 1000$  to  $100,000$ . This proposed regularization model is not a turbulence model, and no additional equations are introduced. Recipes for the choice of the regularization parameter are presented.

**Keywords:** Navier - Stokes equations, Boundary Layer, Regularization, Finite element method

### 1 Introduction

Driven cavity problem is widely used as a benchmark for comparison of numerical codes. The agreement between different codes is within 1% or better. Published 2D Navier-Stokes (NS) solutions can qualitatively de-

scribe the flow structure, the number and location of vortexes and their size, but show poor agreement with the experimentally measured velocity profiles by Kosseff and Street (1984) for  $Re = 3200$  and  $10^4$  (see [1] and references therein).

Results obtained by Ghia et al. [2] on a fine mesh ( $256 \times 256$ ) for Reynolds number up to  $Re = 10^4$  are only the stationary solutions. While the actual fluid flow is essentially transient and 3D, the measured mean velocities in the plane of symmetry ( $y = 1.5$ ) appear to be 2D. A disagreement of 2D numerical solution with experimental data is by a factor of 2 to 3 (Fig. 1, 2). A 3D NS solution still can not improve this discrepancy, and known 3D results differ significantly (see 1992 GAMM-workshop [3]). One may justify that the flow turbulence is a reason for a disagreement. We tested this and solved the problem using a standard  $k - \epsilon$  turbulence model that is available in most commercial CFD codes. Our results obtained with the CFD2000 code [4] are presented in Fig. 1, 2 as well. One can see that the agreement of the  $k - \epsilon$  model results with experiments is still very poor.

We observed a similar discrepancy with the experiment in the numerical modeling of weakly turbulent thermal convection in a vertical slot ( $H/L = 11.2$ ) heated from a side, the Rayleigh number was  $Ra_L = 3.75 \cdot 10^8$ , and  $Pr = 15$ . A direct numerical solution (using Boussinesq approximation) allowed us to describe basic features of the flow evolution and large vortex dynamics [5],[6].

Mean vertical temperature profile obtained agrees well with the experimental data [7], but mean velocity profiles differ significantly from those data. Local magnitudes of computed velocity were about twice higher than ones in the experiments [7]. The Reynolds number based on the computed velocity was of the order  $10^4$ . A use of more detailed time and space discretization did



not improve the results.

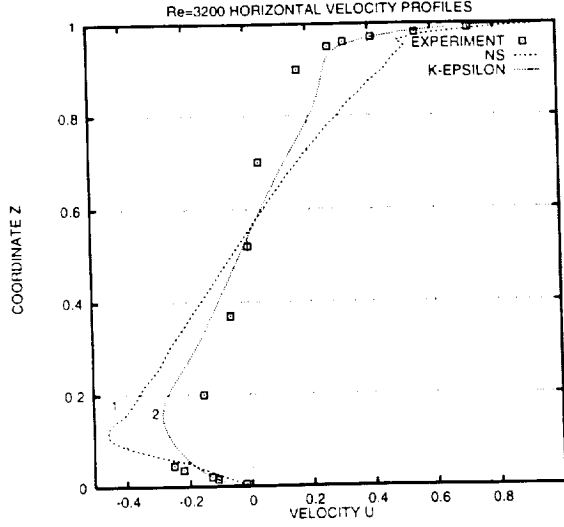


Figure 1: Driven cavity problem,  $Re = 3200$ : Comparison of horizontal velocity profiles at  $x = 0.5$  for numerical (lines) and experimental (squares) results : 1- Navier-Stokes solution, 2 -  $k - \epsilon$  model solution

Recently a poor ability of grid methods to deal with boundary layer has been proved theoretically by Shishkin [8]. The estimation for the solution error is given as  $O(1)$  for uniform meshes, if thin boundary layer is present. Shishkin pointed out that the remedy for these difficulties is the construction of a special meshes in the boundary layer (now called as Shishkin meshes). To construct a mesh, one needs to use the boundary layer thickness, that is not known in advance.

Shishkin's theory received confirmation for a driven cavity flow problem in [9]. It was shown that the computational results are extremely mesh sensitive for  $Re = 3200$  and higher. Still, with some special fine mesh resolution near the walls, proposed in this paper, it was possible to obtain a solution that agrees well with the experimental data [1].

In this paper, we present an alternative approach that is efficient and less mesh dependent. It is based on the regularization of the Navier-Stokes equations. Mathematical and physical aspects of this approach are discussed. Presented model is a major simplification of the higher order continuum model for incompressible viscous flow proposed in [10].

The governing equations are presented, a model is described and applied to a several viscous fluid flow and thermal convection problems. Comparison with the experimental data and results obtained by different meth-

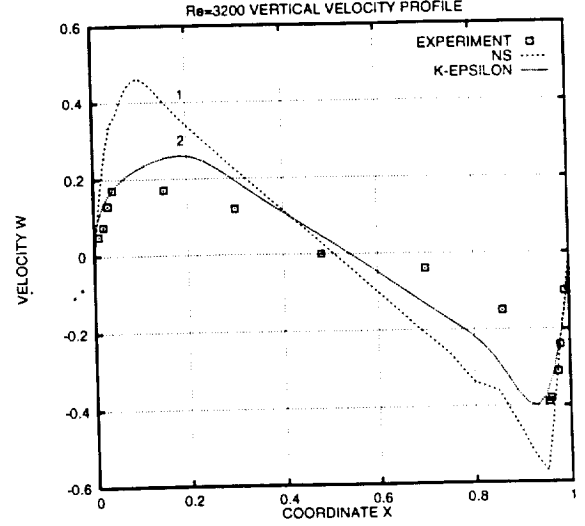


Figure 2: Driven cavity problem,  $Re = 3200$ : comparison of vertical velocity profiles at  $z = 0.5$  for numerical (lines) and experimental (squares) results : 1-Navier-Stokes solution, 2 -  $k - \epsilon$  model solution

ods are discussed as well.

## 2 Governing equations

We consider a flow of incompressible viscous fluid in a closed domain. The governing equations are the following. The momentum equation is

$$\frac{\partial \mathbf{V}}{\partial t} + (\mathbf{V} \cdot \nabla) \mathbf{V} - Re^{-1} \nabla^2 \mathbf{V} + \nabla p - \mathbf{F} = 0 \quad (1)$$

while continuity equation is

$$\nabla \cdot \mathbf{V} = 0 \quad (2)$$

where  $Re = V_0 L / \nu$  - the Reynolds number,  $V_0$  - velocity scale,  $L$  - hydrodynamic length scale,  $\nu$  - kinematic viscosity,  $\mathbf{F}$  is a body force. For a case of thermal convection the body force is  $\mathbf{F} = Gr Re^{-1} \cdot \Theta \cdot \mathbf{e}_g$  (Boussinesq approximation), where  $\Theta$  is a nondimensional temperature,  $Gr$  is the Grashoff number and  $\mathbf{e}_g$  is a unit vector in the direction of gravity. In the case of thermal convection the energy equation complete the formulation:

$$\frac{\partial \theta}{\partial t} + (\mathbf{V} \cdot \nabla) \theta = Pr^{-1} Re^{-1} \nabla^2 \theta \quad (3)$$

where  $\theta$  is a nondimensional temperature scaled by  $\theta = (T - T_{cold}) / \Delta T$ ,  $\Delta T = T_{hot} - T_{cold}$ . The Prandtl, Grashoff and Rayleigh numbers are respectively  $Pr =$

$\nu/k$ ,  $Gr = Ra/Pr$ , and  $Ra = \beta \Delta T g L^3 k^{-1} \nu^{-1}$ , where  $\beta$ ,  $g$ ,  $k$  are respectively the coefficient of thermal expansion, gravitational acceleration, and the thermodiffusivity.

Boundary and initial conditions accomplish the problem formulation and will be given for each of problem considered below.

### 3 Regularized Navier - Stokes equations

The regularization proposed consist in the modification of the continuity equation (2) that becomes as follows

$$\nabla \cdot \mathbf{V} = \tau^* \nabla \cdot (\nabla p - \mathbf{F}) \quad (4)$$

where  $\tau^*$  is a small regularization parameter. For  $\tau^* \rightarrow 0$  we approach the original equation (2). A boundary condition for the pressure on a wall is

$$(\nabla p - \mathbf{F}) \cdot \mathbf{n} = 0, \quad (5)$$

where  $\mathbf{n}$  is a unit wall normal vector. Equations (4) and (5) present the main feature of this method, and ensure a balance of the normal component of the momentum on the wall. We will show in the following sections that equations (1), (3), and (4) with (5), called here as regularized Navier-Stokes equations (RNS), are more suitable for use with the finite element method (FEM). The solution of the RNS by FEM can result in a better agreement with the experimental measurements for high Reynolds number flows. The RNS model showed also a good agreement with the analytical solutions for a very slow flows with thin boundary layer in the case of magnetic field suppression of the semiconductor melt flow in crystal growth [11].

For a justification of this regularization one can be referenced to the new hydrodynamic equations proposed in [12] that have the fluctuation terms of this kind. Equation (5), according to the theory in [12], means the absence of the hydrodynamic fluctuations on the wall.

Similar term, as in the right-hand side of eq. (4), has been obtained as a result of the "consistent treatment of time-advancement for the divergence-equation" by Löhner [13]. A discretization time step  $\Delta t$  was used in [13] instead of parameter  $\tau^*$  as in our RNS model.

A nondimensional regularization parameter  $\tau^*$  is expressed through dimensional scales as following,  $\tau^* = \tau L^{-1} \nu_0$ , where  $\tau$  is some time scale. Note, that the dimension of a product  $\tau \nu$  is a square of length. We introduce a regularization length scale  $l$ ,  $l^2 = \tau \nu$  and rewrite  $\tau^*$  as  $\tau^* = l^2 L^{-2} Re = K \cdot Re$ , where  $K = l^2/L^2$ .

The value of  $\tau$  (or  $l$ ) is not known in advance, and we provide recipes on a choice of these values at the discussion of the results.

Such a regularization has an additional useful feature for the FEM. It allows to use the same order finite element approximation for the velocity and pressure with all the unknowns located at the same nodal points.

### 4 Problems solved

We apply the RNS model for the solution of the following problems:

**1) Lid-driven cavity problem (2D and 3D).** We compare our results with experimental data obtained by Koseff and Street[1] for  $Re = 3200$  and  $10^4$ . We solve equations (1) and (4) numerically for the unknowns  $(\mathbf{V}, p)$  in the 2D region  $(x, z) = [0, 1][0, 1]$ . A 3D version of the problem corresponds to Koseff & Street experiment [1] with the domain  $(x, y, z) = [0, 1][0, 3][0, 1]$ . The boundary conditions are:  $\mathbf{V} = (u, v, w) = (1, 0, 0)$  at the driven lid ( $z = 1$ );  $\mathbf{V} = 0$  on the other walls, and eq. (5) holds on all the walls. The undefined constant in the pressure field is eliminated by setting  $p = 0$  at  $(x, y, z) = (0, 0, 0)$ .

**2) Backward facing step flow (2D).** We solve for a flow in a plane channel with sudden (step) expansion that corresponds to the experiment by Kim et al. [14]. The ratio of a step height  $H$  to the channel outlet width  $L$  is  $H/L = 1/3$ . The Reynolds number for the experimental flow is  $Re = 4.4 \cdot 10^4$  with  $H$  as a length scale [14], or  $Re_L = 1.32 \cdot 10^5$  in [15] when the channel outlet width  $L$  is used as a length scale. The flow profile  $\mathbf{V}(y)$  is given at the inlet and  $p = 0$  and stress free conditions at the outlet. We have used the following domain geometry:  $H = 1$ ,  $L = 3$ , total length  $L_T = 12$ , and the length from the inlet to the step  $L_s = 4$ .

**3) Thermal convection in a cylinder (3D).** Thermal convection flow in a differentially heated horizontal cylinder is considered. The experimental data by Bogatirev et al. [16] have been used for comparison. These data have been obtained during the ground tests for this device, a thermal convection sensor designed for the space micro-acceleration measurements; it was later flown in space on *Mir* station. Numerical results from the 3D finite volume simulations by Bessonov [17] have been also used for a comparison. The temperature distribution on a cylinder wall was (i) linear temperature profile, and (ii) computed using a real, finite wall conductivity (adjoint problem). The body force in (1) is  $\mathbf{F} = (0, 0, RaPr\theta)$ , and  $Re^{-1}$  in (1) is to be replaced by Prandtl number  $Pr = \nu/k$ . Experimental data are available for the Rayleigh number  $Ra$  in a range from  $10^3$  to

$10^5$  that present the temperature difference between two points inside a cylinder.

## 5 Finite element model and solution method

Proposed model allows efficient implementation by the finite element method. Both velocity and pressure are approximated by the same order finite element basis functions. We used linear basis functions on triangle finite elements in 2D and trilinear on hexahedral elements in 3D.

Note that when  $\tau^* = 0$ , we obtain the NS equations, and the FEM equations become incompatible. It is a well known problem, and can be resolved if a different order FE basis is used for the velocity and pressure approximation (see e.g. [18]). When  $\tau^*$  is in the range of  $10^{-7}$  to  $10^{-4}$ , our solution coincides with the NS one up to  $Re = 10^4$  in a case of driven cavity problem. The value of  $\tau^*$  smaller than  $10^{-8}$  results in the wiggles in the velocity profiles. At low  $Re$ ,  $Re < 1000$  the solution practically coincides with the NS one for any  $\tau^*$  between  $10^{-7}$  to  $10^{-2}$ .

A CFD code FEMINA/3D [18],[19] modified for a new model was used in the numerical experiments. Three scalar equations (or four in 3D case) from (1), (4) are solved simultaneously. The nonlinear algebraic system of equations, resulting from the FEM discretization, is solved iteratively by a Newton method. Corresponding linear system is solved by robust preconditioned iterative CGS-type method with preconditioning by the high order incomplete decomposition. We used a CNSPACK linear solver with a compact sparse matrix storage (see on details of the solver in [20],[22]). A first order decomposition was found to be quite enough for the RNS, while the second or third order is required for the NS related linear systems [20].

The solution is considered converged when an algebraic equations residual norm is  $\|r\|_\infty < 10^{-14}$  (typical initial residual value were 1 to  $10^2$ ). In the case of the thermal convection problem, the energy equation is solved separately at each time step or Newton iteration. Selected solution method and a corresponding software implementation make it possible to solve large time-dependent problems (up to 300,000 unknowns) on the SGI O2 workstation.

## 6 Results and discussion

Initially for each problem we varied the value of  $\tau$  or  $K$  and compared numerical results with the experimental

ones and with the NS. At low  $Re \leq 1000$  the solution practically coincides with the NS one for any  $\tau^*$  between  $10^{-7}$  to  $10^{-2}$  for problems 1 and 2. We solved the transient problem equations (1), (4), or (1), (4) and (3) and have been able to obtain stationary solutions. A more efficient approach in such a case was a solution of the stationary problem by the Newton technique. In those cases there is a good agreement between the NS and the experiment when it is available (for example,  $Re = 50$  to 500 in [21]).

Mass conservation in the continuity equation was thoroughly analyzed. The local values of  $divV$  of the numerical solution were examined. Note, that the numerical solution satisfies the discretized equation exactly only at specific points (nodes, integration points or collocation points etc. depending on the method used), and only approximately at an arbitrary point of the domain. As the mesh size decreases, the accuracy of the approximation of the equation improves (typically as  $h^2$ , the square of the mesh size).

The value of  $divV$  for the numerical solution at an arbitrary point is non-zero, and we found that it was of the same order both for the RNS and NS numerical solutions. The values of  $divV$  exhibited spatial oscillations with amplitudes of  $10^{-3}$  to  $10^{-2}$ . The averaged value of  $divV$  (integral over the region near the vicinity of any point) was the same order for RNS solutions as for the NS ones. The integral over the whole domain of  $divV$  is of the same order for both RNS and NS. Therefore, we see that in the numerical solution, a regularization term in the RNS continuity equation does not create more numerical mass fluxes, than in the case of NS.

For a comparison we also present the results obtained with a standard  $k - \epsilon$  turbulence model, using the commercial code CFD2000 [4]. A  $k - \epsilon$  turbulence model was developed for computations of turbulent flows, when the NS equations can not provide reasonable results. Viscous term in the NS momentum equation is replaced by a different stress term with a turbulent Reynolds number  $Re_t$ . Two more nonlinear equations are added to the system, that govern the turbulent kinetic energy  $k$ , dissipation rate  $\epsilon$  and provide evaluation of the  $Re_t$ . These equations contain eight empirical constants for a standard model (11 or more in improved models). The standard  $k - \epsilon$  turbulence model is implemented in many commercial CFD codes and widely used in the solution of engineering problems.

### 6.1 Driven cavity problem

We used  $81 \times 81$  nodes with a homogeneous triangular mesh for 2D computations. Same mesh with quadratic (6-noded) triangles and linear basis FE functions for

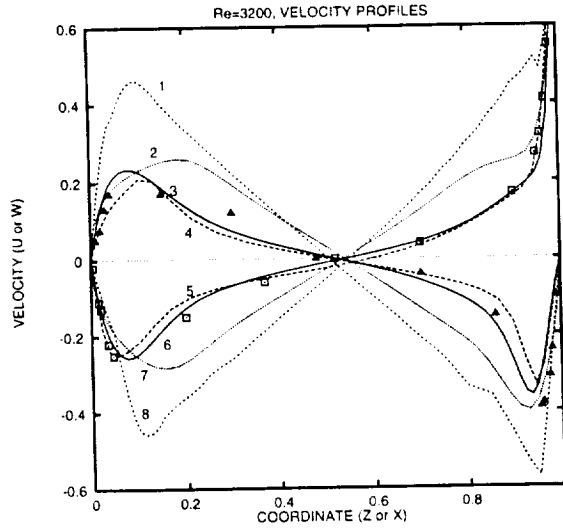


Figure 3: Driven cavity problem,  $Re = 3200$ . Comparison of horizontal velocity profiles (1-4) for numerical (solid and dashed lines) and experimental (squares) results and vertical velocity profiles (5-8) for numerical (solid and dashed lines) and experimental (triangles) results: 1-NS, 2- $k-\epsilon$  model, 3-RNS (2D), 4-RNS (3D); 5-RNS (3D), 6-RNS (2D), 7- $k-\epsilon$  model, 8-NS

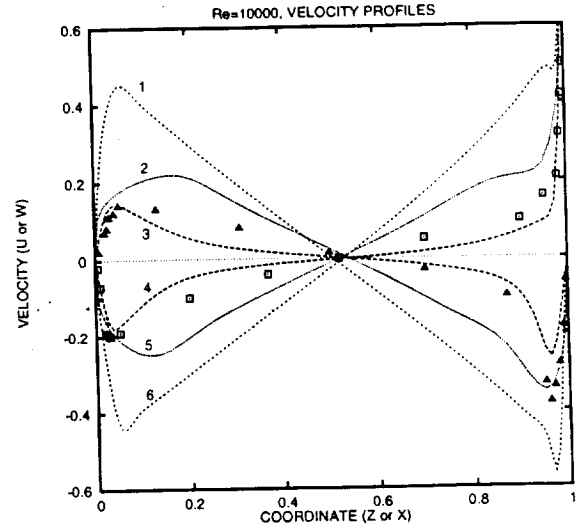


Figure 4: Driven cavity problem,  $Re = 10,000$ . Comparison of horizontal velocity profiles (1-3) for numerical (dashed lines) and experimental (squares) results and vertical velocity profiles (4-6) for numerical (dashed lines) and experimental (triangles) results: 1-NS, 2- $k-\epsilon$  model, 3-RNS (2D); 4-RNS (2D), 5- $k-\epsilon$  model, 6-NS

pressure and quadratic for velocity was used for the NS computations. We note at once that further mesh refinement did not influence the results for both flow regimes considered. For  $Re > 10^3$  the RNS and NS solutions become noticeably different for  $\tau^* > 10^{-2}$ . We varied the value of  $K$  to match the experimental velocity profiles at  $Re = 3200$  presented in [1]. Good agreement was obtained, when  $K \approx 1.5 \cdot 10^{-5}$ .

Using the same value of  $K$  as above, we computed the RNS solution at  $Re = 10^4$ , for that [1] also provides the data. The results are presented in Fig. 3. The error estimates for experimental points are 1 to 10%, according to [1]. Therefore, we can conclude, that the RNS solution is in better agreement with the experimental data than the NS solution. Indeed, at this value of  $Re$  there is significantly greater difference between the NS solution and the experimental results. The  $k-\epsilon$  model results also disagree with the experimental data.

Fig. 3 and 4 present the experimental measurements and numerical results for  $u$  and  $w$  velocity components obtained from the RNS (2D and 3D), 2D NS, and 2D  $k-\epsilon$  model. The experimental data are shown for the symmetry plane ( $x, z$ ) at  $y=1.5$  along the lines  $x=0.5$  and  $z=0.5$  of the 3D cavity, that has relative ( $x:y:z$ ) dimensions 1:3:1. Since strong instantaneous velocity fluctuations were observed, the experimental points cor-

respond to time averaged values of the measured velocities [1].

The results obtained with RNS model are in good agreement with the experimental data for  $Re=3200$  and 10,000 and are an improvement upon previous results obtained using the Navier-Stokes equation.

An important feature of our numerical experiments is the parameter  $K = l^2/L^2$ . We can estimate  $l$ , using the value of  $K$  found and the experiment description from [1]:  $L = 15\text{cm}$ , so  $l \sim 0.58\text{ mm}$ . This value of  $l$  is a good approximation of the "Kolmogorov microscale"  $l_{exp} \sim 0.5\text{mm}$  (the smallest scale of the flow nonhomogeneity, viscous dissipation scale) that was observed in the experiment ([1], p.398).

That is one of the ways to determine the actual value of  $\tau^*$  or  $K$  for the RNS model in advance, that is the experimental approach. We remind the reader that for low  $Re$  numbers the value of  $\tau^*$  is actually insignificant and can be chosen in a rather wide range. It is the case for the problem 3 (thermal convection).

For 3D flows we have solved the RNS for  $Re = 3200$  with the mesh of  $41 \times 41 \times 33$  nodes (221,892 unknowns), refined near the walls, for a half of the cavity. The symmetry condition was used on a symmetry plane. Our results of modeling are presented in Fig. 3 as well. One can see that velocities obtained for both 2D and 3D pro-

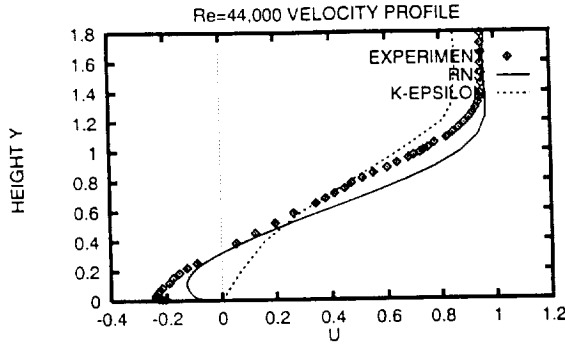


Figure 5: Backward facing step flow,  $Re = 44,000$ . Comparison of the horizontal velocity profiles at  $x = 5.33$  for the experimental [14], RNS and  $k - \epsilon$  model results.

files are close to the experimental data except in one region. For the  $Re = 10^4$  we did not see any 3D numerical results published for this case. The numerical solution for our model does not exhibit strong oscillations as a measured experimental velocities for both flow regimes considered. In the case of  $Re = 3200$  we are even able to obtain a stationary solution by the Newton technique.

## 6.2 Backward facing step flow

The numerical results for a 2D backward facing step flow at  $Re = 4.4 \cdot 10^4$  (referenced as  $Re = 1.32 \cdot 10^5$  in [15]) were obtained and compared with experimental measurements [14]. We used a  $110 \times 60$  mesh refined near the walls and did computations starting at low Reynolds number and increasing  $Re$  by small increments until 44,000. Fig. 5 presents the computed velocity profile at  $x = 5.33$  ( $x = 0$  at the begin of the step), the experimental mean velocity measurements [14] and the  $k - \epsilon$  model results.

The RNS model results agree with experiment for both the velocity profile and the recirculation zone length  $X_r$ . Our result is  $X_r/H = 7.50$  and the experimentally obtained one is  $X_r^{exp}/H \approx 7 \pm 0.5$ . The value of  $\tau^*$  used in the computations was in a range from  $10^{-2}$  to  $10^{-5}$ . It did not influence noticeably the results. For a smaller  $\tau^*$  it was more difficult to reach the steady state solution at  $Re = 44,000$ ; we have to use more and smaller increments in  $Re$  number to reach the final value of  $Re$ . If the increment in  $Re$  number was large, the flow pattern bifurcated to the unsteady flow with the vortexes periodically originating from the recirculation zone and flowing downstream. Our conclusion is that the numerical RNS solution for this problem does not depend on

the value of  $\tau^*$ .

The solution with a standard  $k - \epsilon$  model gives the velocity profile at  $x = 5.33$  that has no backward flow at all [15]. A standard  $k - \epsilon$  model underpredicts the reattachment point (recirculation zone length  $X_r$ ) by a substantial amount of 20-25% according to paper [15], where different turbulence models have been analyzed for this problem.

## 6.3 Thermal convection in a differentially heated horizontal cylinder

The RNS model is applied to the solution of the problem of convective 3D flow in a differentially heated horizontal cylinder. Initially a linear temperature profile was assumed to be given on a cylinder wall. Experimental data by Bogatirev et al. [16] and finite volume simulations by Bessonov [17] are used for the comparison at Rayleigh number in the range  $10^3$  to  $1.2 \cdot 10^5$  (Fig. 6a). For the linear temperature distribution on a cylinder wall we obtained a good agreement with the numerical results by Bessonov [17], obtained by the 3D finite volume method for the NS equations. The agreement with the experimental data was not good for  $Ra$  number more than 2000 (solid line in Fig. 6b). The computations have been also done in [17] for a real, finite wall conductivity. A thermodiffusivity data for a stainless steel was used and adjoint problem was solved. The agreement with the experimental data has been significantly improved (dashed line in Fig. 6b).

The value of  $\tau^*$  used was  $10^{-7}$  to  $10^{-3}$ , and it did not change noticeably the RNS results.

Another successful application of the RNS model to a 3D thermal convection flows with vibrations applied is presented in [23]. The application to the problem of magnetic field suppression of the semiconductor melt flow in crystal growth is considered in [11], where a good agreement with the theoretical asymptotic solution is obtained.

## 7 Conclusions

A numerical model for incompressible viscous flow is proposed. It is based on the regularization of the Navier-Stokes equations. Good agreement with the experiment is obtained for a driven cavity flow at  $Re = 3200$  and  $10^4$ . The regularization parameter found to be related to the experimentally observed spatial fluctuation scale.

The RNS model solution approaches the NS one for small  $Re$  number. For high  $Re$  number the RNS solution is more close to the experimental data than the NS solution (driven cavity flow, backward facing step flow).

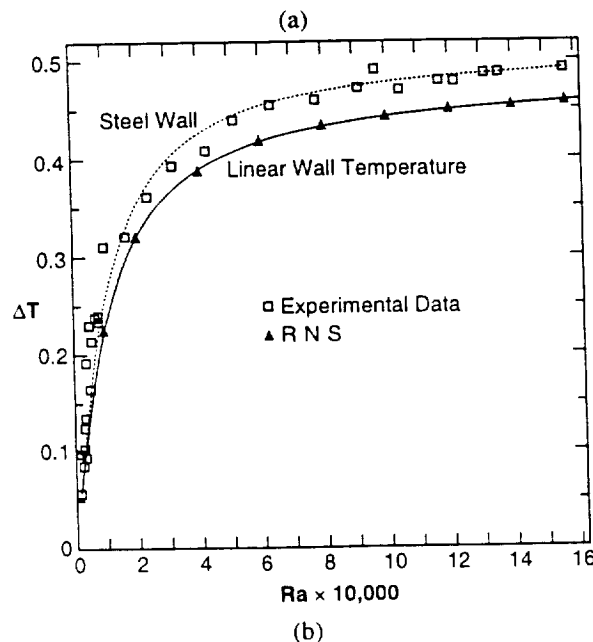
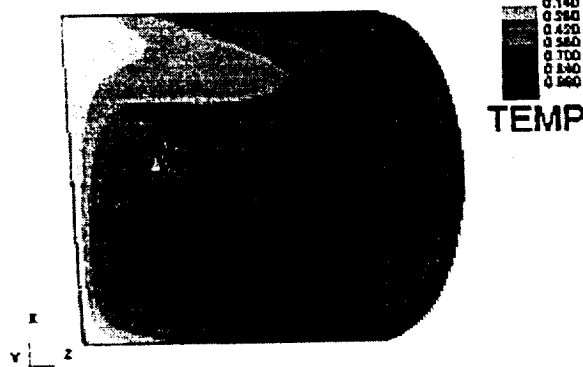


Figure 6: (a) Thermal convection in 3D differentially heated horizontal cylinder, temperature field in the central X-Z plane,  $Ra = 10^5$ ; (b) Comparison of temperature difference  $\Delta T$  versus  $Ra$  number with experiment [16] and finite-volume computations: squares - experimental data, solid line - numerical results for perfect wall conductivity with the NS [17], triangles - results with RNS; dashed line - real wall conductivity (steel) is used [17]; here  $\Delta T$  is a measured temperature difference between locations marked as "1" and "2" in (a).

Good agreement with the experimental data for a 3D thermal convection in a horizontal cylinder has been obtained at  $Ra = 10^3$  to  $10^5$ .

The optimal value of the regularization parameter  $\tau^*$  still remains an open problem. We have found that the numerical solution depends on the regularization length  $l$  for the driven cavity problem, and the optimal value of  $l$  is the same for both the 2D and 3D RNS solutions and for all the flow regimes considered ( $Re = 3200$  and  $10,000$ ). The value of  $l$  agrees with the "Kolmogorov microscale" observed in the experiment [1].

The value of  $\tau^*$  (or  $l$ ) is not significant for a 3D thermal convection in a horizontal cylinder and for a backward facing step flow ( $Re = 44,000$ ). The RNS solutions agree with the experimental data and do not change even if  $\tau^*$  is changed by few orders of magnitude.

## Acknowledgements

Author is grateful to O.A. Bessonov (IPM), A. A. Chernov (USRA) and E. J. Kansa (LLNL) for fruitful discussions. Support from NASA NAG8-1229 grant is gratefully acknowledged.

## References

- [1] K. R. Koseff and R. L. Street. The Lid-Driven Cavity Flow: A Synthesis of Qualitative and Quantitative Observations. *Trans. ASME/Journal of Fluids Engineering* **106** (1984) 390-398.
- [2] U. Ghia, K.N. Ghia and C. T. Shin. Solution of Incompressible Navier-Stokes Equations by Strongly Implicit Multi-Grid Method. *J. Comp. Phys.*, **48** (1982) 387.
- [3] M. Deville, T.-H. Le, Yv. Morchois (Editors), Numerical Simulation of 3-D Incompressible Unsteady Laminar Flows, A GAMM Workshop, Notes on Numerical Fluid Mechanics, **36**, 1992.
- [4] CFD2000 version 3.0, Adaptive Research/Pacific-Sierra Research Corporation, Santa Monica, California, 1997.
- [5] A. G. Daykovsky, V. I. Polezhaev, A. I. Fedoseyev. Investigation of the Structure of Transient and Turbulent Convection Regimes in a Vertical Layer. *Fluid Dynamics*, **13** (1978) 846 - 854.
- [6] V. I. Polezhaev, V. L. Gryaznov, A. G. Daykovsky, A. I. Fedoseyev, Numerical Models of Turbulent Convection Based on the Unsteady Navier-Stokes

- Equations. Lecture Notes in Physics, **90** (1978) 454-459.
- [7] S. S. Kutateladze, A. G. Kirdeyashkin, V. P. Ivakin, Turbulent Natural Convection on a vertical plate and in a Vertical Layer. *Int. J. Heat and Mass Transfer*, **15** (1977).
  - [8] G. I. Shishkin, On Finite Difference Fitted Schemes for Singularly Perturbed Boundary Value Problems with a Parabolic Boundary Layer, *Journal of mathematical analysis and application*, **208**, 1997, 181-197.
  - [9] S. Sundaresan, S. Nagarajan, S. M. Deshpande and R. Narasima, 2D Lid-Driven Cavity at High Reynolds Numbers: Some Interesting Fluid-Dynamical Issues, *Lecture Notes in Physics*, **515**, 1999, 231-236.
  - [10] A. I. Fedoseyev, B. V. Alexeev. Higher Order Continuum Model for Incompressible Viscous Fluid Flow. In: *Continuum Models and Discrete Systems*, Eds. E. Inan, A. Markov, World Scientific, London, 1998, 130-137
  - [11] A. I. Fedoseyev, E. J. Kansa, C. Marin, A.G. Ostrogorsky, Magnetic field suppression of semiconductor melt flow in crystal growth: comparison of three methods for numerical modeling, *CFD Journal (accepted)*.
  - [12] B. V. Alexeev, The generalized Boltzmann equation. generalized hydrodynamic equations and their applications. *Phil. Trans. Roy. Soc. London*, A. **349** (1994) 417-443.
  - [13] R. Löhner, Design of Incompressible Flow Solver: Practical Aspects, In: *Incompressible computational fluid dynamics*, Eds. M. D. Gunzberger and R. A. Nicolaides, Cambridge Press, 1993, 267-294.
  - [14] J. Kim, S. J. Kline, and J. P. Johnston. Investigation of a reattaching turbulent shear layer: flow over a backward-facing step. *ASME J. Fluids Engng.*, **102**, 1980, 302-308.
  - [15] S. Thangam and C. G. Speziale. Turbulent separated flow past a backward-facing step: a critical evaluation of two-equation turbulence models. ICASE Report 91-23, NASA Langley Research Center, Hampton, Virginia, 1991.
  - [16] G. P. Bogatirev, G. F. Putin, V. I. Polezhaev. A System for Measurement of Convection aboard Space Station, *Proc. 3rd Microgravity Fluid Physics Conf.*, Cleveland, Ohio, July 13-15, 1996, NASA Conf. Publ., 813-818.
  - [17] O.A. Bessonov, 1998. Private communications.
  - [18] V. I. Polezhaev, A. I. Prostomolotov, A. I. Fedoseyev. Finite Element Method in Viscous Fluid Mechanics Problems, In: *Advances in Science and Technology, Fluid Mechanics series*, **21**, No. 3, VINITI, Moscow, 1987, 3-92.
  - [19] V. I. Polezhaev, A. V. Bune, A. I. Fedoseyev et al. *Mathematical Modeling of Convective Heat and Mass Transfer Problems on the Basis of Navier-Stokes Equations*, Nauka, Moscow, 1987.
  - [20] A. I. Fedoseyev, O. A. Bessonov. Efficient Solution of Viscous Fluid Flow Problems in Finite Element Method. *Proc. of the Seminar on Numerical Methods in Heat and Mass Transfer, Institute for Problems in Mechanics of the Russian Academy of Sciences*, Moscow, 1997, 109-138.
  - [21] K. Morgan, J. Periaux, and F. Thomasset (Editors), *Analysis of Laminar Flow over a Backward Facing Step, A GAMM Workshop, Notes on Numerical Fluid Mechanics*, **9**, 1984.
  - [22] A. I. Fedoseyev, J. I. D. Alexander. An Inverse Finite Element Method for Pure and Binary Alloys. *J. Comp. Physics*, **130** (1997) 243-255.
  - [23] A. I. Fedoseyev and J. I. D. Alexander. Investigation of vibrational control of convective flows in Bridgman melt growth configurations. (*To appear in J. Cryst. Growth*).

# Higher Accuracy Numerical Solution Methods for High $Re$ number Viscous Flows and Flows with Boundary Layer

Alexandre I. Fedoseyev

Center for Microgravity and Materials Research,  
University of Alabama in Huntsville, Huntsville, Alabama 35899, USA  
E-mail: alex@cmmr.uah.edu; <http://uahtitan.uah.edu/alex/>

## Abstract

A hierarchical family of methods for highly accurate solution for viscous flows at high Reynolds number, flows with boundary layer is presented. Note, that thin boundary layer can occur even at low  $Re$ , e.g. in flows of electrically conductive fluids under strong magnetic field at Hartman number  $Ha \gg 1$ . The main feature of the methods proposed is the restoring of conservation laws at the boundary. Numerical solutions using this new approach compare favorably with available exact or asymptotic ones and experimental data.

## Introduction

Difficulties with the numerical solutions of Navier-Stokes (NS) equations for high  $Re$  number flows have been referenced usually to insufficient mesh resolution, complicated flow physics, turbulence etc. Shishkin et al. in series of papers (1995-1997) shows theoretically that grid methods perform poorly in dealing with the boundary layer and provides the estimation for numerical solution error as  $O(1)$  for uniform meshes [1]. It was proposed the construction of special meshes as a remedy for these difficulties with more optimistic error estimation as  $O(h^{1/m})$ ,  $h$  is a mesh size, with  $m = 9$  or more. Failures of numerical solutions to obtain good agreement with experimental data during last decades can be referenced as confirmation of Shishkin estimates (lid-driven cavity flow: experiments [2] versus simulations [3]; thermal convection in a vertical slot: experiments [4] versus [5], etc.). Successful results with implementing Shishkin-type strategy are obtained in [6]. To construct Shishkin mesh, one has to use the boundary layer thickness that is not known in advance. Meshless methods have similar drawbacks in such problems (see e.g. [7]).

The facts above and recent experiments with different formulations [8] and regularizations [10] for the viscous flow problem resulted in uncovering the main reason for poor numerical results: conservation laws are violated at the boundary in numerical treatments. The violation is done explicitly in FEM by dropping the weak formulation at the Dirichlet boundary (there is no choice); the same is not explicit but present in traditional FDM, spectral or multiquadric (MQ) collocation methods (governing equations are not used at the boundary). That can be ignored for well-posed problem, but becomes crucial for a singularly perturbed boundary value problem, e.g. viscous flow with boundary layer.

We present the new alternative numerical solution methods that are more accurate, efficient and less mesh dependent. These methods, ranging in the increasing of accuracy (and complexity of implementation), restore the conservation laws at the boundary: (i) a regularization approach, the RNS [10], (ii) a projection approach, (iii) an extension of basis function space (for FEM or MQ[15]).

## Higher accuracy numerical solution methods for boundary layer

### A regularization approach to solving the Navier-Stokes equations

We consider a flow of incompressible viscous fluid in a closed 2D or 3D domain  $\Omega$ . The Navier-Stokes momentum and continuity equations are:

$$\frac{\partial \mathbf{V}}{\partial t} + (\mathbf{V} \nabla) \mathbf{V} - Re^{-1} \nabla^2 \mathbf{V} + \nabla p - \mathbf{F} = 0 \quad (1)$$



$$\nabla \cdot \mathbf{V} = 0 \quad (2)$$

where  $Re = V_0 L / \nu$  is the Reynolds number,  $V_0$  is the velocity scale,  $L$  is the hydrodynamic length scale,  $\nu$  is the kinematic viscosity, and  $\mathbf{F}$  is a body force. In the case of thermal convection the body force is  $\mathbf{F} = Gr Re^{-1} \cdot \Theta \cdot \mathbf{e}_g$  (Boussinesq approximation), where  $\Theta$  is a nondimensional temperature,  $Gr$  is the Grashoff number and  $\mathbf{e}_g$  is the unit vector in the direction of gravity. The energy equation is:

$$\frac{\partial \theta}{\partial t} + (\mathbf{V} \nabla) \theta = Pr^{-1} Re^{-1} \nabla^2 \theta \quad (3)$$

where  $\theta$  represents nondimensional temperature, scaled by  $\theta = (T - T_{cold}) / \Delta T$  with  $\Delta T = T_{hot} - T_{cold}$ . The Prandtl, Grashoff and Rayleigh numbers are respectively  $Pr = \nu / k$ ,  $Gr = Ra / Pr$ , and  $Ra = \beta \Delta T g L^3 k^{-1} \nu^{-1}$ , where  $\beta$ ,  $g$ ,  $k$  are the coefficients of thermal expansion, gravitational acceleration, and of thermodiffusivity.

Boundary and initial conditions complete the problem formulation and they will be given for each problem.

A **proposed regularization** consists in modifying the continuity equation (2) to become

$$\nabla \cdot \mathbf{V} = \tau^* \nabla \cdot (\nabla p - \mathbf{F}) \quad (4)$$

where  $\tau^*$  is a small regularization parameter. For  $\tau^* \rightarrow 0$  eq. (4) approaches the continuity equation (2). The boundary condition for the pressure on a wall is

$$(\nabla p - \mathbf{F}) \cdot \mathbf{n} = 0, \quad (5)$$

where  $\mathbf{n}$  is a unit vector normal to the wall. Equations (4) and (5) present the basis of this method. Equation (5) ensures a balance of the components of the forces that are normal to the region boundary.

First results with a more complicated model have been presented in [8] and [9]. Further numerical experiments have shown that accurate results can be obtained with the simpler model [10]. In [10] we have shown that equations (1), (3), and (4) with (5), called as the regularized Navier-Stokes equations (RNS model), give a better agreement with the experimental measurements for high Reynolds number flows than the traditional NS solution by FEM.

The pressure Laplacian term on the right-hand side of eq. (4), has also been obtained by Löhner as a result of consistent treatment of the time-advancement for the continuity eq. (2) [11]. There a discretization time step  $\Delta t$  is used in place of our parameter  $\tau^*$  and the boundary condition for the pressure was not specified.

The regularization parameter  $\tau^*$  is expressed dimensionally as  $\tau^* = \tau L^{-1} V_0$ , where  $\tau$  is time. The dimension of  $\tau \nu$  is length squared. We introduce the regularization length scale  $l$  with  $l^2 = \tau \nu$  and rewrite  $\tau^*$  as  $\tau^* = l^2 L^{-2} Re = K \cdot Re$ , where  $K = l^2 / L^2$ . The optimal value of  $\tau$  (or  $l$ ) is not known in advance. We found that for problem with smooth boundary condition the solution is undependable of the value of  $\tau^*$ , with  $\tau^*$  is the range from  $10^{-8}$  to  $10^{-4}$ .

Such a regularization has an additional useful feature for the FEM. It allows to use the same order finite element approximation for the velocity and pressure.

**Numerical results** that we obtained for 2D/3D flow problems are in dramatically better agreement with analytical solutions and experimental flow measurements. The numerical 2D/3D solutions by FEM with this strategy employed, called RNS, against the 3D driven cavity flow data [2] and results by other methods are shown in Fig. 1. The residuals of numerical solutions, shown in Fig. 2(a), demonstrate by one to two order residual reduction in the boundary layer for the Navier-Stokes momentum equation. We recognized that eq. (4) is an approximation of the eq. (1) in projection to the wall normal.

Further development of the method can be the use of the governing equations at the boundary. This task is complicated in the frame of the low-order FEM scheme; a projection approach can be implemented with Hermite finite elements (not presented here). This can be done simpler in the frame of the multiquadric method (MQ) [12].

Another approach, that is being developed for the FDM, involves high order finite difference schemes that are specially constructed to deal with the boundary layer solution [16], [17].

## PDE collocation at the boundary

To have the *PDE to be satisfied at the boundary* one needs to extend the basis function space in the MQ by  $N_b$  functions for each PDE, where  $N_b$  is the number of boundary nodes. It can be done by adding the layer of nodes adjacent to the boundary and related MQ basis functions, thus allowing to add a set of equations obtained via collocation of the PDE on the boundary.

A solution of 1D singular perturbation problem from [7] by multiquadric global basis function method [12], using this strategy with 21 nodes, versus exact solution is shown in Fig.2(b) for  $\varepsilon = 10^{-3}$ ; 41 nodes are enough for  $\varepsilon = 10^{-4}$

(not shown). The gain in the accuracy with this strategy is two to three orders compared to the original Kansa-MQ method with 101 nodes[15].

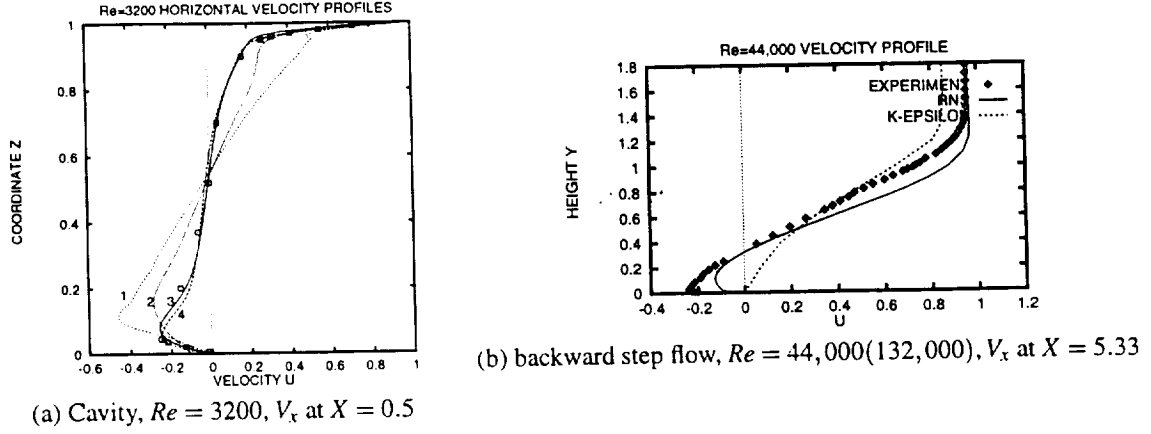


Figure 1: (a) Lid-driven cavity problem,  $Re = 3200$ . Comparison of horizontal velocity profiles (lines 1 to 4) for numerical solution and experimental data (squares) by Koseff and Street (1984): 1-NS, 2 -  $k - \epsilon$  model, 3-RNS (2D), 4-RNS (3D); (b) Flow over a backward facing step,  $Re = 44,000(132,000)$ . Comparison of the horizontal velocity profiles for the numerical solutions with RNS [10],  $k - \epsilon$  model [14] and experimental data (squares) [13] at  $x = 5.33$ .

## Summary

Proposed higher accuracy solution methods are used in applications to 2D and 3D flows at high Reynolds number and flows with thin boundary layer, and compared favorably with experimental data and asymptotic solutions (when available): flow in channels, thermal and vibrational convection (Fig. 3, [18]), electrically conductive fluid flows under strong magnetic fields etc. [10].

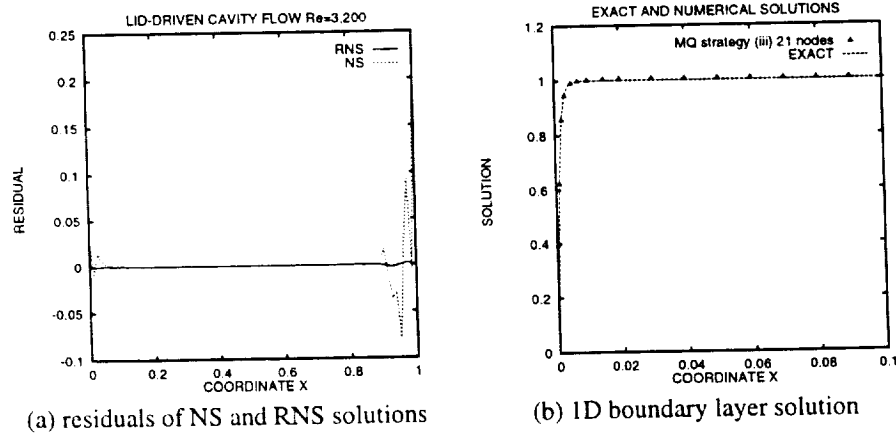


Figure 2: (a) Residuals of numerical solution in the X-momentum equation at  $z = 0.5$  for lid-driven cavity problem,  $Re = 3,200$  for the 2D NS solution and RNS solution on the same  $81 \times 81$  mesh. Residuals are estimated by differentiation of numerical solutions, using interpolating polynomials. The RNS residual is lower by one to two order than the NS one; (b) 1D problem with boundary layer:  $\epsilon u_{xx} + u_x = 0$ ,  $u(0) = 0$ ,  $u(1) = 1$ , comparison of numerical (multiquadric method, 21 nodes, strategy (iii)) and exact  $u = (1 - e^{-x/\epsilon}) / (1 - e^{-1/\epsilon})$  solutions for  $\epsilon = 10^{-3}$ . Plot for  $x$  in  $[0, 0.1]$ .

## References

- [1] G. I. SHISHKIN, J. Math. Anal. Appl., **208** (1997) 181-197.

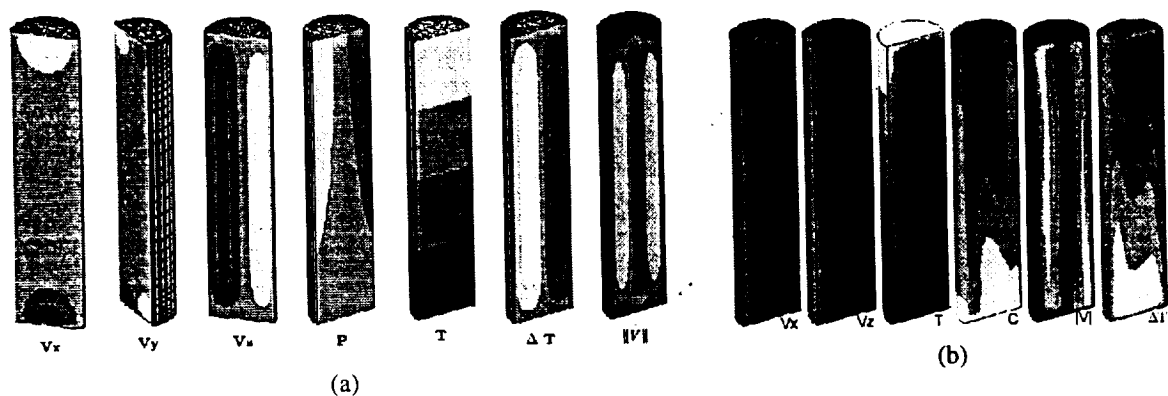


Figure 3: Typical instantaneous 3D thermovibrational melt flow patterns for: (a) translational vibration at 0g,  $Ra = 0$ ,  $Ra_v = 7.25 \cdot 10^4$ ,  $Pr = 0.01$ ,  $\omega = 100Hz$ , lateral vibration is applied along x-direction (horizontal): velocity components  $V_x, V_y, V_z$ , pressure  $P$ , temperature  $T$ , temperature disturbance  $\Delta T$ , and velocity module; (b) circular polarized vibration,  $Ra = 7.25 \cdot 10^3$ ,  $Ra_v = 7.4 \cdot 10^6$ ,  $Pr = 15$ ,  $\omega = 10Hz$ : velocity components  $V_x, V_z$ , temperature  $T$ , concentration  $C$ , velocity module, and temperature disturbance  $\Delta T$ .

- [2] K. R. KOSEFF and R. L. STREET, Trans. ASME/Journal of Fluids Engineering **106** (1984) 390-398.
- [3] U. GHIA, K.N. GHIA and C. T. SHIN, J. Comp. Phys., **48** (1982) 387-411.
- [4] S. S. KUTATELADZE et al., Int. J. Heat and Mass Transfer, **15** (1977) 193-202.
- [5] V. I. POLEZHAEV et al., Lecture Notes in Physics, **90** (1978) 454-459.
- [6] S. SUNDARESAN et al., Proc. of 16th ICNMF D Conf., C.H. Brunau, Ed., Lect. Notes Phys., **515** (1998) 231-236.
- [7] Y.C. HON, Int. J. Appl. Sci. Comput., **6**, No. 3 (1999).
- [8] A. I. FEDOSEYEV, B. V. ALEXEEV, *Continuum Models and Discrete Systems*, Ed. by E. Inan and A. Markov, World Scientific, London, 1998, 130-137.
- [9] A.I. FEDOSEYEV and B.V. ALEXEEV, *Proc. IMACS98, Advances in Scientific Computing and Modeling*, Ed. by S.K. Dey, J. Ziebarth, and M. Ferrandiz, University of Alicante, Spain, 1998, 158-163.
- [10] A. I. FEDOSEYEV, *Proc. of ISCFD-99 Conf*, Ed. by G. Schmidt, Bremen, Germany; also CFD Journal (*accepted*).
- [11] R. LÖHNER, In: *Incompressible computational fluid dynamics*, Ed. by M. D. Gunzberger and R. A. Nicolaides, Cambridge Press, 1993, 267-294.
- [12] E. J. KANSA, Comput. Math. Applic., **19**, No. 8/9 (1990) 127-161.
- [13] J. KIM, S. J. KLINE, and J. P. JOHNSTON, ASME J. Fluids Engng., **102**, 1980, 302-308.
- [14] M. ZIJLEMA, A. SEGAL AND P. WESSELING, Report DUT-TWI-94-24, The Netherlands, 1994.
- [15] A.I. FEDOSEYEV, M.J. FRIEDMAN, and E.J. KANSA, An Improved Multiquadric Method Algorithms for Elliptic PDEs, IMACS 2000, University of Wisconsin, Milwaukee, Wisconsin, May 25-27, 2000.
- [16] J.Y. CHOO, D.H. SCHULTZ, Computers & mathematics with applications. **27**, No. 11, (1994).
- [17] D.H. SCHULTZ and F.O. ILICASU, *Proc. IMACS98, Advances in Scientific Computing and Modeling*, Ed. by S.K. Dey, J. Ziebarth, and M. Ferrandiz, University of Alicante, Spain, 1998, 1-6
- [18] A.I. FEDOSEYEV and J.I.D. ALEXANDER, J.Cryst. Growth, (2000), to appear.

## Iterative Solution of Large Linear Systems for Unstructured Meshes with Preconditioning by High Order Incomplete Decomposition

Alexander I. Fedoseyev, Oleg A. Bessonov\*

Center for Microgravity and Materials Research,  
University of Alabama in Huntsville, Huntsville, Alabama, U.S.A.  
E-mail: alex@cmmr.uah.edu, <http://uahtitan.uah.edu/alex/>

\*Institute for Problems in Mechanics, Russian Academy of Sciences,  
Moscow, RUSSIA, E-mail: bess@ipmnet.ru

**Keywords:** Navier - Stokes equations, Finite element method, Iterative solution, Preconditioning

### Abstract

We present an efficient solution technique for large sparse nonsymmetric algebraic linear systems, related to the coupled solution of incompressible viscous fluid flow equations. An iterative solution technique with high order incomplete decomposition as preconditioning is used in this method. A developed CNSPACK linear solver for flow problems on 2D/3D unstructured meshes is briefly described. Analysis of the efficiency of the proposed approach is demonstrated on 2D and 3D flow problems. Numerical experiments show that the computational complexity of the proposed method appears to be  $O(N^{5/4})$ .

### Introduction

Numerical solution of incompressible viscous flow problems by the finite-element method leads to large linear systems of equations with sparse non-symmetric matrices. For the Navier-Stokes equations in primitive variables with the continuity equation, treated directly, the system of related linear equations combines many unwanted properties of algebraic systems. It is non-symmetric, not positive definite and has zero diagonals in rows related to the discretized continuity equation. The advantage of the coupled solution is in the improved stability of the numerical solution for stationary flow at high Reynolds numbers. Also, much larger discrete time steps for transient flow analysis can be used. The drawback of the coupled solution is that it is expensive in terms of computer resources, such as memory and computation time.

Recent advances in iterative solution techniques resulted in more efficient solvers, based on CGS and BiCGS [1,2] and GMRES methods [3,2]. A preconditioning technique can be used to accelerate the convergence of iterative solution, thus resulting in dramatically fewer iterations, typically 10 to 100 instead of the order of 1000 iterations without preconditioning.

Recurrent formulas have been published to construct a preconditioner for structured (3- or 5-diagonal) matrices [4]. Simple first order preconditioners are typically used for unstructured matrices that are related to unstructured meshes for complicated domain geometry. The efficiency of such preconditioning is low and, in a case of the incompressible Navier-Stokes equations, solved with quadratic for velocity and linear for pressure finite elements, such a preconditioning may result in a divergence of iterations. In [5] we proposed the high order preconditioners for unstructured matrices, which improve convergence of the iterative solution process. In this paper,

we analyze the efficiency of this approach on 2D and 3D flow problems. Numerical experiments show that the computational complexity of the proposed method appears to be  $O(N^{5/4})$ .

### Problem formulation

The following are governing equations for viscous flow in closed domain  $G$ . The momentum equation is

$$\frac{\partial \mathbf{U}}{\partial t} + (\mathbf{U} \cdot \nabla) \mathbf{U} - \frac{1}{Re} \Delta \mathbf{U} + \nabla p = 0 \quad (1)$$

while the continuity equation is

$$\text{div}(\mathbf{U}) = 0. \quad (2)$$

Here  $\mathbf{U}$  is velocity vector,  $p$  is pressure, and  $Re$  is the Reynolds number. We present the following examples: (i) flow in a square cavity with driven lid; (ii) viscous flow around the system of circular cylinders; (iii) a flow in ion-exchanger channel (Fig. 1), and (iv) flow in a 3D cavity (Fig. 2).

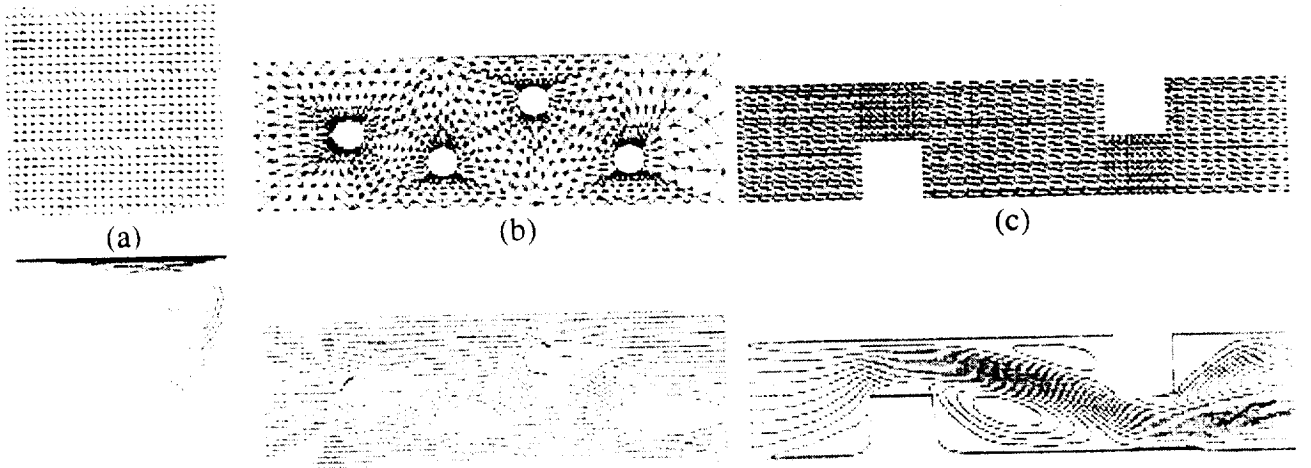


Fig. 1: Test problems, meshes and flow patterns: (a) driven cavity, 2D, (b) flow around the system of circular cylinders, and (c) flow in ion-exchanger channel.

Boundary conditions are: (i) velocity is equal to zero at the bottom and side walls, and a horizontal component  $u$  of velocity is equal to 1 on a driven top lid; (ii,iii) inlet velocity profile  $u=u(y)$ ,  $v=0$  is given at the left domain side, zero velocity on top and bottom, and at cylinder surfaces, and  $p=0$  and "soft" boundary conditions for velocity at the channel exit, at the right side of the domain. Initial conditions are zero fields for all variables.

### Solution method

We used the finite element method on 6-noded triangles with quadratic for velocity and linear for pressure finite elements for 2D problems. A new regularization method for viscous flows at high

Reynolds numbers with trilinear interpolation for both velocity and pressure was used in the 3D driven cavity example [7,8] with a geometry corresponding to the experiments [16].

The discretized linear algebraic systems are solved using the CGS-type iterative method with preconditioning by the incomplete decomposition of the original matrix. Comparing the CGS and GMRES methods [1, 3] in our examples, we found that both methods convergence well, if a good preconditioner is used. The CGS method needs comparably less memory to store only eight work vectors.

To reduce the memory requirements, a compact storage scheme for matrices was used. We stored only the nonzero entries. The incomplete decomposition (ID) was a product of triangular and diagonal matrices,  $\mathbf{P} = \mathbf{LDU}$ . To avoid a diagonal pivot degeneration we use the Kershaw diagonal modification [6]. If the value of diagonal element was small, i.e.  $|a_{ii}| < \alpha = \sqrt{2^{-t} \sigma \mu}$ , the diagonal was replaced by  $\alpha$ . Here  $\sigma$  and  $\mu$  are the maximum magnitudes of row and column elements, and  $2^{-t}$  is a machine precision ( $t$  bits in mantissa, see details in [6]).

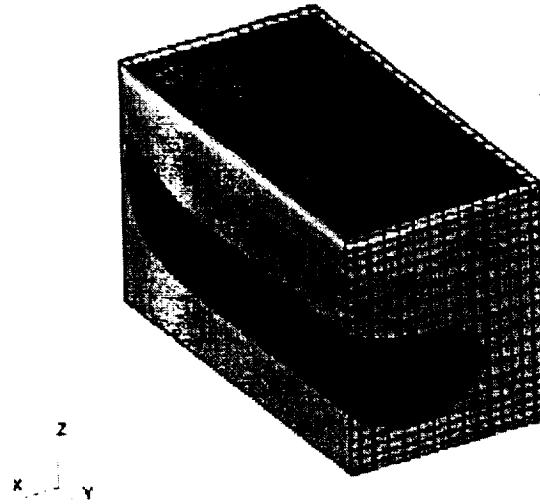


Fig.2: 3D driven cavity problem: mesh and horizontal velocity component is shown (dark gray color shows larger velocity component magnitude).

For the first order ID, the matrix  $\mathbf{P}$  has the same non-zero entry pattern as the original matrix. For a second order or higher ID, matrix  $\mathbf{P}$  has one or more additional entries near the locations of the non-zero matrix entries, where the original matrix entries are zeros.

### Numerical experiments

The computations were done on the SGI O2 machine for different mesh resolutions and different incomplete decomposition orders. Iteration termination criteria was the value of the module of the residual:  $r < 10^{-6}$ ,  $10^{-8}$ , or  $10^{-12}$ . The solution times for a driven cavity problem were compared for different solution methods (Fig. 3).

The results of our numerical experiments can be summarized as follows:

- (1) The iterative solution without a preconditioning,  $ID = 0$ , is time-expensive, the number of iterations is of the order of the number of unknowns. The memory requirements are smallest.
- (2) A simple incomplete decomposition of the first order,  $ID = 1$ , can result in the divergence of the iterations. That may be a reason, why this approach is not widely used yet.
- (3) The incomplete decomposition of the second or third order can reduce the number of iterations dramatically, e.g. for  $N$  up to 10,000 the number of iteration did not exceed 200, and, for most cases, just 50 iterations were enough for convergence. The memory requirements are about twice as high as for  $ID = 0$ .

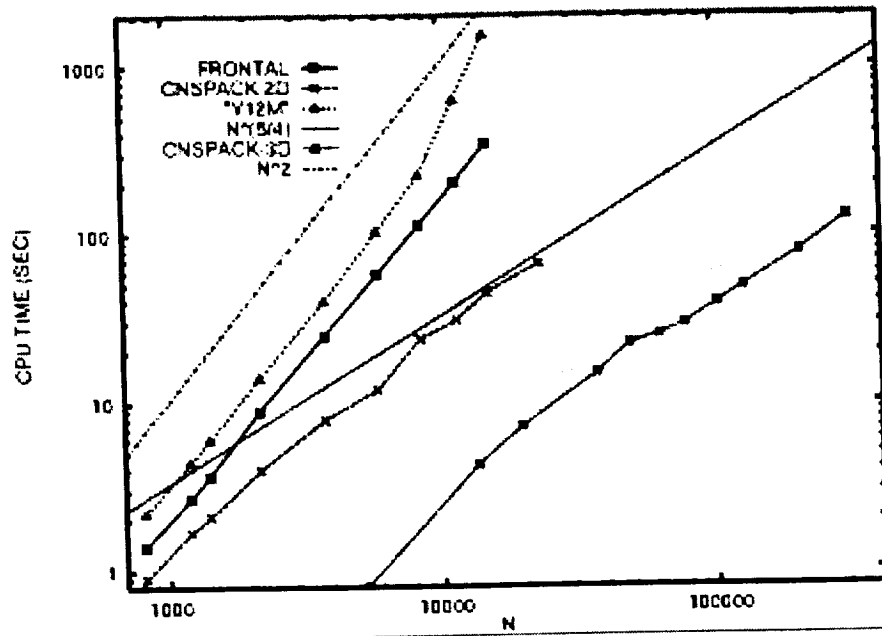


Fig.3: Solution time versus number of unknowns  $N$  for 2D and 3D driven cavity problem. comparison of different software packages. FRONTAL – direct solution by frontal method; CNSPACK-2D– solution with proposed method, P2-P1 finite elements, matrices stored in double precision, incomplete decomposition of the second order; Y12M – solution with Y12M sparse matrix solver package; CNSPACK-3D (lower curve) – solution of 3D problem; matrices are stored in single precision, a first order incomplete decomposition is used. Theoretical asymptotics for direct solution and proposed method, the  $N^2$ , and  $N^{5/4}$  lines, are plotted for comparison.

- (4) A new regularization approach for viscous flows, that works well with thin boundary layers [7,8], was used in our tests for 3D cavity problem. It resulted in a much faster solution convergence. For  $N$  up to 300,000 the number of iterations to converge was of the order of 30 to 50. And in this case, the first order incomplete decomposition worked quite well.
- (5) We compared the solution time for the same linear system by different methods: direct solution by frontal method [5], iterative solution with Y12M sparse matrix package [15] and by our CNSPACK software (Fig. 3). We have been unable to use the SPARSKIT [11] and SPARSE [12] solvers, as those failed for zero matrix diagonal elements.

- (6) Convergence rate of the proposed method does not reduce with increasing the Reynolds number  $Re$  (from 10 to 1000). We observed even faster convergence for larger  $Re$ .
- (7) Proposed method can solve the linear system with a high accuracy, much higher than obtained by a direct solution.
- (8) The node/equation numbering is of great importance for the rate of convergence [13, 14]. We found that the optimal node or equation renumbering is quite necessary for unstructured meshes, and ID = 2 should be used for fast convergence.
- (9) It appears that the computational complexity of the proposed method is  $O(N^{5/4})$  (see Fig. 3).

Aspects of the efficiency of the method on superscalar pipelined microprocessors and parallel architectures were considered. We found the solution time can be reduced by a factor of three by using special optimization techniques for a superscalar pipelined architecture.

Proposed method is used in FEMINA/3D code that is used for solving 2D/3D incompressible viscous flows, 3D thermal convection, magneto-hydrodynamics flows, and 3D thermal vibrational convection in Bridgman crystal growth configurations [7-10]. If the number of unknowns is in the range of  $N = 50,000$  to  $500,000$ , the problems are solved on a low-end SGI workstation or PC, using our FEMINA/3D code (for  $N$  of the order of  $10^6$ , the supercomputer is needed). For example, we solve large 3D time-dependent problems of thermo-vibrational convection with 300,000 unknowns on the low-end SGI O2 workstation within a couple of hours [8],[9].

## Conclusions

We have presented an efficient solution technique for large sparse nonsymmetric algebraic linear systems for coupled solution of incompressible viscous flow equations. An iterative solution technique with high order incomplete decomposition as preconditioning is used in this method. Analysis of the efficiency of this proposed approach is demonstrated on 2D and 3D flow problems. Numerical experiments show that the computational complexity of the proposed method appears to be  $O(N^{5/4})$ .

## References

- [1] P. Wesseling, P. Sonneveld. Numerical experiments with a multiple grid and a preconditioned Lanczos type methods. Lecture Notes in Mathematics, **771**, Berlin: Springer, 1980, 543-562.
- [2] R. Barrett, M. Berry, T. Chan, J. Demmel, J. Donato, J. Dongarra, V. Eijkhout, R. Pozo, C. Romine, and H. van der Vorst. Templates for the Solution of Linear Systems: Building Blocks for Iterative Methods, Philadelphia: SIAM, 1994.
- [3] Y. Saad. GMRES: A generalized minimal residual algorithm for solving nonsymmetric linear systems, SIAM J. Sci. Statist. Comput., **7** (1986) 856-869.



- [4] H. Van Der Vorst. Iterative solution methods for certain sparse linear systems with a non-symmetric matrix arising from PDE-problems. *J. Comput. Phys.*, **44** (1981) 1-19.
- [5] V. I. Polezhaev, A. I. Prostomolotov, A. I. Fedoseyev. Finite Element Method in Viscous Fluid Mechanics Problems, In: *Advances in Science and Technology, Fluid Mechanics series*, **21**, No. 3, VINITI, Moscow, 1987, 3-92 (in Russian).
- [6] D. S. Kershaw. The incomplete Cholesky-conjugate gradient method for the iterative solution of systems of linear equations. *J. Comput. Phys.*, **2** (1978) 43-65.
- [7] A. I. Fedoseyev, B. V. Alexeev. Higher Order Continuum Model for Incompressible Viscous Fluid Flow. In: *Continuum Models and Discrete Systems*, Eds. E. Inan, A. Markov, World Scientific, London, 1998, 130-137.
- [8] A. I. Fedoseyev, A regularization approach to solving boundary layer problems for Navier-Stokes equations, *Computational Fluid Dynamics Journal*, **9**, No.1 (2000), (accepted, in print).
- [9] A. I. Fedoseyev and J. I. D. Alexander. Investigation of vibrational control of convective flows in Bridgman melt growth configurations. *J. Crystal Growth*, **211** (2000) 34-42.
- [10] A. I. Fedoseyev, E. J. Kansa, C. Marin, A.G. Ostrogorsky, Magnetic field suppression of semiconductor melt flow in crystal growth: comparison of three methods for numerical modeling, *Computational Fluid Dynamics Journal*, **9**, No.1 (2000), (accepted, in print).
- [11] K. S. Kundert, A. S. Sangiovanni-Vincentelli. A Sparse linear equation solver, Manual version 1.3a. University of California at Berkeley, 1988, 68p.
- [12] T. Skalicky. LASPACK user manual, version 1.12.2. Technical University of Dresden, 1995. <http://www.tu-dresden.de/mwism/skalicky/laspack/laspack.html>
- [13] L. C. Dutto. The Effect of Ordering on Preconditioned GMRES Algorithm, for Solving the Compressible Navier-Stokes Equations. *Int. J. Numer. Meth. Eng.*, **36** (1993) 457-497.
- [14] N.E. Gibbs, W.G. Pool, Jr. and P.K. Stockmeyer. An algorithm for reducing the bandwidth and profile of a sparse matrix, *SIAM J. Numer. Anal.*, **13** (1976) 236-250.
- [15] Z. Zlatev et al. Y12M solution of large and sparse systems of linear algebraic equations. *Lecture Notes in Computer Science*, **121**, Springer, Berlin-Heidelberg-New York, 1981.
- [16] K.R. Koseff and R.L. Street. The Lid-Driven Cavity Flow: A Synthesis of Qualitative and Quantitative Observations. *Trans. ASME/Journal of Fluids Engineering*, **106** (1984) 390-398.

# A Higher Accuracy Finite Element Model for Viscous Flows with Boundary Layer

Alexandre I. Fedoseyev

Center for Microgravity and Materials Research, University of Alabama in Huntsville, Huntsville, AL. E-mail:  
alex@cmmr.uah.edu, <http://uahtitan.uah.edu/alex/>

## Abstract

The RNS method was used to solve viscous flow problems at high Reynolds numbers with a thin boundary layer. This method is related to the generalized hydrodynamic equations proposed by Alexeev (1994). It can be interpreted as a regularization of the Navier-Stokes equations. Numerical solutions using this approach compare favorably with experimental data. The method is discussed and numerical solutions are compared with the experimental data for a 3D driven cavity flow at  $Re = 3200$  and  $10,000$ , 2D backward facing step flow at  $Re = 44,000$ , 2D channel flow at  $Re$  number up to  $10^6$ , and a 3D thermal convection in a cylinder at  $Ra = 1000$  to  $150,000$ . Comparison with the analytical asymptotic solution is provided for a thermal convection, in the electrically conducting fluid suppressed by a strong magnetic field at Hartman numbers  $Ha$  up to  $20,000$ . This proposed model is not a turbulence model, and no additional equations are introduced.

**Keywords:** High Reynolds number flows, Alexeev equations, Regularization, Finite element method.

## 1 Introduction

Difficulties with the numerical solutions of Navier-Stokes (NS) equations for high  $Re$  number flows have usually been referenced to insufficient mesh resolution, complicated flow physics, turbulence, etc. In series of papers, Shishkin et al. (1995-1997, see e.g. [1]) demonstrated theoretically that grid methods perform poorly when dealing with the boundary layer and provided an estimation for numerical solution error as  $O(1)$  for uniform meshes [1]. As a remedy for these difficulties, the construction of special meshes was proposed, with more optimistic error estimation, as  $O(h^{1/m})$ ,  $h$  is the mesh size, with  $m = 7$  or more. During last decades the failure of numerical solutions to obtain good agreement with experimental data confirms Shishkin estimates (lid-driven cavity flow: experiments [2] versus simulations [3]; thermal convection in a vertical slot: experiments [4] versus simulations [5], etc.). Successful results implementing Shishkin-type strategy are obtained in [6]. The boundary layer thickness, which is not known in advance, is used, to construct Shishkin mesh. Meshless methods have similar drawbacks [7].

We have developed an alternate approach, that is more accurate, less mesh-dependent and can be interpreted as a regularization of the Navier-Stokes equations. It is based on the mathematical model associated with the generalized hydrodynamic equations by Alexeev [8], [9]. The numerical solutions agree well with the experimental measurements for a set of flow problems at high Reynolds number and for flows with thin boundary layer [10], [11], [12], [13], [14][15]. This is not a turbulence model, and no additional equations are introduced.

The model was successfully compared to: (1) 3D driven cavity flow data by Koseff and Street (1982) at  $Re = 3200$  and  $Re = 10,000$ ; (2) 2D backward facing step flow by Kim et al. (1980) at  $Re = 44,000$ ; (3) 3D thermal convection in a cylinder at  $Ra = 1000$  to  $150,000$ ; and (4) asymptotic solution for a thermal convection in the semiconductor melt suppressed by the magnetic field at Hartman numbers  $Ha$  up to  $Ha = 20,000$ . Numerical results for 2D channel flow at  $Re$  number up to  $10^6$  are also presented.

## 2 A regularization approach to solving Navier-Stokes equations

**Governing equations.** To consider a flow of incompressible viscous fluid, in a closed 2D or 3D domain  $\Omega$ , Navier-Stokes momentum and continuity equations are:

$$\frac{\partial \mathbf{V}}{\partial t} + (\mathbf{V} \nabla) \mathbf{V} - Re^{-1} \nabla^2 \mathbf{V} + \nabla p - \mathbf{F} = 0 \quad (1)$$

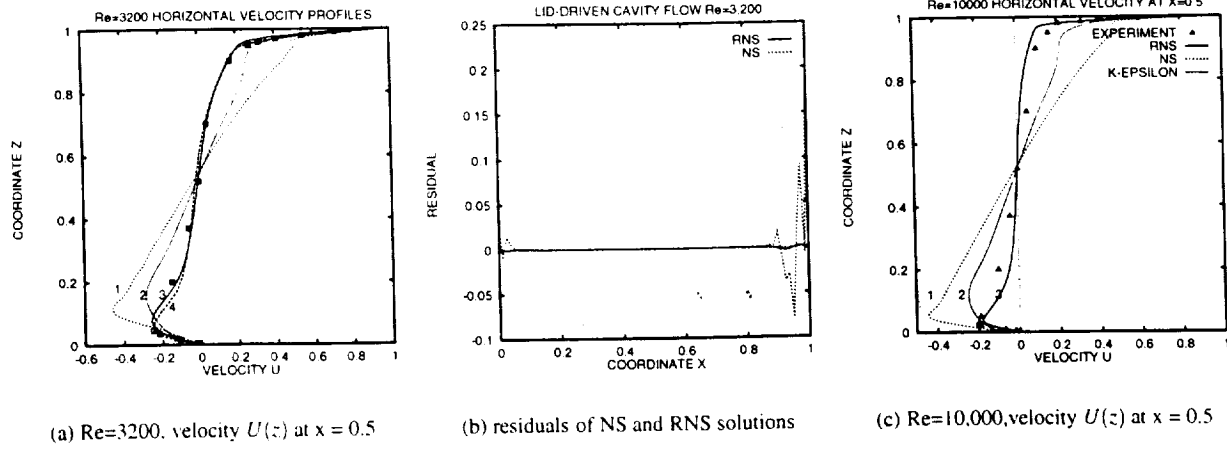


Figure 1: Lid-driven cavity problem,  $Re = 3200$ : (a) horizontal velocity profiles (1-4) for numerical solution (solid and dashed lines): 1-NS, 2 - standard  $k - \epsilon$  model, 3-RNS (2D), 4-RNS (3D); squares - experimental data by Koseff and Street (1982) in the symmetry plane  $Y = 1.5$ . (b) residuals of numerical solution in the momentum equation (1) for the 2D NS and RNS solutions at  $x = 0.5$ . Residuals are estimated by differentiation of numerical solutions, using interpolating polynomials. (c)  $Re = 10^4$ , numerical horizontal velocity profiles (1-3) and experimental data (triangles). A  $k - \epsilon$  model solution is obtained with commercial code CFD2000.

$$\nabla \cdot \mathbf{V} = 0 \quad (2)$$

where  $Re = V_0 L / \nu$  is the Reynolds number,  $V_0$  is the velocity scale,  $L$  is the hydrodynamic length scale,  $\nu$  is the kinematic viscosity, and  $\mathbf{F}$  is a body force. In the case of thermal convection the body force is  $\mathbf{F} = Gr Re^{-1} \cdot \Theta \cdot \mathbf{e}_g$  (Boussinesq approximation), where  $\Theta$  is a nondimensional temperature,  $Gr$  is the Grashoff number and  $\mathbf{e}_g$  is the unit vector in the direction of gravity. The energy equation is:

$$\frac{\partial \theta}{\partial t} + (\mathbf{V} \nabla) \theta = Pr^{-1} Re^{-1} \nabla^2 \theta \quad (3)$$

where  $\theta$  represents nondimensional temperature, scaled by  $\theta = (T - T_{cold}) / \Delta T$  with  $\Delta T = T_{hot} - T_{cold}$ . The Prandtl, Grashoff and Rayleigh numbers are respectively  $Pr = \nu / k$ ,  $Gr = Ra / Pr$ , and  $Ra = \beta \Delta T g L^3 k^{-1} \nu^{-1}$ , where  $\beta$ ,  $g$ ,  $k$  are the coefficients of thermal expansion, gravitational acceleration, and of thermodiffusivity.

We have analyzed the generalized hydrodynamic equation, proposed in [8] (a review in [9]), for the case of incompressible viscous flow and kept only a few main order terms, *spatial fluctuations*, in the continuity equation. This may be interpreted as a regularization of the Navier-Stokes equations.

A **proposed regularization** involves modifying the continuity equation (2) to become

$$\nabla \cdot \mathbf{V} = \tau^* \nabla \cdot (\nabla p - \mathbf{F}) \quad (4)$$

where  $\tau^*$  is a small regularization parameter. For  $\tau^* \rightarrow 0$ , eq. (4) approaches the continuity equation (2). The boundary condition for pressure on a wall is

$$(\nabla p - \mathbf{F}) \cdot \mathbf{n} = 0, \quad (5)$$

where  $\mathbf{n}$  is a unit vector normal to the wall. Equations (4) and (5) present the basis of our method, which takes into account only a few of many additional terms of the generalized hydrodynamic equations, called *fluctuations* (temporal and spatial), in [8]. Equation (5) is a condition of absence of the fluctuations on walls, according to [8].

Preliminary results with a more complicated model are presented in [10] and [11]. Further numerical experiments have shown that satisfactory results can be obtained with the simpler model presented above [12]. Numerical solutions of eqs. (1), (3), and (4), called *regularized Navier-Stokes equations* (RNS), with the boundary condition (5), give a better agreement with the experimental measurements for high Reynolds number flows than the traditional solution of Navier-Stokes eqs. (1) and (2), (NS), with the finite element method (FEM).

Note that numerical formulations, containing extra terms in the momentum and continuity equations, have been proposed in the frame of kinetically consistent numerical schemes, developed by Elizarova and Chetverushkin [17], [18]. The justification of introducing extra terms into hydrodynamic equations is discussed in [19] from a physical

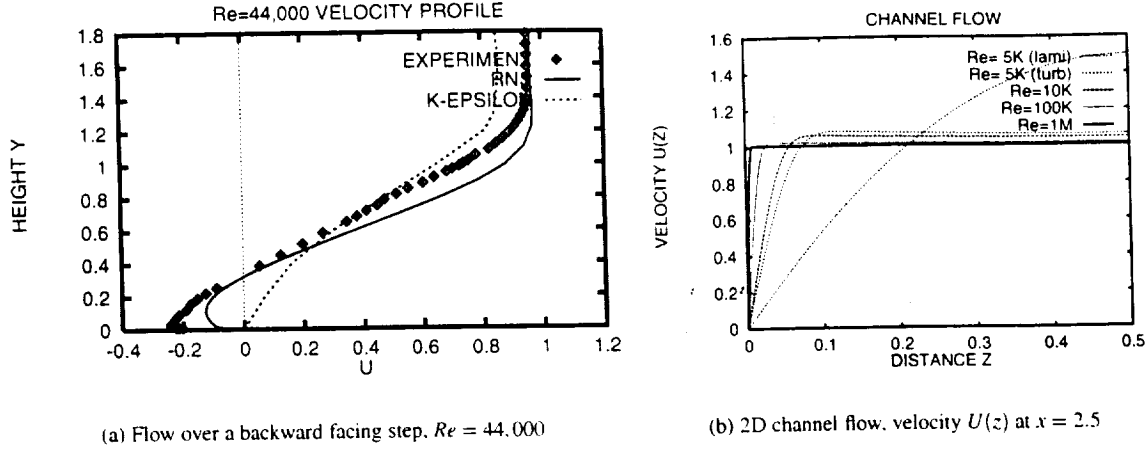


Figure 2: (a) Flow over a backward facing step,  $Re = 44,000(132,000)$ , comparison of the horizontal velocity for the RNS solution,  $k-\epsilon$  model [25], and the experimental data (squares) [23] at  $x = 5.33$ ; (b) 2D channel flow, horizontal velocity profiles  $U(z)$  at  $x = 2.5$ , computed with RNS  $Re = 5 \cdot 10^3$  (laminar and turbulent),  $10^4$ ,  $10^5$  and  $10^6$ .

kinetics viewpoint. The pressure Laplacian and other terms in the discretized continuity equation, have also been proposed by Löhner as a result of consistent treatment of the time-advancement for the continuity eq. (2) [16].

Further, eqs. (1), (3), and (4) with the boundary condition (5) are treated as mathematical model, having a control (regularization) parameter  $\tau^*$ . This regularization parameter  $\tau^*$  is expressed dimensionally as  $\tau^* = \tau L^{-1} V_0$ , where  $\tau$  is time. The dimension of  $\tau v$  is a length squared. We introduce the regularization length scale  $l$  with  $l^2 = \tau v$  and rewrite  $\tau^*$  as  $\tau^* = l^2 L^{-2} Re = K \cdot Re$ , where  $K = l^2 / L^2$ . The optimal value of  $\tau$  (or  $l$ ) is not known in advance. We found that, for problems with smooth boundary conditions, the numerical solution only slightly depends on the value of  $\tau^*$ , with  $\tau^*$  in the range of  $10^{-8}$  to  $10^{-2}$ . This proposed regularization has an additional useful feature for the FEM. It uses the same order finite element approximation for velocity and pressure for RNS.

### 3 Numerical experiments with RNS

In this section, we present the numerical results of a few flow problems, and compare these with experimental data. The FEM was used to discretize the governing equations. Algebraic equations for momentum and continuity were solved simultaneously using the iterative CNPACK solver [20], with preconditioning by a high order incomplete decomposition. Iteration termination criterion was a convergence of relative residuals to  $10^{-8}$  (or  $10^{-12}$ ).

**Driven cavity problem.** Shown in Fig. 1 are the numerical solutions, with RNS employed [10],[12], against the 2D and 3D driven cavity flow data at  $Re = 3,200$  and  $10,000$  [2], and results by other methods. We used  $81 \times 81$  node uniform triangular mesh for the RNS. The same mesh, with quadratic for velocity and linear for pressure elements, was used in a standard FEM solution of eqs. (1, 2). These results are labeled as NS in Fig. 1(a) and 1(c). The RNS model parameter,  $\tau^*$  (or  $l^2$  in  $l^2 L^{-2}$ ), was varied to match one of the experimental velocity profiles. A value,  $l^2 L^{-2} \approx 1.5 \cdot 10^{-5}$ , resulted in good agreement for all the velocity profiles and both flow regimes,  $Re = 3,200$  and  $10,000$ . To our surprise, the dimensional value of  $l \approx 0.58 \text{ mm}$  was a good approximation to the experimentally observed "Kolmogorov microscale"  $l_{exp} \approx 0.5 \text{ mm}$  (see [2], p. 398).

For 3D flow we solved the RNS at  $Re = 3200$  for half of the cavity with a mesh of  $41 \times 41 \times 33$  nodes (221,892 unknowns), refined near the walls. The symmetry condition was used on the vertical symmetry plane  $y = 1.5$ . The same 2D value of  $K = 1.5 \cdot 10^{-5}$  was used in the 3D computations, the modeling results are presented in Fig. 1 as well. One can see that the velocities obtained for both the 2D and 3D profiles are close to the experimental data, except in one region. We did not obtain the 3D stationary solution at  $Re = 10^4$ . The solution went unstationary at  $Re \geq 8,450$ . According to Baggett and Trefethen [22], the stationary solution exists, but the basin of attraction of this solution may be extraordinarily narrow, having a width of  $O(Re^\alpha)$  for some  $\alpha < -1$ .

**Mass conservation** in the continuity equation was thoroughly analyzed. The local values of  $\text{div} \mathbf{V}$  for the numerical solution were examined. The conclusion was that a numerical solution for the RNS model has the same order of error in the mass conservation as the NS solution with the same number of mesh nodes [12].

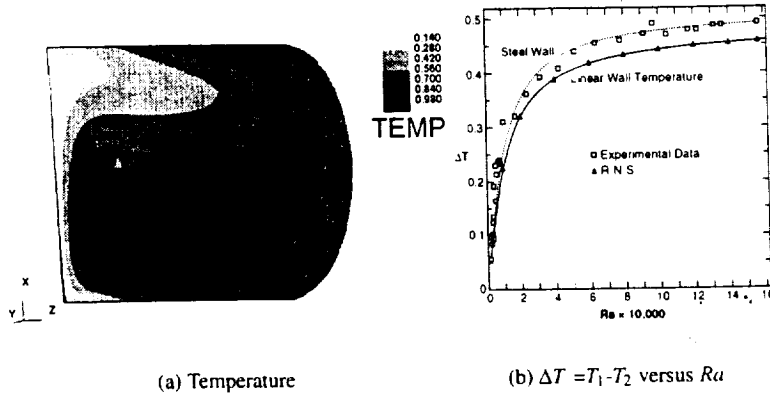


Figure 3: (a) Thermal convection in a 3D differentially heated cylinder; (b) comparison of the temperature difference  $\Delta T$ , versus  $Ra$  with the experimental data [27] and finite-volume computations: squares - experimental data, solid line - numerical results for perfect wall conductivity [26], triangles - RNS results; dashed line - numerical results when the steel properties for the wall conductivity have been used (adjoint problem); here  $\Delta T$  is a temperature difference between locations marked as 1 and 2 in (a). Both the NS and RNS solutions are nearly identical here.

The residuals of numerical solutions in the momentum equation (1) are presented in Fig. 1b. It shows one to two order reductions for the RNS solution residual in the boundary layer, compared to the NS solution residual.

**Flow over a backward facing step.** The numerical results for a 2D flow over a backward facing step of height  $H$ ,  $H = L/3$  ( $L$  is a channel height) at  $Re = 4.4 \cdot 10^4$  (or  $Re_L = 1.32 \cdot 10^5$  in [24]) were obtained and compared with the experimental measurements of [23]. We used a  $110 \times 60$  mesh, refined near the walls, and started the computations at a low Reynolds number. We raised  $Re$  in small increments until reaching 44,000. Fig. 2(a) presents the computed velocity profile, at  $x = 5.33H$  ( $x = 0$  at the edge of the step), and the experimental mean velocity measurements [23].

The RNS model output satisfactorily agrees with the experimental data for both the velocity profile and the recirculation zone length  $X_r$ . We computed  $X_r/H = 7.50$ , while  $X_r^{exp}/H \approx 7 \pm 0.5$  was obtained experimentally. The value of  $\tau^*$  used in the computations was in the range of  $10^{-2}$  to  $10^{-4}$ . This did not noticeably influence the results. For smaller values of  $\tau^*$ , it was more difficult to reach the steady state solution at  $Re = 44,000$ ; more and smaller increments in  $Re$  had to be used. If the increments in the  $Re$  number were large, the flow pattern bifurcated to an unsteady flow, with vortices periodically originating from the recirculation zone and flowing downstream.

The solution with a standard  $k - \epsilon$  model shows the velocity profile at  $x = 5.33$  that has no backward flow. A standard  $k - \epsilon$  model underpredicts the recirculation zone length  $X_r$  by a substantial amount, 20-25% according to [24], where more sophisticated turbulence models have been proposed for this problem.

**Flow in a 2D channel**, of height  $H = 1$  and length  $L = 4$ , was the subject of a few experiments with the RNS at Reynolds numbers  $Re = 5 \cdot 10^3$ ,  $10^4$ ,  $10^5$  and  $10^6$ . An  $81 \times 100$  mesh refined near the walls was used. Inlet flow profiles were (i)  $U = 1$ , and (ii)  $U = 6z(1 - z)$ . We were obtained both parabolic and "turbulent" flow profiles for  $Re$  up to  $10^5$ , depending on the inlet flow conditions and the value of  $\tau^*$ . To obtain a "turbulent" flow profile at  $Re = 5,000$ , with the inlet condition (ii), we started with  $\tau^* = 0.01$ , and were then able to keep this "turbulent" profile type at reduced  $\tau^*$ , down to  $10^{-4}$  (Fig. 2b). The boundary layer thickness is about  $\delta \sim Re^{-1/2}$  (obtained graphically from Fig. 2b).

**3D Thermal convection in a differentially heated horizontal cylinder.** A linear temperature profile is given assumed on a cylinder wall. Experimental data by Bogatirev et al. [27] and finite volume simulations by Bessonov [26] are used for comparison at Rayleigh numbers in the range of  $10^3$  to  $1.2 \cdot 10^5$ ,  $Pr = 0.9$  (Fig. 3a). For the linear temperature distribution on a cylinder wall, we obtained good agreement with the numerical results [26]. We used a 17,4357 node hexaedral mesh refined near the walls. Agreement with the experimental data was not good for  $Ra > 2000$  (solid line in Fig. 3b). Therefore computations were done for a real, finite wall conductivity [26]. The thermodiffusivity data for stainless steel was used, and the adjoint problem was solved. Thereby, agreement with the experimental data has been significantly improved (Fig. 3b, dashed line). The value of  $\tau^*$  used was  $10^{-7}$  to  $10^{-3}$ , which did not noticeably affect the RNS results.

**Magnetic field suppression of the semiconductor melt flow**, modeling with RNS, is considered in [13] and [14]. The application of magnetic fields is a promising approach for reducing convection during directional solidification of electrically conductive melts. Current technology allows for experiments using very strong static fields, for which nearly convection free segregation is expected in melts exposed to stabilizing temperature gradients (vertical Bridgman

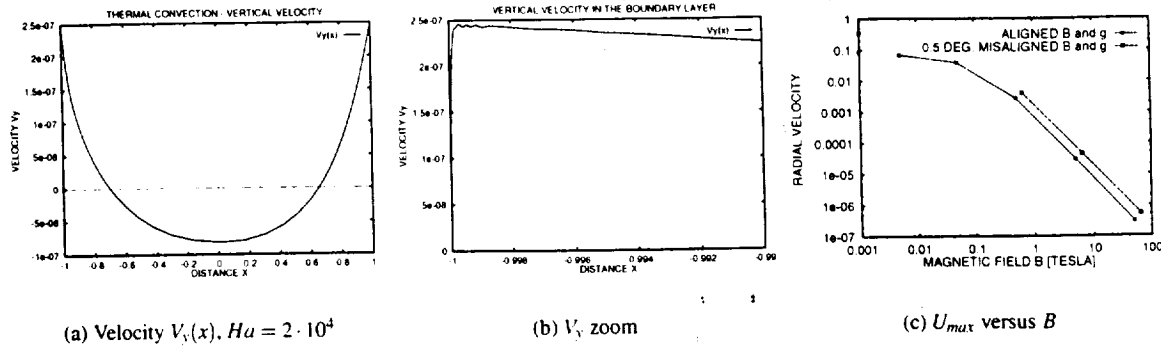


Figure 4: (a) Vertical velocity profile  $V_y(x)$  at  $y = 0.25H$ ,  $x$  in  $[-1, 1]$ ,  $Ha = 2.2 \cdot 10^4$  ( $B = 50$  Tesla); (b) details of the velocity profile (a) in a boundary layer,  $x$  from  $-1$  to  $-0.99$ ; (c) Summary: maximum value of horizontal velocity magnitude versus magnetic field  $B$  for aligned and misaligned by  $0.5$  degree magnetic field and gravity vectors. Predicted theoretical asymptotic  $U_{max} \sim Ha^{-2}$  is observed starting from  $B = 0.5$  Tesla ( $Ha = 220$ ).

method) [28]. The governing equations solved for this problem are eqs. (1), (3), and (4), where  $\mathbf{F}$ , the body force due to the magnetic field (Lorenz force), is given by

$$\mathbf{F} = PrHa^2[(\mathbf{V} \times \mathbf{e}_B) \times \mathbf{e}_B]. \quad (6)$$

Here  $\mathbf{F} = (Pr(Ha)^2 U, 0)$  for the 2D case of a vertical magnetic field and  $U$  is the horizontal component of the velocity. The Hartmann number, given by  $Ha = LB_0 \sqrt{\frac{\sigma}{\rho \eta}}$ , is in the range of  $Ha = 100$  to  $10^4$ , for the materials and magnetic fields under investigation. Here  $\rho, \sigma$  are the density and electrical conductivity,  $B_0$  is the magnetic field intensity, and  $\mathbf{e}_B$  is the unit vector in the direction of the magnetic field.

The computations are difficult because of the thin boundary layer, although the velocity of the generated flows is extremely low,  $Re \sim 10^{-1}$  to  $10^{-6}$ . A high value of the Hartmann number results in a relatively small coefficient at the highest derivative of the velocity in the momentum equation. Solutions of such problems exhibit thin boundary layers of thickness  $\delta \sim Ha^{-1}$ , along with "equivalent" Reynolds number  $Re_{eqv} \sim Ha^2$ ,  $Re_{eqv} = 4 \cdot 10^4$  for  $B=0.5$  Tesla, and  $Re_{eqv} = 4 \cdot 10^8$  for  $B=50$  Tesla. Some of the results for 2D models are shown in Fig. 4. The RNS numerical solution is rather smooth even for a very thin boundary layer, with thickness  $\delta \sim 10^{-4}$  ( $Ha = 2 \cdot 10^4$ ). Other methods tested in [13], [14] (including industrial code) did not provide acceptable results or failed for  $Ha > 100$ .

## Conclusions

The RNS method was reviewed with applications to 2D and 3D flows at high Reynolds number and flows with thin boundary layers. The numerical results compared favorably with experimental data for driven cavity flow, flows in channels, thermal convection, and asymptotic solutions for electrically conductive fluid flows under strong magnetic fields. The RNS method is used for modeling 3D thermo-vibrational convection in Bridgman melt configurations [15]. Similar ideas have been used successfully to improve the accuracy of the meshless multiquadric radial-basis function methods [29], [30].

## References

- [1] G. I. SHISHKIN, J. Math. Anal. Appl., **208** (1997) 181-197.
- [2] K. R. KOSEFF and R. L. STREET, Trans. ASME/Journal of Fluids Engineering **106** (1984) 390-398.
- [3] U. GHIA, K.N. GHIA and C. T. SHIN, J. Comp. Phys., **48** (1982) 387-411.
- [4] S. S. KUTATELADZE et al., Int. J. Heat and Mass Transfer, **15** (1977) 193-202.
- [5] V. I. POLEZHAEV et al., Lecture Notes in Physics, **90** (1978) 454-459.
- [6] S. SUNDARESAN et al., Proc. of 16th ICNMF Conf., C.H. Brunau, Ed., Lect. Notes Phys., **515** (1998) 231-236.

- [7] Y.C. HON, Int. J. Appl. Sci. Comput., **6**, No. 3 (1999).
- [8] B. V. Alexeev, The generalized Boltzmann equation, generalized hydrodynamic equations and their applications. Phil. Trans. Roy. Soc. London, A. **349** (1994), 417-443.
- [9] B.V. Alexeev, Physical principles of the generalized Boltzmann kinetic theory of gases, Physics-Uspekhi, **43**(2000)
- [10] A. I. FEDOSEYEV, B. V. ALEXEEV, *Continuum Models and Discrete Systems*, Ed. by E. Inan and A. Markov, World Scientific, London, 1998, 130-137.
- [11] A.I. FEDOSEYEV and B.V. ALEXEEV, *Proc. IMACS98, Advances in Scientific Computing and Modeling*, Ed. by S.K. Dey, J. Ziebarth, and M. Ferrandiz, University of Alicante, Spain, 1998, 158-163.
- [12] A. I. FEDOSEYEV, A regularization approach to solving the Navier-Stokes Equations for Problems with Boundary Layer, CFD Journal, **9**, No.1 (2000) (in print).
- [13] A. I. Fedoseyev, E. J. Kansa, C. Marin, A.G. Ostrogorsky, Magnetic field suppression of semiconductor melt flow in crystal growth: comparison of three methods for numerical modeling, CFD Journal , **9**, No.1 (2000)(in print).
- [14] A. I. Fedoseyev, E. J. Kansa, C. Marin, M. Volz, A.G. Ostrogorsky, AIAA Paper 2000-0698.
- [15] A.I. Fedoseyev and J.I.D. Alexander, Investigation of Vibrational Control of Convective Flows in Bridgman Melt Growth Configurations, J. of Crystal Growth. **211**, (2000) 34-42.
- [16] R. LÖHNER, In: *Incompressible computational fluid dynamics*, Ed. by M. D. Gunzberger and R. A. Nicolaides, Cambridge Press, 1993, 267-294.
- [17] T. G. Elizarova, B. N. Chetverushkin, in: *Mathematical Simulation*, Eds A. A. Samarski et al., Moscow: Nauka, 1986, 261.
- [18] B. N. Chetverushkin, Kinematically consistent numerical schemes, Moscow State Univ., Moscow, 1999, 232p.
- [19] Yu. L. Klimontovich, Statistical Theory of Open Systems, In: *Fundamental Theories of Physics*, **67** (1995), Dordrecht: Kluwer Acad. Publ., 1995.
- [20] V. I. Polezhaev, A. I. Prostomolotov, A. I. Fedoseyev. Finite Element Method in Viscous Fluid Mechanics Problems, In: *Advances in Science and Technology, Fluid Mechanics series*, **21**, No. 3, VINITI, Moscow, 1987.
- [21] A. G. Daykovsky, V. I. Polezhaev, A. I. Fedoseyev, Fluid Dynamics, **13** (1978) 846 - 854.
- [22] J. S. Baggett, L. N. Trefethen, Physics of Fluids, **9**, (1997)1043.
- [23] J. KIM, S. J. KLINE, and J. P. JOHNSTON. ASME J. Fluids Engng., **102**, 1980, 302-308.
- [24] S. Thangam and C. G. Speziale. ICASE Report 91-23, NASA Langley, Hampton, Virginia, 1991.
- [25] M. ZIJLEMA, A. SEGAL AND P. WESSELING, Report DUT-TWI-94-24, The Netherlands, 1994.
- [26] O.A. Bessonov, et al., Numerical Simulation of Convective Processes in the "Dacon" Sensor for Realistic Space Flight Conditions, Cosmic Research, No.2, 2001(accepted); V.V. Sazonov et al., AIAA 2000-0569 paper.
- [27] G. P. Bogatirev, G. F. Putin, V. I. Polezhaev. A System for Measurement of Convection aboard Space Station, Proc. 3rd Microgravity Fluid Physics Conf., Cleveland, Ohio, July 13-15, 1996, NASA Conf. Publ., 813-818.
- [28] J. P. Garandet and T. Alboussiere, Bridgman growth: Modeling and experiments, In: "The role of magnetic field in Crystal Growth", Pergamon Press (to be published).
- [29] A.I. Fedoseyev, M.J. Friedman, and E.J. Kansa, Continuation for Nonlinear Elliptic Partial Differential Equations Discretized by the Multiquadric Method, Int. J. Bifur. Chaos, **10**, No. 2, (2000) 481-492
- [30] A.I. Fedoseyev, M.J. Friedman, and E.J. Kansa, Improved Multiquadric Method for Elliptic Partial Differential Equations via PDE Collocation on the Boundary, Comput. Math. Applic. (2001),(accepted).